

PARITY-VIOLATING ASYMMETRY IN THE NUCLEON TO  $\Delta$   
TRANSITION

A Study of Inelastic Electron Scattering in the  $G^0$  Experiment

Carissa Lee Capuano

Virginia Beach, Virginia

Master of Science, The College of William and Mary, 2005

Bachelor of Science, Christopher Newport University, 2002

A Dissertation presented to the Graduate Faculty  
of the College of William and Mary in Candidacy for the Degree of  
Doctor of Philosophy

Department of Physics

The College of William and Mary

January, 2012

© Copyright 2012 Carissa Lee Capuano

All Rights Reserved

## APPROVAL PAGE

This Dissertation is submitted in partial fulfillment of  
the requirements for the degree of

Doctor of Philosophy

---

Carissa Lee Capuano

Approved by the Committee, November, 2011

---

Committee Chair

Professor David S. Armstrong, Physics  
College of William and Mary

---

Professor Todd D. Averett, Physics  
College of William and Mary

---

Associate Professor Joshua Erlich, Physics  
College of William and Mary

---

Assistant Professor Michael A. Kordosky, Physics  
College of William and Mary

---

Dr. Stephen A. Wood  
Hall C Leader, Jefferson Lab

## ABSTRACT PAGE

The parity-violating asymmetry arising from inelastic electron scattering at backward angle ( $\sim 95^\circ$ ) near the  $\Delta$  resonance has been measured for both hydrogen and deuterium targets as part of the  $G^0$  experiment. For  $Q^2 = 0.34$  (GeV/c) $^2$  and  $W = 1.18$  GeV, the asymmetries were found to be

$$A_{inel}^H = -33.4 \pm (5.3)_{stat} \pm (5.1)_{sys} \text{ ppm} ,$$
$$A_{inel}^D = -43.6 \pm (14.6)_{stat} \pm (6.2)_{sys} \text{ ppm} .$$

From the hydrogen asymmetry, the axial transition form factor,  $G_{N\Delta}^A$ , can be extracted.  $G_{N\Delta}^A$  is related to probability of the quark spin-flip that occurs as the proton transitions to the  $\Delta$ . From the measured asymmetry, the form factor is found to be

$$G_{N\Delta}^A = -0.046 \pm (0.35)_{stat} \pm (0.34)_{sys} \pm (0.06)_{theory} .$$

Though  $G_{N\Delta}^A$  has been previously studied using charged current reactions, the  $G^0$  measurement represents the first measurement of the asymmetry in the neutral weak sector. These findings agree within errors with the theoretical predictions.

## TABLE OF CONTENTS

	Page
<b>List of Tables</b> . . . . .	<b>vi</b>
<b>List of Figures</b> . . . . .	<b>viii</b>
<b>Acknowledgments</b> . . . . .	<b>xiii</b>
 <b>CHAPTER</b>	
<b>1 Introduction</b> . . . . .	<b>1</b>
1.1 The Electroweak Interaction and Parity Violation . . . . .	2
1.2 Form Factors and Parity-Violating Asymmetry . . . . .	5
1.3 The $\Delta$ Resonance . . . . .	7
1.4 The $G^0$ Experiment . . . . .	9
1.5 Summary . . . . .	11
<b>2 Theory</b> . . . . .	<b>13</b>
2.1 General Expression for the Asymmetry . . . . .	14
2.1.1 Elastic Scattering . . . . .	18
2.1.2 Inelastic Scattering - Resonant $\Delta$ Electroproduction . . . . .	20
2.2 $G^0$ Elastic Measurement: Strange Form Factors . . . . .	25
2.3 Full Inelastic Asymmetry Model . . . . .	28
2.3.1 Notation . . . . .	31
2.3.2 Resonant Vector Term, $\Delta_{(1)}^\pi$ . . . . .	34

2.3.3	Non-Resonant Vector Term, $\Delta_{(2)}^\pi$ . . . . .	34
2.3.4	Axial Term, $\Delta_{(3)}^\pi$ . . . . .	37
2.3.5	Secondary Inelastic Model . . . . .	45
2.4	Inelastic Asymmetry at the $Q^2 = 0$ limit . . . . .	47
2.5	Summary . . . . .	51
<b>3</b>	<b>The <math>G^0</math> Experiment at Backward Angle . . . . .</b>	<b>54</b>
3.1	Experimental Design Overview . . . . .	55
3.2	The Electron Beam . . . . .	56
3.2.1	Polarized Source and Injector . . . . .	58
3.2.2	Accelerator . . . . .	62
3.3	Beam Monitoring . . . . .	63
3.4	Polarimetry . . . . .	67
3.4.1	The Møller Polarimeter . . . . .	68
3.4.2	The Mott Polarimeter . . . . .	71
3.4.3	Measurements and Conclusion . . . . .	72
3.5	The $G^0$ Experiment . . . . .	74
3.5.1	Target . . . . .	75
3.5.2	Superconducting Magnet System (SMS) . . . . .	79
3.5.3	Detectors . . . . .	81
3.5.4	Electronics . . . . .	91
3.6	Data Acquisition and Online Analysis . . . . .	95
3.7	Data . . . . .	97
3.7.1	Data Collected for Background Studies . . . . .	102

<b>4</b>	<b>Data Analysis: Corrections for Beam and Instrumentation . . . . .</b>	<b>105</b>
4.1	Data Blinding . . . . .	106
4.2	The Analyzer: g0analysis . . . . .	108
4.2.1	Analysis Pass 1: Raw Pass . . . . .	109
4.2.2	Analysis Pass 2: Scaler Counting Correction . . . . .	110
4.2.3	Analysis Pass 3: Rate Corrections . . . . .	114
4.2.4	Analysis Pass 4: Helicity-Related Beam Properties . . . . .	124
4.3	Data Quality . . . . .	126
4.3.1	Bad PMTs . . . . .	127
4.3.2	Bad Octants . . . . .	128
4.4	Beam Polarization Corrections . . . . .	129
4.4.1	Longitudinal Beam Polarization Correction . . . . .	129
4.4.2	Transverse Beam Polarization Correction . . . . .	130
4.5	Summary of Beam and Instrumentation Corrections . . . . .	136
<b>5</b>	<b>Data Analysis: Corrections for Backgrounds and Radiative Effects . . .</b>	<b>138</b>
5.1	The <i>G0GEANT</i> Simulation . . . . .	139
5.1.1	Cross Section Models . . . . .	140
5.1.2	Inelastic Asymmetry Models . . . . .	142
5.2	Background Correction . . . . .	145
5.2.1	Contributing Processes . . . . .	147
5.2.2	Determining the Dilution Factors . . . . .	155
5.2.3	Determining the Dilution Factor Uncertainty . . . . .	163
5.2.4	Summary of Dilution Factors . . . . .	167
5.2.5	Applying the Correction to the Asymmetry . . . . .	174

5.2.6	Background Correction Summary . . . . .	179
5.3	Radiative Corrections . . . . .	185
5.3.1	Electromagnetic Radiative Corrections . . . . .	187
5.3.2	Electroweak Radiative Corrections . . . . .	189
5.4	Acceptance Averaging . . . . .	191
5.5	Final Corrected Asymmetry . . . . .	193
<b>6</b>	<b>Theoretical Asymmetry and Interpretation of Results . . . . .</b>	<b>195</b>
6.1	Theoretical Asymmetry . . . . .	196
6.1.1	Computing $A_{theory}$ . . . . .	196
6.1.2	Electroweak Radiative Corrections . . . . .	203
6.1.3	Corrected Theoretical Asymmetry . . . . .	208
6.2	Theoretical Uncertainty . . . . .	210
6.2.1	Uncertainty on $\Delta_{(2)}^\pi$ . . . . .	210
6.2.2	Uncertainty in the Axial Term . . . . .	213
6.2.3	Summary of Theoretical Uncertainty . . . . .	214
6.3	Extracting the Axial Contribution from $A_{inel}$ . . . . .	215
6.4	Additional Extracted Quantities . . . . .	221
6.4.1	Axial Mass . . . . .	221
6.4.2	Standard Model Test . . . . .	222
6.4.3	Electroweak Radiative Effects: Anapole and Siegert terms . . . . .	224
<b>7</b>	<b>Conclusion . . . . .</b>	<b>226</b>
7.1	Potential Improvements . . . . .	227
7.2	Final Summary . . . . .	229
<b>APPENDIX A</b>		
	<b>Experimental Kinematics . . . . .</b>	<b>231</b>

**APPENDIX B**

**Details of the Scaler Counting Problem and the Correction Applied . . . . . 239**

B.1 Discovery and Diagnosis of the Problem . . . . . 240

    B.1.1 Impact on the Data . . . . . 242

    B.1.2 Testing the Electronics . . . . . 244

    B.1.3 Description of the Problem . . . . . 246

    B.1.4 Possible Causes of the Narrow Signals . . . . . 249

    B.1.5 Solution . . . . . 250

B.2 Applying a Correction . . . . . 250

    B.2.1 Determining the Size of the Cut . . . . . 251

    B.2.2 Applying the Correction: Locus vs. Cell-by-cell . . . . . 255

    B.2.3 Residual False Asymmetry . . . . . 260

B.3 Conclusion . . . . . 262

**APPENDIX C**

**Background Correction . . . . . 265**

C.1 Contributions to the Yield . . . . . 265

C.2 Comparisons to Other Methods . . . . . 270

**Bibliography . . . . . 275**

## LIST OF TABLES

Table		Page
1.1	Summary of the $\Delta$ . . . . .	7
3.1	Summary of $G^0$ beam specifications. . . . .	67
3.2	Summary of $G^0$ data. . . . .	98
4.1	Summary of blinding factors. . . . .	107
4.2	Summary of false asymmetries due to detector dead time for the elastic locus . . . . .	120
4.3	Elastic locus averages for fractions of pions ( $f_\pi$ ), Cherenkov randoms ( $f_e$ ) and CED·FPD randoms ( $f_{rdm}$ ) in the electron matrix . . . . .	124
4.4	Fit parameters for the measured inelastic transverse asymmetry as a function of octant. . . . .	133
4.5	Longitudinal and transverse LUMI asymmetries and their ratio for both data sets. . . . .	133
4.6	Estimate of the detector misalignment, $M_{det}$ . . . . .	136
4.7	Inelastic asymmetry following each stage of beam and instrumentation corrections applied. . . . .	137
5.1	Summary of errors on the dilution factors for each process. . . . .	166
5.2	Per octant total background dilutions for the elastic and inelastic loci . . .	169
5.3	Summary of simulated elastic asymmetry, averaged across the elastic and inelastic loci. . . . .	178
5.4	Inelastic asymmetry with error before and after applying the background correction. . . . .	180

5.5	Summary of the asymmetry error study . . . . .	182
5.6	Background corrected inelastic locus asymmetry for various locus definitions . . . . .	184
5.7	Comparison of the final corrected elastic asymmetry using two different methods to determine the backgrounds . . . . .	186
5.8	Summary of average kinematics determined from simulation . . . . .	192
5.9	Summary of simulated $\langle A(P_i) \rangle$ and $A(\langle P_i \rangle)$ . . . . .	193
5.10	Inelastic asymmetry following each stage of corrections applied. . . . .	194
6.1	Current world values for the quantities associated with the Standard Model couplings at tree level and with electroweak radiative effects included. . .	205
6.2	Summary of the theoretical asymmetry components with and without electroweak radiative corrections. . . . .	209
6.3	$A_3$ computed using different values for $C_i^\gamma$ at $Q^2 = 0$ . . . . .	215
6.4	Summary of theoretical uncertainties. . . . .	216
6.5	Summary of quantities needed to extract $A_3$ and $G_{N\Delta}^A$ from $A_{inel}$ . . . . .	219
B.1	D 362: Elastic locus average RCS for each octant after applying the scaler counting correction using different cut values. . . . .	254
B.2	D 362: Percentage of quartets cut from the elastic locus by the scaler counting correction for several cut values . . . . .	256
B.3	D 362: Octant average elastic locus asymmetry after applying the scaler counting correction using different cut values. . . . .	257
B.4	D 362: NA and FR octant average elastic locus asymmetry after applying the scaler counting correction using different cut values. . . . .	258
B.5	D 362: Comparison of percentage of quartets removed by scaler counting correction between locus cut and cell cut. . . . .	259
B.6	Asymmetries from all run periods with and without the scaler counting correction applied. . . . .	264
C.1	Per octant inelastic dilution factors for the elastic and inelastic loci. . . . .	267
C.2	Per octant elastic dilution factors for the elastic and inelastic loci. . . . .	267
C.3	Per octant $\pi^0$ decay dilution factors for the elastic and inelastic loci. . . . .	268
C.4	Per octant empty target dilution factors for the elastic and inelastic loci. . . . .	268

## LIST OF FIGURES

Figure	Page
1.1	Diagrams of electron-nucleon scattering for both the electromagnetic and neutral weak interactions. . . . . 4
1.2	Cross section data from inclusive inelastic $ep$ scattering. . . . . 9
2.1	Diagram of an electron scattering from a nucleon. . . . . 14
2.2	Sample diagram of a resonant interaction . . . . . 30
2.3	Axial term of the asymmetry, $A_3$ , as a function of axial mass, $M_A$ . . . . . 44
2.4	Theoretical asymmetry as a function of $Q^2$ . . . . . 52
3.1	$G^0$ experimental setup for the backward angle phase. . . . . 57
3.2	Diagram of Jefferson Lab's CEBAF accelerator. . . . . 58
3.3	Diagram of the Hall C laser table at Jefferson Lab's CEBAF . . . . . 59
3.4	Layout of the Hall C Møller Polarimeter. . . . . 69
3.5	Layout of the 5 MeV Injector Mott Polarimeter at Jefferson Lab. . . . . 72
3.6	Measurements taken with the Hall C Møller for $G^0$ at a beam energy of $\sim 687$ MeV. . . . . 73
3.7	Measurements taken with the 5 MeV injector Mott for $G^0$ . . . . . 74
3.8	Photograph of $G^0$ experimental apparatus in the backward-angle configuration installed in Hall C. . . . . 75
3.9	Diagram of the $G^0$ target loop. . . . . 76
3.10	The $G^0$ detector system for a single octant shown with sample particle trajectories. . . . . 83
3.11	Photograph of full $G^0$ backward angle detector system in Hall C. . . . . 85
3.12	Photograph of FPDs for a single octant. . . . . 86
3.13	Diagram and photo of a single $G^0$ Cherenkov detector. . . . . 89

3.14	Octant averaged electron yields for the high energy hydrogen and deuterium run periods. . . . .	99
3.15	Octant averaged pion yields for the high energy hydrogen and deuterium run periods . . . . .	99
3.16	Simulated $Q^2$ , $W$ and $\theta$ distributions for hydrogen . . . . .	101
4.1	Overview of the analysis strategy employed to determine $G_{N\Delta}^A$ . . . . .	106
4.2	Comparison of quartet Yield and Asymmetry in a single cell for data affected by the scaler counting problem . . . . .	111
4.3	Comparison of Pass 1 and Pass 2 quartet Yield and Asymmetry in a single cell . . . . .	113
4.4	Measured inelastic transverse asymmetry as a function of octant for hydrogen and deuterium . . . . .	132
4.5	LUMI asymmetry, both transverse and longitudinal, as a function of octant for hydrogen and deuterium . . . . .	134
5.1	Pion contamination values cell by cell for the entire matrix . . . . .	153
5.2	Fit result for the hydrogen CED 2 yields as a function of FPD . . . . .	157
5.3	Fit result for the hydrogen CED 4 yields as a function of FPD . . . . .	158
5.4	Fit result for the deuterium CED 1 yields as a function of FPD . . . . .	159
5.5	Fit result for the deuterium CED 3 yields as a function of FPD . . . . .	160
5.6	Scale factor as a function of CED for the hydrogen simulated processes .	161
5.7	Scale factor as a function of CED for the deuterium simulated processes .	162
5.8	Cell dilutions for the total H inelastic background . . . . .	170
5.9	Cell dilutions for the total D inelastic background . . . . .	171
5.10	Inelastic locus sum dilutions for each individual process as a function of octant for the hydrogen target. . . . .	172
5.11	Inelastic locus sum dilutions for each individual process as a function of octant for the deuterium target. . . . .	173
5.12	Comparison of inelastic method, field scan method and matrix fit method elastic locus dilutions for hydrogen . . . . .	175
5.13	Comparison of inelastic method and field scan method elastic locus dilutions for deuterium . . . . .	176
5.14	Cell by cell simulated elastic asymmetry for H and D. . . . .	177
5.15	Diagrams of lowest order EM radiative corrections . . . . .	187

6.1	Simulated inelastic asymmetry distributions for events in all inelastic locus cells. . . . .	198
6.2	Cell-by-cell plot of simulated inelastic asymmetry. . . . .	199
6.3	Theoretical calculation for each of the three asymmetry terms as a function of $Q^2$ . . . . .	200
6.4	Simulated $A_2$ distribution for the Musolf and Matsui models. . . . .	201
6.5	Simulated $A_3$ distribution for the Musolf and Matsui models. . . . .	202
6.6	Theoretical asymmetry as a function of $Q^2$ for $A_2$ and $A_3$ for both models. . . . .	203
6.7	Ratio of the contribution from total axial and multi-quark electroweak radiative corrections to the total asymmetry as a function of $Q^2$ . . . . .	209
6.8	Measured asymmetry, $A_{inel}$ , plotted with the theoretical value from the Musolf model. . . . .	217
6.9	Theoretical $A_3$ as a function of $Q^2$ with the extracted value and error shown as a point. . . . .	218
6.10	Extracted value of $A_3$ plotted with the theoretical $A_3$ as a function of axial mass, $M_A$ . . . . .	222
A.1	Simulated $Q^2$ distributions for the hydrogen and deuterium targets. . . . .	232
A.2	Simulated $W$ distributions for the hydrogen and deuterium targets. . . . .	233
A.3	Simulated $\theta$ distributions for the hydrogen and deuterium targets. . . . .	234
A.4	Simulated $E$ distributions for the hydrogen and deuterium targets. . . . .	235
A.5	Simulated $E'$ distributions for the hydrogen and deuterium targets. . . . .	236
A.6	Simulated cell-by-cell $Q^2$ distribution for the hydrogen and deuterium targets. . . . .	237
A.7	Simulated cell-by-cell $W$ distribution for the hydrogen and deuterium targets. . . . .	238
B.1	RCS values as a function of run number for each octant for runs performed during the D 362 run period before the scaler counting problem was solved. . . . .	241
B.2	MPS yield distributions for selected elastic locus cells in a typical NA octant. . . . .	242
B.3	Quartet asymmetry distributions for selected elastic locus cells in a typical NA octant. . . . .	243

B.4	MPS yield distribution for a single cell for runs taken at different beam currents . . . . .	245
B.5	Example of timing that leads to the scaler counting problem . . . . .	248
B.6	Comparison of Pass 2 corrected quartet Yield and Asymmetry in a single cell for different cut values . . . . .	252
B.7	Corrected octant-by-octant RCS as a function of run number for the entire D 362 run period. . . . .	263
C.1	Cell dilution factors for each individual process for all octants for H . . .	266
C.2	Cell dilution factors for each individual process for all octants for D . . .	269
C.3	Comparison of inelastic, field scan and matrix fit method total dilution factors for individual inelastic locus cells . . . . .	271
C.4	Comparison of inelastic, field scan and matrix fit method hydrogen dilution factors for each process for inelastic locus cells . . . . .	272
C.5	Comparison of inelastic method, field scan method and matrix fit method elastic dilution factors cell-by-cell for hydrogen . . . . .	273
C.6	Comparison of inelastic method and field scan method elastic dilution factors cell-by-cell for deuterium . . . . .	274

To my mother

## ACKNOWLEDGMENTS

This thesis is the culmination of many years of work that was completed with the assistance, both direct and indirect, of many people, including professors, peers, friends and family. I should say up front that I'm not very good with these sorts of things, but I will try my best to convey my gratitude.

I would first like to thank my advisor, David Armstrong, for his help and support throughout the years. Thank you for your guidance both in determining the direction I would take with my research and in completing the task once it had been decided. Thank you for your calming words when the stress of grad school was overwhelming me. To my thesis and annual review committees, thank you all for your input and advice, both during this final phase and over the years in annual reviews. To my professors at William and Mary, CNU and TCC, I thank you for all the guidance throughout the years, for pushing me to work hard, and for giving me the tools needed to prepare me for the future. It wasn't always easy, but things worth doing rarely are.

To the administrative staff in the Physics Department at William and Mary, thank you for all that you do in keeping things running smoothly. To Paula Perry, thank you for your patience and for always being available to answer my questions and help me when I was struggling to make my way through paperwork and guidelines. To Sylvia Stout and Carol Hankins, thank you for all of your help throughout the years.

I also want to thank Doug Beck, Betsy Beise and the rest of the  $G^0$  collaboration for their help and support both during the experimental run and during the analysis phase. To Steve Wells, thank you for your help with theoretical interpretations and for your input on this thesis. To Fatiha Benmokhtar, thank you for all of your help and encouragement. To my fellow  $G^0$  grad students, Juliette Mammei, Colleen Ellis, Maud Versteegen, Mathew Muether, Alex Coppens, and John Schaub, I enjoyed working with all of you and wish you the best of luck in your lives and careers.

To Sadie Tedder and Angie Cutshaw, thank you both for your friendship and for helping me to survive grad school. To Sadie, you helped me get started on writing this

thesis when I was struggling with where to begin. To Angie, my “study buddy”, I never could have passed the qualifier without you - that is no exaggeration. I learned more during the time we spent studying and working through problems than I did in some of the classes I’ve taken.

To the rest of my friends, you know who you are. I have spent many a night ranting to you over the years about the work, the professors or that stupid homework problem that I just couldn’t figure out. The level of whining increased as the thesis and defense deadlines approached, yet I could always find a shoulder to cry on and an encouraging word. Thank you for all the times you told me “You can do it!” and for helping me to relax when the stress was too much to handle. Thank you for the countless hours of silly, pointless conversations about nothing and for the deeper conversations that had meaning. Thank you for the fun times with meerkats and leopards, and the beast that rules them all, and for the birds and the midgets that are three apples tall.

Finally, I want to thank my family for all the love and support they have provided throughout this process. The last several years were a very trying time for me in many ways and for many different reasons. Without having my family to lean on, I never would have made it through. To my sisters Amy and Julie, and my niece Cyndi, you were always supportive and available for those times when I needed a kind word, a distraction and a little fun. Thank you guys for keeping me (mostly) sane.

Most importantly, I want to thank my mother, Sandy, for everything she has done for me. Things were not always easy for our family and she had a lot on her plate at any given time - raising three daughters is no easy task. I am where I am today because of her support and the solid foundation that she provided for me. She taught me to be independent and to think for myself, to work hard and to always do the right thing. Thank you, Mom, for always being there. Thank you for listening, for your advice and the occasional humoring head-nod when I went on vaguely about subjects you knew nothing about. Thank you for trying to solve my problems even when the situation was out of your hands. I love you and appreciate everything that you have done for me. While university professors imparted the knowledge to excel in a career, you imparted the wisdom needed to survive in this very imperfect world. The value of what you have given me cannot be quantified.

# CHAPTER 1

## Introduction

Scattering experiments have long been used to measure the properties of particles and nuclei. Electron scattering experiments are particularly useful because the reactions are dominated by the well-defined electromagnetic interaction. The use of electron scattering to measure cross sections as a way of determining nuclear structure was first accomplished by Lyman, Hansen and Scott in 1951 [1]. An additional benefit of electron scattering is that the electrons offer a non-intrusive probe that allows access to the quarks contained within nucleons and other hadrons. As such, electron scattering has proven to be valuable in the study of how quarks contribute to the structure of hadrons.

An electron scattering experiment involving a longitudinally polarized electron beam scattering from unpolarized proton and deuteron targets was performed at Jefferson Lab by the  $G^0$  collaboration. The  $G^0$  experiment measured parity-violating asymmetries in elastic and inelastic  $ep$  and  $ed$  scattering, and pion photoproduction on deuterium. Additional measurements of the parity-conserving asymmetry in elastic  $ep$  and  $ed$  scattering using transversely polarized electrons were also performed and used to study the  $2\gamma$

exchange. The determination of the inelastic parity-violating asymmetry, which is dominated at the  $G^0$  kinematics by resonant electroproduction of the  $\Delta$  particle, will be the topic of this thesis. In this chapter, a brief introduction of the topic of electroweak interactions and the parity-violating asymmetry that arises from electroweak interference will be presented. Details of the asymmetry model and the  $G^0$  measurement will be given in later chapters.

## 1.1 The Electroweak Interaction and Parity Violation

The weak interaction is a short-range interaction that describes particle decay and other reactions involving changes to quark flavor and spin within hadrons. The interaction is carried by one of two gauge bosons, the  $Z^0$  or  $W^\pm$ . The  $W^\pm$  has a mass of  $80.398 \pm 0.023$  GeV [2] and can be either positively or negatively charged, depending on the reaction. The  $Z^0$  is a neutral boson with a mass of  $91.188 \pm 0.0021$  GeV [2]. The two are related through the weak mixing angle,  $\theta_W$ , according to

$$M_W^2 = M_Z^2 \cos^2 \theta_W . \quad (1.1)$$

The presence of two different gauge bosons with different charges leads to two different types of weak interactions. Weak interactions involving the neutral  $Z^0$ , called neutral current weak interactions, can change the intrinsic spin of the hadron without changing its charge. In the constituent quark model, the change in intrinsic spin is due to the  $Z^0$  interacting with one of the constituent quarks in the hadron and flipping its spin. Interactions involving the  $W^\pm$  gauge bosons are referred to as charged current weak interactions. Charged current interactions can not only result in a spin flip but also in a change of the hadron's charge. The change in hadron charge is the result of the  $W$  boson interacting

with one of the constituent quarks and changing its flavor. A change in intrinsic (or quark) spin is also possible in charged current interactions.

The weak interaction is unique among the other fundamental interactions in that it violates parity, which means that it does not treat all particles the same under spatial inversion. The first experimental evidence of parity violation was observed in decays of the  $K^+$  meson which lead to two possible final states that have differing parity, a result that would not be possible if parity were conserved [3]. In the late 1950's, measurements of nuclear  $\beta$  decay [4] and muon decay [5] confirmed that this parity violation existed.

A second discovery made through  $\beta$  decay experiments was that all emitted leptons had negative helicity and the antileptons had positive helicity. This places a constraint on the operator that defines the interaction. Operators that change sign under spatial inversion are referred to as vectors (V), while those that do not change sign are referred to as axial vectors (A). In order to explain the behavior seen in  $\beta$  decay, it is necessary that the weak interaction be described as a combination of vector and axial vector, leading to an operator of the form  $V - A$  [6].

In the case of electron scattering, the parity violation in the weak interaction means that incident electrons with different helicities will interact with target hadrons in a different manner. The end result is that the probability of the hadron interacting with the electron is not independent of helicity. Thus, if one sets up a detector to count the scattered electrons, grouping results by helicity, the two counts will not be equal. The scale of the parity violation is small, on the order of  $10^{-6}$  or parts-per-million (ppm) for the kinematics of the present experiment, but the presence of this parity violation provides a valuable tool with which to measure weak interactions. Unfortunately, the interaction is so weak that such measurements are difficult to make precisely.

The electroweak interaction is a unification of the electromagnetic and weak inter-

actions wherein leptons interact with hadrons through either the electromagnetic or the weak interaction. As was discussed previously, the weak interaction is a combination of vector and axial responses. The electromagnetic interaction, however, is purely vector. When the two interactions are combined, the axial portion of the weak interaction can interfere with the vector electromagnetic interaction. The resulting interaction maintains the  $V - A$  structure of the weak interaction and, as a result, violates parity. Thus, the electroweak interaction can be used to study the effects of parity violation. By coupling the weak interaction to the much stronger electromagnetic interaction, the signal is amplified and the parity violation can be more easily measured. Measurements of the asymmetry that arises from parity violation in neutral current electroweak interactions can be used to study hadronic structure. One such measurement, performed during the  $G^0$  experiment, is the topic of this thesis.

Figure 1.1 contains two Feynman diagrams representing generic electron-nucleon scattering processes involving the electromagnetic and neutral weak interactions. In the weak interaction, the  $V - A$  structure discussed above leads to one of the vertices in Figure 1.1b being described using a vector operator and the other using an axial vector operator. Either vertex can have either operator structure.

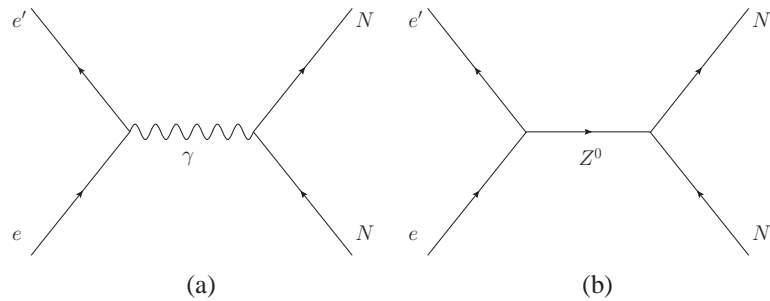


FIG. 1.1: Diagrams of electron-nucleon scattering for the (a) electromagnetic and (b) neutral weak interactions.

## 1.2 Form Factors and Parity-Violating Asymmetry

In order to understand hadronic structure, it is useful to measure distributions of properties such as electric charge, magnetic moment and spin within the nucleon. The information about hadronic structure is contained within functions defined in momentum transfer, or  $Q^2$ , space called form factors. These form factors are accessed through measurement of the scattering cross section, a quantity that can be thought of as the scattering rate weighted by the probability that a scattered particle with a given initial state will end up in a given final state.

The form factors can be defined by taking the differential cross section for interactions where the target is treated as a point particle and multiplying it by a  $Q^2$  dependent function such that

$$\frac{d\sigma}{d\Omega} = \frac{d\sigma}{d\Omega_{point}} |F(Q^2)|^2 . \quad (1.2)$$

The form factor  $F(Q^2)$  then provides information on how the structure of the target particle differs from a point particle. Neglecting nucleon recoil effects, one arrives at the spatial distribution of a given property by taking the Fourier transform of the appropriate form factor. In the  $Q^2 \rightarrow 0$  limit, the exponential (see Equation 1.3 below) tends to 1, the integral simplifies to the total distribution summed over the full volume and the structure can no longer be seen. Thus, at  $Q^2 = 0$ , the particle behaves as a point charge.

As an example, the charge and magnetization form factors of the proton,  $G_{E/M}^p$ , are related to the charge and magnetization distributions of the proton,  $\rho_{E/M}(r)$ , according to

$$G_{E/M}^p(Q^2) = \int \rho_{E/M}(r) e^{iq \cdot r} d^3r . \quad (1.3)$$

Note again that this neglects nucleon recoil. When  $Q^2 = 0$ , the form factors simplify to

the charge and magnetic moment of the proton,

$$G_E^p(0) = 1, \quad G_M^p(0) = \mu_p. \quad (1.4)$$

The charge and magnetic moment of the neutron can be defined in an analogous manner.  $G_{E/M}^p$  are related to the electromagnetic response of the hadron and, as such, are vector in nature. These form factors can be measured using parity-conserving electromagnetic interactions.

If one wishes to study the spin-dependent nature of hadrons, the weak or electroweak interaction can be used instead. Axial form factors, which arise from the axial component of the weak interaction, describe the distribution of spin in hadrons. In electroweak interactions, the total cross section involves a sum of charge, magnetization and axial form factors. One can measure the axial form factor by taking advantage of the parity-violating nature of the interaction. As was discussed in the previous section, electrons with differing helicity have different probabilities of scattering off of a given hadron, e.g. their cross sections will be different. The cross sections of electrons scattered with differing helicities can be combined to define the parity-violating asymmetry as the ratio of the difference in the cross sections to its sum, or

$$A = \frac{\left(\frac{d\sigma}{d\Omega}\right)_R - \left(\frac{d\sigma}{d\Omega}\right)_L}{\left(\frac{d\sigma}{d\Omega}\right)_R + \left(\frac{d\sigma}{d\Omega}\right)_L}, \quad (1.5)$$

where the R and L subscripts have been used to denote positive, or right-handed, and negative, or left-handed, electron helicity, respectively. The structure of the asymmetry in terms of form factors is dependent on the reaction studied and the parameterization of  $Q^2$  that is used. A general formalism for the parity-violating asymmetry in electron-nucleon scattering in terms of generic form factors will be given early in the next chapter, followed by the specific formalism used for the  $G^0$  elastic and inelastic electron scattering measurements.

### 1.3 The $\Delta$ Resonance

Nucleons are comprised primarily of three quarks, with the proton consisting of two up and one down quark,  $uud$ , and the neutron consisting of two down and one up,  $udd$ . In the simplest quark model, the spins of the quarks sum to create the total spin,  $J$ , of the nucleon. Since nucleons are spin  $J = \frac{1}{2}$ , two of the quarks are spin aligned and the third is anti-aligned. The  $\Delta$  resonances are excited states of nucleons that can be created when weak interactions between leptons and nucleons flip the spin of the anti-aligned quark. This quark spin flip leads to a spin for the  $\Delta$  of  $J = \frac{3}{2}$ . In addition to the spin flip, charged current weak interactions with nucleons can lead to flavor changes among the quarks, changing the charge and isospin of the resulting particle. The  $\Delta$  has an isospin of  $I = \frac{3}{2}$ , leading to four different  $\Delta$  with differing isospin projections,  $I_3$ . The four possible versions of the  $\Delta$ , along with their charges, constituent quarks and isospin, are given in Table 1.1. The resonance can be studied through several processes, including electromagnetic, weak charged current and weak neutral current reactions. Examples of reactions that can lead to each  $\Delta$  are given in the last column of Table 1.1. The  $\Delta$  is short lived, usually decaying into a nucleon and a pion. The charge of the emitted pion depends on the reaction.

Particle	Charge	Quarks	Spin	Isospin	$I_3$	Sample reaction
$\Delta^-$	-1	$ddd$	$\uparrow\uparrow\uparrow$	$\frac{3}{2}$	$-\frac{3}{2}$	$\bar{\nu}_\mu + n \rightarrow \mu^+ + \Delta^-$
$\Delta^0$	0	$udd$	$\uparrow\uparrow\uparrow$	$\frac{3}{2}$	$-\frac{1}{2}$	$e + n \rightarrow e + \Delta^0$
$\Delta^+$	+1	$uud$	$\uparrow\uparrow\uparrow$	$\frac{3}{2}$	$+\frac{1}{2}$	$e + p \rightarrow e + \Delta^+$
$\Delta^{++}$	+2	$uuu$	$\uparrow\uparrow\uparrow$	$\frac{3}{2}$	$+\frac{3}{2}$	$\nu_\mu + p \rightarrow \mu^- + \Delta^{++}$

TABLE 1.1: Summary of the different forms of the  $\Delta$ , including their charge, constituent quarks and a sample reaction leading to each.

There are multiple  $\Delta$  resonances, each representing a different excited state of the nucleon. The first, and largest, of these resonances occurs at an invariant mass of  $W = 1232$  MeV and has a width of  $\sim 118$  MeV. The Particle Data Group (PDG) lists 10 additional higher  $\Delta$  resonances with masses ranging from 1600 MeV to over 2400 MeV in their most recent edition [2]. There have been measurements that have reported many more resonances but the PDG only includes those that have been confirmed by at least two independent studies of elastic scattering and do not have large errors. As more data become available, the number of resonances recognized may increase. The  $\Delta(1232)$  resonance can be seen in Figure 1.2, which shows scattering cross sections measured through inelastic  $ep$  scattering as a function of  $W$ . These data were taken at a scattering angle of  $30^\circ$  and an electron beam energy of 2.445 GeV. In the figure, the peak at  $W \sim 1.2$  GeV is the  $\Delta(1232)$ , while the two remaining peaks are superpositions of several other resonances, including the higher  $\Delta$  resonances.

Understanding how the quarks within a nucleon are redistributed in the transition to its first excited state, the  $\Delta(1232)$ , is a topic of theoretical and experimental interest. Models of this behavior have been developed over the years, with a model proposed by Adler in 1968 [8] being the most commonly used. In recent years, lattice QCD measurements have also been used to study the  $N \rightarrow \Delta$  transition. Experimentally, the transition has been most commonly studied by measuring cross sections in charged current neutrino reactions. In this thesis, a measurement of the parity-violating asymmetry in electron-proton scattering near this resonance will be used to study the axial transition form factor,  $G_{N\Delta}^A$ , which describes how the quark spin is redistributed during the transition.

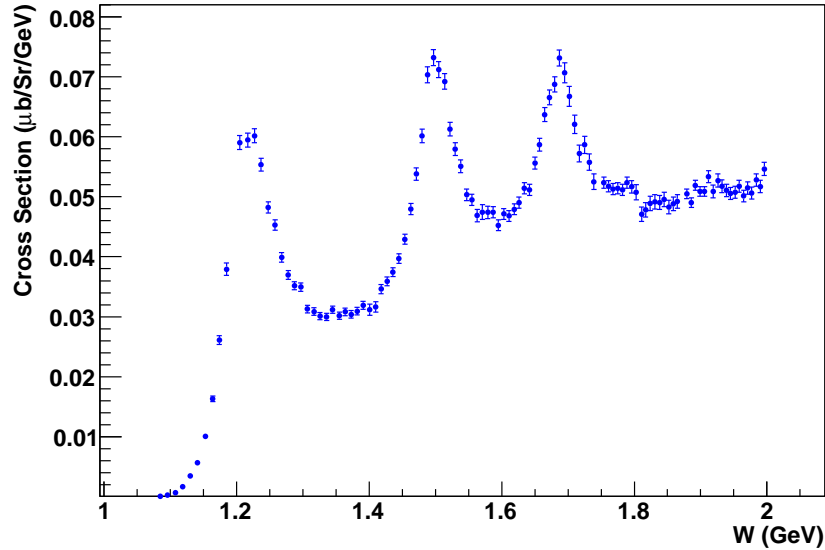


FIG. 1.2: Cross section data from inclusive inelastic  $ep$  scattering at an angle of  $30^\circ$  and a beam energy of 2.445 GeV. These data show the  $\Delta(1232)$  peak along with higher overlapping resonances. Plot created with data taken from [7].

## 1.4 The $G^0$ Experiment

The  $G^0$  experiment was proposed as a measure of the strange quark contribution to the electric and magnetic form factors of the proton. The form factors are accessed through a measurement of the parity-violating asymmetry in weak neutral  $ep$  scattering at both forward and backward angles and backward angle  $ed$  scattering. Three measurements with differing kinematics were needed to separate out the electric, magnetic and axial terms contributing to the asymmetry. The experiment was performed using a beam of polarized electrons provided by the Continuous Electron Beam Accelerator Facility, or CEBAF, at Jefferson Lab. The polarized electrons were scattered from an unpolarized liquid hydrogen or deuterium target.

Data collected as part of the  $G^0$  experiment contained information relevant to addi-

tional physics topics, three of which were studied separately. The first was a study of the two photon exchange through a transverse asymmetry measurement. Though the elastic measurement used a longitudinally polarized electron beam, real-world limitations dictate that no beam will be perfectly longitudinal. Any small transverse component that was present in the beam would constitute a background that could impact the measured asymmetry. In order to understand this background, data were taken with transversely polarized beam. Measurements of the transverse asymmetry performed in each of the three phases of the experiment were then used for a study of the beam-normal spin asymmetry ( $B_n$ ) arising from interference between the single and two photon exchanges. A brief discussion of the transverse asymmetry will be given in Section 4.4.2, while detailed discussions of the  $G^0$  transverse measurements are available elsewhere [9] [10].

During the forward angle phase,  $G^0$  used a time of flight measurement to detect recoiling protons. This measurement allowed for the separation of the elastic electron peak from inelastic and pion backgrounds. At backward angle, the scattered electron was instead detected. The difference in detection method necessitated a new procedure to separate the backgrounds from the elastic electrons. Additional detectors were added to provide kinematic separation between elastic and inelastic events in the detector space, and a means of particle identification. This resulted in the collection of inelastic scattering and pion photoproduction asymmetry data alongside the elastic scattering data. The deuterium data, in particular, provided useful information on pion photoproduction in the  $Q^2 \rightarrow 0$  limit. By analyzing these data, a constraint was able to be placed on the size of a coupling constant that describes the  $\gamma N \Delta$  vertex. More will be said about the motivation behind the pion measurement in Section 2.4.

The final physics topic of the  $G^0$  experiment, and the topic of this thesis, involves the electroproduction of the  $\Delta^+$  near the resonant peak at a  $Q^2$  of about  $0.34 \text{ (GeV/c)}^2$ . The

use of electron scattering to measure a parity-violating inelastic asymmetry in the weak neutral sector was first proposed by Cahn and Gilman [11] as a potential test of the Standard Model. The measurement presented here will instead be used to extract information on the axial response of the proton as it transitions to the  $\Delta$ . This response is described by the axial transition form factor,  $G_{N\Delta}^A$ . The inelastic asymmetry measured for both the hydrogen and deuterium targets will be presented in this thesis. However, due to the lack of a model for the neutron asymmetry, only the hydrogen result can be fully analyzed. The currently available information on  $G_{N\Delta}^A$  was determined through charged-current neutrino scattering experiments. As was discussed in Section 1.1, such interactions lead to both a quark flavor change and a spin flip. The neutral current measurement performed by  $G^0$  involves only a spin flip. While it is believed that these two should be equivalent due to the isospin symmetry that is present in the strong interaction, a suitably precise measurement of  $G_{N\Delta}^A$  could provide confirmation. The  $G^0$  inelastic measurement represents the first measurement of the axial response using a neutral weak reaction.

## 1.5 Summary

Electron-nucleon scattering provides a useful probe for studying the structure of nucleons. The distributions of nucleon properties, such as charge and spin, can be described through the use of form factors which can be accessed by measuring scattering cross sections. In the weak interaction, which violates parity, the cross section differs depending on the helicity of the incident electron. In order to quantify this difference, the parity-violating asymmetry can be calculated as the difference in cross sections between the two helicity states divided by their sum. Because the scale of the parity violation is very small ( $\sim 10^{-6}$ ), precise measurements of parity violation in weak interactions are difficult. The

interference of the weak interaction with the electromagnetic interaction simplifies such measurements, as the electromagnetic interaction amplifies the weak response.

In the chapters that follow, the results from the measurement of inelastic scattering from the proton and deuteron as part of the  $G^0$  experiment will be presented. The purpose of this measurement was to use a measured parity-violating asymmetry to gain insight into the axial transition form factor,  $G_{N\Delta}^A$ , which describes redistribution of intrinsic spin that occurs at the  $\Delta^+$  resonance. While information on  $G_{N\Delta}^A$  has been found previously using charged current reactions, the  $G^0$  measurement represents the first measurement of the asymmetry in the neutral weak sector. The theoretical basis for the measurement will be given first in Chapter 2, followed by a description of the experimental setup in Chapter 3. The corrections applied to the measured asymmetry will be presented in the two chapters that follow with the analysis separated into two main categories: beam and instrumentation corrections (Chapter 4) and corrections for backgrounds and physics effects (Chapter 5). Once the full analysis procedure has been described and the final asymmetry presented, interpretations of the result will be discussed in Chapter 6. The final chapter, Chapter 7, contains a summary of the findings presented in this thesis.

# CHAPTER 2

## Theory

While the  $G^0$  experiment covered several physics topics, the topic of interest in this thesis is the determination of the parity-violating asymmetry due to inelastic electron scattering near the  $\Delta$  resonance. The primary focus of this chapter will be to present a detailed description of the inelastic asymmetry model used in this thesis. To introduce this topic, the general formalism for electron-nucleon scattering via the electroweak interaction will be briefly presented, with an emphasis on the parity-violating asymmetry which arises from interference between the electromagnetic and weak interactions. Once the formalism is established, an overview of elastic  $ep$  scattering in the context of the  $G^0$  strange form factor measurement will be given. The remainder of the chapter will be dedicated to the derivation of an expression for the inelastic asymmetry.

## 2.1 General Expression for the Asymmetry

In order to derive the inelastic asymmetry, it is useful to start by introducing a formalism to describe a generic scattering process. As an example, Figure 2.1 depicts an electron scattering from a nucleon. In the neutral-current electroweak interaction, the electron and nucleon interact by exchanging either a photon or a  $Z^0$  boson. The interaction can be described in terms of the weak and electromagnetic currents and how they couple to each of the interacting particles. For the nucleon vertex, the coupling depends on the reaction being studied. Because of the dependence on the reaction mechanism, a presentation of the form of the couplings at this vertex will be postponed until the specific examples of elastic  $ep$  scattering and  $\Delta$  electroproduction are discussed in the next two sections. At the electron vertex, however, the couplings can be described in general terms that depend only on the interaction type (i.e. weak or electromagnetic).

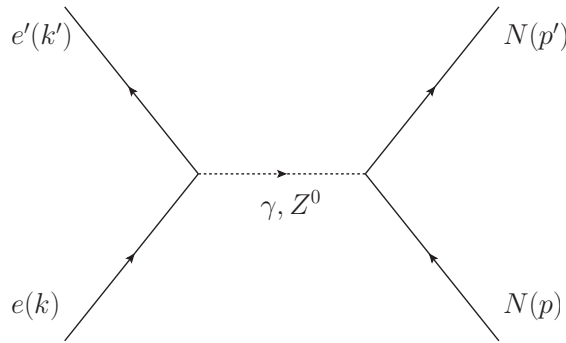


FIG. 2.1: Diagram of an electron scattering from a nucleon. In neutral-current electroweak interactions, the exchanged particle is either a photon or a  $Z^0$  boson. The momenta of each particle is indicated in parenthesis.

The electron couples to the photon,  $\gamma$ , in the electromagnetic interaction according to

$$\langle k' | J_\mu^\gamma | k \rangle = \bar{u}(k') (e \gamma_\mu) u(k) , \quad (2.1)$$

where  $e$  is the electron charge,  $\gamma_\mu$  are the Dirac matrices,  $J_\mu^\gamma$  is the electromagnetic current,  $k$  and  $k'$  are the initial and final state electron momenta, and  $u(k)$  and  $\bar{u}(k')$  are electron spinors. In the neutral-current weak interaction, the electron- $Z^0$  coupling can be written

$$\langle k' | J_\mu^Z | k \rangle = \bar{u}(k') (g_V^e \gamma_\mu + g_A^e \gamma_\mu \gamma_5) u(k), \quad (2.2)$$

where  $J_\mu^Z$  is the weak current, and  $\gamma_\mu$  and  $\gamma_5$  are the Dirac matrices. The couplings  $g_V^e$  and  $g_A^e$ , which represent vector and axial vector couplings, are given in the minimal  $SU(2) \times U(1)$  model in terms of the weak mixing angle,  $\theta_W$ , by

$$g_V^e = -\frac{e}{4 \sin \theta_W \cos \theta_W} (1 - 4 \sin^2 \theta_W), \quad (2.3)$$

$$g_A^e = \frac{e}{4 \sin \theta_W \cos \theta_W}. \quad (2.4)$$

The differences in the physics involved for the electromagnetic versus the weak interaction can be seen by comparing the structure of Equations 2.1 and 2.2. The electromagnetic interaction consists of a single vector term ( $e\gamma_\mu$ ) whereas the weak interaction contains both a vector term ( $g_V^e \gamma_\mu$ ) and an axial vector term ( $g_A^e \gamma_\mu \gamma_5$ ). The vector-axial vector ( $V - A$ ) structure of the weak interaction is such that, for a parity-violating reaction, one vertex will involve a vector coupling while the other is axial. For example, if for a given event the  $eZ$  coupling is vector, the  $ZN$  vertex will be axial and vice versa. As will be discussed later, the  $\gamma N$  and  $ZN$  vertices are described by the hadronic current which is more complex than the leptonic current given in Equations 2.1 and 2.2, and provides insight on hadron structure.

In an experiment like  $G^0$ , the electron's initial state is defined through the properties of the beam and the final state is the quantity of interest. The equations above describe the mechanism through which the electron transitions from its initial state to its final state. The likelihood that a scattered particle with a given initial state transitions to a

given final state depends on the scattering amplitude,  $\mathcal{M}$ . The scattering amplitude for electroweak interactions is given as the sum of the amplitudes from the electromagnetic and weak interactions. The scattering cross section is then proportional to the square of this amplitude, which is given by

$$\begin{aligned} |\mathcal{M}_{EW}|^2 &= |\mathcal{M}_{EM} + \mathcal{M}_Z|^2 \\ &= |\mathcal{M}_{EM}|^2 + |\mathcal{M}_Z|^2 + 2\Re(\mathcal{M}_{EM}^* \mathcal{M}_Z) . \end{aligned} \quad (2.5)$$

Though the electromagnetic interaction is parity-conserving, the weak interaction is not. Thus, the parity-violating nature of the weak interaction causes parity violation to occur in the electroweak interaction. The final term in Equation 2.5 represents an interference between the parity-conserving electromagnetic and parity-violating weak interactions. The violation of parity in the scattering amplitude creates a helicity dependence in the cross section. The helicity-correlated difference in cross section can be quantified by computing the asymmetry,

$$A = \frac{d\sigma_R - d\sigma_L}{d\sigma_R + d\sigma_L} , \quad (2.6)$$

where  $d\sigma$  is the scattering cross section and the subscripts R and L are used to denote the left- and right-handed helicity states for the incoming electron. Framing it in terms of  $\mathcal{M}_{EW}$ , the form of the asymmetry can be simplified to a ratio of the difference in left and right weak amplitudes to the electromagnetic amplitude,

$$\begin{aligned} A &= \frac{|\mathcal{M}_{EW}^R|^2 - |\mathcal{M}_{EW}^L|^2}{|\mathcal{M}_{EW}^R|^2 + |\mathcal{M}_{EW}^L|^2} \\ &\sim \frac{\mathcal{M}_Z^R - \mathcal{M}_Z^L}{\mathcal{M}_{EM}} . \end{aligned} \quad (2.7)$$

The simplification is made by noting that the electromagnetic interaction, and as a result, its scattering amplitude, is significantly stronger than the weak interaction. Therefore, the

$|\mathcal{M}_{EM}|^2$  term in the denominator is much larger than the remaining terms, all of which contain weak amplitudes. The denominator then can be adequately approximated with only the electromagnetic amplitude. Additionally, the squared weak terms in the numerator,  $|\mathcal{M}_{R/L}|^2$ , can be neglected since they are small compared to  $|\mathcal{M}_{EM}|^2$ . This leaves only the interference term in the numerator, leading to the final form of the asymmetry shown in Equation 2.7.

Cross sections and scattering amplitudes are a useful way of looking at asymmetries from an experimental point of view. However, if one wishes to extract information about hadronic structure, such as the charge and magnetization distributions in the nucleon, from a measured asymmetry it is useful to cast the electroweak interaction in terms of structure functions,  $W_{\mu\nu}$ , which parameterize hadronic structure through the use of form factors. Though the form factors themselves typically depend on the interaction being studied, a general equation for  $W_{\mu\nu}$  can be written in terms of generic combinations of form factors  $W_i$ . In this notation, the interference term can be written [12]

$$\begin{aligned} W_{\mu\nu} &= (2\pi)^3 \overline{\sum} \delta^4(p + q - p') \langle p | J_\mu^{EM} | p' \rangle \langle p' | J_\nu^Z | p \rangle \\ &= -g_{\mu\nu} W_1 + \frac{p_\mu p_\nu}{M^2} W_2 - i \epsilon_{\mu\nu\alpha\beta} \frac{p^\alpha q^\beta}{M^2} W_3, \end{aligned} \quad (2.8)$$

where  $M$  is the hadron mass,  $g_{\mu\nu}$  is the metric tensor and  $\epsilon_{\mu\nu\alpha\beta}$  is the antisymmetric Levi-Civita tensor. The electromagnetic and weak neutral currents are given by  $J_\mu^{EM}$  and  $J_\nu^Z$ , respectively, and  $p$  and  $p'$  represent the hadron momentum before and after the interaction. The quantity  $q$  is the difference between the incoming and outgoing hadron momenta, or  $p - p'$ . Finally, the symbol  $\overline{\sum}$  denotes the summation over the initial hadron state and average over the final hadron state. Note that the  $V - A$  structure of the weak interaction is visible in  $W_{\mu\nu}$ . The form factors contained within  $W_1$  and  $W_2$  are related to reactions that are vector at the hadron vertex and axial at the electron while  $W_3$  is related to the

axial hadron vertex.

Combining equations 2.8 and 2.2 yields a general equation for the parity violating asymmetry in terms of the three  $W_i$ ,

$$\begin{aligned}
A &= \frac{d\sigma_R - d\sigma_L}{d\sigma_R + d\sigma_L} \\
&= -\frac{2Q^2}{(Q^2 + M_Z^2)} \frac{1}{e^2} \left[ g_A^e \left( 2W_1 \sin^2 \frac{\theta}{2} + W_2 \cos^2 \frac{\theta}{2} \right) + g_V^e \frac{2(E + E')}{M} W_3 \sin^2 \frac{\theta}{2} \right] \\
&\quad \times \left[ 2W_1^{EM} \sin^2 \frac{\theta}{2} + W_2^{EM} \cos^2 \frac{\theta}{2} \right]^{-1}, \tag{2.9}
\end{aligned}$$

where  $e$  is the electron charge,  $\theta$  is the scattering angle,  $M_Z$  is the mass of the  $Z^0$  boson and  $g_A^e$  and  $g_V^e$  are given in Equations 2.3 and 2.4.

The  $W_i$  terms describe the electroweak interference, while those with the superscript EM are their electromagnetic analogue. The form of  $W_{1,2}^{EM}$  is given by replacing  $J_\nu^Z$  with  $J_\nu^{EM}$  in Equation 2.8. The  $W_i^{EM}$  are accessible through parity-conserving lepton scattering experiments and, as such, are well known. The  $W_i$  contain the information of interest in  $G^0$  including the axial response, which is described by  $W_3$ .

### 2.1.1 Elastic Scattering

Now that a general form has been provided, the asymmetry can be written for the specific case of elastic  $ep$  scattering. The couplings at the hadron vertex can be written in terms of form factors as

$$\langle p' | J_\mu^{EM} | p \rangle = \bar{u}(p') \left( \gamma_\mu F_1^\gamma + i \frac{\sigma_{\mu\nu} Q^\nu}{2M} F_2^\gamma \right) u(p), \tag{2.10}$$

$$\langle p' | J_\mu^Z | p \rangle = \bar{u}(p') \left( \gamma_\mu F_1^Z + i \frac{\sigma_{\mu\nu} Q^\nu}{2M} F_2^Z + \gamma_\mu \gamma_5 G_A^Z \right) u(p), \tag{2.11}$$

where  $\sigma_{\mu\nu}$  are Pauli matrices,  $F_i^\gamma$  are the standard Pauli and Dirac form factors describing the electromagnetic interaction, and  $F_i^Z$  and  $G_A^Z$  are form factors describing the vector

and axial vector portion of the weak interaction, respectively. The spinors  $u(p)$  and  $\bar{u}(p')$  describe the initial and final state of the proton. Using the above forms for the couplings and Equation 2.8, the structure functions for elastic scattering can be written in terms of form factors such that

$$\begin{aligned}
W_1^{el} &= G_M^\gamma G_M^Z Q^2 \delta(W^2 - M^2), \\
W_2^{el} &= 4M^2 \left[ F_1^\gamma F_1^Z + F_2^\gamma F_2^Z \frac{Q^2}{4M^2} \right] \delta(W^2 - M^2), \\
W_3^{el} &= 2M^2 G_A^Z G_M^\gamma \delta(W^2 - M^2), \\
W_1^{el,EM} &= (G_M^\gamma)^2 Q^2 \delta(W^2 - M^2), \\
W_2^{el,EM} &= 4M^2 \left[ (F_1^\gamma)^2 + (F_2^\gamma)^2 \frac{Q^2}{4M^2} \right] \delta(W^2 - M^2),
\end{aligned} \tag{2.12}$$

where the superscript “ $el$ ” is used to denote elastic scattering. The new term,  $G_M$ , introduced in this equation is referred to as a Sachs form factor and the M indicates magnetic. In this notation, which is preferred by experimentalists,  $G_M$  is defined as a linear combination of  $F_1$  and  $F_2$ . An equivalent electric form factor,  $G_E$ , can also be defined. The Sachs form factors are

$$G_M = F_1 + F_2, \tag{2.13}$$

$$G_E = F_1 - \frac{Q^2}{4M^2} F_2, \tag{2.14}$$

where  $Q^2$  is the momentum transfer and  $M$  is nucleon mass.

By combining Equations 2.12 and 2.9 and making use of the Sachs form factors, the parity-violating asymmetry in elastic  $ep$  scattering can be written [13]

$$A^{el} = -\frac{G_F Q^2}{4\pi\alpha\sqrt{2}} \left[ \frac{\epsilon G_E^\gamma G_E^Z + \tau G_M^\gamma G_M^Z - (1 - 4\sin^2\theta_W)\epsilon' G_M^\gamma G_A^e}{\epsilon (G_E^\gamma)^2 + \tau (G_M^\gamma)^2} \right], \tag{2.15}$$

where the coefficients  $\epsilon$ ,  $\epsilon'$  and  $\tau$  are simple kinematic variables that depend on  $\theta$  and  $Q^2$

and are defined according to

$$\tau = \frac{Q^2}{4M_N^2}, \quad (2.16)$$

$$\epsilon = \frac{1}{1 + 2(1 + \tau) \tan^2 \frac{\theta}{2}}, \quad (2.17)$$

$$\epsilon' = \sqrt{\tau(1 + \tau)(1 - \epsilon^2)}. \quad (2.18)$$

$G_{E(M)}^\gamma$  and  $G_{E(M)}^Z$  are the Sachs form factors describing the electromagnetic and weak interactions, respectively. The subscripts  $E$  and  $M$  denote the electric and magnetic components of the form factors. The final form factor,  $G_A^e$ , is equivalent at tree-level to  $G_A^Z$  above, describing the axial vector coupling between the nucleon and the  $Z$  boson that occurs as part of the neutral current weak interaction.

## 2.1.2 Inelastic Scattering - Resonant $\Delta$ Electroproduction

The form of the inelastic asymmetry can be given by following the same steps used in the previous section to determine the elastic asymmetry. The derivation that follows begins with an early representation of the inelastic asymmetry given in terms of a general electroweak  $SU(2) \times U(1)$  model that does not include non-resonant terms. Once this basic form has been established, the full form with both resonant and non-resonant reactions included will be given in terms of Standard Model couplings. It is important to note that the discussion presented here relates to tree-level interactions and does not include higher-order effects. Higher-order radiative effects, including the emission of real photons through bremsstrahlung, the presence of virtual photon loops and weak interactions among quarks within the nucleon, will be presented later.

As with the elastic, it is useful to first write the electromagnetic and weak neutral currents for the inelastic reaction in terms of form factors. For the process  $e+p \rightarrow e+\Delta^+$ ,

the matrix element for the electromagnetic interaction is given by [12]

$$\langle p' | J_\mu^{EM} | p \rangle = \bar{u}^\lambda(p') \left[ \left( \frac{C_3^\gamma}{M} \gamma^\nu + \frac{C_4^\gamma}{M^2} p'^\nu + \frac{C_5^\gamma}{M^2} p^\nu \right) (g_{\lambda\mu} g_{\rho\nu} - g_{\lambda\rho} g_{\mu\nu}) q^\rho \gamma_5 \right] u(p), \quad (2.19)$$

where  $\gamma^\nu$  and  $\gamma_5$  are Dirac matrices,  $p$  is the momentum of the incoming proton,  $p'$  is that of the  $\Delta^+$  and  $q$  is the difference between them. The four  $g_{\alpha\beta}$  represent the metric tensor. Following the notation of Llewellyn Smith [14], the Dirac spinor  $u(p)$  is used to describe the initial proton state, while the Rarita-Schwinger spinor  $\bar{u}^\lambda(p')$  [15] is used to describe the final  $\Delta^+$  state. The Rarita-Schwinger spinors are the spin- $\frac{3}{2}$  equivalent of the Dirac spinors used for spin- $\frac{1}{2}$  particles. The  $C_i^\gamma$  are the electromagnetic form factors.

Similarly, the weak neutral current coupling is given by

$$\begin{aligned} \langle p' | J_\mu^Z | p \rangle = \bar{u}^\lambda(p') \left[ \left( \frac{C_{3V}^Z}{M} \gamma^\nu + \frac{C_{4V}^Z}{M^2} p'^\nu + \frac{C_{5V}^Z}{M^2} p^\nu \right) (g_{\lambda\mu} g_{\rho\nu} - g_{\lambda\rho} g_{\mu\nu}) q^\rho \gamma_5 + C_{6V}^Z g_{\lambda\mu} \gamma_5 \right. \\ \left. + \left( \frac{C_{3A}^Z}{M} \gamma^\nu + \frac{C_{4A}^Z}{M^2} p'^\nu \right) (g_{\lambda\mu} g_{\rho\nu} - g_{\lambda\rho} g_{\mu\nu}) q^\rho \right. \\ \left. + C_{5A}^Z g_{\lambda\mu} + \frac{C_{6A}^Z}{M^2} p_\lambda q_\mu \right] u(p), \quad (2.20) \end{aligned}$$

where the Dirac matrices, momenta, metric tensors and spinors are as defined above. The vector form factors of the weak interaction are denoted  $C_{iV}^Z$  and the axial form factors are  $C_{iA}^Z$ . Note that in both equations above the mass,  $M$ , included is that of the proton, not the  $\Delta^+$ .

In general, the weak neutral current can be written as a sum of isovector and isoscalar terms

$$J_\mu^Z = \alpha' V_\mu^3 + \beta' A_\mu^3 + \text{isoscalar terms}. \quad (2.21)$$

where  $V_\mu^3$  and  $A_\mu^3$  are vector and axial isovector terms, and the electroweak coupling

constants  $\alpha'$  and  $\beta'$  are given in the Standard Model by

$$\alpha' = \frac{e}{2 \sin \theta_W \cos \theta_W} (1 - 2 \sin^2 \theta_W) \quad (2.22)$$

$$\beta' = -\frac{e}{2 \sin \theta_W \cos \theta_W} \quad (2.23)$$

For the specific case of  $\Delta^+$  electroproduction, the resonant reaction results in a change in isospin of  $\Delta I = 1$  as the  $I = \frac{1}{2}$  proton transitions to the  $I = \frac{3}{2}$   $\Delta^+$ . Thus, the reaction being considered here is purely isovector and the isoscalar terms do not contribute.

The form factors for neutral current electroproduction are not well understood, as there is little data available in this sector. However, information available on the form factors for the charged current weak and electromagnetic interactions can be used in their place. The vector neutral current form factors are related to the electromagnetic form factors through the conserved vector current (CVC) hypothesis [16]. Meanwhile, the charged and neutral current form factors can be related through a rotation in isospin space. Thus, using CVC and an isospin rotation, the unknown weak neutral form factors in Equation 2.20 can be replaced by better-known electromagnetic and charged current form factors according to

$$C_{iV}^Z = \alpha' C_i^\gamma, \quad i = 3, 4, 5, \quad (2.24)$$

$$C_{6V}^Z = 0, \quad (2.25)$$

$$C_{iA}^Z = -\beta' C_i^A, \quad i = 3, 4, 5, 6, \quad (2.26)$$

where the  $C_i^\gamma$  are the same electromagnetic form factors that appear in Equation 2.19 and the  $C_i^A$  are  $-\frac{1}{\sqrt{3}}$  times the axial charged current form factors. Eliminating the neutral current form factors allows for a parameterization of the form factors that can be tested using existing data from charged current experiments. Information about the parameterization of the form factors will be given in Section 2.3.4.

As an aside, it should be noted that the use of a simple isospin rotation to relate the charged current and neutral current axial form factors is an assumption. In the neutral current reaction described here, the  $\Delta^+$  is created by flipping the spin of one of the constituent quarks of the proton. The  $\Delta^+$  then decays, leaving a proton and a  $\pi^0$  meson. Charged current  $\Delta$  production from the proton (e.g.  $\nu + p \rightarrow \mu^- + \Delta^{++}$ ), however, requires not only a spin flip, but a change in quark flavor for the  $uud$  proton to transition to the  $uuu$   $\Delta^{++}$ . When the  $\Delta^{++}$  decays, a  $\pi^+$  meson is emitted. In using the charged current form factors, the assumption is made that, in spite of the difference in the specifics of the two reactions, the systems are essentially equivalent at each stage of the process. This assumption is supported by the fact that the differences in the two resulting systems are related to the differences in mass between the up and down quarks and between the different  $\pi$  mesons, which are negligible. A precise measurement of the neutral current form factors would provide a test of this assumption.

Before defining the structure functions ( $W_i$ ), it is useful to define some additional functions to simplify the notation. First, define  $D_i$  as linear combinations of the electromagnetic form factors such that

$$\begin{aligned} D_3(Q^2) &= -\frac{M}{M'} C_3^\gamma(Q^2), \\ D_4(Q^2) &= \frac{M}{M'} C_3^\gamma(Q^2) + C_4^\gamma(Q^2), \end{aligned} \tag{2.27}$$

where  $M$  and  $M'$  are the initial and final state hadron masses, in this case the proton and the  $\Delta^+$ . Kinematic variables can then be collected into three functions of  $Q^2$ , called  $a$ ,  $b$ ,

and  $c$ , such that

$$\begin{aligned}
a(Q^2) &= (M + M')^2 + Q^2, \\
b(Q^2) &= (M + M')(M - M') + Q^2, \\
c(Q^2) &= (M - M')^2 + Q^2.
\end{aligned} \tag{2.28}$$

Using these newly defined functions in conjunction with  $\alpha'$  and  $\beta'$  from above, the structure functions for inelastic scattering can be written

$$\begin{aligned}
W_1 &= \alpha\delta(W^2 - M'^2)\frac{c}{6M^4}(a^2D_3^2 + b^2D_4^2 + abD_3D_4), \\
W_2 &= \alpha\delta(W^2 - M'^2)\frac{2Q^2}{3M^2}(aD_3^2 + cD_4^2 + bD_3D_4), \\
W_3 &= \beta\delta(W^2 - M'^2)\frac{1}{3M^2}(2aD_3 + bD_4)\left[(b - 2c)\frac{M}{2M'}C_3^A + \frac{1}{2}bC_4^A - M^2C_5^A\right].
\end{aligned} \tag{2.29}$$

Note that the  $W_i$  defined here are completely different than those defined for elastic scattering in Section 2.1.1.

Because only the isovector piece of the weak current  $J_\mu^Z$  contributes to the resonance, the separation of terms presented Equation 2.21 can be used to deduce a form for the electromagnetic structure functions  $W_{EM}$ . A comparison of the form of Equation 2.21 to that of 2.29 implies that  $W_i = \alpha'W_i^{EM}$  for  $i = 1, 2$ . Making this replacement, the general asymmetry presented in equation 2.9 can be rewritten to give the form for the inelastic asymmetry as

$$A_{inel}^{res} = -\frac{2Q^2}{(Q^2 + M_Z^2)}\frac{1}{e^2}\left[\alpha g_A^e + g_V^e\frac{2(E + E')}{M}\left(\frac{W_3 \sin^2 \frac{\theta}{2}}{2W_1^{EM} \sin^2 \frac{\theta}{2} + W_2^{EM} \cos^2 \frac{\theta}{2}}\right)\right]. \tag{2.30}$$

In this form, the first term represents reactions where the hadron vertex is vector, while the second represents those in which it is axial vector. The vector portion of the

asymmetry contains no dependence on hadronic structure and relies only on the well-known Standard Model coupling,  $g_A^e$ . Additionally, since the electromagnetic structure functions,  $W_i^{EM}$ , are accessible through parity-conserving reactions, their behavior is understood. This leaves  $W_3$  as the only unknown contribution to the asymmetry. As a result, Equation 2.30 provides direct access to the axial response contained in  $W_3$ . The determination of this axial response is the focus of this thesis.

## 2.2 $G^0$ Elastic Measurement: Strange Form Factors

Before continuing to a discussion of the inelastic asymmetry, this section will provide a brief discussion of the strange quark measurement that was the primary goal of the  $G^0$  experiment. In the simplest sense, nucleons can be thought of as consisting of only up and down quarks and their properties can be described by combining those of the three valence quarks,  $uud$  for the proton and  $udd$  for the neutron. This simplification ignores the presence of sea quarks, the additional quarks that exist in the nucleon in the form of quark-antiquark pairs, and any contribution they may have to properties such as magnetic moment and electric charge. In addition to pairs of up ( $u\bar{u}$ ) and down ( $d\bar{d}$ ) quarks, it is known that strange quark pairs ( $s\bar{s}$ ) also exist in the sea, along with higher mass quarks that are neglected. The impact of these strange quarks can be studied through the neutral current electroweak interaction by measuring the parity-violating asymmetry. The  $G^0$  experiment measured this asymmetry through elastic electron scattering from both the proton and the deuteron.

Recall that the elastic asymmetry can be written,

$$A^{el} = -\frac{G_F Q^2}{4\pi\alpha\sqrt{2}} \left[ \frac{\epsilon G_E^\gamma G_E^Z + \tau G_M^\gamma G_M^Z - (1 - 4\sin^2\theta_W)\epsilon' G_M^\gamma G_A^e}{\epsilon (G_E^\gamma)^2 + \tau (G_M^\gamma)^2} \right], \quad (2.31)$$

where the form factors  $G^\gamma$ ,  $G^Z$  and  $G_A^e$  represent the electromagnetic, neutral weak vector and neutral weak axial vector components. Since the  $G^0$  measurement is concerned not with the nucleon as a whole but rather with attempting to separate out the contributions of individual quarks, it is useful to write the form factors in terms of quark flavors. To this end, Equations 2.10 and 2.11 can be used to define the coupling of the  $\gamma$  and  $Z^0$  to the up, down and strange quarks by rewriting the electromagnetic ( $J_\mu^{EM}$ ) and the vector portion of the neutral weak ( $J_\mu^{Z,V}$ ) currents as a sum of the individual quark contributions,

$$J_\mu^{EM} = \frac{2}{3}\bar{u}\gamma_\mu u - \frac{1}{3}\bar{d}\gamma_\mu d - \frac{1}{3}\bar{s}\gamma_\mu s, \quad (2.32)$$

$$J_\mu^{Z,V} = \left(1 - \frac{8}{3}\sin^2\theta_W\right)\bar{u}\gamma_\mu u + \left(-1 + \frac{4}{3}\sin^2\theta_W\right)\bar{d}\gamma_\mu d \\ + \left(-1 + \frac{4}{3}\sin^2\theta_W\right)\bar{s}\gamma_\mu s, \quad (2.33)$$

Note that the axial vector portion of  $J_\mu^Z$  has been neglected here. The determination of  $G_A^e$  in terms of quark flavors will be discussed separately below. The electromagnetic form factors can be written as the sum of the individual quark form factors such that [13]

$$G_E^\gamma = \frac{2}{3}G_E^u - \frac{1}{3}G_E^d - \frac{1}{3}G_E^s, \quad (2.34)$$

$$G_M^\gamma = \frac{2}{3}G_M^u - \frac{1}{3}G_M^d - \frac{1}{3}G_M^s, \quad (2.35)$$

while their weak neutral vector counterparts are

$$G_{E,M}^Z = \left(1 - \frac{8}{3}\sin^2\theta_W\right)G_{E,M}^u + \left(-1 + \frac{4}{3}\sin^2\theta_W\right)G_{E,M}^d \\ + \left(-1 + \frac{4}{3}\sin^2\theta_W\right)G_{E,M}^s. \quad (2.36)$$

The form of  $G_{E,M}^Z$  can be simplified by first noting that the quark form factors in Equations 2.34, 2.35 and 2.36 are identical. This is because the quark form factors are dependent only on hadronic structure, and, as a result, are independent of the interaction

used to study them. The second thing to note is that the proton and neutron form factors are related through charge symmetry according to

$$G^{u,p} = G^{d,n} , \quad (2.37)$$

$$G^{d,p} = G^{u,n} . \quad (2.38)$$

Thus, using an isospin rotation, the  $u$  and  $d$  quark contributions to  $G_{E,M}^Z$  can be grouped together to write the neutral weak vector form factor of the proton as a combination of electromagnetic proton and neutron form factors along with the strange form factors,

$$G_{E,M}^{Z,p} = (1 - 4 \sin^2 \theta_W) G_{E,M}^{\gamma,p} - G_{E,M}^{\gamma,n} - G_{E,M}^s . \quad (2.39)$$

This form of  $G_{E,M}^{Z,p}$  provides useful information because the electromagnetic form factors,  $G_{E,M}^\gamma$ , which can be measured through parity-conserving processes, are known. Thus, Equation 2.39 indicates that by measuring  $G_{E,M}^{Z,p}$ , one gains direct access to the strange form factors  $G_{E,M}^s$ . Before this can be done, however, there is one final important consideration that must be taken into account: the axial vector portion of the weak current.

Referring back to the asymmetry given in Equation 2.31, the axial response is present in the third term of the equation, represented by the form factor  $G_A^e$ . Using quark form factors, the axial form factor for the proton can be written [17],

$$G_A^e = -\frac{1}{2} G_A^{(1)} + \frac{1}{4} F_A^s , \quad (2.40)$$

where  $F_A^s$  is the axial strange form factor and  $G_A^{(1)}$  is a combination of the axial up and down quark form factors given by,

$$G_A^{(1)} = \frac{1}{2} (F_A^u - F_A^d) . \quad (2.41)$$

Though the impact of the axial term at tree level is suppressed by the presence of the  $(1 - 4 \sin^2 \theta_W)$  multiplier, precise measurements of the asymmetry can still be affected

by an axial electroweak radiative effect known as the anapole moment. The anapole moment arises from quark weak interactions at the  $\gamma NN$  vertex and has been found to be potentially large [18]. As such, it is a factor that must be taken into account when interpreting the elastic asymmetry.

In order to determine  $G_E^s$  and  $G_M^s$ , measurements need to be performed at two different angles. In the case of  $ep$  scattering, forward angles are sensitive to  $G_E^s$  while backward angles are sensitive to  $G_M^s$ . Thus, measuring the asymmetry at a given  $Q^2$  for both a small and a large angle allows for the contribution of the two form factors to be disentangled. In addition to these two measurements, a third measurement is needed to separate out the axial component,  $G_A^e$ . Backward angle scattering off the deuteron,  $d$ , is a useful probe of the axial response as the deuteron is less sensitive to  $G_M^s$ . The  $G^0$  experiment measured the asymmetry for elastic  $ep$  scattering at a proton recoil angle of  $\sim 70^\circ$  for several  $Q^2$ . This allowed for a determination of the strange quark contribution as a linear combination of the electric and magnetic components [19]. In order to achieve a full separation,  $G^0$  measured the asymmetry from elastic  $ep$  scattering and quasi-elastic  $ed$  scattering at an angle of  $\sim 110^\circ$  for two of the  $Q^2$  values measured at forward angle [20]. The  $G^0$  results provided a precise measurement of  $G_E^s$ ,  $G_M^s$  and  $G_A^e$  at these two  $Q^2$  points which, when taken along with data from other experiments, helps to constrain the contribution of the strange quark to the proton's form factors [21].

## 2.3 Full Inelastic Asymmetry Model

The derivation in Section 2.1.2 showed how the inelastic asymmetry for the transition to the  $\Delta$  resonance can be written in a way analogous to the elastic asymmetry, but it does not include non-resonant reactions. Non-resonant reactions are any reactions resulting in

pions that do not involve the creation of the  $\Delta$ . Historically, only the resonance was considered, as it is the dominant reaction and the non-resonant reactions contribute very little to the asymmetry at kinematics near the peak of the resonance. In order to fully model the asymmetry, however, one needs to expand Equation 2.30 to include non-resonant terms.

The asymmetry presented in Equation 2.30 is written in such a way as to separate vector reactions at the hadron vertex from axial vector reactions. This grouping can be maintained while adding non-resonant terms by simply adding separate non-resonant terms for vector and axial reactions. The purely isovector nature of the asymmetry, as presented through Equation 2.21, will change with the introduction of non-resonant reactions, as non-resonant reactions can be either isovector or isoscalar. With these considerations in mind, the inelastic asymmetry can be written as a sum of three terms such that [22]

$$\begin{aligned} A_{inel} &= A_1 + A_2 + A_3 \\ &= \frac{1}{2}A^0 [\Delta_{(1)}^\pi + \Delta_{(2)}^\pi + \Delta_{(3)}^\pi] , \end{aligned} \quad (2.42)$$

where the  $\pi$  superscript is used to indicate single pion production and  $A^0$  is defined as

$$A^0 = -\frac{G_F Q^2}{2\pi\alpha\sqrt{2}} . \quad (2.43)$$

The three terms represent different possible combinations of vector and axial vector interactions at the two vertices for both resonant and non-resonant reactions. Recall the simple scattering diagram presented in Figure 2.1. Due to the nature of the electroweak interaction, the form of the parity-violating interaction will be vector at one vertex and axial vector at the other. The vector (axial vector) can appear at either vertex. The first two terms,  $\Delta_{(1)}^\pi$  and  $\Delta_{(2)}^\pi$ , contain information related to vector reactions at the hadron vertex. The resonant terms, which are all isovector, are contained within  $\Delta_{(1)}^\pi$ , while the

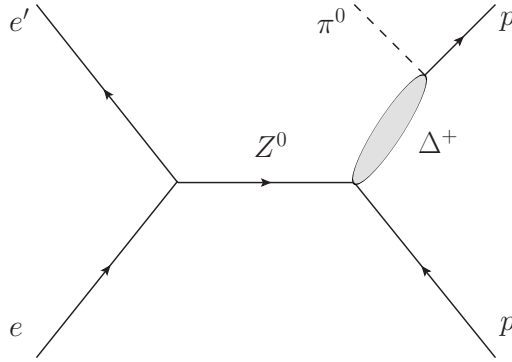


FIG. 2.2: Diagram of resonant electron-proton scattering. The  $Z^0$  excites the proton to its first excited state, the  $\Delta^+$ , which soon decays into a  $\pi^0$  and a proton. This is just one example of the reactions that contribute to  $A_{inel}$ .

non-resonant terms, both isovector and isoscalar, are described by  $\Delta_{(2)}^\pi$ . The final term,  $\Delta_{(3)}^\pi$ , contains all axial vector reactions at the hadron vertex, whether they be resonant or non-resonant, isovector or isoscalar.

Figure 2.2 shows one possible resonant reaction when scattering from the proton. In this figure, the  $\Delta^+$  decays into a  $\pi^0$  and a proton, however there are other possible decay modes. Since the present measurement detects electrons and not hadrons, the measured asymmetry will be an average across the different possible states and knowledge of which of these reactions is occurring is not important.

The introduction of  $\Delta_{(2)}^\pi$  allows for the separation of the non-resonant background from the more well-known resonant piece of the axial vector electron/vector hadron reaction. This separation is performed by treating the isospin structure of the vector piece of the weak interaction in an analogous manner to the electromagnetic interaction, which is purely vector [22]. A similar subdivision of the axial piece into resonant and non-resonant components cannot be as easily performed as the isospin structure of this reaction is not known. Because of the limitations on information available at the present time, the axial piece ( $\Delta_{(3)}^\pi$ ) is considered as a whole with no further separation performed.

In the sections that follow, details of the form of each of the three  $\Delta_{(i)}^\pi$  terms will be presented along with information about the specific implementation of these models used in this thesis. A number of authors have discussed  $A_{inel}$ , often using slightly differing notation. The discussion that follows will combine these different resources into a full formalism for  $A_{inel}$  that allows for the extraction of the axial transition form factor,  $G_{N\Delta}^A$ . The formalism presented here is mainly a combination of those derived by Musolf *et al.* [22] and Nath *et al.* [12], although other works will also be utilized.

### 2.3.1 Notation

It is important to note that there is a difference in notation between Equation 2.42 and Equation 2.30, as evidenced by the terms present outside the parenthesis. Before continuing with a detailed description of the individual terms in the asymmetry, the link between the full and resonant forms of the asymmetry will be presented.

The resonant asymmetry derived in the previous section can be written as a sum of two asymmetry terms such that

$$\begin{aligned}
 A_{inel}^{res} &= -\frac{2Q^2}{(Q^2 + M_Z^2)} \frac{1}{e^2} \left[ \alpha' g_A^e + g_V^e \frac{2(E + E')}{M} \left( \frac{W_3 \sin^2 \frac{\theta}{2}}{2W_1^{EM} \sin^2 \frac{\theta}{2} + W_2^{EM} \cos^2 \frac{\theta}{2}} \right) \right] \\
 &= A_1 + A_3^{res}, \tag{2.44}
 \end{aligned}$$

where the vector and axial vector terms have been grouped separately in  $A_1$  and  $A_3^{res}$ , respectively, so that the subscripts match those of Equation 2.42. The “*res*” superscript is used here to indicate that the non-resonant axial contribution has been neglected. To simplify notation, this superscript will be suppressed for the remainder of this section.

Starting with  $A_1$ , assume that  $Q^2 \ll M_Z^2$ , and substitute in the forms of  $g_A^e$  and  $\alpha'$ ,

as given in Equations 2.4 and 2.22 respectively, to yield

$$\begin{aligned}
A_1 &= -\frac{2Q^2}{M_Z^2} \frac{1}{e^2} \alpha' g_A^e \\
&= -\frac{2Q^2}{M_Z^2} \frac{1}{e^2} \left[ \frac{e}{2 \sin \theta_W \cos \theta_W} (1 - 2 \sin^2 \theta_W) \right] \left[ \frac{e}{4 \sin \theta_W \cos \theta_W} \right] \\
&= -\frac{2Q^2}{M_Z^2} \frac{1}{8 \sin^2 \theta_W \cos^2 \theta_W} (1 - 2 \sin^2 \theta_W) .
\end{aligned} \tag{2.45}$$

Then, noting the following Standard Model identities [23],

$$M_W^2 = M_Z^2 \cos^2 \theta_W , \tag{2.46}$$

$$\frac{G_F}{\sqrt{2}} = \frac{g^2}{8M_W^2} , \tag{2.47}$$

$$e = g \sin \theta_W , \tag{2.48}$$

where  $g$  is the gauge coupling of SU(2),  $M_W$  is the mass of the  $W^\pm$ ,  $M_Z$  is the mass of the  $Z^0$  and  $G_F$  is the Fermi coupling constant, the form of  $A_1$  can be simplified to obtain

$$A_1 = -\frac{2Q^2}{e^2} \frac{G_F}{\sqrt{2}} (1 - 2 \sin^2 \theta_W) . \tag{2.49}$$

Finally, note that

$$e^2 = 4\pi\alpha , \tag{2.50}$$

where  $\alpha$  is the fine structure constant, and define  $\tilde{\alpha}$  as  $-(1 - 2 \sin^2 \theta_W)$  to rewrite Equation 2.49 as

$$\begin{aligned}
A_1 &= \frac{Q^2}{2\pi\alpha} \frac{G_F}{\sqrt{2}} [-(1 - 2 \sin^2 \theta_W)] \\
&= \frac{Q^2}{2\pi\alpha} \frac{G_F}{\sqrt{2}} \tilde{\alpha} .
\end{aligned} \tag{2.51}$$

$A_1$  is now identical to  $\frac{1}{2} A^0 \Delta_{(1)}^\pi$ , as given in Equation 2.42.

A similar process can be performed for  $A_3$  as given in Equation 2.44 using the structure functions  $W_i$  defined in 2.29. First, pull the  $\beta'$  out of  $W_3$  to define  $W'_3 = \beta'W_3$ , then substitute  $W'_3$  into  $A_3$  to yield

$$\begin{aligned}
A_3 &= -\frac{2Q^2}{e^2(Q^2 + M_Z^2)}\beta'g_V^e \left( \frac{E + E'}{M} \frac{2W'_3 \sin^2 \frac{\theta}{2}}{2W_1^{EM} \sin^2 \frac{\theta}{2} + W_2^{EM} \cos^2 \frac{\theta}{2}} \right) \\
&= -\frac{2Q^2}{e^2(Q^2 + M_Z^2)} \left[ \frac{-e}{2 \sin \theta_W \cos \theta_W} \right] \left[ \frac{-e}{4 \sin \theta_W \cos \theta_W} (1 - 4 \sin^2 \theta_W) \right] \\
&\quad \times \left( \frac{E + E'}{M} \frac{2W'_3 \sin^2 \frac{\theta}{2}}{2W_1^{EM} \sin^2 \frac{\theta}{2} + W_2^{EM} \cos^2 \frac{\theta}{2}} \right) \\
&= -\frac{2Q^2}{e^2(Q^2 + M_Z^2)} \left[ \frac{e^2}{8 \sin^2 \theta_w \cos^2 \theta_W} (1 - 4 \sin^2 \theta_W) \right] \\
&\quad \times \left( \frac{E + E'}{M} \frac{2W'_3 \sin^2 \frac{\theta}{2}}{2W_1^{EM} \sin^2 \frac{\theta}{2} + W_2^{EM} \cos^2 \frac{\theta}{2}} \right). \tag{2.52}
\end{aligned}$$

Next, make the same substitutions as were made in  $A_1$  to eliminate  $M_Z$  and  $e$ , and define  $\tilde{\beta} = -(1 - 4 \sin^2 \theta_W)$  to write

$$A_3 = \frac{Q^2}{2\pi\alpha} \frac{G_F}{\sqrt{2}} \left[ \tilde{\beta} \frac{E + E'}{M} \frac{2W'_3 \sin^2 \frac{\theta}{2}}{2W_1^{EM} \sin^2 \frac{\theta}{2} + W_2^{EM} \cos^2 \frac{\theta}{2}} \right] \tag{2.53}$$

Combining Equations 2.51 and 2.53, the total resonant asymmetry,  $A_{inel}^{res}$ , is then written

$$\begin{aligned}
A_{inel}^{res} &= \frac{Q^2}{2\pi\alpha} \frac{G_F}{\sqrt{2}} [\tilde{\alpha} + \tilde{\beta}F(Q^2, s)] \\
&= -\frac{Q^2}{4\pi\alpha} \frac{G_F}{\sqrt{2}} [\Delta_{(1)}^\pi + \Delta_{(3)}^\pi] \tag{2.54}
\end{aligned}$$

where the notation for  $A_3$  has been simplified by defining the function  $F(Q^2, s)$  such that it includes both electromagnetic ( $C_i^\gamma$ ) and axial ( $C_i^A$ ) form factors. More details on the form of  $F(Q^2, s)$  will be given in Section 2.3.4. With this equation, it has been shown that the resonant portions of Equation 2.44 and Equation 2.42 are equivalent to one another.

### 2.3.2 Resonant Vector Term, $\Delta_{(1)}^\pi$

The resonant vector hadron term,  $\Delta_{(1)}^\pi$ , is the dominant term in the asymmetry and the only one that is not dependent on hadronic structure.  $\Delta_{(1)}^\pi$  contains the full contribution of the resonant vector current at the hadronic vertex to the asymmetry. The form of  $\Delta_{(1)}^\pi$  is given by [22]

$$\Delta_{(1)}^\pi = g_A^e \xi_V^{T=1} \quad (2.55)$$

$$= 2(1 - 2 \sin^2 \theta_W), \quad (2.56)$$

where  $g_A^e$  is the axial vector coupling to the  $Z$  boson, which is equal to 1 in the Standard Model, and  $\xi_V^{T=1}$  is the isovector hadron coupling to the vector  $Z$ , which is given as  $2(1 - 2 \sin^2 \theta_W)$  in the Standard Model.

Because of the direct relationship between  $\Delta_{(1)}^\pi$  and  $\sin^2 \theta_W$ , it was proposed early in the study of  $A_{inel}$  that a precise measurement of this asymmetry could be used as a Standard Model test [11] [12]. However, more recent studies [24] have found that theoretical uncertainty surrounding the non-resonant contribution,  $\Delta_{(2)}^\pi$ , limits the ability to interpret experimental results. Further, axial electroweak radiative effects present in  $\Delta_{(3)}^\pi$  add an additional layer of theoretical uncertainty [25]. These considerations would mean a potentially large and theoretically uncertain background on  $\Delta_{(1)}^\pi$ , leading the authors of those works to conclude that a measure of  $A_{inel}$  is not practical for use as a Standard Model test.

### 2.3.3 Non-Resonant Vector Term, $\Delta_{(2)}^\pi$

The second term in the asymmetry,  $\Delta_{(2)}^\pi$ , describes the non-resonant part of the vector hadron reaction. While important physics is contained in the other two terms,  $\Delta_{(2)}^\pi$  is

a less interesting background term that has been separated out from  $\Delta_{(1)}^\pi$  for the purposes of isolating the uncertainty in the vector hadron contribution to the asymmetry [24].

By using an isospin decomposition analogous to techniques used for describing purely electromagnetic reactions [22],  $\Delta_{(2)}^\pi$  can be written as a sum over angular momentum such that

$$\begin{aligned}
F^2 \Delta_{(2)}^\pi = & -2g_A^e \xi_V^n \sum_l \Re \times \left\{ v_T \left[ l(l+1)^2 \left( \frac{3}{\sqrt{2}} M_{l+}^{0*} M_{l+}^{\frac{1}{2}} - 3|M_{l+}^0|^2 \right) \right. \right. \\
& + l^2(l+1) \left( \frac{3}{\sqrt{2}} M_{l-}^{0*} M_{l-}^{\frac{1}{2}} - 3|M_{l-}^0|^2 \right) \\
& + (l+2)(l+1)^2 \left( \frac{3}{\sqrt{2}} E_{l+}^{0*} E_{l+}^{\frac{1}{2}} - 3|E_{l+}^0|^2 \right) \\
& + l^2(l-1) \left( \frac{3}{\sqrt{2}} E_{l-}^{0*} E_{l-}^{\frac{1}{2}} - 3|E_{l-}^0|^2 \right) \left. \right] \\
& + v_L \left[ (l+1)^3 \left( \frac{3}{\sqrt{2}} S_{l+}^{0*} S_{l+}^{\frac{1}{2}} - 3|S_{l+}^0|^2 \right) + l^3 \left( \frac{3}{\sqrt{2}} S_{l-}^{0*} S_{l-}^{\frac{1}{2}} - 3|S_{l-}^0|^2 \right) \right] \left. \right\}, \tag{2.57}
\end{aligned}$$

where the  $E_{l\pm}^i$  and  $M_{l\pm}^i$  are the transverse electric and transverse magnetic multipoles and the  $S_{l\pm}^i$  are the longitudinal multipoles. The subscripts  $l\pm$  on the multipoles indicate the angular momentum and parity for which they have been computed. The superscripts ( $i = 0, \frac{1}{2}$ ) denote the isospin decomposition, with the value of  $i$  indicating the change in isospin,  $\Delta I$ , for the reaction in question. For the non-resonant processes described here,  $\Delta I$  can be 0, indicating isoscalar reactions, or  $\frac{1}{2}$ , indicating isovector. As with  $\Delta_{(1)}^\pi$ ,  $g_A^e$  can be replaced by its Standard Model value of 1, while  $\xi_V^n$  represents a linear combination of the  $\xi_V^{T=0}$  (isoscalar) and  $\xi_V^{T=1}$  (isovector) vector hadron couplings that is equal to -1 in the Standard Model. The terms  $v_{T/L}$  contain kinematic quantities related to the electron

and are defined as

$$v_T = \frac{1}{2} \left| \frac{Q^2}{q^2} \right| \tan^2 \frac{\theta}{2}, \quad (2.58)$$

$$v_L = \left| \frac{Q^2}{q^2} \right|^2. \quad (2.59)$$

The term on the left-hand side of the equation,  $F^2$ , is the ratio of the inclusive electromagnetic cross section ( $\sigma$ ) to the Mott cross section ( $\sigma_{Mott}$ ),

$$F^2 = \frac{f_{rec}}{4\pi} \left( \frac{\sigma}{\sigma_{Mott}} \right), \quad (2.60)$$

where

$$\sigma_{Mott} = \frac{\alpha \cos \frac{\theta}{2}}{E \sin^2 \frac{\theta}{2}}, \quad (2.61)$$

and  $f_{rec}$  is a function of electron energy  $E$ , scattering angle  $\theta$ , and target mass  $M$  that has been included to account for target recoil.  $f_{rec}$  is defined as [22]

$$f_{rec} = 1 + \frac{2E}{M} \sin^2 \frac{\theta}{2}. \quad (2.62)$$

$F^2$  corresponds to the linear combination of electromagnetic structure functions ( $W_i^{EM}$ ) present in the denominator of Equation 2.9.

Since the resonant reaction dominates in the kinematics studied in this thesis,  $\Delta_{(2)}^\pi$  is expected to be small. The uncertainty in the calculation of  $\Delta_{(2)}^\pi$  is dependent on the uncertainty in the multipoles and on any approximations made in calculating the sum over angular momentum states. More detail on the calculation of this term for the purposes of the  $G^0$  measurement will be given in Chapter 5, while its uncertainty will be discussed in Chapter 6.

### 2.3.4 Axial Term, $\Delta_{(3)}^\pi$

The final term in the asymmetry,  $\Delta_{(3)}^\pi$ , contains all of the information about the axial hadron response, both resonant and non-resonant. It can be written as a sum of multipoles in a manner similar to that of  $\Delta_{(2)}^\pi$ , such that [22]

$$F^2 \Delta_{(3)}^\pi = 2g_V^e v_T' \sum_l \Re [l(l-1)^2 \tilde{E}_{l+}^{5*} M_{l+} - (l+1)^2(l+2) \tilde{M}_{l+}^{5*} E_{l+} - l^2(l+1) \tilde{E}_{l-}^{5*} M_{l-} + l^2(l-1) \tilde{M}_{l-}^{5*} E_{l-}] , \quad (2.63)$$

where  $F^2$  is defined as in Equation 2.60 and  $v_T'$  is a function of kinematic variables similar to  $v_T$  and  $v_L$  defined as

$$v_T' = \tan \frac{\theta}{2} \sqrt{\left| \frac{Q^2}{q^2} \right|} \tan^2 \frac{\theta}{2} . \quad (2.64)$$

In this notation,  $E$  and  $M$  are electric and magnetic multipoles, the 5 superscript is present to indicate the axial nature of the response and the tilde distinguishes between the multipoles and their conjugates. As was discussed previously, further decomposition of this formalism into individual  $\Delta I = 0$ ,  $\frac{1}{2}$  and  $\frac{3}{2}$  isospin components requires knowledge of the isospin structure that is not currently available. Thus, to determine the theoretical asymmetry a calculable model must be found.

A model that includes the non-resonant contribution was developed by Hammer and Dreschel [26] using effective Lagrangians to describe the asymmetry in the range from threshold to the resonance. As there were no asymmetry data to compare to, the accuracy of the model was tested by computing the cross section and comparing it to available cross section data. Their results found the model to be accurate to within about 5%. Computing the full asymmetry, they found that, when calculated at the resonance ( $W = 1232$  MeV) with an incident energy similar to that of the present measurement ( $E = 800$  MeV), the resonant term was dominant and their results matched reasonably well, to within 10%,

with those of Nath *et al.* [12], and Cahn and Gilman [11] who each considered only the resonant terms. Additionally, Mukhopadhyay *et al.* [24] used this model as the basis for computing the asymmetry and found that the non-resonant axial processes can be classified into two categories: purely non-resonant processes and interferences between resonant and non-resonant processes. Though they did not perform calculations at the present kinematics, the behavior they found indicates that these two effects contribute to the asymmetry with opposing signs. This leads to a cancellation and leaves only a small net effect on the asymmetry.

These findings, coupled with the limited experimental precision of the present measurement, indicate that a reasonable approximation for  $\Delta_{(3)}^\pi$  can be made by neglecting the non-resonant axial terms. Thus, the resonant asymmetry first presented in Equation 2.30 will be used here. As was shown in Section 2.3.1,  $\Delta_{(3)}^\pi$  for the purely resonant processes can be written using a function,  $F(Q^2, s)$ , which contains the axial and electromagnetic form factors,

$$\begin{aligned}\Delta_{(3)}^\pi &\approx g_V^e \xi_A^{T=1} F(Q^2, s) \\ &\approx 2(1 - 4 \sin^2 \theta_W) F(Q^2, s),\end{aligned}\tag{2.65}$$

where  $s$  is the Mandelstam  $s$ , and  $g_V^e$  and  $\xi_A^{T=1}$  have been replaced with their respective Standard Model tree level values of  $g_{V,e} = (-1 + 4 \sin^2 \theta_W)$  and  $\xi_A^{T=1} = -2$ . The “ $\approx$ ” is used as a reminder that, since the non-resonant terms are being ignored, this form of  $\Delta_{(3)}^\pi$  is not exact. As an aside, note that the presence of  $g_V^e$ , which works out to roughly 0.1, acts to suppress the value of  $\Delta_{(3)}^\pi$  relative to  $\Delta_{(1)}^\pi$  and  $\Delta_{(2)}^\pi$ , which are each instead multiplied by  $g_A^e = 1$ . This suppression complicates the ability to make a precise measurement of this term.

In order to compute  $\Delta_{(3)}^\pi$ , the function  $F(Q^2, s)$  can be written

$$F(Q^2, s) = \frac{E + E'}{M} H^{EM}(Q^2, \theta) G_{N\Delta}^A(Q^2), \quad (2.66)$$

where  $H^{EM}(Q^2, \theta)$  and  $G_{N\Delta}^A(Q^2)$  are linear combinations of the electromagnetic and axial form factors, respectively. Using the notation of Equation 2.30,  $F(Q^2, s)$  can be alternatively written as a sum of structure functions,

$$F(Q^2, s) = \frac{E + E'}{M} \frac{2 \sin^2 \frac{\theta}{2} W'_3}{2 \sin^2 \frac{\theta}{2} W_1^{EM} + \cos^2 \frac{\theta}{2} W_2^{EM}}, \quad (2.67)$$

where the  $W_i$ 's are defined according to equation 2.29 with  $\alpha'$  and  $\beta'$  removed according to  $W_{1,2}^{EM} = \frac{1}{\alpha'} W_{1,2}$  and  $W'_3 = \frac{1}{\beta'} W_3$ . Since no measurements will be made at  $\theta = 180^\circ$ , both the numerator and denominator can be divided by  $\cos^2 \frac{\theta}{2}$ , leading to

$$F(Q^2, s) = \frac{E + E'}{M} \frac{2 \tan^2 \frac{\theta}{2} W'_3}{2 \tan^2 \frac{\theta}{2} W_1^{EM} + W_2^{EM}}. \quad (2.68)$$

Substituting the values for the  $W_i$ 's into the equation leads to

$$F(Q^2, s) = \frac{E + E'}{M} \left( 2 \tan^2 \frac{\theta}{2} \right) \times \left[ \frac{(2aD_3 + bD_4)}{3M^2} \left( (b - 2c) \frac{M}{2M'} C_3^A + \frac{1}{2} b C_4^A - M^2 C_5^A \right) \right] \times \left[ \frac{(2 \tan^2 \frac{\theta}{2}) c}{6M^4} (a^2 D_3^2 + b^2 D_4^2 + ab D_3 D_4) + \frac{2Q^2}{3M^2} (aD_3^2 + cD_4^2 + bD_3 D_4) \right]^{-1} \quad (2.69)$$

where the  $D_i$  contain the form factors  $C_i^\gamma$  as defined in equation 2.27, and  $a$ ,  $b$  and  $c$  are combinations of kinematic variables defined in Equation 2.28. Note that the structure functions  $W_i^{EM}$  depend only on electromagnetic form factors ( $C_i^\gamma$ ), while  $W'_3$  is a product of electromagnetic and axial ( $C_i^A$ ) form factors. This form allows for a grouping of the form factors such that  $F(Q^2, s)$  is written as a product of a function containing only  $C_i^\gamma$  and one containing only  $C_i^A$ , as in Equation 2.66.

The function containing the electromagnetic form factors,  $H^{EM}$ , is then written,

$$\begin{aligned} H^{EM}(Q^2, \theta) &= \frac{\frac{2}{3M^2}(2aD_3 + bD_4) \tan^2 \frac{\theta}{2}}{2 \tan^2 \frac{\theta}{2} \frac{c}{6M^4}(a^2D_3^2 + b^2D_4^2 + abD_3D_4) + \frac{2Q^2}{3M^2}(aD_3^2 + cD_4^2 + bD_3D_4)} \\ &= \frac{h_3C_3^\gamma + h_4C_4^\gamma}{h_{33}(C_3^\gamma)^2 + h_{34}C_3^\gamma C_4^\gamma + h_{44}(C_4^\gamma)^2}, \end{aligned} \quad (2.70)$$

where the  $D_i$ 's have been replaced with their corresponding definitions. For the purpose of simplification, functions  $h_i$  and  $h_{ij}$  have been introduced to represent the kinematical coefficients that multiply the form factors. The notation is such that the subscripts on each coefficient denote the indices of the form factor or form factors it multiplies. These functions are defined as

$$h_3(Q^2, \theta) = (b - 2a) \frac{2}{3MM'} \tan^2 \frac{\theta}{2}, \quad (2.71)$$

$$h_4(Q^2, \theta) = b \frac{2}{3M^2} \tan^2 \frac{\theta}{2}, \quad (2.72)$$

$$h_{33}(Q^2, \theta) = \frac{1}{3M'^2} \left[ \frac{c(a^2 + b^2 - ab)}{M^2} \tan^2 \frac{\theta}{2} + 2(a + c - b)Q^2 \right], \quad (2.73)$$

$$h_{34}(Q^2, \theta) = \frac{1}{3MM'} \left[ \frac{bc(2b - a)}{M^2} \tan^2 \frac{\theta}{2} + 2(2c - b)Q^2 \right], \quad (2.74)$$

$$h_{44}(Q^2, \theta) = \frac{1}{3M^2} \left[ \frac{b^2c}{M^2} \tan^2 \frac{\theta}{2} + 2cQ^2 \right]. \quad (2.75)$$

Similar steps can be followed for the axial piece of  $F(Q^2, s)$ ,  $G_{N\Delta}^A$ , leading to

$$G_{N\Delta}^A = g_3C_3^A + g_4C_4^A + g_5C_5^A, \quad (2.76)$$

where the kinematic terms have been collected into the coefficients  $g_i$  using  $b$  and  $c$  defined in Equation 2.28. The  $g_i$  are defined by

$$g_3(Q^2) = \frac{M}{2M'}(b - 2c), \quad (2.77)$$

$$g_4(Q^2) = \frac{1}{2}b, \quad (2.78)$$

$$g_5(Q^2) = -M^2. \quad (2.79)$$

$F(Q^2, s)$  is now written in a form that consists of known kinematical coefficients multiplying form factors,  $C_i^\gamma$  and  $C_i^A$ . In order to compute a theoretical asymmetry, it is necessary to have a way to compute these form factors. One convenient way to express the  $Q^2$  dependence of the form factors is through the use of a dipole form. In this notation, referred to as the Adler parameterization [8] [27], the form factors are written

$$C_i^\gamma(Q^2) = C_i^\gamma(0)G_D^V(Q^2), \quad (2.80)$$

$$C_i^A(Q^2) = C_i^A(0)G_D^A(Q^2)\xi^A(Q^2), \quad (2.81)$$

where the functions  $G_D^{V,A}(Q^2)$  are dipole form factors defined as

$$G_D^{V,A}(Q^2) = \left[1 + \frac{Q^2}{M_{V,A}^2}\right]^{-2}. \quad (2.82)$$

$M_{V,A}$  are the vector/axial dipole masses, which have been determined from fits to data. The current world values for these masses are  $M_V = 0.84$  GeV [28] and  $M_A = 1.03 \pm 0.02$  GeV [29]. It should be noted that the dipole parameterization was chosen because it is a convenient way to express the  $Q^2$  dependence and has no deeper physics meaning. The elastic form factors for the nucleon charge and magnetic moment,  $G_{E/M}^p$  and  $G_{E/M}^n$ , have been found experimentally to fit reasonably well with this form, though some important small deviations exist [28].

The function  $\xi^A$  is used to give additional structure to the  $Q^2$  dependence of the axial term and is written

$$\xi^A(Q^2) = 1 + \left(\frac{a'Q^2}{b' + Q^2}\right), \quad (2.83)$$

with the parameters  $a'$  and  $b'$  determined from a fit to model form factors performed by Schreiner and von Hippel [30]. For the Adler model form factors,  $a'$  was found to be  $-1.2$  and  $b'$  was  $2$  (GeV/c)<sup>2</sup>. These results hold only for  $Q^2 < 0.5$  GeV, but this range sufficiently covers the  $G^0$  experimental acceptance.

The values for  $C_i(0)$  are determined from fits to charged current data and are fit-dependent. In this thesis, the Adler values of these coefficients, as quoted by Nath [12], will be used. They are

$$\begin{aligned}
 C_3^A(0) &= 0, & C_3^\gamma(0) &= 1.85, \\
 C_4^A(0) &= -0.35, & C_4^\gamma(0) &= -0.89, \\
 C_5^A(0) &= 1.20.
 \end{aligned}
 \tag{2.84}$$

Note that not all of the  $C_i$ 's contribute to the final value of  $F(Q^2, s)$ . If the electron mass is assumed to be zero, a reasonable approximation in the present kinematics, the  $i = 6$  component of the axial form factor also vanishes. Further, the photo- and electroproduction data can be fit using the assumption that  $C_5^\gamma = 0$  and that  $C_4^\gamma = -\frac{M}{M+M'}C_3^\gamma$  [31]. Additionally, as can be seen in Equation 2.84, the value of  $C_3^A(0)$  was found to be zero, eliminating the first term of  $G_{N\Delta}^A$ . Thus, in the model used in this thesis, only the  $i = 3,4$  terms of the electromagnetic and the  $i = 4,5$  terms of the axial form factors contribute to the asymmetry.

With the parameterization of the form factors chosen, a theoretical prediction for  $\Delta_{(3)}^\pi$  can be determined. The uncertainty on the calculation stems from several sources, including the parameterizations and the coefficients associated with them. The vector dipole mass has been studied extensively through both charged current neutrino reactions and through elastic electron scattering, but the axial mass is less well understood. Recent data have suggested a trend of the axial mass being larger than the world value by several sigma. As such, this is an area that has significant experimental and theoretical interest. The axial mass will be discussed in more detail in the next section. An additional consideration for uncertainty is the assumption that the non-resonant contribution is negligible. A sufficiently precise determination of the inelastic asymmetry could be used to

determine the accuracy of this assumption.

### **Axial Mass**

The axial mass is a term that arises from the dipole parameterization of the axial form factor shown in Equation 2.82. The world value quoted previously has been determined from fits to neutrino data, most of which were taken prior to 1990. From these fits, an uncertainty of 0.02 GeV has been established for  $M_A$ . Bernard *et al.* also computed an axial mass using pion electroproduction data [29], leading to an average value higher than that of the original neutrino data, at  $M_A \sim 1.1 \pm 0.02$  GeV. Though these two values differ somewhat, they still agree within about  $2\sigma$ . The more recent data from neutrino scattering, taken since 2005, has indicated that the axial mass could be as high as 1.35 GeV. As an example, the MiniBooNE collaboration reported an axial mass of  $M_A \sim 1.35 \pm 0.06$  GeV from their measurement of quasi-elastic nucleon-neutrino cross sections using a carbon target [32]. Similar findings have been reported by the K2K [33] [34] and MINOS [35] collaborations. The NOMAD collaboration, however, found  $M_A = 1.05 \pm 0.06$  GeV, which is consistent with the world value [36].

Much of the older data were taken using deuterium targets, while the newer data is on heavier nuclei such as carbon. As such, it was postulated that the discrepancies could be due to deficiencies in the available theoretical models of nuclear effects. The nuclear models that are used, however, have shown reasonable agreement with electron scattering data, indicating that the discrepancy may be due to interpretation of the neutrino data. Recent theoretical re-interpretations of these data include the use of a model-independent analysis [37] and a re-analysis of the MiniBooNE cross sections with a model developed using results from photon, electron and pion data [38]. These analyses each found an  $M_A$

consistent with the world value, indicating that the anomaly reported may be due to problems with the interpretation of the recent neutrino data. Given the recent controversy, the axial mass continues to be a topic of much study from both the experimental and theoretical neutrino community. A measurement of the axial mass through  $A_{inel}$  would add to this

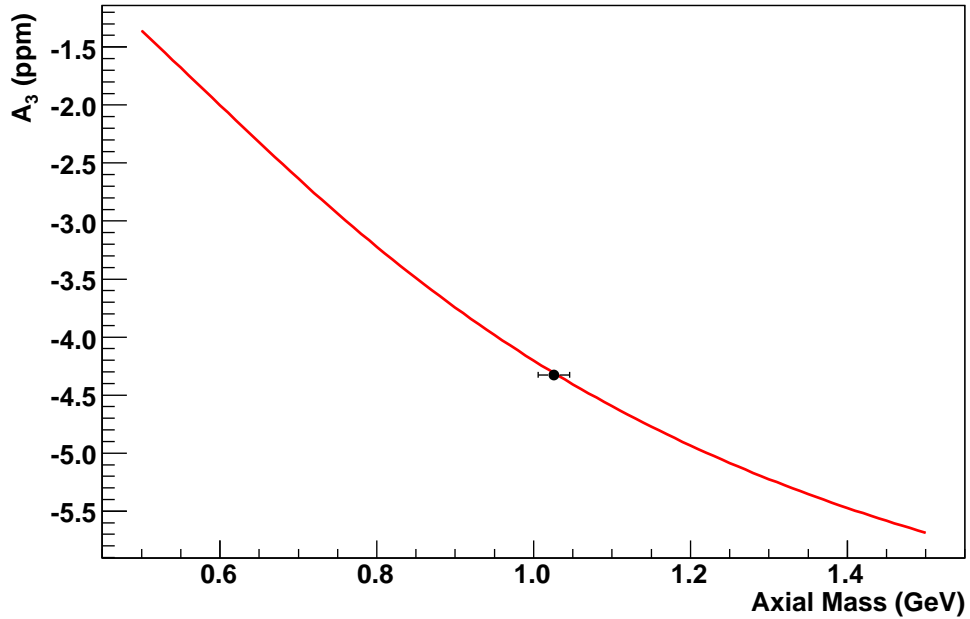


FIG. 2.3: Axial term of the asymmetry,  $A_3$ , as a function of axial mass,  $M_A$ , using the Adler parameterization. The point shown on the plot represents the current world value  $M_A = 1.03 \pm 0.02$  GeV.

discussion since it would offer a result gathered through a previously untested reaction. However, using this measurement to gain insight on the recent controversy would be difficult as the asymmetry is not very sensitive to changes in  $M_A$ . Figure 2.3 shows the axial component of the asymmetry,  $A_3$ , computed using the model in this thesis as a function of  $M_A$  over a range large enough to encompass all of the current predictions. A single black point is used to indicate the world average and its error. The range of  $A_3$  contained within the errors of  $M_A$  is  $\sim 0.1$  ppm. In order to distinguish between the world value and

the recent neutrino results, one would need to determine  $A_3$  to within 1 ppm. Note that this is a single component of the measured asymmetry. In order to find  $M_A$ ,  $A_3$  would first need to be extracted from  $A_{inel}$ . This would require a knowledge of  $A_{inel}$ ,  $A_1$  and  $A_2$  to an even greater precision. Ignoring any experimental limitations, theoretical uncertainty associated with non-resonant processes in both  $A_2$  and  $A_3$ , and with electroweak radiative corrections at the axial hadron vertex are expected to be sufficiently large to rule out such a precise measurement. In order for a measurement of  $M_A$  through the inelastic asymmetry to provide meaningful insight, theoretical understanding of the axial response and the non-resonant backgrounds would need to be significantly improved.

### 2.3.5 Secondary Inelastic Model

Matsui, Sato and Lee have developed a dynamical model of pion electroproduction near the  $\Delta$  resonance [39] and performed a calculation of the inelastic asymmetry at the  $G^0$  kinematics. A brief introduction to the notation used by Matsui *et al.* and how it compares to the primary model of this thesis will be presented here. Like the primary model, they derive an asymmetry in terms of a sum of resonant vector, non-resonant vector and axial vector hadron pieces. Using their notation,  $A_{inel}$  is given by

$$A = \frac{1}{2}A^0 \left[ (2 - 4 \sin^2 \theta_W) + \Delta_V + \Delta_A \right], \quad (2.85)$$

where  $A^0$  was defined in Equation 2.43 and the quantity  $(2 - 4 \sin^2 \theta_W)$  is identical to  $\Delta_{(1)}^\pi$  as defined in Section 2.3.2. The two remaining terms,  $\Delta_V$  and  $\Delta_A$  are equivalent to  $\Delta_{(2)}^\pi$  and  $\Delta_{(3)}^\pi$ , respectively. However, the formalism used to calculate these terms differs from that which was presented previously. For the purposes of distinguishing between the two formalisms, the asymmetry presented here will be referred to as the Matsui model and the formalism discussed previously will be referred to as the Musolf model.

In the Matsui model,  $A$  is derived by starting with the resonant asymmetry in terms of structure functions first presented in Section 2.1.2. Equation 2.30 is then expanded to include a non-resonant term containing isoscalar structure functions  $W_{1,2}^{is}$  by treating the neutral weak vector current as a sum of isovector and isoscalar terms,

$$J_\mu^{Z,V} = (1 - 2 \sin^2 \theta_W) J_\mu^{EM} - V_\mu^{isoscalar} . \quad (2.86)$$

They obtain  $W_{1,2}^{is}$  using their definition of  $W_{1,2}^{EM}$  by replacing the electromagnetic current  $J_\mu^{EM}$  with the scalar current  $V_\mu^{isoscalar}$ . The resulting  $\Delta_V$  is given in terms of structure functions as

$$\Delta_V = \frac{2 \sin^2 \frac{\theta}{2} W_1^{is} + \cos^2 \frac{\theta}{2} W_2^{is}}{2 \sin^2 \frac{\theta}{2} W_1^{EM} + \cos^2 \frac{\theta}{2} W_2^{EM}} . \quad (2.87)$$

This form allows for a computation of the non-resonant asymmetry using their dynamical model rather than through the use of multipoles.

For the axial term, the definitions of  $\Delta_A$  and  $\Delta_{(3)}^\pi$  in terms of structure functions are the same. Where the Matsui model differs is in the parameterization of the form factors. Their form factors,  $c_j$  and  $d_j$ , are related to the Adler form factors  $C_i^\gamma$  and  $C_i^A$  according to [40],

$$\begin{aligned} c_1(0) &= 2\sqrt{3}C_3^\gamma(0) , & d_1(0) &= \sqrt{3}C_5^A(0) , \\ c_2(0) &= 4\sqrt{3}C_4^\gamma(0) , & d_2(0) &= \frac{\sqrt{3}}{2}C_4^A(0) , \\ c_3(0) &= 4\sqrt{3}[C_4^\gamma(0) + C_5^\gamma(0)] , & d_3(0) &= \frac{\sqrt{3}}{2}[2C_6^A(0) - C_4^A(0)] , \\ c_4(Q^2) &= \sqrt{3}C_6^\gamma(Q^2) = 0 , & d_4(Q^2) &= \frac{\sqrt{3}M}{2M'}C_3^A(Q^2) = 0 . \end{aligned} \quad (2.88)$$

Like the Musolf model, a dipole form is used for both the vector and the axial vector form factors. However, the additional  $Q^2$  parameterization present in the function  $\xi^A$  takes on an exponential form rather than that of Equation 2.83. This results in the following form

for the vector and axial form factors:

$$c_i(Q^2) = c_i(0)G_D^V(Q^2) , \quad (2.89)$$

$$d_{1,2}(Q^2) = d_{1,2}(0)\xi(Q^2)G_D^A(Q^2) , \quad (2.90)$$

$$d_3(Q^2) = d_3(0)\frac{M^2}{Q^2 + M_\pi^2}\xi^A(Q^2)G_D^A(Q^2) , \quad (2.91)$$

where  $G_D^{V,A}$  are given in Equation 2.82 and  $\xi^A$  is given by

$$\xi^A(Q^2) = (1 + aQ^2)e^{-bQ^2} , \quad (2.92)$$

The coefficients  $a = 0.154 \text{ (GeV/c)}^{-2}$  and  $b = 0.166 \text{ (GeV/c)}^2$  were determined by fits to neutrino data.

Since its form differs from that of the Musolf model, a calculation of the asymmetry using the Matsui *et al.* model is useful for comparison purposes and the determination of model uncertainty. Additionally, a precise determination of  $A_3$  from data would provide insight into the reliability of this model. A comparison between the two models presented in this chapter, and a comparison of each to the extracted  $A_3$ , will be presented in Chapter 6.

## 2.4 Inelastic Asymmetry at the $Q^2 = 0$ limit

The discussion of the asymmetry in this chapter has thus far only included contributions from tree-level processes. To properly model real-world interactions it is necessary to also include higher order processes, referred to as radiative effects, involving both the photon and the  $Z^0$ . Radiative effects can be grouped into three categories: electromagnetic, one quark electroweak and multi-quark electroweak. Electromagnetic radiative effects involve single photon loops and the real emission of photons through

bremsstrahlung. Electroweak radiative effects involve interactions between the exchanged particle,  $\gamma$  or  $Z^0$ , and the constituent quarks of the nucleon (one-quark), and weak interactions among the constituent quarks within the nucleon (multi-quark). Theoretical interpretations of these effects are available and can be used to apply corrections to the tree-level asymmetry. More detail on the radiative effects and corrections applied for them will be given in Chapters 5 and 6. In this section, a brief discussion of one particular multi-quark electroweak radiative effect that has drawn theoretical and experimental interest will be presented.

Zhu *et al.* have studied multi-quark electroweak radiative effects at the axial hadron vertex in both elastic electron scattering [18] and  $\Delta$  electroproduction [25] and have found that these effects, which have the potential to be large, have a high theoretical uncertainty. In the low  $Q^2$  limit, the presence of an electric dipole coupling at the  $\gamma N \Delta$  vertex prevents the parity-violating asymmetry from vanishing at  $Q^2 = 0$ . This coupling, of order  $G_F$ , does not exist in the elastic channel, as it arises from the difference in energy between the initial and final states of the hadron. The behavior at the  $\gamma N \Delta$  vertex can be characterized by a low-energy coupling constant,  $d_\Delta$ . Additional radiative effects stemming from reactions in which the parity violation occurs at the  $\pi N \Delta$  vertex, called  $d$ -wave reactions, also are expected to contribute to the inelastic asymmetry, but to a lesser extent than the other contributions for  $Q^2 < 1 \text{ (GeV/c)}^2$ .

With these additional contributions in mind, the total  $\Delta_{(3)}^\pi$  can be written [25]

$$\Delta_{(3)}^\pi(\text{tot}) = \Delta_{(3)}^\pi(\text{NC}) + \Delta_{(3)}^\pi(\text{Siegert}) + \Delta_{(3)}^\pi(\text{anapole}) + \Delta_{(3)}^\pi(\text{d-wave}), \quad (2.93)$$

where  $\Delta_{(3)}^\pi(\text{NC})$  is the resonant value given in Equation 2.65. The added terms are the radiative corrections that Zhu *et al.* find contribute most significantly in the low  $Q^2$  region. The anapole and Siegert terms are those which characterize the parity-violating

$\gamma N\Delta$  coupling, with the Siegert term so named because its form is derived from Siegert's theorem describing electric multipole transitions [41] [42]. The asymmetry at  $Q^2 = 0$  is dominated by the Siegert term and can be written [25]

$$A(Q^2 = 0) \approx -\frac{2d_\Delta}{C_3^\gamma} \frac{M}{\Lambda_\chi} + \dots, \quad (2.94)$$

where  $C_3^\gamma$  is the Adler form factor described in Section 2.3.4,  $M$  is the nucleon mass, and  $\Lambda_\chi$ , which represents the scale of chiral symmetry breaking, is  $4\pi F_\pi \sim 1$  GeV. The “...” denotes corrections due to higher-order chiral effects and  $1/M$  terms.

The radiative corrections can be grouped together such that

$$\Delta_{(3)}^\pi(tot) = 2(1 - 4 \sin^2 \theta_W^0)(1 + R_A^\Delta)F(Q^2, s). \quad (2.95)$$

where  $\sin^2 \theta_W^0$  is the tree-level value of  $\theta_W$ . The quantity  $R_A^\Delta$  is simply the sum of the contributions from one-quark electroweak reactions in addition to those from anapole, Siegert and  $d$ -wave reactions. At tree level,  $R_A^\Delta = 0$  and the form of  $\Delta_{(3)}^\pi$  is the same as presented in Equation 2.65. The application of these radiative corrections to the inelastic asymmetry measurement in this thesis will be discussed in more detail in Chapters 5 and 6.

The low-energy constant  $d_\Delta$  can be determined by measuring the asymmetry from pion photoproduction at very low  $Q^2$  and making use of Equation 2.94 to deduce the value of  $d_\Delta$ . Ideally, one would wish to take measurements at the photoproduction limit, when the electromagnetic propagator ( $\gamma$ ) becomes a real photon, so as to directly measure this quantity. However, as this is not a practical experimental measurement at this time, measurements are instead made at kinematics approaching the limit. Such measurements contain a mixture of pions that have been electro- and photoproduced, meaning a mixture of both real and virtual photons. In order to extract the contribution from photoproduction,

estimates for the relative contributions of real versus virtual photons need to be made along with an extrapolation to the  $Q^2 = 0$  limit.

One such measurement was included as part of the backward angle portion of the  $G^0$  experiment using the pion data collected during the low-energy deuterium run period [43]. During this measurement, the beam energy was  $\sim 360$  MeV, leading to a  $Q^2$  for the detected  $\pi^-$  of  $Q^2 = 0.0032 \pm 0.0003$  (GeV/c)<sup>2</sup>. The  $\pi^-$  were photo-produced from bremsstrahlung photons which originated in the long deuterium target and then interacted with the neutrons in deuterium ( $\gamma + n \rightarrow \pi^- + p$ ). This measurement was then used to constrain the value of  $d_\Delta$  to the  $\pm 25 g_\pi$  level. According to Equation 2.94, this  $\pm 25 g_\pi$  bound limits the asymmetry to  $|A(Q^2 = 0)| < 1$  ppm.

A second measurement sensitive to  $d_\Delta$  will be performed by measuring the parity-violating asymmetry in inelastic  $ep$  scattering at very low  $Q^2$  ( $0.02 < Q^2 < 0.03$  (GeV/c)<sup>2</sup>) as part of the Qweak experiment being conducted in Jefferson Lab's Hall C [44] [45]. In this measurement, the inelastic asymmetry will be determined using the same reaction as used in the  $G^0$  measurement discussed in this thesis. Unlike  $G^0$ , however, the Qweak measurement will include dedicated inelastic periods where the magnetic field of the spectrometer is lowered so as to focus the inelastic events into the detectors. The dedicated measurement, coupled with a longer target and higher beam current, will allow for a higher precision measurement than the  $G^0$  inelastic measurement was able to attain. This high precision is crucial to the measurement, as  $A(Q^2 = 0)$  is expected to be less than 1 ppm. Qweak has already completed its first phase, which will result in a rough measurement of the asymmetry, and is scheduled to complete its second phase, which will lead to full precision, in mid-2012 [46].

## 2.5 Summary

In the electroweak interaction, interference between the electromagnetic and weak amplitudes leads to an observable violation of parity. The asymmetry arising from this parity violation is sensitive to the physics of the weak interaction and can be used to study the structure of hadrons such as the proton. In inelastic  $ep$  scattering near the  $\Delta$  resonance, the asymmetry provides insight into the behavior of the proton as it transitions to the  $\Delta$ . The formalism presented in this chapter provides the theoretical basis of the measurement of the inelastic asymmetry that was performed during the  $G^0$  experiment.

The tree-level parity-violating asymmetry for inelastic  $ep$  scattering can be written as a sum of vector and axial vector components as

$$A_{inel} = \frac{1}{2}A^0 [\Delta_{(1)}^\pi + \Delta_{(2)}^\pi + \Delta_{(3)}^\pi] , \quad (2.96)$$

where the three  $\Delta_{(i)}^\pi$  terms represent the asymmetry at the resonant vector, non-resonant vector and axial hadron vertices, respectively. The measured asymmetry also includes higher-order electromagnetic and electroweak radiative effects, which will be accounted for in Chapters 5 and 6. When these higher order effects are taken into account, it is believed that an electric dipole coupling at the parity-violating  $\gamma N\Delta$  vertex, referred to as the Siegert term, causes the asymmetry to be non-zero when  $Q^2 = 0$ .

The theoretical asymmetry,  $A_{tot}$ , has been plotted using the Musolf Model in Figure 2.4, along with the three sub-terms ( $A_1$ ,  $A_2$ ,  $A_3$ ), as a function of  $Q^2$  for a fixed beam energy and scattering angle consistent with the  $G^0$  kinematics. The range of  $Q^2$  plotted was chosen to be large enough to include both the low  $Q^2$  region and the full the  $G^0$  inelastic acceptance. The average  $Q^2$  for the measurement is shown as a vertical dotted line on the plot. The asymmetry computed here is the tree-level asymmetry from Equation 2.96, with no radiative effects included.

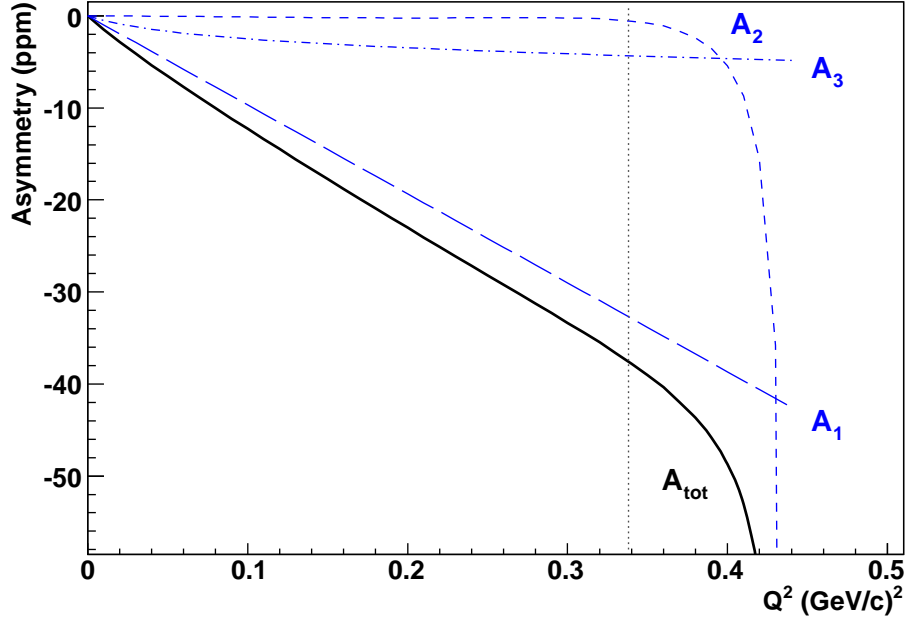


FIG. 2.4: The theoretical asymmetry is plotted as a function of  $Q^2$  for a fixed scattering angle ( $\theta = 95^\circ$ ) and beam energy ( $E = 0.687$  GeV). The solid black line represents the total theoretical asymmetry,  $A_{tot}$ , while the blue curves represent the three components of the asymmetry,  $A_1$  (long-dash),  $A_2$  (dash) and  $A_3$  (dash-dot). The dotted vertical line represents the average  $Q^2$  of the  $G^0$  experimental acceptance. The rapid fall-off of  $A_2$  for  $Q^2 > 0.4$  (GeV/c) $^2$  is due to the kinematics reaching the edge of the range where the  $A_2$  model can be used.

For  $Q^2 < 0.4$  (GeV/c) $^2$ , the dominant term in the asymmetry is expected to be the resonant vector term,  $A_1$ . Since it depends only on Standard Model couplings,  $A_1$  is the most well-understood portion of the asymmetry. The non-resonant vector term,  $A_2$ , which is computed as a sum of multipoles determined using fits to data, is found to be a significantly smaller contribution to the total asymmetry. The axial term,  $A_3$ , which contains the physics of interest in computing quantities such as the axial transition form factor or the axial mass, is larger than the  $A_2$  but is still small, contributing only about 10% of the total asymmetry at the experimental  $Q^2$ . Note that because the non-resonant axial contribution is expected to be small in this region, the model used in this thesis

computes only the resonant axial asymmetry.

In the  $Q^2 > 0.4 \text{ (GeV/c)}^2$  region, the model for the non-resonant term becomes unstable due to the fact that  $A_2$  is inversely proportional to the scattering cross section. The cross section tends to zero as  $W$  approaches 1.07 GeV, the pion threshold, which translates to about  $Q^2 = 0.45 \text{ (GeV/c)}^2$  for these kinematics. Though this could be problematic for theoretical predictions of  $A_{tot}$  in this  $Q^2$  region, the  $Q^2$  of the  $G^0$  measurement is sufficiently away from threshold that  $A_2$  is stable.

## CHAPTER 3

# The $G^0$ Experiment at Backward Angle

The  $G^0$  experiment was performed at the Thomas Jefferson National Accelerator Facility, or Jefferson Lab, in two phases over a period of 4 years. Measurements were taken at two  $Q^2$  values at both forward and backward electron scattering angles using a hydrogen target. At backward angle, data were also obtained for the same  $Q^2$  values using a deuterium target. The three target and angle combinations are needed to determine the elastic strange and axial form factors as described in Section 2.2. Data from additional  $Q^2$  values in the range  $0.1 \leq Q^2 \leq 1.0 \text{ GeV}^2$  were taken at forward angles allowing for some understanding of the form factors in this range but not the full separation afforded by the additional backward angle data. The experimental design and kinematic range of the backward measurements also allowed for the study of inelastic scattering near the  $\Delta$  resonance.

An overview of the experiment, including both the incident electron beam and the design specifications of the target, magnet and detectors for the backward angle measurement, will be given in the sections that follow. Additionally, a description of the data

structure and summary of the data collected will be presented. All details of positioning of the experimental apparatus in this chapter will be in reference to the backward angle setup.

### 3.1 Experimental Design Overview

$G^0$  first took data at forward angles over a 3 month period in 2003. The bulk of the design of the experiment was driven by forward angle considerations, with the added consideration of the ability to easily transition from forward to backward angles. For the forward angle measurement, asymmetry in several  $Q^2$  bins was measured by detecting recoiling protons. The electron scattering angles of interest ranged from  $16^\circ$  to  $21^\circ$ , resulting in recoiling protons detected at an angle of  $\sim 70^\circ$ . The basic setup consisted of a cryogenic target for the electrons to scatter from, a magnet and collimator system to steer particles with the appropriate kinematics to the detectors, and the detectors themselves. Details of the design and implementation of experimental equipment as used for the forward angle measurement are available elsewhere [47].

While the backward angle measurement was able to make use of most of the same experimental equipment as the forward angle, there were a few major differences in the setup and how the measurement was performed. In addition to the changes in physical location needed to transition from forward angles to backward, the primary difference in the two phases of the experiment was the detected particles, with the scattered electron being detected in the backward angle phase rather than the recoiling proton. The target and magnet were used in the backward angle phase without any changes other than positioning, while the scintillators that detected the forward angle protons, labeled Focal Plane Detectors (FPDs), were used with minor changes to detect electrons.

For the forward angle measurement, each FPD represented a bin in  $Q^2$  and the time of flight (TOF) for a particle traveling from the target to a given detector was used to separate elastic events from inelastic events, and also to separate out pion backgrounds. The differing kinematics of the backward angle electron measurement limited the measurement to a single  $Q^2$  value for a particular beam energy and required additional detectors to be added to differentiate between elastic and inelastic events and between different types of detected particles. A second set of scintillators, the Cryostat Exit Detectors (or CEDs), was placed between the target and the FPDs to allow for a crude tracking of the scattered electron's path. This led to a two dimensional detector space which allowed for a kinematic separation between elastic and inelastically scattered electrons. The last major change to the detector system to prepare for the backward angle measurement was the addition of Cherenkov detectors, mounted together with the CEDs, used to distinguish between electrons and pions.

The detector system was segmented into octants arranged symmetrically around the beamline with each detector octant corresponding to one of the magnet's eight coils. Figure 3.1 shows a cutaway view of the target cell, magnet and detector system as they were configured for the backward angle phase of the experiment. Note that, for simplicity, only a single detector octant and magnet coil has been included in the figure.

## 3.2 The Electron Beam

In order to study parity violation, it is necessary to have the ability to produce electrons polarized in the two different helicity states. Jefferson Lab is home to the Continuous Electron Beam Accelerator Facility, or CEBAF, an electron accelerator presently capable of producing a roughly 85% polarized electron beam at energies up to 6 GeV

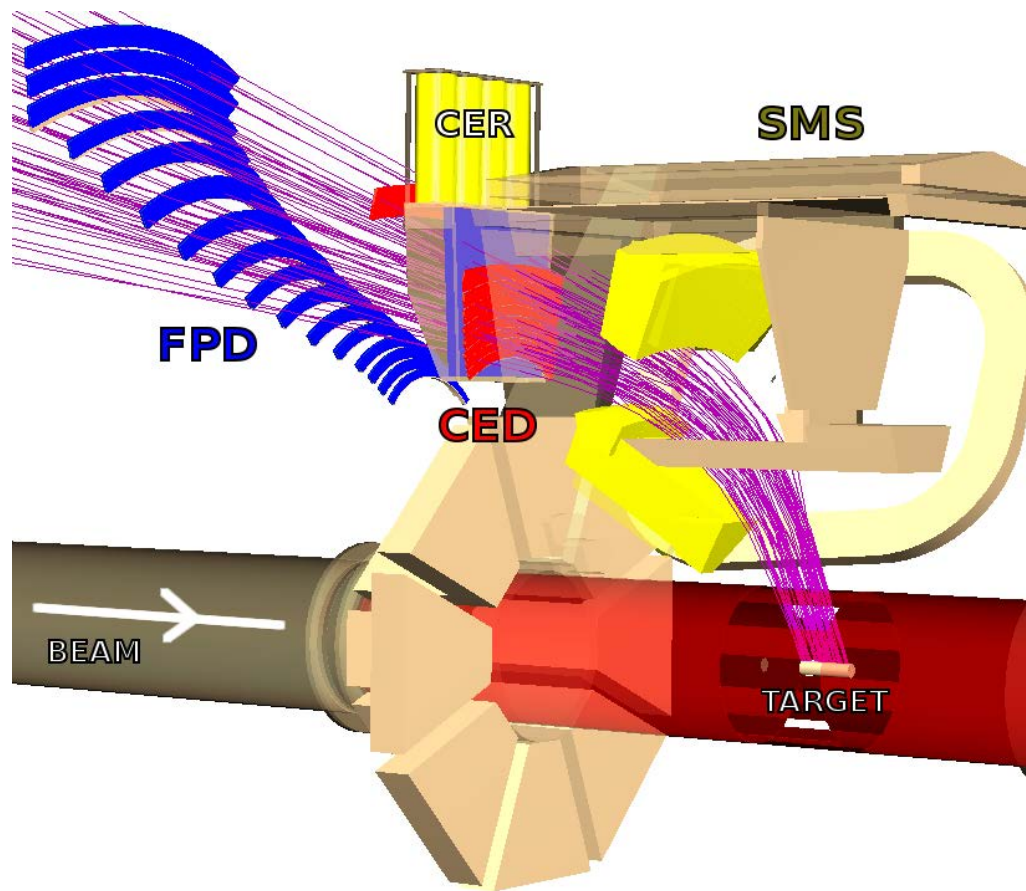


FIG. 3.1: Cutaway view of the  $G^0$  target, magnet and detector system in the backward angle configuration. Note that only a single detector octant and the corresponding magnet coil have been shown.

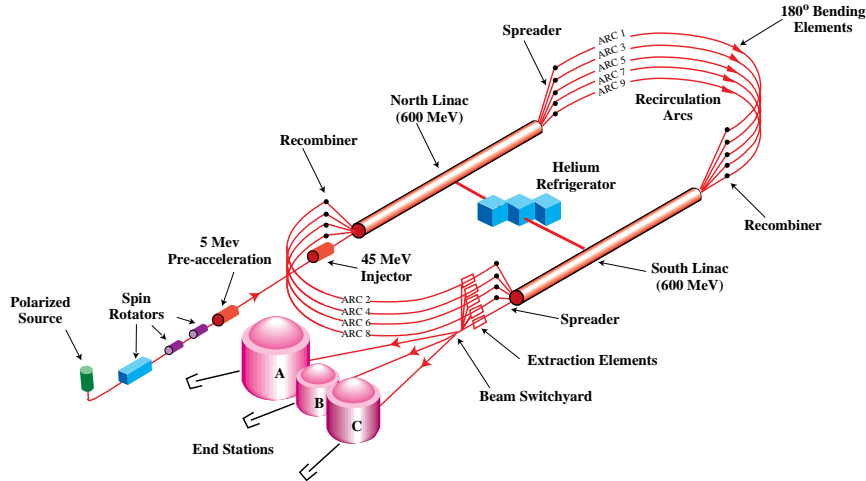


FIG. 3.2: Diagram of Jefferson Lab's CEBAF accelerator.

[48]. An accelerator upgrade, set to begin in the summer of 2012, will increase the maximum energy of the electron beam to 12 GeV [49]. The accelerator is designed with the ability to simultaneously deliver polarized beam to three separate experimental halls, Halls A, B and C. These halls are available for use by outside experimenters interested in studies involving both user-specific apparatus (such as  $G^0$ ) and permanently installed spectrometers within the halls. A fourth experimental hall, Hall D, will be added as part of the 12 GeV upgrade. The  $G^0$  experiment was installed in Hall C. While an experiment is running in a given hall, collaborators are on site at all times monitoring the equipment and data from a dedicated area, called the counting house, in a building located above the halls.

### 3.2.1 Polarized Source and Injector

The electron beam begins with polarized electrons that are emitted from GaAs photocathodes. In this process, laser light from a 5 W fiber laser is shone on one of two

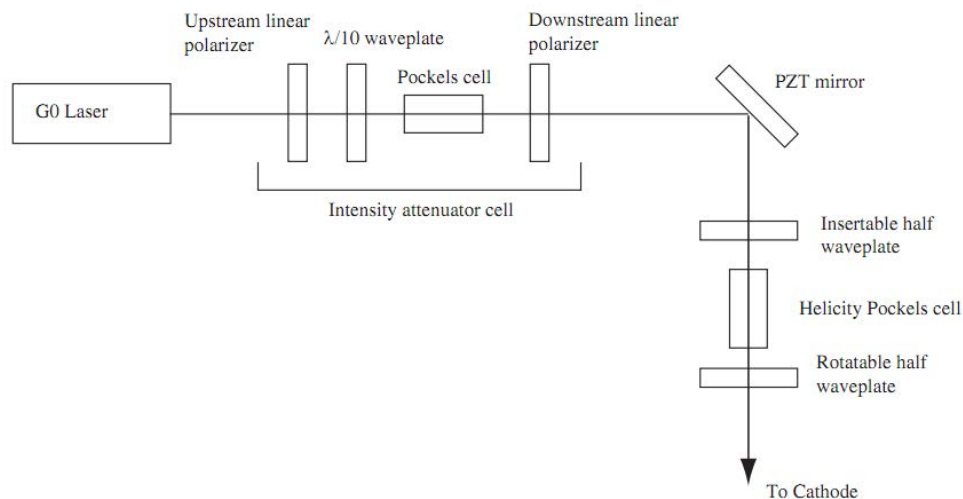


FIG. 3.3: Diagram of the laser table that represents the starting point for the Hall C helicity beam. Light from the fiber laser passes through several optical devices to refine its polarization and helicity before being shone on the GaAs photocathodes that produce the polarized electrons.

identical 100 kV GaAs electron guns. Electrons within the GaAs absorb photons from the laser, gaining enough energy to break free of the lattice. The specific form of GaAs used at CEBAF consists of a strained superlattice structure that allows for emission of highly polarized electrons [50]. Before the laser light reaches the photocathodes it passes through a series of optical devices that set the polarization and helicity of the emitted electrons. Figure 3.3 shows a diagram of the various components of this system .

The helicity of the beam is determined by a Pockels cell (PC) that takes linearly polarized light and produces light that is circularly polarized in either a left or right handed manner. The cell is comprised of a birefringent crystal that reacts to an applied voltage. The crystal is oriented at an angle of  $45^\circ$  with respect to the polarization of the incoming beam, leading to a  $\pm \lambda/4$  phase shift of the light as it travels through the crystal, with the sign of the shift depending on the sign of the applied voltage. The shift retards one component of the light relative to the other, resulting in circular polarization. The helicity

pattern and rate of the helicity flip are determined by experimental requirements. For  $G^0$ , the helicity was flipped at a rate of 30 Hz, resulting in a series of 1/30 s segments of common helicity called macropulses (MPSs). The helicity pattern was generated as a collection of four MPSs, referred to as a quartet. The use of quartets, coupled with the fast helicity reversal, cancels linear drifts that can affect the asymmetry.

The sequence of the helicity reversal for each quartet was chosen to be either  $+ - - +$  or  $- + + -$  depending on a randomly generated initial MPS. The asymmetry is then defined as the difference in yields between each helicity state within the quartet such that

$$A_{qrt} = \frac{(Y_1^+ + Y_4^+) - (Y_2^- + Y_3^-)}{(Y_1^+ + Y_4^+) + (Y_2^- + Y_3^-)}, \quad (3.1)$$

$$A_{qrt} = \frac{(Y_2^+ + Y_3^+) - (Y_1^- + Y_4^-)}{(Y_2^+ + Y_3^+) + (Y_1^- + Y_4^-)},$$

with the form used dependent on which of the two helicity patterns is represented by a particular quartet. Here the  $Y_i^\pm$  is the MPS yield for the  $i^{th}$  MPS within the quartet and the sign represents the helicity of the MPS. The final measured asymmetry is the average of all measured quartet asymmetries.

In order to reduce helicity-correlated systematic effects, an insertable half-wave plate (IHWP) can be placed into the beam line just before the PC. The insertion of the IHWP flips the helicity of the polarized laser light incident on the PC. When the IHWP is moved, no other change is made to the beam, the detectors or the electronics. Therefore, the resulting measured asymmetry should be identical in magnitude for both IHWP positions, with only the signs differing. Any difference in the magnitude of the asymmetry would indicate possible helicity-correlations in the detectors or electronics, which would lead to false asymmetries that would need to be corrected in analysis. In order to cancel these effects, data were taken with the IHWP in both the IN and OUT positions, with the position

changed at regular intervals throughout the run. The total accumulated data for a given run period consisted of an even split between the two IHWP states and the final measured asymmetry is taken to be the sign-corrected average of the states.

False asymmetries can also arise from a difference in beam current, or intensity, between the two helicity states. This asymmetry, referred to as charge asymmetry, is controlled using an intensity attenuator (IA), which is a system of optics located in the path of the Hall C laser before the helicity control optics. When the laser light enters the IA, it is first linearly polarized with a polarizer, then the polarization is rotated using a half-wave plate before the light passes through a PC. This results in circularly polarized light with an intensity driven by the voltage applied to the PC. Before the beam exits the IA, it passes through a second linear polarizer so that the resulting beam is polarized in the same direction as the incident light. The IA operates on a feedback system, allowing for real-time adjustments to the PC voltage in order to keep the charge asymmetry within the specifications of a given experiment. The charge asymmetry is measured constantly, with an average value determined every three minutes. The PC voltage is then adjusted automatically based on the present value of this asymmetry.

After passing through the optics described above, the circularly polarized laser light strikes the GaAs photocathode leading to the emission of polarized electrons. These electrons then enter the injector system where their polarity is adjusted by a Wein filter and they are given an initial boost in energy before entering the accelerator. The electrons emitted from the photocathode will ideally be completely longitudinally polarized, as required for  $G^0$ , but due to real-world limitations, there will likely be some component of the polarization in the transverse direction. Additionally, because the electrons are relativistic, their spin precesses as they travel within the accelerator. The Wein filter, located just after the photocathodes, rotates the polarization of the beam by an angle, known as

the Wein angle, chosen to offset these two effects such that the beam polarization will be fully longitudinal when the beam enters the hall. After the Wein filter, the beam passes through a series of solenoids that focus the beam and a 45 MeV injector before entering the accelerator.

### 3.2.2 Accelerator

After the electrons leave the injector, they enter the accelerator where they are circulated around a loop until they achieve the energy required for a given experiment. The CEBAF accelerator consists of two parallel linear accelerators (LINACs) and recirculating arcs which use dipole magnets to guide electrons in an arc connecting the two LINACs, forming a closed loop (see Figure 3.2). Each LINAC consists of a series of resonant cavities that use an oscillating radio frequency signal to create a uniform electric field in the center of the cavity. When the electrons enter the electric field, they experience a force, accelerating them through to the next cavity. The total amount of acceleration in the LINAC is determined by the magnitude of the field in the cavities. Although the beam provided by the accelerator is considered continuous, it is actually a pulsed beam with electrons sent to the accelerator in bunches at a frequency that matches the accelerator's resonant frequency of 1497 MHz. Every third bunch of electrons is directed to a particular experimental hall, and, as such, the frequency of the beam seen in the individual experimental halls is 499 MHz, or one third of the total frequency of the accelerator.

The electrons begin in the North LINAC, where their energy is increased by up to 600 MeV. Once they reach the end of the LINAC, they are steered by a magnetic field that changes their direction  $180^\circ$  before entering the second LINAC for further acceleration. Since each LINAC is capable of providing an acceleration up to 600 MeV, each

trip around the loop, called a *pass*, results in an addition of approximately 1.2 GeV, at most, to the electrons' energy. Electrons that have attained the appropriate energy enter an extractor at the end of the South LINAC which steers them from the accelerator loop into the beam switchyard which then directs them to the appropriate experimental hall. The remaining electrons are sent through the second set of recirculation arcs to make another pass through the accelerator loop. The electrons can travel a maximum of 5 passes, attaining a total maximum energy of about 6 GeV.

By using varying numbers of passes, the accelerator is capable of sending beam of differing energies to the three halls simultaneously provided the energies required are integer multiples of each other. For the  $G^0$  experiment, the high  $Q^2$  measurement was performed using a beam energy of  $\sim 690$  MeV which was attained by running a single pass through the accelerator. The low  $Q^2$  measurement required a beam energy lower than that at which CEBAF normally operates, necessitating the use of a new method in the accelerator. In order to achieve the desired  $\sim 360$  MeV, a "half-pass" was run wherein the North LINAC was used to provide all the acceleration while the South LINAC was essentially switched off, allowing the electrons to drift the length of the LINAC without any further acceleration.

### 3.3 Beam Monitoring

The asymmetry measured is dependent on the number of events scattered in each helicity state (see Section 3.2.1), with the assumption that the only change between the two states is the helicity. Because no beam is perfect, fluctuations in energy and intensity or drifts in beam position will always be present. If a particular beam parameter changes as the helicity changes, the kinematics of the system can change as well, leading to a

different number of scattered events than would have been present if the parameter had not changed and altering the asymmetry. The false asymmetry due to helicity-correlated changes in the beam is given by

$$A_{false} = \sum \frac{1}{2Y} \frac{\partial Y}{\partial P_i} \Delta P_i, \quad (3.2)$$

where  $Y$  is the detector yield and  $P_i$  represents the different beam parameters including position and angle in the  $x$  and  $y$  directions along with beam intensity and energy. The  $\Delta P_i$  terms represent the helicity-correlated changes in the beam parameters  $P_i$  and the derivatives  $\frac{\partial Y}{\partial P_i}$  represent detector sensitivities to these changes.

In order to correct for  $A_{false}$  with minimal impact on the systematic uncertainty, it is necessary to know the precise position and intensity of the beam as data are being collected. Individual systems measuring beam parameters were used to monitor the position, current, energy and focus of the beam throughout data taking. These parameters were able to be monitored in real time as data were being collected so that if any beam parameter was outside the accepted range, adjustments could be made immediately to fix it. These data were also recorded for use during the analysis phase of the experiment. Information about the beam parameters collected during the experimental run was used to compute  $\Delta P_i$  and  $\frac{\partial Y}{\partial P_i}$ , which were then used to determine the false asymmetry according to Equation 3.2. Once this asymmetry was known, a correction could be made to subtract out the contribution from the helicity-correlation. The correction will be discussed in Section 4.2.4.

The beam current was measured using two microwave cavity monitors located in the Hall C beamline 40 m upstream of the  $G^0$  target. The cavities were designed such that electrons excite a resonance as they pass through, leading to a signal that could be read out by antennas in the cavity. Since this was a non-intrusive method, the current could be

monitored concurrent with data taking. With typical MPS-to-MPS fluctuations in beam current on the order of hundreds of parts-per-million (PPM), the beam current monitors, which are able to resolve changes in current to the 40 ppm level, had sufficient sensitivity.

Beam position monitors collected information on the position of the beam at several locations as it traveled through the hall to the target. The monitors consisted of four thin wires, each of which had a length equal to one quarter wavelength at 1497 MHz, symmetrically arranged around the beam line. The signal read out from the wires was converted from voltage to frequency and recorded. By looking at linear combinations of the detector outputs in software, the beam's position and angle at a given location could be determined. The position and angle at the target was determined from the combination of two sets of detectors located about 6 m and 3.5 m upstream of the target.

A similarly designed monitor located in the Hall C arc was used to determine the beam energy. This was done by varying the field in the steering magnets and then measuring the beam position at the center of the arc, where the dispersion of the beam is the highest at 40 mm/%. The dispersion and position of the beam are then used to determine the energy. Because of the change in magnet current needed, beam energy measurements required special runs to be performed where nominal data collection was not able to be done.

The final beam property measured relates to the profile of the beam. If the beam is not focused to a sufficiently small diameter, it can lead to increased backgrounds as the wayward electrons scatter from the walls of the beampipe or parts of the experimental apparatus close to, but not intended to be in, the path of the beam. The vast majority of the electrons will be focused within a small beam diameter, but because of possible drift and interactions within the accelerator there may be some electrons that are far out from the center creating a halo around the beam. The specifications for the  $G^0$  beam required that

fewer than 1 ppm of the electrons be outside a 3 mm radius. This specification was chosen in part to avoid interference between the beam and an 11 mm diameter flange within the target cell. The beam halo was measured using a 2 mm thick ring of carbon with an inner diameter of 6 mm placed concentric with the beam line at a location about 8 m upstream of the target. The diameter of the ring was chosen so as to be close enough to the beam to give insightful information but far enough that it did not interfere with the bulk of the beam, allowing it to be used while data were collected. Electrons that scattered from the ring at angles of  $3^\circ$  and  $15^\circ$  were detected using several plastic scintillation detectors connected to photomultiplier tubes.

The beam position monitoring systems described above were in place monitoring the natural motion of the beam constantly as data was being collected. In order to interpret these data and learn the impact the small natural changes in the beam had on the main measurement, it was useful to take measurements while deliberately forcing large changes to position, angle and energy of the beam. By using steering coils located upstream of where the electrons enter the hall, the angle and position of the beam at the target could be varied over a range of  $\pm 5$  mm and  $\pm 5$  mr, respectively. This process, referred to as coil pulsing, was performed at regular intervals throughout the experimental run. The beam's energy was similarly varied periodically within the accelerator by altering the output of one of the South LINACs accelerator cavities. Data collected with these deliberate variations were used during the experimental run to monitor the systematics due to beam motion. Additionally, the detector sensitivities computed during these runs were compared to those computed using natural beam motion as a cross-check. Variations measured from natural beam motion, not coil-pulsing or energy variation, were used in the computation of  $A_{false}$ .

The beam monitors described above provided measurements of important beam pa-

rameters and allowed for corrections to be made, but, in order to reduce systematic errors from these corrections, ideally one wishes any fluctuations be small. Before taking data, the  $G^0$  collaboration determined specifications for the beam that would allow the experiment to meet its systematic error goals. Table 3.1 outlines the beam specifications for the backward angle phase of  $G^0$  and summarizes the actual fluctuations seen. In all cases, the CEBAF accelerator operators were able to provide beam that was well within the specifications requested.

Parameter	Spec	Actual
$\Delta x$ (nm)	40	$-19 \pm 3$
$\Delta y$ (nm)	40	$-17 \pm 2$
$\Delta\theta_x$ (nrad)	4	$-0.8 \pm 0.2$
$\Delta\theta_y$ (nrad)	4	$-0.0 \pm 0.1$
$\Delta E$ (eV)	34	$2.5 \pm 0.5$
$A_Q$ (ppm)	2	$0.09 \pm 0.08$

TABLE 3.1: Summary of  $G^0$  beam specifications.

### 3.4 Polarimetry

Given the polarized source currently in place at CEBAF, the polarization of the electron beam is expected to be greater than 70%, but, due to real-world limitations and imperfections, will never be 100%. Since theoretical predictions and the equations used to interpret the asymmetry assume full polarization, a correction must be applied to take this reduced polarization into account. Thus, it is important to know the exact polarization of the beam during the experimental run. In order to reduce systematic effects on the final asymmetry, it is desirable to have the ability to measure this polarization precisely.

Using polarimeters available at Jefferson Lab, the polarization of the beam was measured periodically throughout the  $G^0$  run. The primary system used was a Møller polarimeter located in the Hall C beamline just as the beam enters the hall [51]. Because it was designed for high energy measurements, precise results for the lower  $G^0$  beam energy were unable to be determined using the Møller. Instead, a 5 MeV Mott polarimeter located near the injector was used [52]. Measurements were also taken at high energy using the Mott as a consistency check between the two polarimeters and the two energies. An overview of the design of each polarimeter is given below.

### 3.4.1 The Møller Polarimeter

The Hall C Møller polarimeter is designed to provide a precise measurement of the beam's polarization as it enters the hall. The polarization is determined by measuring the asymmetry in electron-electron scattering, or Møller scattering, with both the beam and the target electrons polarized. The cross section for Møller scattering of longitudinally polarized electrons, which can be precisely predicted using QED, is given by

$$\frac{d\sigma}{d\Omega} = \frac{d\sigma_0}{d\Omega} [1 + P_t P_b A_{zz}(\theta)] , \quad (3.3)$$

$$A_{zz}(\theta) = \frac{-\sin^2 \theta (8 - \sin^2 \theta)}{(4 - \sin^2 \theta)^2} , \quad (3.4)$$

where  $P_t$  and  $P_b$  are the target and beam polarizations,  $\theta$  is the Møller scattering angle,  $A_{zz}$  is the analyzing power and  $\frac{d\sigma_0}{d\Omega}$  is the unpolarized cross section, defined as

$$\frac{d\sigma_0}{d\Omega} = \left( \frac{\alpha(4 - \sin^2 \theta)}{2m_e \gamma \sin^2 \theta} \right)^2 , \quad (3.5)$$

where  $\theta$  again represents the Møller scattering angle,  $m_e$  is the electron mass,  $\alpha$  is the fine structure constant and  $\gamma$  is the Lorentz factor. By measuring the cross section asymmetry

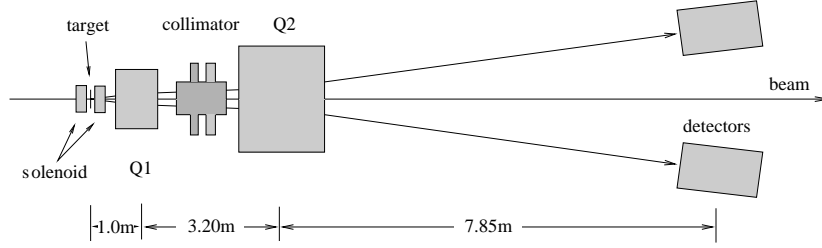


FIG. 3.4: Layout of the Hall C Møller Polarimeter. The polarimeter involves scattering polarized electrons from an iron foil target which has been polarized in the magnetic field produced by the solenoid. The two quadrupole magnets, labeled Q1 and Q2, steer the scattered electrons through the collimator system and away from the beamline such that those with appropriate kinematics enter the detector system.

between beam electrons polarized parallel and anti-parallel to the beam direction,  $P_b$  can be determined according to

$$A_{Møll} = \frac{\left(\frac{d\sigma}{d\Omega}\right)^{\uparrow\uparrow} - \left(\frac{d\sigma}{d\Omega}\right)^{\uparrow\downarrow}}{\left(\frac{d\sigma}{d\Omega}\right)^{\uparrow\uparrow} + \left(\frac{d\sigma}{d\Omega}\right)^{\uparrow\downarrow}} = P_t P_b A_{zz}(\theta), \quad (3.6)$$

assuming  $P_t$  is known. The arrows on the cross section represent the orientation of the electron polarization relative to the beam direction, with  $\uparrow\uparrow$  ( $\uparrow\downarrow$ ) indicating beam polarization parallel (anti-parallel) to the direction.

The Hall C Møller measures this asymmetry at a scattering angle of  $90^\circ$  in the center of mass frame, which maximizes  $A_{zz}$ , allowing for high statistical precision to be attained in a short period of time. In addition to increasing the analyzing power, the scattering angle chosen helps reduce the effect of backgrounds from Mott scattering.

A diagram of the Hall C Møller is given in Figure 3.4. In the figure, the beam direction is from left to right. The target consists of a foil made from pure iron placed in a 3 T magnetic field provided by the solenoid and magnetized out of plane to saturation. The target was designed so as to yield a polarization that is well known ( $8.00 \pm 0.04\%$ ) [52], thus reducing the systematic uncertainty on the final polarization measurement. After

scattering from the target, the electrons pass through a quadrupole magnet (labeled Q1 in the figure) and then through a collimator system that allows for the selection of a range of desired scattering angles by blocking electrons outside the set range. This system consists of a series of adjustable windows that place cuts in the horizontal and vertical directions and one fixed circular window centered on the beamline. Additional slits located just before the detectors provide added precision in the angle selection. By eliminating small angles, the collimators reduce the background from Mott scattering, leading to reduced uncertainty. The electrons that make it past the collimators then pass through a second quadrupole magnet (Q2) that steers them away from the central beamline into the lead-glass detectors. Electron pairs are measured as coincidences in the left and right detectors.

There are several sources of systematic error on the polarization measurements. Beam related uncertainties include the beam position and angle at the Møller target, while polarimeter design related issues such as the stability of the field within the magnets are also taken into account. There are also uncertainties related to the Møller target, such as the uncertainty on the magnitude and direction of the target polarization and the purity of the iron foil used. Additional considerations, such as backgrounds from multiple scattering, are outlined elsewhere [51]. Taking all of these sources of uncertainty into account leads to a total systematic error on the backward angle measurements of less than 2 % [53].

Because the Møller is located in the beamline between the accelerator and the  $G^0$  target, the polarization measurements are destructive measurements that cannot be taken during nominal running. Instead, the polarization was measured in dedicated runs periodically throughout the experimental run. Møller measurements were taken every 7-14 days during the high energy run periods, resulting in a total of 17 measurements.

### 3.4.2 The Mott Polarimeter

Due to design constraints, the Hall C Møller was unable to be used at the lower  $G^0$  beam energy of 362 MeV, so instead the polarization measurements were made using the Mott polarimeter located in the 5 MeV region of the injector. Unlike the Møller, the Mott polarimeter is not directly in the path of the beam but rather is on a dedicated line that branches off from the main beamline. Measurements using the Mott require transverse polarization, so before a measurement can be taken, the Wein filter (located upstream of the Mott) must be adjusted such that the electron beam entering the Mott is transversely polarized. The beam polarization is then determined through Mott scattering in which electrons scatter from the coulomb potential of a nucleus. In this reaction, the electron's spin couples to the coulomb field of the nucleus, leading to an asymmetry.

The layout of the Mott is given in Figure 3.5. Electrons enter from the left and scatter off an unpolarized gold foil target, with those scattered at an angle of  $172^\circ$  detected to maximize the analyzing power [52]. Four detectors, two in the horizontal plane and two in the vertical plane, allow for a measure of the asymmetry in the  $x$  and  $y$  directions, respectively. These asymmetries lead to a determination of  $P_x$  and  $P_y$  according to [54]

$$A_{Mott} = \frac{\sigma_+ - \sigma_-}{\sigma_+ + \sigma_-} = P_i S_{eff}(\theta), \quad (3.7)$$

where  $\sigma_{\pm}$  is the cross section of the right(up) and left(down) polarized electrons,  $P_i$  is the relevant component of the polarization ( $x$  or  $y$ ) and  $S_{eff}(\theta)$ , the Sherman function [55], is the analyzing power. Since  $S(\theta)$  was defined relative to scattering from a single atom, the effective value used here has been determined for scattering from multiple atoms and is dependent on the target material and its thickness.

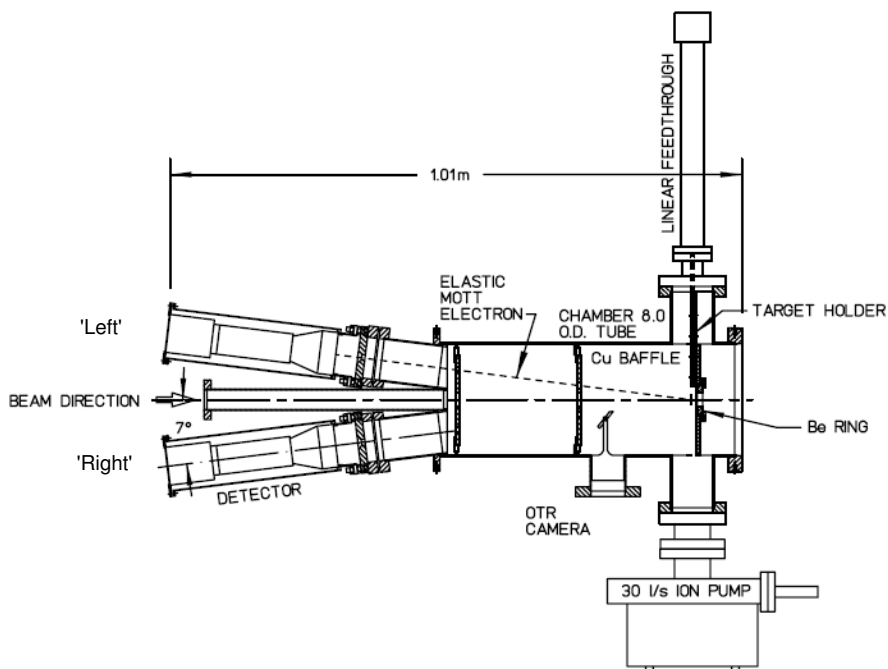


FIG. 3.5: Layout of the 5 MeV Injector Mott Polarimeter at Jefferson Lab.

### 3.4.3 Measurements and Conclusion

Several measurements of the beam polarization were made throughout the  $G^0$  experimental run, resulting in 17 data points using the Møller and 20 at each energy using the Mott. The average polarization for each of the three data sets was determined by fitting the data to a constant. Figure 3.6 shows the polarization measurements taken using the Hall C Møller polarimeter. The beam polarization as measured by the Møller was found to be stable throughout the high energy portion of the  $G^0$  backward-angle run. The measurements made using the Mott, shown in Figure 3.7, also show consistency within each set. In addition, a comparison of the high and low energy Mott measurements indicates that the beam polarization did not change with beam energy.

Based on these findings, it is fair to use the same central value for the beam polarization for the entire  $G^0$  experimental run. Since the Møller polarimeter gives a more precise

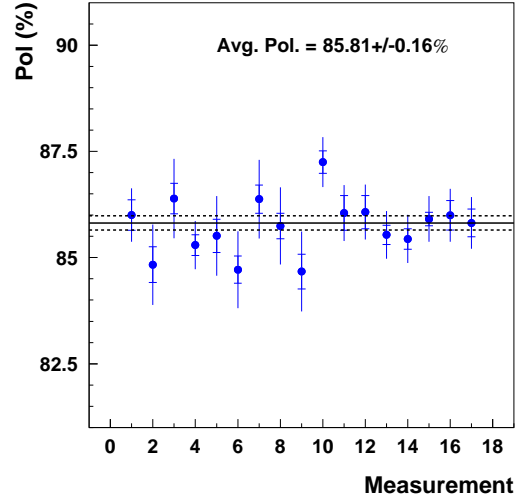


FIG. 3.6: Measurements taken with the Hall C Møller for  $G^0$  at a beam energy of  $\sim 687$  MeV. Each data point represents an individual measurement, the outer errorbars show the total error and the inner errorbars show the statistical error. The solid line represents the average value of the polarization as found when performing a constant fit ( $\chi^2/\nu = 0.80$ ) to all data points. The dashed lines represent a  $\pm 1\sigma$  error band.

measurement than the Mott, and because it measures the polarization of the beam as it enters the hall rather than before entering the accelerator, the high energy Møller result was used for the correction in all data sets. For the uncertainty, the statistical error from the Møller fit was used in all cases, but the systematic error was increased for the low energy to account for fluctuations in the Mott measurement. The final beam polarization and error determined for each energy is [53]

$$P_{687} = 85.78\% \pm (0.07)_{stat} \pm (1.38)_{sys} ,$$

$$P_{362} = 85.78\% \pm (0.07)_{stat} \pm (1.95)_{sys} .$$

The correction to the asymmetry due to the reduced polarization will be discussed in the Chapter 4, Section 4.4.1.

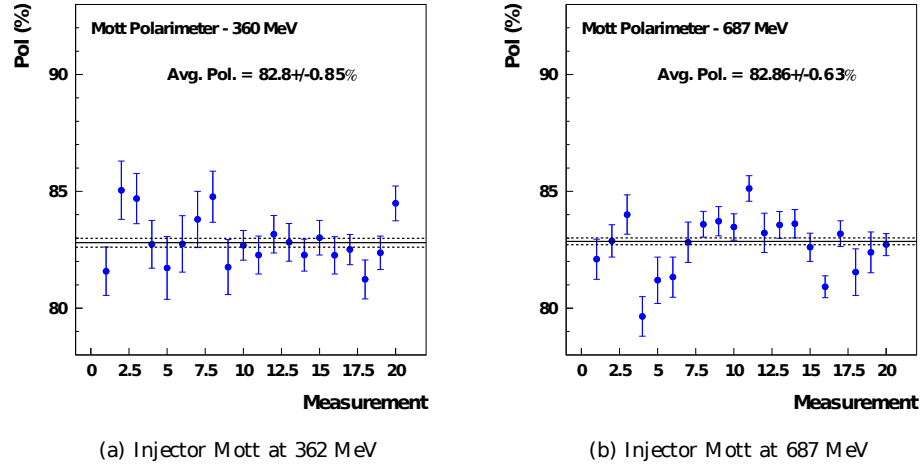


FIG. 3.7: Measurements taken with the 5 MeV injector Mott for  $G^0$ . The left figure shows measurements taken at a beam energy of  $\sim 362$  MeV while the right shows measurements taken at  $\sim 687$  MeV. Each data point represents an individual measurement and the errorbars represent statistical errors only. The solid line shows the average value of the polarization as found when performing a constant fit to all data points. The reduced  $\chi^2$  for the fits are (a)  $\chi^2/\nu = 1.25$  and (b)  $\chi^2/\nu = 3.59$ . The dashed lines represent a  $\pm 1\sigma$  error band.

### 3.5 The $G^0$ Experiment

Once the electrons reach the appropriate energy within the accelerator, the beam is steered to the appropriate experimental hall where it encounters the experimental target and detectors. For the  $G^0$  experiment, installed in Hall C, electrons were scattered from a cryogenic target liquid and data were collected through thousands of signals being read out from hundreds of individual detectors. The detectors were mounted together as one unit on a frame that was roughly 5.5 m in diameter, with the beam going through the frame's center 3.5 m off the floor. A photograph of the experimental setup in Hall C can be seen in Figure 3.8. The sections that follow will outline the various components of the experimental apparatus, giving information on design specifications and their use in the experiment.

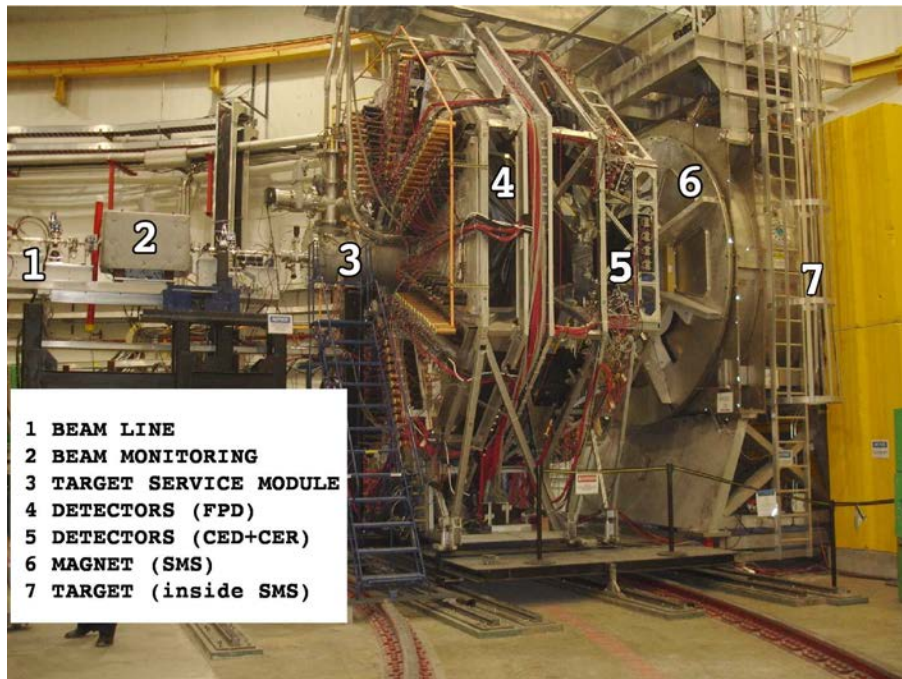


FIG. 3.8: Photograph of  $G^0$  experimental apparatus in the backward-angle configuration installed in Hall C. The direction of the beam is left to right.

### 3.5.1 Target

The  $G^0$  cryotarget was a horizontal closed loop system that was filled with either liquid hydrogen or deuterium and cooled using liquid helium. The main components of the target system were the target cell, a heat exchanger to cool the target liquid, a pump to drive the liquid, a power source and several solid targets used for background measurements. In this section, an overview of the basic design specifications and components of the target loop will be presented. A more detailed description of the design, testing and performance of the  $G^0$  target is available elsewhere [56].

The main limiting factor in the target's design was its location within the vacuum enclosure of the magnet. This not only placed constraints on the size and shape of the target (the diameter of the enclosure was 61 cm) but also limited the ability to access

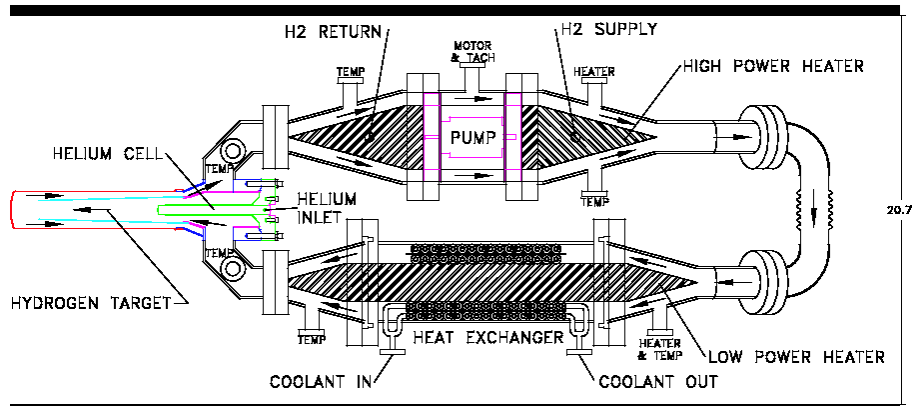


FIG. 3.9: Diagram of the  $G^0$  target loop. The direction of the beam is from right to left in this diagram. The arrows within the figure indicate the flow of liquid around the loop.

the target. Because of this limited access, the target needed to be designed in such a way as to allow it to go for long periods of time with limited maintenance. Another important design consideration for the target was the ability to absorb the energy from the beam without boiling. Boiling of the target liquid results in fluctuations in density that can impact the scattering rates. At forward angles, scattering rates are such that even a small percentage of the liquid boiling could impact the results. Sensitivity studies were performed at the forward angle kinematics in order to determine the effect of density fluctuations and found that they contributed at most a 2% increase in the asymmetry width at a given  $Q^2$ . At backward angle, because the rates are much lower than at forward angle, these fluctuations have an even smaller impact.

A diagram of the full target system can be seen in Figure 3.9, where the beam direction is right to left. At the downstream end of the target, or the left-hand side of the figure, is the target manifold, which houses the hydrogen and helium cells. While the hydrogen cell contains the target liquid for the measurement, the helium cell was present to reduce systematic effects by allowing both ends of the target cell to have the same radius of curvature. Both cells were cylindrical in shape and made from thin aluminum. The hydrogen

cell was 23 cm long and had an inner diameter of 5 cm and a wall thickness of 0.178 cm. The helium cell was placed upstream of the hydrogen cell, overlapping slightly with it at its upstream end. The cell was 16 cm long and had an inner diameter of 12.7 mm. The hydrogen and helium cells were maintained at the same pressure and temperature. When the hydrogen cell contained hydrogen, the liquid was kept at 19 K, while for deuterium it was kept at 22 K. The pressure for both target liquids was held at 1.7 atm.

The design of the hydrogen cell was such that there were three aluminum windows in the path of the electron beam. The first window electrons passed through, the upstream end of the helium cell, had a thickness of 0.178 mm. Next was the exit window on the helium cell which served as the entrance window to the hydrogen cell and was 0.228 mm thick. Finally, the unscattered electrons passed through a specially thinned 0.076 mm thick, 8 mm diameter spot on the upstream end of the hydrogen cell before exiting the target.

The two legs of the target loop housed components necessary to maintain the proper temperature and liquid flow within the system. On one leg, the top of the loop in Figure 3.9, was a pump that circulated the target liquid through the loop at a high rate so as to offset heating effects due to the beam. A heat exchanger which used helium gas (15 K, 12 atm) to cool the target liquid was located on the other leg, shown at the bottom of the loop in the figure. The coolant was provided by the lab's End Station Refrigerator. Regulation of the target liquid temperature was important to avoid the damaging effects freezing or boiling of the target liquid would have on the target cell.

Target monitoring software loaded on a dedicated computer in the counting house allowed the target operator to track and record the pressure and temperature of the target liquid and refrigerant. Sensors within the target loop recorded the target liquid temperature at multiple locations in the loop along with the liquid flow rates and pressures. Flow

valves for the target liquid and coolant could also be controlled as needed to keep temperatures steady. Alarms programmed into the software warned the operator if the pressures or temperatures exceeded a given range. The alarms were set to a sensitive enough range to allow the target operator, upon receiving a warning alarm, time to make changes to avoid conditions that could be damaging to the target, such as freezing or boiling of the target liquid. Separate from the target software, a manual control for the target heater was available to temporarily maintain optimal target temperature for short periods of time in the event the automatic controls were not working. For example, if the target monitoring software became frozen or the target computer needed to be restarted, the manual heater controls allowed the problem to be dealt with without needing to turn off the beam.

While the primary measurements were taken on a liquid target, data were also taken on gaseous hydrogen by warming the liquid within the target cell. Since gaseous hydrogen has a much lower density than the liquid, the scattering rates from hydrogen will be reduced, amplifying the effect of backgrounds from the target windows. Once data were collected, the scattering rates from the gas could be subtracted using the liquid hydrogen rates and the difference in density between gas and liquid hydrogen. While ideally one might wish to measure the aluminum rates alone, the gas within the cell was needed to absorb the heat from the beam allowing the measurements to be taken without damaging the cell.

In addition to the target cell, measurements could be taken on solid targets as a way of measuring backgrounds. On the upstream end of the cryogenic loop, a spot on the target arm was milled to a known thickness to allow for testing of the aluminum background. Additionally a 5 mm thick carbon target and 5.6 mm hole were also available on this arm for systematic studies. The target cell and solid targets could be moved into and out of the beamline using motors mounted on the target loop frame that were controlled remotely

using controls on the target computer. The target system could also be positioned such that none of the targets were in the beamline. Target positioning was precise to within 0.1 mm.

### **Beam Raster**

To aid in the reduction of target boiling, the power density of the beam at the target was reduced through the use of rastering. The electron beam produced by the accelerator has a nominal width of about  $200 \mu\text{m}$ , which when run at the currents used for both phases of  $G^0$ , produces a large power density at the target ( $\sim \text{kW}/\text{mm}^2$ ). Through the use of two magnets located about 20 m upstream of the target, the beam was spread out into a  $2 \times 2 \text{ mm}^2$  square. This leads to a reduction in power density which reduced the likelihood of boiling. The raster system that was used was able to produce the square pattern with a density that was 95% uniform.

### **3.5.2 Superconducting Magnet System (SMS)**

After scattering through the target, electrons were bent through a magnetic field and passed through a collimator system before reaching the detectors. The magnet and collimator effectively placed a  $Q^2$  cut on the particles that reached the detectors, defining the kinematics, optimizing the electron rates and reducing backgrounds. Where this cut was placed was dependent on the strength of the magnetic field. For nominal running, the field strength used was chosen so as to focus the elastically scattered particles onto the detectors. At backward angle, the optimum field for elastic electron scattering was obtained by running the magnet at a current of 3500 A for the high beam energy and 2650 A for the low beam energy.

The superconducting magnet consisted of 8 coils arranged around a central bore. The toroidal shape was chosen because it provided a symmetric field that was easily used for both forward and backward angle scattering of electrons and protons. The magnet design also yielded a low field in the center of the magnet, which reduced the effects of the magnetic field on the electron beam and the target liquid. The transition from forward to backward mode required both that the magnet's direction be physically reversed in the hall and that the polarity be reversed to account for the opposing charge of the detected particles.

The design of the magnet was driven by forward angle proton considerations, with the scale of the magnet being driven by the large proton momenta and the bending angle of  $35^\circ$  defined by the need to keep the detectors a safe distance from the target. The momentum resolution was defined by the desired forward angle  $Q^2$  range of  $0.1 \leq Q^2 \leq 1.0$  (GeV/c)<sup>2</sup>. A 10% resolution in  $Q^2$  lead to a sufficient number of forward angle  $Q^2$  points. For the backward angle measurements, since the only  $Q^2$  consideration was the separation of elastic and inelastic events detected, this 10% resolution was sufficient.

Contained within the magnet's structure were lead collimators to limit which particle trajectories reached the detectors. There were two main collimators, the first of which was located at a bending point in particle trajectories and provided a limitation on the dispersion of the accepted particles. The second set of main collimators, located close to the beam line, was responsible for setting the effective momentum transfer range of the detected particles. In addition to these collimators, azimuthal collimators, located along the trajectory, limited the effect of abnormal field at the edges of the coils, leading to an effective  $\pm 10^\circ$  phi acceptance. In addition to placing acceptance cuts on the desired protons and electrons, the collimators also helped to reduce backgrounds from electron and photon showers.

Like the target, the magnet had monitoring and control systems that could be accessed through software on a computer in the counting house. Temperature, pressure and voltage sensors placed at differing locations along the magnet allowed for constant monitoring to ensure that the cryogenic cooling system was working properly. Additionally, changes could be made to the current flowing through the magnet to alter the magnetic field strength. This system, however, could not control the polarity of the field as it required a physical swapping of the leads on the power supply.

### 3.5.3 Detectors

The detector package consisted of three sets of detectors that were used in coincidence to define measured events. The detection system was segmented into eight octants that coincided with the SMS coils and were arranged symmetrically around the beam. Each octant contained an identical, independent collection of detectors that consisted of two sets of plastic scintillators and a Cherenkov detector. The two sets of scintillators were used to measure the track of the particles in order to separate elastic, inelastic and background events from each other, while the Cherenkov detector differentiated between electrons and pions. The following sections provide an overview of the design and technical specifications of each set of detectors. Figure 3.10 shows a cut-away view of the target, magnet and detector system with simulated trajectories for elastic (green) and inelastic (red) electrons scattered from the target as they enter the  $G^0$  detector system.

The basic measured quantity was the detector yield, or the number of events that trigger the detectors in coincidence. Using this yield and knowledge of the beam's helicity structure, an asymmetry was computed from the yields in software. More will be said about the handling and structure of the data output in Sections 3.5.4 and 3.7.

In order to manage costs, the design and construction of the detector system and the associated electronics were split between two different collaborations. The odd-numbered octants (1,3,5,7) were made by a North American (NA) collaboration, consisting of institutions from the U.S. and Canada, while the even-numbered octants (2,4,6,8) were made by a collaboration of French (FR) institutions. The division of the octants between the two groups was done such that azimuthal pairs of octants would be made by the same collaboration, allowing for cancellation of systematic effects. Although the decision to divide the octants between the two groups was driven by funding related issues, having detectors designed and built by two different collaborations provided a useful cross-check of the measurement. The primary differences between FR and NA octants exist in the electronics, with the detectors seeing only minor design differences in the FPDs. The CEDs and Cherenkov detectors are identical in all octants. The small differences in the FPDs between FR and NA octants are described elsewhere [47].

In addition to the primary detector system, a secondary set of Cherenkov detectors, referred to as the luminosity monitors, located downstream of the target, were in place to measure electron asymmetries at forward angles. These monitors were initially designed to study the effects of density fluctuations in the target during the forward angle measurement, but were able to be used as a systematic check for the backward angle measurement. A brief description of these detectors is provided at the end of this section.

### **Scintillators**

A scintillator is a particle detector that makes use of the property of certain materials that causes them to emit light during ionization. When a charged particle passes through a scintillator, a portion of its energy is absorbed by molecules in the material and then

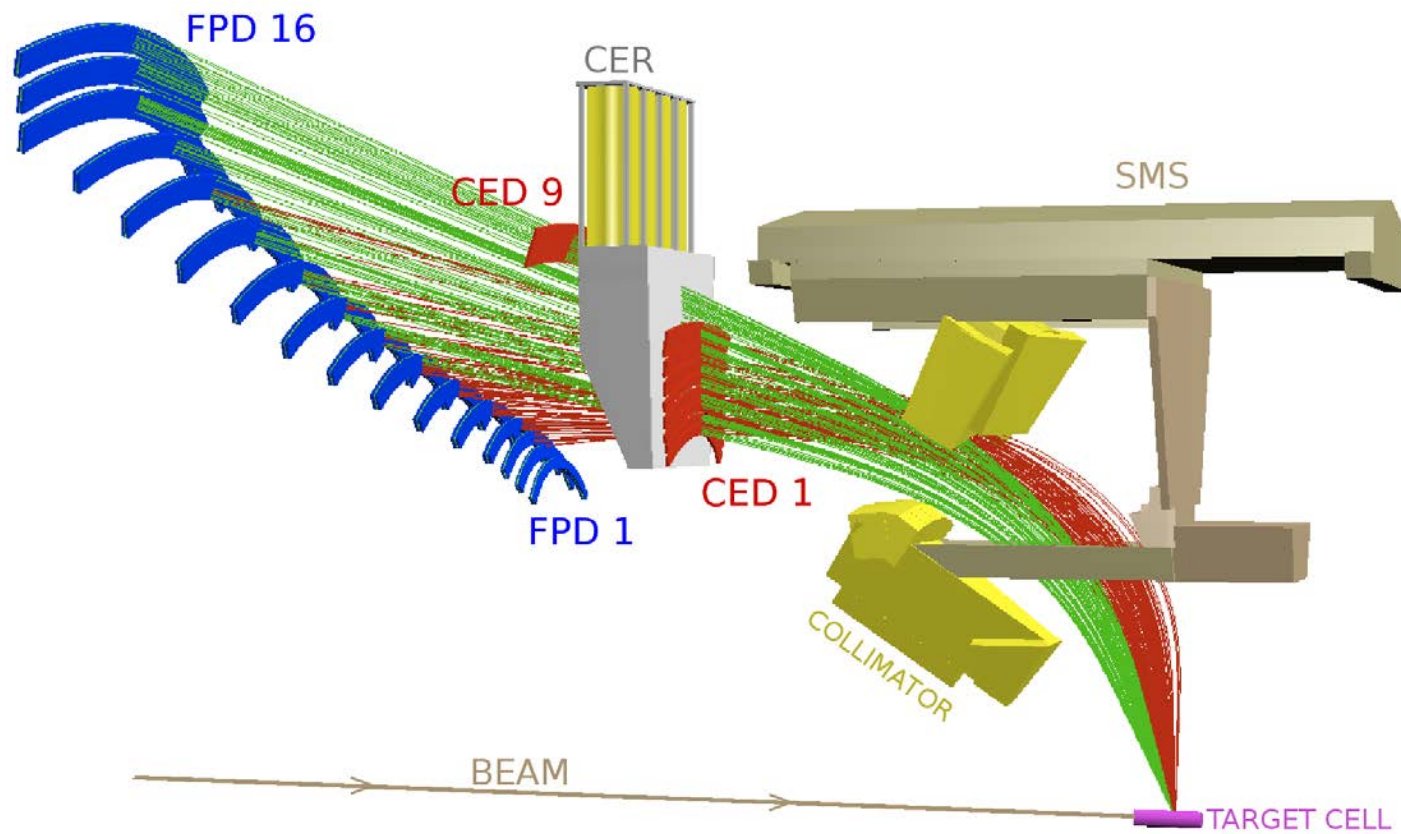


FIG. 3.10: The  $G^0$  detector system for a single octant shown with sample particle trajectories. The green (red) trajectories represent elastically (inelastically) scattered electrons. In this figure, the electron beam direction is left to right.

re-emitted as light. In an experiment such as  $G^0$ , the number of scattered electrons or pions can be measured by incrementing a counter every time one of these flashes of light appears.  $G^0$  used two such sets of detectors in coincidence to define an event.

The first set of scintillators, located just upstream of the magnet, are referred to as the Cryostat Exit Detectors (CEDs). Each CED consisted of a 1cm thick arc-shaped bar of plastic scintillator ranging in length from 53 - 66 cm [57]. Attached to each end of the bar were lucite light guides that steered the light emitted during scintillation into photomultiplier tubes (PMTs) which then amplified the light signal and translated it into a signal that could be read by the electronics. The lightguides were needed in order to keep the PMTs a safe distance from the magnet so that the magnetic field did not interfere with their performance. The CEDs were mounted first in individual octant housings along with the Cherenkov detector and then the octant housings were mounted onto a circular structure, or Ferris wheel, shown in Figure 3.11. Each octant contained 9 CEDs, 8 of which were mounted at increasing vertical distance from the beamline in the same plane. Due to space constraints, the detector furthest from the beamline, CED 9, was located at a different  $z$  location than the lower 8, and was immediately upstream of the box containing the Cherenkov detector (See Figure 3.10) The electron beam passed through the center of the Ferris wheel, leading to an azimuthally symmetrical detector system.

The second set of scintillators, the Focal Plane Detectors (FPDs), were located upstream of the CEDs (or further down the path of the backward scattered particles). The FPDs were designed for and used as the primary detectors in the forward angle phase of the experiment. There, they were used to detect recoiling protons from scattering at multiple values of  $Q^2$ . The shape and dimensions of the individual scintillator bars were determined from simulation with each representing a  $Q^2$  bin. For the backward angle measurement, the multiple detectors were instead used, in concert with the CEDs, to

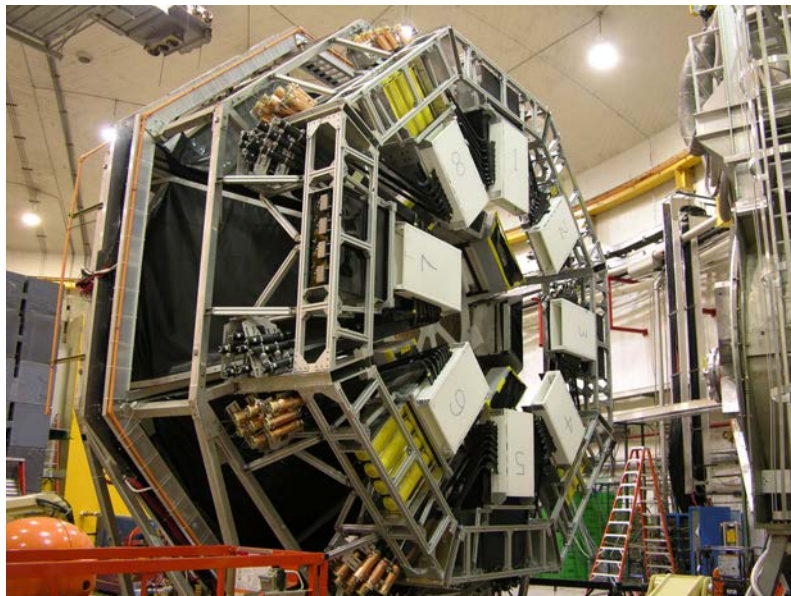


FIG. 3.11: Photograph of full  $G^0$  backward angle detector system in Hall C. The CEDs are contained in the white boxes, numbered according to their octant, which are located directly in front of the Cherenkov detectors. The FPDs are located behind the black light-absorbing sheet.

resolve the separation between different kinematic regions over a narrow range of  $Q^2$ , resulting in a single elastic measurement. The detectors were arranged such that those closest the beamline in radius were also closest the target in  $z$ . The remaining detectors extended radially outward, with the distance in  $z$  increasing with the radial distance. The FPDs were arc shaped and had varying dimensions, with the surface area increasing with distance from the beamline. Lengths of the detectors varied from 60 - 120 cm and widths from 5-10 cm, while thicknesses varied from 0.5-1 cm. The smallest dimensions represent the detectors closest the beamline. A photograph of the FPDs for a single octant can be seen in Figure 3.12.

In order to reduce backgrounds, each FPD consisted of two identical scintillator bars mounted with one placed in front of the other. Requiring both detectors to fire before triggering an event leads to a reduction in low energy backgrounds. As with the CEDs,



FIG. 3.12: Photograph of FPDs for a single octant. Eight such octants existed and were mounted together on a Ferris wheel that can be seen in Figure 3.11.

light produced within the scintillators was transmitted through lucite light guides attached to either end of each scintillator bar. Because the FPDs were mounted at varying distances from the target, the light guides also varied in length, with the longest, attached to the lowest FPD, being 2 m long. In the original forward angle configuration, PMTs that amplified the light signal and translated it to a digital signal were attached to the end of each light guide. This led to a total of four output signals coming from each FPD. A single octant was comprised of 16 FPDs attached to a support structure, shown in Figure 3.12, which was then mounted together with the other octants on a Ferris wheel.

The FPDs were able to be used for the backward angle measurement with the only changes made being in the selection of which signals were read out. While all 16 detectors were used for forward angle measurements, the two closest the beamline (labeled FPD 1 and 2) were not used at backward angle. This was due to the detectors being physically blocked by the structure of the CED/Cherenkov Ferris wheel. The other change to the FPDs was in which PMT signals were used. Initially, it was thought that since this was no

longer a ToF measurement, the resolution provided by requiring the coincidence between the front and back planes would not be needed. Thus, it was not necessary to read in the signals from the back layer of the FPDs. Because this meant that only two PMTs were needed for each FPD, the PMTs were removed from the back layer of FPDs and used for the CEDs. After taking initial measurements, it was discovered that the background rates were higher than had been expected and the decision was made to add the signals from the second layer back in to improve resolution. In order to accomplish this without the need for additional PMTs, one of the PMTs was attached to each layer of scintillator such that the PMTs were on opposing ends.

The FPD Ferris wheel was a free standing structure that was attached to rails on the floor of the experimental hall to allow for movement of the detectors relative to the target. The CEDs and Cherenkov detectors were mounted in a similar manner, however their support structure, dubbed the mini Ferris wheel, was not free standing. The mini Ferris wheel was instead mounted to the front of the FPD Ferris wheel. This design allowed for the entire detector system to be moved in the hall relative to the target and magnet without changing the detectors positions relative to each other.

### **Cherenkov Detectors**

The final set of detectors within the detector system was the Cherenkov detectors, which were used to differentiate between electrons and pions. The principle behind a Cherenkov detector involves charged particles traveling through a medium. If the particle travels at a speed faster than the speed of light in the medium, light is emitted in the form of Cherenkov photons. By choosing a material with an appropriate index of refraction, a momentum threshold can be set such that particles with slower speeds or higher mass do

not emit light. The  $G^0$  Cherenkov consisted of 5.5 cm of a clear aerogel with an index of refraction of 1.03. This index of refraction resulted in a momentum threshold for electrons of roughly 2 MeV/c, while the pion threshold was 570 MeV/c. For beam energies of 687 and 362 MeV, this lead to the majority of electrons that entered the detector producing light, while the majority of pions did not.

The physical design of the Cherenkov, which can be seen in Figure 3.13, was chosen such that a maximum amount of the  $G^0$  acceptance could be covered while still maintaining a limited time spread between emitted photons. It was also important that the detectors be as independent of particle trajectories as possible. There were 8 such detectors, one for each octant, which were physically located between the CEDs and FPDs and mounted on the same structure as the CEDs. The inside of the box that housed the aerogel was covered with a reflective material to maximize the number of photoelectrons that made it to the four PMTs that received the signal. In order for an event to be counted, a coincidence of these PMT signals was used, such that each Cherenkov resulted in a single output signal. Roughly 4% of the light produced was collected by the PMTs. Through simulation, it was found that electron events generate 6-7 photoelectrons, leading to a 95% efficiency in electrons and a rejection factor of 125 to 1 for pions.

The efficiency of the Cherenkov detectors was determined both through measurements taken during running and through simulation. These studies showed that the average efficiency in the elastic region of the detector space was  $\sim 85\%$  while in the inelastic region it was  $\sim 75\%$ . Because of this low efficiency in the inelastic region, it is especially important that it be understood for the purposes of rate corrections and when one wishes to compare measured yields to those from simulation. A more detailed discussion of the determination of the Cherenkov efficiency will be provided in Section 5.2.1.

When the backward angle experiment began, PMTs made using borosilicate glass

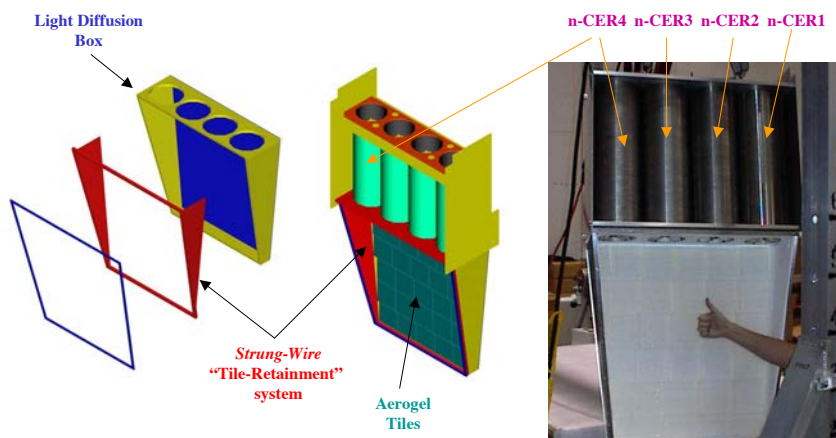


FIG. 3.13: Diagram and photo of a single  $G^0$  Cherenkov detector. The aerogel is contained within the lower portion of the detector and the cylinders at top contain the PMTs. The cylinders provide shielding to protect the PMTs from the magnet's field.

windows were in use for all octants. Unfortunately, in the early days of running it was discovered that neutrons hitting the surface of the PMTs at certain angles led to emission of  $\alpha$  particles from the boron nuclei in the glass. The charged particles produced in this reaction ( $\alpha$  and  ${}^7\text{Li}$ ) would then create scintillation light in the glass, thereby generating photoelectrons which created a signal within the PMT itself leading to false triggers that swamped the Cherenkov signals. The false triggers created a high rate background that reduced the detector efficiency and limited the beam current that could be used [58]. The problem was discovered when the target was first tested with deuterium and higher than expected counting rates were seen within the PMTs.

Once this problem was diagnosed, it was determined that new PMTs that did not contain boron would be needed in order to achieve the statistical goals of the experiment in the time allotted. Quartz window PMTs were ordered to replace all existing Cherenkov PMTs just before a break in data taking. It was hoped that the new PMTs would be in place before the break ended, but due to manufacturing delays this was not possible. As a result, all hydrogen data were taken using the borosilicate PMTs. After transitioning

to deuterium, the new PMTs began to arrive and were immediately put into use upon receipt, with PMTs being replaced octant by octant until all were installed. The use of the original PMTs for the hydrogen data was not detrimental to the measurement because, when using the hydrogen target, the only source of free neutrons was electrons scattered from the aluminum target windows. Since the rates from the windows were much lower than the rates from hydrogen, the impact of false triggers from free neutrons was minimal. The quartz window PMTs were mainly needed for the deuterium measurements, where the presence of neutrons within the target nucleus led to high numbers of free neutrons entering the detector system.

As was mentioned previously, a Cherenkov event is determined by a combination of triggers from the four PMTs. For the majority of the  $G^0$  run, two PMTs were sufficient to determine an event. However, when initially taking data using the deuterium target, the pion rates were so high that the borosilicate PMTs that were still in use at the time could not resolve the events. For this period, three PMTs were needed for any octant that still had the old PMTs in order to resolve individual particles. Once all of the borosilicate PMTs were replaced, the increase in efficiency allowed for the return to the requirement of two signals. This increased efficiency also allowed for the use of an increased beam current leading to a quicker accumulation of counting statistics.

### **Luminosity Monitors**

The luminosity monitors, or LUMIs, were a set of 8 quartz Cherenkov counters placed downstream of the target that detected scattered electrons at an angle of  $\sim 2^\circ$ . The individual LUMIs were arranged symmetrically around the beam in a manner similar to the main detector octants. However, their physical setup and readout electronics were

completely separate from the main detector system. The LUMIs were designed and implemented for target sensitivity studies at forward angles, but they were useful for beam quality studies during the backward angle phase. Because they detected forward-scattered electrons, the rates on the LUMIs were much higher than the backward scattering rates on the primary detectors. These high rates allowed for quick accumulation of counting statistics within these detectors, making it easier to see small fluctuations in asymmetry that would not be visible otherwise. Although the asymmetry measured by the LUMIs was for kinematics that differed greatly from the primary asymmetry measurement, there was information about the beam contained within the LUMI asymmetry that could be applied to the experiment in general. In addition to target density and beam quality studies, the LUMI asymmetries were also used to determine the size of the transverse component of the beam polarization during nominal running so that a correction could be applied. The transverse correction will be discussed in Section 4.4.2.

### 3.5.4 Electronics

Signals collected by the detectors were read in and recorded by specially designed input boards. Though the electronics for the NA and FR octants were designed and manufactured by their respective collaborations, resulting in some design differences, the basic logic used for the backward angle configuration was the same for both sets of electronics. An overview of the basic logic of these electronics will be given in this section, while detailed descriptions of the assorted electronic components are available elsewhere [47].

The electronic signals originated from the photomultiplier tubes (PMTs) connected to each detector. Each CED and FPD was connected to two PMTs, while each Cherenkov had 4 PMTs. The signal from each PMT was read in by a Constant Fraction Discriminator

(CFD). For the CEDs and FPDS, the two CFDs were read in to a mean-timer (MT). If these signals arrived within a specified time window (10-30 ns, depending on the length of the scintillator bar), the MT would average their signals to create a single time-averaged output for each individual detector. This averaging was performed to correct for time dispersion due to the location of the hit on the scintillator bar, effectively altering the timing to assume the hit was at the center of the detector. For the Cherenkov detectors, the CFD signals from the four PMTs were combined such that a signal was output if two of the four fire within a 20 ns window.

A Programmable Logic Devices (PLD) was then used to determine coincidences of CED and FPD MT signals with a Cherenkov signal, routing each coincidence to a specified channel on a separate scaler board. There were two sets of scalers that stored coincidence data for each octant; one for electron events and one for pion events. Each scaler group had a total of 126 channels, one for each possible combination of CED and FPD. If an MT from a single CED and one from a single FPD produced a signal within a 15 ns time window, the two MT signals were combined to form a single coincidence signal. The output from the Cherenkov was then combined with the CED·FPD coincidence. If a Cherenkov signal was present at the same time as the CED·FPD signal, the event was sent to the appropriate coincidence channel in the scalers that store electron data. If the CED·FPD signal was present with no Cherenkov signal, the event was recorded in the appropriate channel in the pion scalers.

The coincidences described above were the events of interest for the asymmetry measurement but additional information was collected for the purposes of applying corrections to the measured rates. Two important types of events, recorded in their own scalers, were single and multihit events. Singles rates were recorded for both the CFDs and the MTs. The CFD singles rates represented the outputs from the individual PMTs

for each scintillator, recorded before the signals entered the MT. The MT singles were the outputs for all MT events and were recorded prior to the coincidence logic. Multihits were events in which an MT signal from a single CED (FPD) occurred in coincidence with multiple FPD (CED) signals or two of the same type of detector fired within the coincidence window. The recorded singles and multihit events are used in the computation of the rate corrections that will be discussed in Section 4.2.3.

### **Scaler Counting Problem**

During the low-energy deuterium run period, a problem was discovered that could have potentially affected the measured asymmetry. The problem was seen initially in the ratio to counting statistics (RCS), which is defined as the standard deviation of the asymmetry divided by the standard deviation expected from counting statistics,  $\sqrt{N_{events}}$ . An RCS  $\sim 1$  indicates that the experimental measurement obeys counting statistics, while an RCS that is very different from 1 indicates that some other source of error is present in the data. For the low energy deuterium data, the RCS for the French (FR) octants was within 1% of 1 for all runs, but for the North American (NA) octants was consistently 10 to 20% higher. Upon further inspection, it was discovered that the high RCS values in the affected octants were due to tails present in the distributions of the measured cell yields. That the problem occurred only in the NA octants indicated that it was related to the electronics and not a problem with the beam or the detectors.

Tests were performed over a period of several days during the low-energy deuterium run period to diagnose the source of the problem. For the majority of the tests performed, the electronics for a single NA octant were used so as to not completely interrupt data taking. Through testing it was determined that the problem was due to a combination of

effects seen in the NA coincidence electronics and the scalers that recorded the coincidence data. The problem arose when two narrow signals from a CED or an FPD arrived in quick succession during a coincidence. In the NA electronics, a coincidence was defined as the logical AND of the CED and FPD output signals with a trigger, with no minimal signal width defined. In certain circumstances, this logic led to two narrow pulses being output by the coincidence board to the same input channel of the scaler. The design of the logic in each 32-bit scaler channel involved the use of an AND gate in each bit that combined the signals from all lower-order bits. The cumulative nature of the AND inputs, coupled with the intrinsic timing of the logic gates, meant that the time taken to process an event increased with increasing bit number and was as high as  $\sim 7.1$  ns. Therefore, if two narrow pulses entered the scaler within 7.1 ns of each other, the scaler would not be ready to accept new data. In these instances, the inputs to the AND gates for higher-order bits were changed before the bit fully processed the previous event, potentially altering the resulting bit value. These errant bit-flips resulted in improper counts being recorded in the affected channel for the MPS and led to the tails seen in the yield distribution. More detail on the diagnosis and causes of the scaler counting problem is given in Appendix B.

The fact that the issue was due to a combination of effects between the coincidence and scaler boards made the problem difficult to diagnose, but, once diagnosed, the problem was quickly resolved. The width of the output signal coming from the NA coincidence electronics was determined by programmable chips. These chips were re-programmed to output a minimum signal width of 10 ns, allowing the problems with the scaler's handling of successive narrow pulses to be avoided. The impact of the electronics fix could be seen immediately in the data. The RCS of the NA octants for runs taken after the fix matched that of the FR octants and the tails on the yield distributions were eliminated.

In this instance, the two sets of electronics provided an excellent test of principle in both diagnosing the problem and in eventually correcting for its effect. By applying a correction to all octants in an identical manner, it could be easily seen if the correction was interfering in any way with the data. Additionally, data taken after the problem was fixed (roughly half of the low-energy and a third of the high-energy deuterium data) could also be used to assure that any correction applied was not detrimental to the data. The correction applied to the data will be described in Section 4.2.2, with more detail available in Appendix B.

Although the electronics issue was present throughout most of the experimental run, the nature of the problem meant that its effect on the physics result was minimal. The primary limiting factor was that the FR octants, representing fully half of the data, were unaffected. The fact that electronics were fixed halfway through the run period during which the problem was the most noticeable also limited the problem's impact. These two factors combined account for more than 60% of the data, leaving less than 40% of the data potentially affected. Additionally, testing showed that even in the affected octants the number of quartets that contained bad counts was less than 1%. Finally, the fact that the problematic events did not appear in an intrinsically helicity-correlated manner meant that the false asymmetry due to the effect was small. Thus, even without a correction applied, the problem would have had a negligible impact on the physics asymmetry.

### **3.6 Data Acquisition and Online Analysis**

Data acquisition (DAQ) was managed by a program called CODA (CEBAF Online Data Acquisition), a system for recording data that was developed at Jefferson Lab [59]. Though the electronics for the individual detector and monitoring systems were contained

in their own crates, a single triggering system was used to control all crates. All inputs were fed to the Trigger Supervisor (TS), which then sent the signal to the appropriate crate to begin processing the event. Information was read out for each MPS, resulting in events recorded at a rate of 30 Hz.

Detector outputs were able to be monitored in real time on dedicated computers in the Hall C counting house. Histograms containing CED-FPD coincidence yields for both electron and pion events could be displayed, with updates appearing in real time. Outputs from the beam monitors, including beam position, current and halo, could also be easily accessed. This constant monitoring of run conditions and output allowed for quick corrections in the event that detectors or electronics malfunctioned or adjustments to beam tune were necessary.

An on-screen interface available through CODA allowed the user to start and stop the data collection process. In order to keep the individual file sizes manageable, data were collected in intervals called *runs*, the length of which was determined by a manual start/stop command from the user. Individual runs typically lasted roughly an hour, resulting in about 25000 quartets per output file. Ending a run automatically executed an analysis program that processed the output from CODA event-by-event. This online analysis placed cuts on the data to account for beam trips and wrote the output to an ntuple. The output file contained raw output from the coincidence electronics, singles rates from the PMTs and outputs from the assorted beam monitors. By default, this analysis was run on an MPS-by-MPS basis, but the analysis software could also be used to process the information on a quartet-by-quartet basis as well. The information obtained from this analysis was of use primarily for data quality checks and calibrations performed throughout the experimental run. The analysis program could also be used to write run-averaged output to a MySQL database. The database was used in the analysis phase of the experi-

ment to apply various corrections to the data to obtain the physics asymmetry. Details of the offline analysis are given in Chapter 4.

During each shift, a series of checks was performed on the data quality by checking certain parameters in the output of the online analysis and recording data from the different online monitors, including the target and magnet monitoring systems. This ensured that variables such as beam position, halo, charge asymmetry, and various target and SMS properties were being checked on a regular basis and allowed for a record to be kept of the running conditions during each shift. More information on the data quality checks performed both online and offline is given in Section 4.3

### 3.7 Data

The backward angle phase of  $G^0$  began in the spring of 2006 and continued through March of 2007. Data were taken on both hydrogen and deuterium targets at two different beam energies ( $\sim 687$  and  $\sim 362$  MeV), leading to four main data sets. The high energy data sets can each be further divided into two run periods, resulting in a total of six separate data sets. Over the course of the run, a total of more than 2000 hours worth of production data were collected, with a total accumulated charge of over 300 C. Table 3.2 summarizes the data taken during the different run periods.

Since  $G^0$  was a counting experiment, the primary data taken was the number of events, which, when taken alongside the measured beam current, could be transformed into a yield measured in Hz/ $\mu$ A. The detectors are treated as CED·FPD coincidence pairs on an octant by octant basis, resulting in a  $14 \times 9$  matrix consisting of 126 CED·FPD coincidence pairs, or cells. Two identical coincidence matrices exist, one containing electron rates and the other pion rates, as determined by the Cherenkov detectors. The matrix

Date	Name	Target	$E_{beam}$ (MeV)	$I_{beam}$ ( $\mu$ A)	Charge (C)	# Runs
Apr '06	H687a	H	685.6	60	16.3	100
Sep-Oct '06	H687b	H	684.9	60	97.1	548
Nov-Dec '06	D687a	D	689.6	20	32.8	532
Mar '07	D687b	D	689.4	17	17.3	332
Jul-Aug '06	H362	H	361.9	60	78.0	475
Jan-Feb '07	D362	D	363.1	35	67.4	649

TABLE 3.2: Summary of  $G^0$  data. The beam current listed is the nominal current during the run period.

space can be divided into kinematic regions based on the particle tracks represented by particular cells. Cells with similar kinematics are grouped together for the purposes of averaging into loci. The electron matrix can be divided into four such loci while only a single pion locus is of interest in the pion matrix.

In the electron matrix, the good events are focused along the diagonal, with inelastic events mainly occurring in the low CED/low FPD region and elastic events in the high CED/high FPD region. Tracks corresponding to elastic and inelastic electron events can be seen in Figure 3.10. A particle triggering a high numbered CED and low numbered FPD indicates a trajectory at an angle not consistent with electrons or pions originating at the target but from showers, decays or other background processes. Thus, the upper left hand corner of the matrix is referred to as the background locus. The lower right-hand area of the matrix, corresponding to low CED and high FPD, represents tracks that are kinematically disallowed. This is referred to as the super-elastic region. For the pion matrix, pion events are concentrated along the diagonal in the low CED/low FPD region. The pion locus overlaps almost entirely with the inelastic locus, leading to more significant pion backgrounds in the inelastic locus than the elastic.

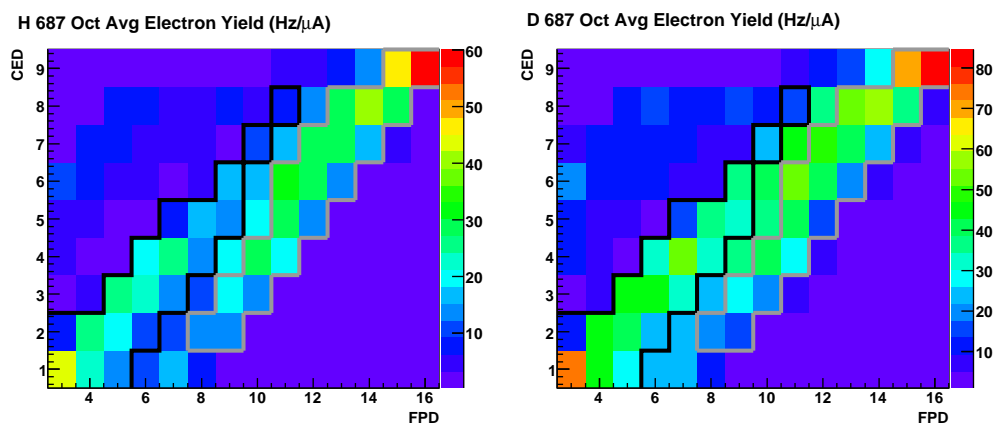


FIG. 3.14: Octant averaged electron yields for the high energy hydrogen (left) and deuterium (right) run periods. On the  $y$  axis is CED number and the  $x$  axis is FPD number and each block represents a CED-FPD coincidence. The color scale indicates cell yield in  $\text{Hz}/\mu\text{A}$ . The collection of cells outlined in black (gray) represents the inelastic (elastic) locus. Note that since FPDs 1 and 2 are not used in the backward angle configuration, the FPD numbering begins with 3.

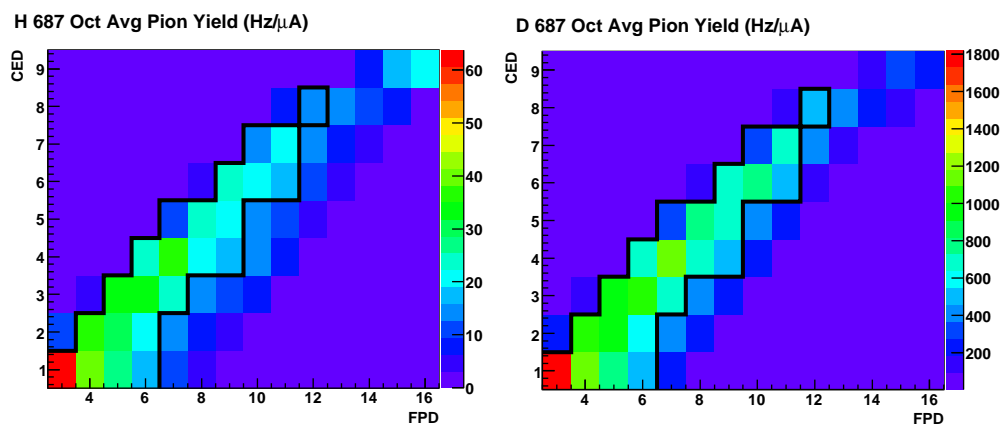


FIG. 3.15: Octant averaged pion yields for the high energy hydrogen (left) and deuterium (right) run periods. On the  $y$  axis is CED number and the  $x$  axis is FPD number and each block represents a CED-FPD coincidence. The color scale indicates cell yield in  $\text{Hz}/\mu\text{A}$ . The cells outlined in black are those contained within the pion locus. Note that since FPDs 1 and 2 are not used in the backward angle configuration, the FPD numbering begins with 3.

Figure 3.14 shows an example of the electron coincidence matrix containing octant averaged yields for scattering from the hydrogen and deuterium targets at high energy. In these plots, the color coding indicates intensity, or yield, in Hz/ $\mu$ A with the red areas being the highest yield cells and the purple being the lowest. The color scale to the right of each matrix shows the translation of cell color to yield value. The majority of the rate is concentrated along the diagonal, in the elastic and inelastic loci. In the background locus, there is some rate but it is much lower than that along the diagonal. The super-elastic region in the lower right corner contains the lowest yields, as would be expected since this is a non-physical region. Figure 3.15 shows pion matrices containing octant averaged yields from the hydrogen and deuterium targets. Again, the color scale represents intensity with the translation between color and yield indicated on the right-hand side of each plot. Note that, while the color scales differ greatly for the two plots due to the pion rates from deuterium being much higher than from hydrogen, the shape of the distribution is consistent across both targets.

Although data were taken for four energy-target combinations, inelastic events were not always present. At 362 MeV, the energy was too low to produce many events at the  $\Delta$  resonance. Simulation indicated that some events were generated (although they had a very small cross section) but due to the magnetic field strength, these particles did not make it past the collimators. By adjusting the magnetic field in simulation, it was possible to have some events reach the detectors, but in so doing, the elastic events were pushed off of the acceptance. While a lower magnetic field may have made it possible to find some events, the rates would have been low, requiring significant beam time to gain any statistical precision. With the lower magnetic field, no measurement of the elastic events would have been possible. Because of these limitations, this was not a practical consideration. As a result, only the high energy data sets will be considered for

the inelastic analysis presented in this thesis.

The distributions of the kinematic variables across the inelastic locus were studied through the use of a Monte Carlo simulation that will be introduced in the next chapter. Figure 3.16 shows the total inelastic locus acceptances for  $Q^2$ ,  $W$  and  $\theta$ , respectively. Distributions of these kinematic variables for the deuterium target are given in Appendix A along with incident ( $E$ ) and scattered ( $E'$ ) electron energy distributions for both targets. The appendix also contains cell-by-cell distributions for  $Q^2$  and  $W$ .

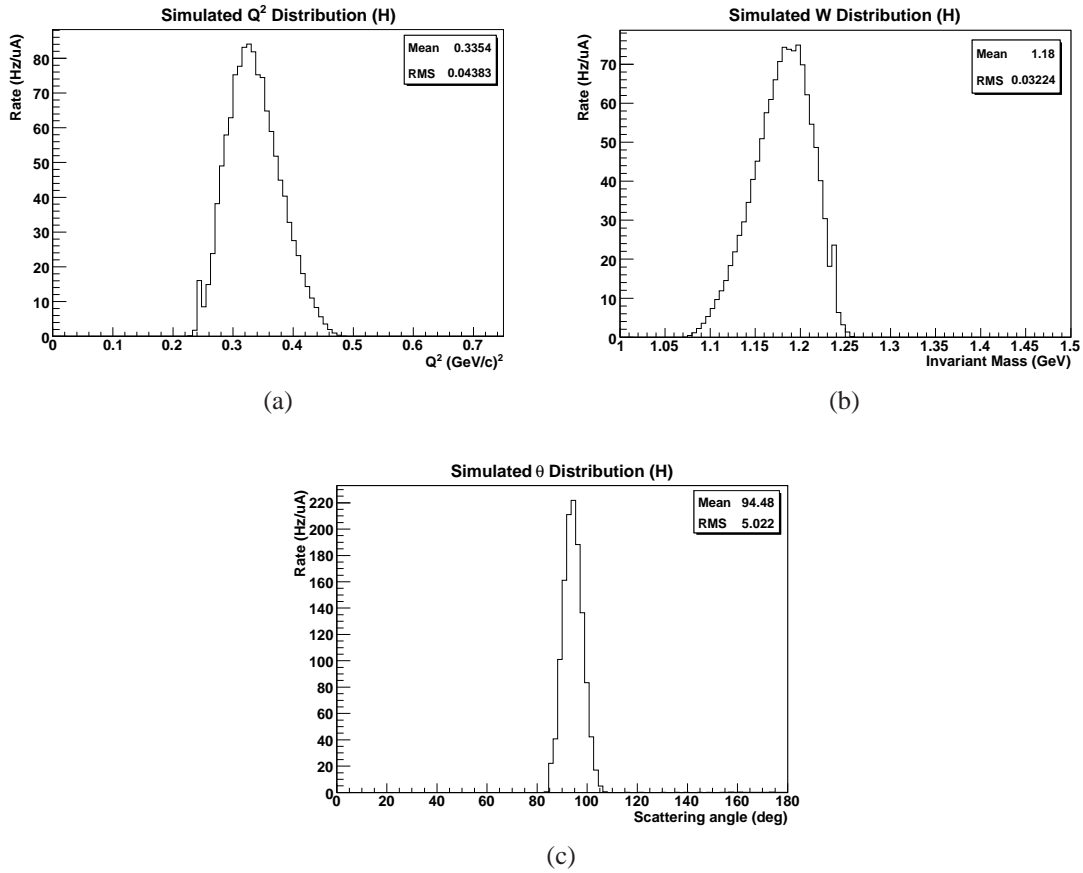


FIG. 3.16: Distributions of (a)  $Q^2$ , (b)  $W$ , and (c)  $\theta$  across the inelastic locus shown for the hydrogen target.

### 3.7.1 Data Collected for Background Studies

In addition to the data taken using nominal settings, explicit background measurements were done including data taken on gaseous hydrogen and aluminum targets. There were also several indirect measurements made for the purposes of understanding backgrounds. Measurements done with the polarity of the magnet reversed were used to study the background due to  $\pi^0$  decay. With the polarity reversed, scattered electrons would be steered into collimators while positively charged particles were detected instead. In hydrogen, the primary source of positively charged particles is positrons,  $e^+$ , resulting from  $\pi^0$  decaying into two photons. These photons can then generate  $e^+e^-$  pairs when interacting with pieces of the experimental apparatus, such as the collimators. Since the  $e^+$  are paired with electrons, a measure of rate from  $e^+$  in the matrix is an indirect measure of the rate from electrons. In deuterium, there is additional rate from misidentified  $\pi^+$  that could complicate the understanding of the  $e^+$  rate, but since the two have differing momenta, they are primarily located in different regions of the detector space.

Data were also taken at differing magnetic field settings by adjusting the magnet's current over a range of about 2000 A, with steps of about 100 A each. These tests, referred to as *field scans*, were performed for each target/energy combination and for both normal and reversed polarity. When yield is plotted as a function of magnet current for a given cell, the resulting curve contains peaks corresponding to areas dominated by elastic, inelastic or background events. The curve can be fitted using simulated yields for the different constituent processes in order to determine and subtract contributions from backgrounds. This process was used to determine the backgrounds for the elastic measurement.

One important background consideration is random coincidences in the detectors.

A random coincidence occurs when a real particle triggers one or more detectors at the same time noise in the PMTs or electronics leads to a false trigger in another detector. One example is a pion that triggers a CED and FPD at the same moment noise in the Cherenkov PMTs yields a signal. In this instance, the electronics would wrongly record this as an electron event. In order to know the true yield in the detectors, this background must be subtracted out. Because of the higher scattering rates and increased presence of pions, random coincidences involving the Cherenkov in the deuterium measurement provided a good atmosphere in which to measure the effect of randoms. Random coincidence rates were able to be measured directly by taking advantage of the dual outputs in place to record pion and electron events in parallel. Under the normal configuration, the pion coincidence matrix is filled with all events that fail to trigger the Cherenkov. During the so-called “randoms mode”, the Cherenkov signal was fed into the pion matrix with a delay. In this configuration, the coincidence recorded would not result from the true Cherenkov signal but from whatever residual background signal may have been present.

When in randoms mode, the pion rates could not be measured, as the randoms signal was being stored in their place. In spite of this, the high pion rates allowed for much of the data taken on deuterium to be taken in randoms mode while still obtaining sufficient statistical precision for the pion asymmetry. Similar data were taken with a delay on either the CED or FPD signals as they entered the electron matrix to measure CED·FPD randoms. These randoms resulted from situations where a CED (FPD) fired randomly in coincidence with an FPD (CED) leading to a false coincidence. Such an event could occur, for example, as the result of a low energy scattered particle triggering a CED and being absorbed followed immediately by a cosmic ray triggering an FPD. Since these events were recorded in the electron matrix, taking data in CED or FPD randoms mode could not be done alongside production running and, as such, this was only done occa-

sionally.

One final consideration involves the direction of the beam polarization. While the beam was nominally polarized longitudinally, due to imperfections in the system, there could be some component of polarization in the transverse direction. Since the longitudinal and transverse asymmetries have differing values, it is necessary that this transverse component be well understood so as to determine its impact on the measured asymmetry. Dedicated measurements were taken with transversely polarized beam in order to measure the asymmetry, while information from the luminosity monitors was used to determine the size of the transverse component of the polarization during longitudinal running. The analysis performed to determine the transverse polarization and asymmetry will be described in Section 4.4.2.

# CHAPTER 4

## Data Analysis: Corrections for Beam and Instrumentation

In order to determine the physics asymmetry,  $A_{inel}$ , there are several layers of corrections that must be applied to the raw asymmetry,  $A_{meas}$ . Corrections for helicity-correlated effects related to the beam, detector related effects, beam polarization, backgrounds and radiative effects were applied according to Figure 4.1. The first set of corrections applied includes corrections related to the electron beam, the electronics and the detectors. In each of these cases, the specific differences in the physics involved in inelastic versus elastic scattering are unimportant. Since all scattered electrons originate with the same beam and all events pass through the same detector and electronic systems, the corrections can be applied in a uniform manner to all measured coincidences. The latter corrections, including backgrounds and radiative effects, require analysis specific to the physics of the inelastic region. The beam and instrumentation corrections will be presented in this chapter, while the remaining corrections will be presented in Chapter 5.

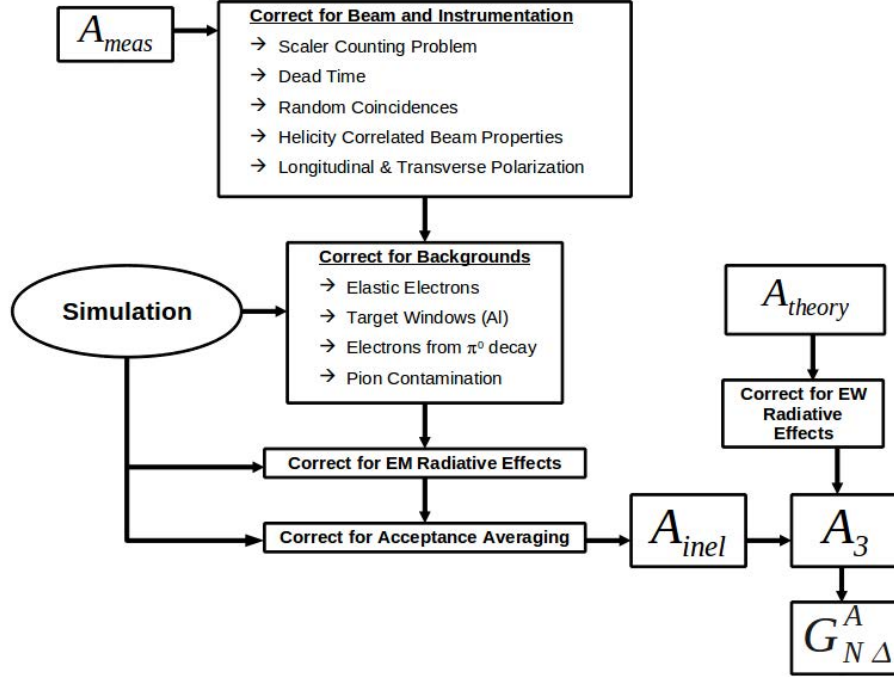


FIG. 4.1: Overview of the analysis strategy employed to determine  $G_{N\Delta}^A$ . The process begins with the measured asymmetry,  $A_{meas}$ , corrections are applied to arrive at the final asymmetry,  $A_{inel}$ , and the axial component of the asymmetry,  $A_3$ , is determined. Once  $A_3$  is known,  $G_{N\Delta}^A$  can be determined.

## 4.1 Data Blinding

Since there was a definite prediction for the value of the elastic asymmetry in the absence of strange quarks, there was a chance that this knowledge could bias the results. In order to avoid this bias,  $G^0$  employed blinding in the calculation of all asymmetries. The blinding was performed by multiplying the calculated asymmetries by a randomly generated blinding factor unique to each data set such that

$$A_{blinded} = bA_{true}, \quad \text{where } 0.75 \leq b \leq 1.25. \quad (4.1)$$

The blinding factors were limited to a range of  $\pm 25\%$  of the true asymmetry and their values were not known by any collaborators. The bound was chosen in order to give

Data Set	Blinding Factor
H 362	1.01295
D 362	1.09657
H 687	1.23932
D 687	1.12257

TABLE 4.1: Summary of blinding factors.

a wide enough range that the true asymmetry was hidden while giving a small enough range that problematic data or errors in the analysis could be seen. Since the factor is multiplicative, unblinding the asymmetry simply requires the division of the final asymmetry by the blinding factor. Using a separate blinding factor for each data set allowed for unblinding one asymmetry result at a time in case the analysis for one of the target/energy combinations was delayed significantly.

The blinding was performed in the first phase of the analysis such that all asymmetries computed and stored, whether from online or offline analysis, were blinded. The asymmetry was only unblinded once all analysis for the elastic measurement was complete and the preliminary elastic asymmetry was known. As the theory surrounding the inelastic asymmetry is not as well defined as that of the elastic, the blinding factor was not as important to the inelastic measurement. Thus, it was not necessary to wait for completion of the inelastic analysis before unblinding. Table 4.1 lists the blinding factors used for all four data sets. For data taken with other targets, such as aluminum, the blinding factor used was that of deuterium at the appropriate energy. All asymmetries presented in this thesis are unblinded.

## 4.2 The Analyzer: *g0analysis*

The main program through which the beam and instrumentation corrections were applied is *g0analysis*, a program written by  $G^0$  collaborators using ROOT [60], a C++ based object-oriented programming language developed at CERN. The program is designed to take the output from the electronics for a given run, apply corrections, calculate quantities such as asymmetry and organize the output in a way that is useful for future study. The analysis can be performed on either an MPS-by-MPS basis or a quartet-by-quartet basis, depending on what is necessary for a given correction.

Through the use of input flags, the user can select which corrections to apply and where the output should be written. The output can be written in two forms: ntuples containing information for each MPS or quartet readable in ROOT and run-averaged values stored in a MySQL database. The ntuples were primarily used for testing purposes as they represent a convenient presentation of the data for a given run. When one needs to look at averages of many runs, however, it is more useful to use output that has been stored in the database. Scripts can be written to interface with the database allowing for user specified cuts on the data and plots of assorted variables. Database queries can also be used to average across multiple runs, detectors or octants to compute a single value of a desired quantity (i.e. total yield in a particular detector or average asymmetry during a run period).

Early in the analysis phase of the experiment, an order for the application of the corrections applied by *g0analysis* was decided upon as the official analysis strategy. The analysis is performed using a multi-stage procedure designed to apply individual corrections in a logical order in consecutive stages, or *passes*. Applying corrections in stages is necessary for those which require the use of previously calculated quantities and also

allows for isolation of the effect of individual corrections. By limiting the number of new corrections applied in each pass, the causes of problematic outputs can be more easily determined. There are a total of four passes, with the output of the first pass being the raw data and the fourth the final beam and instrumentation corrected value. Details of the corrections applied in each of the passes will be given in the remainder of this section.

A run-through of all four passes is referred to as a *replay*. Several replays, some on all runs in a given run period and some on subsets of runs, were done through the course of studying the data quality and testing the implementation of the assorted corrections applied. Once it was shown that all corrections were being applied in the appropriate way and the results were sensible, a final replay was completed. The output of this final replay was then used as the starting point for further corrections. In the sections that follow, details of the corrections applied in each pass and their uncertainties will be given. The impact of these corrections on the asymmetry will be summarized at the end of the chapter in Table 4.7.

### **4.2.1 Analysis Pass 1: Raw Pass**

The first analysis pass can be thought of as a “raw pass”, as there are no corrections made, only cuts to assure data quality. The cuts are applied on an MPS-by-MPS basis to account for beam trips and quartets with no events. During a typical run, it is not unusual for beam trips to occur, leading not only to periods with no beam during the run but also periods of low current. When the beam returns after a trip, it is ramped up incrementally over a brief time period (on the order of several seconds) rather than coming on immediately at the required current. The slow start-up in current is in part necessary to allow sufficient time for the cooling system of the target to offset the heat coming from

the beam. Since it takes time for the target system to reach equilibrium, the target density can fluctuate during periods where the current is changing. By placing a tight cut on the minimum acceptable current ( $\sim 10\%$  of the nominal rate for a given run period) and by cutting the first 500 MPSs measured after a beam trip, false asymmetries arising from these density fluctuations can be avoided. The cut to remove quartets with no events is necessary to avoid division-by-zero errors in the computation of the asymmetry, as such quartets would be comprised entirely of zero-yield MPSs.

Once the cuts are applied, the yield is computed on an MPS-by-MPS basis as the number of events measured by the detector during the MPS divided by the beam current. These yields are then used to compute the quartet asymmetry according to

$$A_{qrt} = \frac{(Y_1^+ + Y_4^+) - (Y_2^- + Y_3^-)}{(Y_1^+ + Y_4^+) + (Y_2^- + Y_3^-)}, \quad (4.2)$$

$$A_{qrt} = \frac{(Y_2^+ + Y_3^+) - (Y_1^- + Y_4^-)}{(Y_2^+ + Y_3^+) + (Y_1^- + Y_4^-)},$$

where the yields,  $Y_i$ , are MPS yields and the subscripts represent the order of the MPSs within the quartet. The two equations are needed to represent the two helicity patterns used by  $G^0$  (+ - -+ and - + +- ) as described in Section 3.2.1

## 4.2.2 Analysis Pass 2: Scaler Counting Correction

As discussed in Section 3.5.4, a programming issue in the North American (NA) electronics led to the occasional dropping of bits in the scaler readout which, in turn, led to improper yields being recorded. The problem occurred only in the NA octants (1,3,5,7), leaving the French (FR) octants (2,4,6,8) unaffected. As the problem was related to timing widths, it was also rate-dependent. The higher the yield in a given CED·FPD coincidence

cell, the higher the probability that events would overlap in such a way as to cause a problem. The effect, which manifested itself as a tail on one side of the yield and as wings on both sides of the asymmetry, was discovered during the low-energy deuterium run period. Figure 4.2 shows an example of the affected data in a single high-yield cell for a typical run during that period. In the figure, the quartet yield and asymmetry are shown for both an FR and an NA octant. Since the number of events in the tail is much lower than in the peak, a logarithmic scale is used on the  $y$ -axis to allow the problem to be more easily seen.

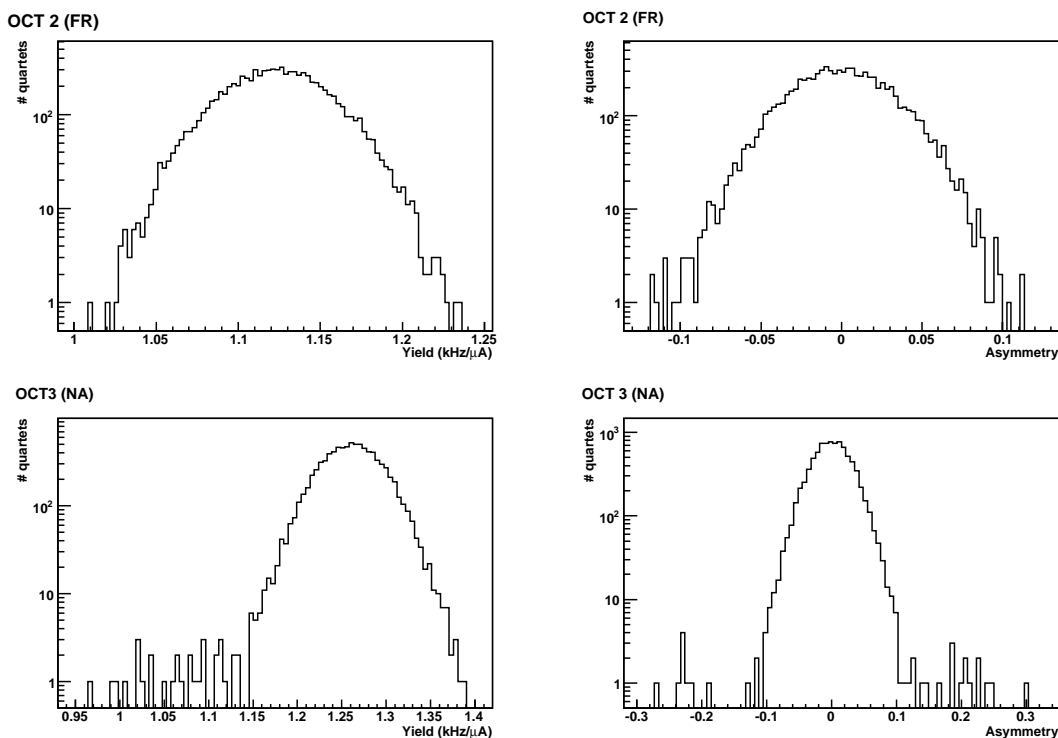


FIG. 4.2: Quartet yield (left) and asymmetry (right) in a single high-yield cell for a single run from the low-energy deuterium run period. The top plots are for a typical French octant (OCT 2), which was not affected by the problem. The bottom plots show a typical North American octant (OCT 3), where the problem is visible. A logarithmic scale is used on the  $y$ -axis to allow the problem to be more easily seen.

This issue was able to be resolved during the experimental run by reprogramming

the NA electronics, but since it was not found until far into data-taking, a correction was needed for the existing data. A cut was placed on an MPS-by-MPS basis such that those with yields outside a certain range were removed. The window of acceptable yield was centered around the run-averaged yield as determined in Pass 1 and had a uniform width for all run periods. The size of the window was defined as an integer multiple of the standard deviation of the yield distribution,  $\sigma$ , for each run. This window width was chosen such that events affected by the problem could be removed without biasing the run-averaged yield. To determine the proper placement of the cut, tests were performed on a subset of runs from each data set wherein the cut was applied for integer widths ranging from  $3\sigma$  to  $7\sigma$ . Fortunately, since only half of the octants were affected, and since the problem was corrected halfway through the low-energy deuterium run period, there was plenty of “clean” data with which to test the cut. It was determined that the optimal setting for the cut was a width of  $5\sigma$ . With this setting, the tail was removed from the affected runs without any changes to the mean asymmetry of the unaffected octants or runs. A detailed description of the tests performed and the cut’s impact on the data is given in Appendix B.

Figure 4.3 shows the quartet yield and asymmetry for a typical octant summed over several runs before (left) and after (right) the cut is applied. As with Figure 4.2, the data set here is low-energy deuterium and the cell is the highest yield cell in the matrix. Applying the cut removes the low yield tail without impacting the peak. Because no events are removed from the peak, any problematic events that are under the peak will still remain. However, since these events are few in number and located under the peak, the effect that they have on the average yield and asymmetry is negligible.

In general, the impact of the cut on the asymmetry was minimal because the problem was not helicity-dependent. Since the bad events were just as likely to occur in each

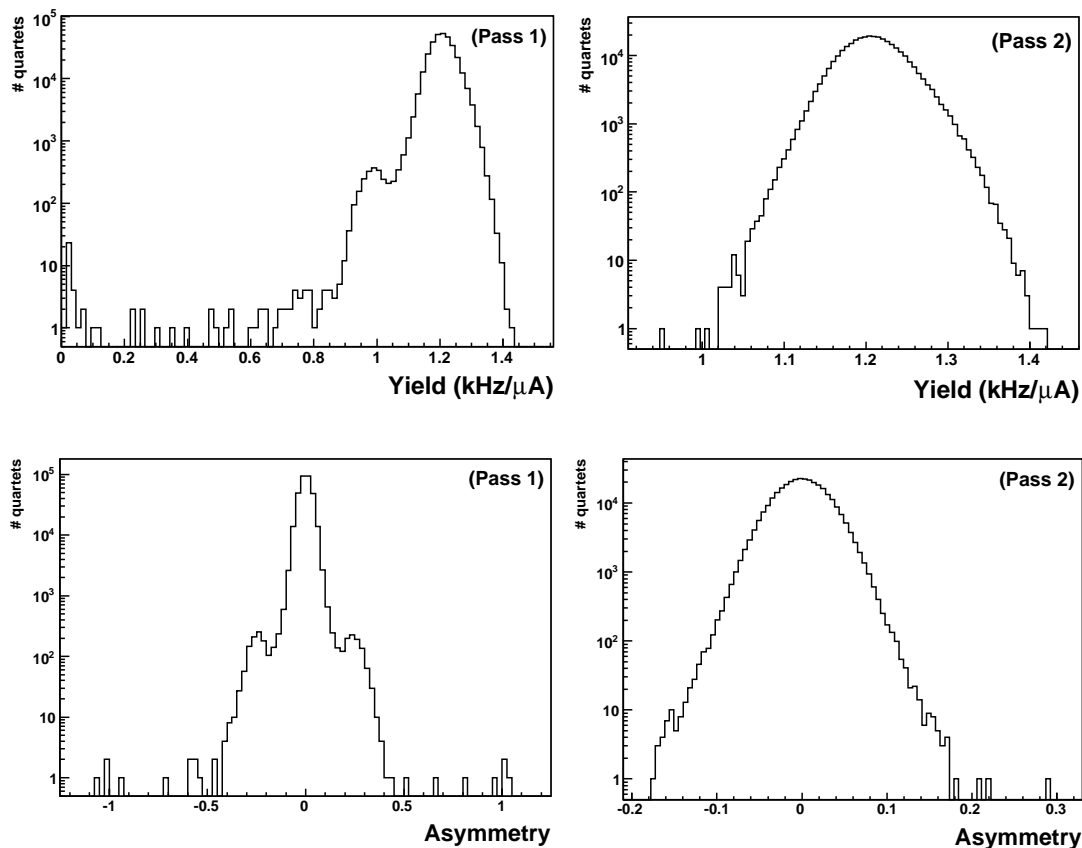


FIG. 4.3: Quartet yield (top) and asymmetry (bottom) in a single high-yield cell summed over several runs from the low-energy deuterium run period. The plots on the left reflect the Pass 1 (uncut) values while those on the right are Pass 2 (cut) values. A logarithmic scale is used on the  $y$ -axis to allow the problem to be more easily seen.

helicity state, the effect cancelled out when computing the asymmetry. Additionally, the rate-dependent nature of the problem meant that it was mostly seen in elastic locus cells, which were generally higher yield than those in the inelastic locus. The rate dependence also made the problem more visible in deuterium where the scattering rates are nearly double those of hydrogen. Further, for the inelastic data, the two data sets of interest are the high energy hydrogen and the second part of the high energy deuterium, which was completed after the electronics were reprogrammed. The combined effect of these factors

results in a negligible change in inelastic asymmetry from Pass 1 to Pass 2.

### 4.2.3 Analysis Pass 3: Rate Corrections

The third pass consists of corrections to the yield to account for detector and electronics dead time and random coincidences. As with Pass 2, these corrections require the use of quantities computed in a previous pass. Corrections are applied to the rate and asymmetry on a quartet by quartet basis. An overview of each of the three corrections (dead time, contamination and randoms) is provided below. Detailed descriptions of the corrections applied and the equations that govern them are available elsewhere [61] [62].

Dead time is defined as the time taken for the electronics to process an event from the moment it is detected until the moment the electronics is ready to accept new data. During this time window, the electronics will not be able to process any new events that may occur. Thus, if two particles enter a detector in quick succession, the second event may not be counted. Typical dead times for the  $G^0$  electronics are on the order of 30 ns. If the electronics chain is well understood, a correction can be made to account for any missed events. The correction is an additive one, where an estimate of missed events is computed and yield is added to the detectors accordingly.

Random events are described as those in which something other than a single particle triggers the appropriate detectors. This can happen if two separate particles hit different detectors within the coincidence time window. Noise in detectors or electronics and cosmic rays or other radiation in the hall can also trigger random coincidences. In the  $G^0$  detector system, a coincidence of two sets of detectors (a CED and an FPD) is required to define an event, and a coincidence of CED and FPD with a third detector, the Cherenkov (CER), is required for it to be counted as an electron. This leads to three types of random

coincidences that can occur. The two primary types of random coincidences that must be accounted for are Cherenkov randoms and CED·FPD randoms. Cherenkov randoms occur when a true pion event is wrongly counted as an electron due to the Cherenkov randomly firing in coincidence with a real CED·FPD coincidence. These randoms result in a contamination of the electron matrix, as real pion events are mislabeled. The contamination correction accounts for these randoms, along with electron events missed due to Cherenkov dead time. CED·FPD randoms are those in which an event is triggered by a CED randomly firing in coincidence with an FPD. In this instance, the electronics will count a pion event when none has occurred. The randoms correction subtracts these false events from the pion matrix. A third possible type of random coincidence would be a fully random CED·FPD·CER coincidence, where all three detectors were randomly triggered in coincidence, resulting in an electron event counted when none occurred.

### **Dead Time Corrections**

Dead time corrections account for missing rate related to the different components of the electronics. Corrections are applied to the rates from the trigger (Trig), Constant Fraction Discriminators (CFD), Mean Timer (MT) and Coincidence (COINC) electronics. These corrections account for missed CED·FPD coincidences but not for particle misidentification due to dead time or random coincidences in the Cherenkov detector. This effect is taken into account in the contamination correction which will be discussed in the next section.

As described in Section 3.5.4, the trigger electronics are the first to fire, signaling that a detector has fired and starting the event recording process. The CFD outputs represent rates from the PMTs attached to either end (left, L, and right, R) of the individual CED

and FPD scintillator bars. The MT outputs are the time-averaged means of the two CFD outputs, L and R, received in coincidence for a given scintillator (CED or FPD). The rates associated with events where only one PMT is triggered are referred to as singles rates and are labeled as left (L) or right (R) in reference to the physical location of the PMT that fired with respect to the detector. Since there is no coincidence of L and R PMT in these instances, these rates do not contribute to the MT rates. The COINC outputs result from a coincidence of MT outputs for CED·FPD coincidences where a single CED and a single FPD have fired. In cases where multiple CEDs or FPDs fire in coincidence, the output is not considered a coincidence but is instead counted as a multihit (MH).

In order to apply the corrections, the rates of singles, coincidences and multihits must be known, along with the beam current and different timing gate widths. The singles rates are measured and stored during data taking along with coincidence rates and the beam current is measured by the beam current monitors. For the gate widths, the nominal values are a property of the components used, and, as such, are known. However, in practice, the gate widths that are actually seen can differ due to differences in cabling. In order to account for this, measurements were done to determine the effective gate widths and these values were used for the corrections.

Because of differences in the design between the North American (NA) and French (FR) octant electronics, the equations that define the corrections differ slightly for the two sets of octants. However, in both cases the measured coincidence rate can be written as a combination of the dead time effects from the various electronics multiplied by the true coincidence rate, according to

$$r_{CED \cdot FPD}^{e, meas} = r_{CED \cdot FPD}^{e, DTCor} (1 - DT_{CFD}^{CED} - DT_{MT}^{CED}) (1 - DT_{CFD}^{FPD} - DT_{MT}^{FPD}) \times (1 - DT_{Trig} - MH_{22}) \overline{MH_{12}}, \quad (4.3)$$

where the term  $r_{CED\cdot FPD}^{e,meas}$  is the measured electron rate for a given CED·FPD coincidence,  $r_{CED\cdot FPD}^{e,DTCor}$  is the dead-time corrected coincidence rate and  $DT_j^i$  is the dead time correction for a given piece of the electronics. The two MH variables represent the probability of multiple hits, with  $MH_{12}$  being those that contain a single CED (FPD) in coincidence with two FPDs (CEDs) and  $MH_{22}$  being those where two CEDs and two FPDs are in coincidence. The values of the individual pieces of the correction,  $DT_j^i$  and  $MH_{uv}$ , are calculated from dead times and rates of the different electronic components and are defined elsewhere [62]. The dead-time corrected rate,  $r_{CED\cdot FPD}^{e,DTCor}$ , is given by inverting Equation 4.3.

In addition to the differences associated with the FR versus NA octants, there was another consideration for the dead time corrections for the deuterium data. The computation of the MT and MH pieces of the correction require the total coincidence rate (electron plus pion). For the deuterium data, many of the runs were performed in what was referred to as “randoms mode”, where the signals from the Cherenkov detectors were delayed with respect to the CED·FPD coincidence signal and the delayed rates stored in place of the pions. Since there was no pion data for these runs, a method for the reconstruction of the missing pion rates was developed. Simulation code that modeled the FR electronics was used to test this method for reconstructing pion rates and the simulated rates were found to be within 1% of the actual rates.

### **Contamination Correction**

The correction for Cherenkov dead time and randoms is referred to as the *contamination correction*. The Cherenkov corrections are treated separately from the dead time and randoms corrections for the other electronic components because their impact is dif-

ferent. Rather than events being left uncounted or non-real events being wrongly counted, these effects lead to real events being recorded incorrectly. Cherenkov dead time results in electron contamination in the pion matrix while Cherenkov randoms lead to pion contamination in the electron matrix. As such, the application of the correction results in events being subtracted from one matrix and added to the other. In general, the contamination correction for the electron matrix uses the measured total coincidence rates ( $e + \pi$ ) along with calculated randoms rates. However, as discussed in the previous section, much of the deuterium data was taken in randoms mode, with Cherenkov randoms being stored in the place of the pions. For these runs, the contamination could be subtracted from the electron rates in a more direct manner.

When pion data are present, the contamination correction is applied to the dead-time corrected rates according to

$$r_{CED.FPD}^{e,ConCor} = \frac{r_{CED.FPD}^{e,DTCor} - (r_{CED.FPD}^{e,DTCor} + r_{CED.FPD}^{\pi,DTCor})Rdm_{Ch_2}}{1 - Rdm_{Ch_2} - DT_{Ch}} \quad (\text{pion mode}), \quad (4.4)$$

where  $r_{CED.FPD}^{e(\pi),DTCor}$  is the dead-time corrected electron (pion) yield,  $Rdm_{Ch_2}$  is the probability of Cherenkov randoms correlated to the CED·FPD trigger, and  $DT_{Ch}$  is the Cherenkov dead time. When there are no pion data, the scaled randoms rates are used according to

$$r_{CED.FPD}^{e,ConCor} = \frac{r_{CED.FPD}^{e,DTCor} - r_{CED.FPD}^{rand,DTCor} \left( \frac{Rdm_{Ch_2}}{Rdm_{Ch_1}} \right)}{1 - Rdm_{Ch_2} - DT_{Ch}} \quad (\text{randoms mode}). \quad (4.5)$$

Here the definitions of  $r_{CED.FPD}^{e,DTCor}$ ,  $Rdm_{Ch_2}$  and  $DT_{Ch}$  are the same as above, while  $r_{CED.FPD}^{rand,DTCor}$  is the dead-time corrected randoms rate and  $Rdm_{Ch_1}$  is the probability of Cherenkov randoms uncorrelated to the CED·FPD trigger.

### **Randoms Correction**

The third and final rate correction applied, the randoms correction, corrects the pion matrix for CED-FPD randoms. The correction is not applied to the electron matrix because in order for these randoms to be counted as electrons the Cherenkov detector would have to also randomly fire in coincidence. Due to constraints on the information available to g0analysis from the electronics, it is not possible to link a given random CED-FPD coincidence to a random Cherenkov event in the code, making the application of this correction to the electron matrix impossible. However, information obtained from special runs is available from which the fraction of CED-FPD-CER can be determined outside the scope of g0analysis. Since CED-FPD-CER randoms are rare, the effect of these randoms on the electron rates is negligible and will be treated as an uncertainty. The uncertainty due to CED-FPD randoms in the electron matrix will be discussed in the following section.

### **Rate Correction Uncertainty**

Detailed error analysis was performed for the rate corrections [61], however much of this analysis focused on the elastic measurement. For the inelastic asymmetry, a separate study of the Pass 3 corrections was done through which elastic locus results were used to estimate bounds on the uncertainty in the inelastic locus. The uncertainty can be separated into two categories: uncertainty due to applying the correction and uncertainty due to residual effects that were not able to be corrected. In the electron data, the corrections applied are dead time and contamination. The uncertainty in the dead time correction stems from the application of the corrections for the various electronic components. Sources of error include those related to precision of rate and timing information

and approximations made in the equations that define the correction.

The false asymmetry arising from the dead time of the various electronic components, along with an uncertainty, was computed for the elastic locus [61] and is presented in Table 4.2. The false asymmetries corrected for in the dead time correction are those arising from single, trigger and multihit events ( $A_{Single}$ ,  $A_{Trig}$  and  $A_{MH12}$ ). Since the dead time corrections are based on the behavior of the electronics, which are the same for all coincidence cells, the false asymmetry for the inelastic locus can be inferred from the elastic results. Further, since the dead time is rate dependent and the inelastic locus has overall lower rates than the elastic locus, the effect of the correction will be smaller. Thus, the false asymmetries in Table 4.2 represent an upper bound on the false asymmetry due to dead time in the inelastic locus. Given the limited statistical precision of the inelastic measurement, these false asymmetries are negligible and will not be included in the determination of the Pass 3 uncertainty.

IHWP		$A_{Single}$	$A_{Trig}$	$A_{MH12}$
H 687	in	$-0.006 \pm 0.002$	$-0.115 \pm 0.002$	$-0.069 \pm 0.005$
	out	$0.008 \pm 0.002$	$0.128 \pm 0.002$	$0.076 \pm 0.005$
D 687	in	$-0.009 \pm 0.002$	$-0.090 \pm 0.003$	$-0.056 \pm 0.007$
	out	$0.003 \pm 0.003$	$0.062 \pm 0.004$	$0.038 \pm 0.008$

*All values are given in ppm*

TABLE 4.2: Summary of false asymmetries due to detector dead time, averaged across the elastic locus. The asymmetry due to each of the individual components (Single, Trigger, Multihit) is shown along with an error. These asymmetries have been computed separately for the two insertable half-wave plate (IHWP) states (IN and OUT). The final asymmetry is the average of the two states. Table taken from [61].

The error due to the contamination correction has a more significant impact than that of the non-Cherenkov dead time, especially with the deuterium target. The high pion rates

when scattering from deuterium lead to an increase in Cherenkov randoms, which leads to increased contamination. Since the pions and electrons have very different asymmetries, the presence of pions in the electron matrix will alter the average asymmetry in a given coincidence cell. How big of an impact the pions have on the average asymmetry depends both on the number of pion events present and on the degree to which the pion and electron asymmetries differ. Accordingly, the false asymmetry due to the contamination correction can be written

$$A_{false}^{contam} = f_{\pi}(A_{pass3}^{\pi} - A_{pass3}^e), \quad (4.6)$$

where  $f_{\pi}$  is the fraction of pions in the electron matrix due to Cherenkov randoms, and  $A_{pass3}^{\pi}$  and  $A_{pass3}^e$  are the rate-corrected pion and electron asymmetries. Values for  $f_{\pi}$  were determined for the elastic locus for each run period using

$$f_{\pi} = \frac{r_{true}^{\pi} Rdm_{Ch}}{r_{pass3}^e}, \quad (4.7)$$

where  $r_{true}^{\pi}$  is the true pion rate,  $r_{pass3}^e$  the rate-corrected electron rate and  $Rdm_{Ch}$  the probability of Cherenkov randoms. This yielded an  $f_{\pi}$  in the elastic locus of 3.08% for hydrogen at 687 MeV and 19.28% for deuterium at 687 MeV during the March run period [61].

The error on  $A_{false}^{contam}$  can be determined through error propagation and will depend on the statistical error of the three quantities involved. Since  $f_{\pi}$  is a ratio of measured rates, the error is negligible, leaving the error on the contamination correction dependent on the statistical error on the pion and electron asymmetries and the pion fraction itself.

$$(\delta A_{false}^{contam})^2 = (f_{\pi})^2 [(\delta A_{pass3}^{\pi})^2 + (\delta A_{pass3}^e)^2]. \quad (4.8)$$

Using this equation and the elastic values for  $f_{\pi}$ , the error due to the contamination correction in the inelastic locus was found to be 0.1 ppm for hydrogen and 1.2 ppm for

deuterium. This is the total uncertainty assigned due to the application of the rate corrections.

The residual asymmetries are due both to remaining higher-order dead time effects after the corrections are applied and to any effect of CED·FPD randoms, as this correction is not applied to the electron matrix. These two main effects will be treated consecutively, starting with the dead time residual, which can be approximated according to

$$A_{res}^{DT} = DT_{res} A_{CFD} , \quad (4.9)$$

where  $DT_{res}$  is the residual dead time determined as a fraction of the total ( $e + \pi$ ) yield and  $A_{CFD}$  is the asymmetry in the CFD rates. The asymmetry in the CFDs is the only asymmetry considered because, for the elastic locus, they were found to have the highest asymmetry. For the elastic result,  $A_{res}^{DT}$  was computed and used as an uncertainty [61]. However, for the inelastic asymmetry, since  $A_{res}^{DT}$  is defined as a fraction of  $A_{CFD}$ , and  $A_{CFD}$  is negligible, this effect will be neglected.

The remaining effect to consider is the false asymmetry arising from CED·FPD randoms in the electron matrix. These randoms contribute to the asymmetry in two ways. The first contribution is from the false asymmetry due to singles,  $A_{single}$ , which contains terms related to both dead time and randoms. The dead time contributions are corrected for in Pass 3, but the randoms contribution remains. The second contribution is the asymmetry of the CED·FPD randoms themselves,  $A_{rdm}$ . The residual asymmetry can be written [62] as the difference between the dead-time corrected asymmetry with and without

CED·FPD randoms taken into account,

$$\begin{aligned}
 A_{res}^{rdm} &= A^{DT}(f_{rdm}) - A^{DT}(f_{rdm} = 0) \\
 &= \{A^{Pass3}[1 - f_e f_{rdm}] + f_e f_{rdm} [A_{single}^{DT} + A_{rdm}]\} - A^{Pass3} \\
 &= f_e f_{rdm} \{-A^{Pass3} + A_{single}^{DT} + A_{rdm}\}, \tag{4.10}
 \end{aligned}$$

where  $f_e$  is the total fraction of Cherenkov randoms in the electron matrix, including those correlated to random CED·FPD coincidences and to true pion events,  $f_{rdm}$  is the total fraction of CED·FPD randoms and  $A_{single}^{DTcor}$  is the dead-time corrected asymmetry in the singles. The quantity  $f_e f_{rdm}$  represents the fraction of CED·FPD·CER randoms.

As was discussed previously, the asymmetry due to residual dead time is negligible. Likewise,  $A_{rand}$  was measured to be small with respect to the electron asymmetry. Thus, both can be neglected and Equation 4.10 can be rewritten to place a bound on  $A_{res}^{rdm}$  such that

$$A_{res}^{rdm} \leq f_e f_{rdm} (-A^{Pass3}). \tag{4.11}$$

As with the pion fraction,  $f_\pi$ , used in computing the contamination from Equation 4.8, the two randoms fractions ( $f_e$  and  $f_{rdm}$ ) were not computed for the inelastic locus. In order to compute the residual asymmetry, the elastic locus values for these fractions were used (See Table 4.3), leading to bounds on  $A_{res}^{rdm}$  of 0.12 ppm for hydrogen and 0.31 ppm for deuterium.

In conclusion, the determination of the uncertainty due to the rate corrections for the inelastic locus depends only on the systematic error on the contamination correction and the residual asymmetry present as a result of the randoms correction not being applied to the electron matrix. Summing the individual errors found using Equations 4.8 and 4.11 in quadrature, the uncertainty due to the rate corrections was found to be 0.16 ppm for hydrogen and 1.2 ppm for deuterium.

	H 687	D 687
$f_\pi$	3.08%	19.28%
$f_e$	18%	11%
$f_{rdm}$	2.95%	10.5%

TABLE 4.3: Elastic locus averages for fractions of pions ( $f_\pi$ ), Cherenkov randoms ( $f_e$ ) and CED·FPD randoms ( $f_{rdm}$ ) in the electron matrix [61].

#### 4.2.4 Analysis Pass 4: Helicity-Correlated Beam Properties

The final analysis pass corrects for false asymmetries arising from helicity-correlated changes in beam properties. As was discussed in Section 3.3, the asymmetry measured between helicity states is assumed to be due only to the change in helicity. However, changes in other beam properties may also occur as the beam alternates between helicity states. The correction applied in this pass accounts for false asymmetries arising from any changes in beam angle and position in both the  $x$  and  $y$  directions, energy and current that occurred during a run. The false asymmetry due to changes in these beam parameters is written as

$$A_{false} = \sum \frac{1}{2Y} \frac{\partial Y}{\partial P_i} \Delta P_i, \quad (4.12)$$

where  $Y$  is the total detector yield for a given CED·FPD coincidence cell and the  $P_i$ 's are the beam parameters listed above. The partials  $\frac{\partial Y}{\partial P_i}$ , referred to as the linear regression slopes, represent detector sensitivities and  $\Delta P_i$  the variation of parameter  $i$  from the run average. Since the calculation of  $\frac{\partial Y}{\partial P_i}$  and  $\Delta P_i$  requires the use of run-averaged values of the beam parameters, this correction cannot be computed without having completed a previous pass. As such, the slopes and run averages are computed during Pass 3 and stored in the database for use in applying the correction in Pass 4.

Using a least squares fit, the locus-averaged slopes,  $\frac{\partial Y}{\partial P_i}$ , were computed for each

of the six beam parameters. Since the parameters are correlated both to each other and to the yield, they cannot be computed independently. Instead, a six-dimensional fit is required. To apply this fit, the yield can be written as the sum of the true yield and the helicity-correlated change in the yield such that

$$\begin{aligned} Y &= Y^{true} + Y^{HC} \\ &= Y^{true} + \sum \frac{\partial Y}{\partial P_i} \Delta P_i, \end{aligned} \quad (4.13)$$

where  $Y^{true}$  is the true electron yield,  $Y^{HC}$  is the helicity-correlated yield and  $\frac{\partial Y}{\partial P_i}$  and  $\Delta P_i$  are defined as above. Using the least squares method and Equation 4.13, the set of equations for determining the slopes can be written [63]

$$\langle \delta P_j \delta Y \rangle = \sum_i \langle \delta P_j \delta P_i \rangle \frac{\partial Y}{\partial P_i}, \quad (4.14)$$

where  $\langle \delta P_j \delta Y \rangle$  represents the average correlation between a given beam parameter,  $P_j$ , and the yield and  $\langle \delta P_j \delta P_i \rangle$  the average correlation between  $P_j$  and the other beam parameters,  $P_i$ . The equation can be solved for  $\frac{\partial Y}{\partial P_i}$  by inverting the beam parameter correlation matrix.

The size of the false asymmetry depends on the variation of the beam parameters from the average values during a given run. Table 3.1 in Chapter 3 summarized the specifications for the different beam parameters and the actual variations measured. In every case, the specifications were not only met, but the measured variations were much smaller than the specified value. Because of the high quality of beam that was provided by the Jefferson Lab accelerator, helicity-correlated effects were negligible. As such, the false asymmetry due to these variations was small ( $< 0.3$  ppm). With a correction so small, detailed error analysis is not necessary. Instead, an error equal to 100% of the correction is assigned.

### 4.3 Data Quality

During the experimental run, the team on shift monitoring the experiment was regularly checking the outputs of beam and target monitors along with the yield from the detectors. Once a given run was completed, a quick analysis script was executed, resulting in an output summary file that contained the important beam parameters and summarized detector outputs. These outputs were checked once per 8-hour shift. The online monitoring allowed the shift team to correct any issues with the beam, target or detectors. Additionally, a running log was kept where the team could make notes of any abnormalities in the beam or detector outputs for later reference. At the end of the shift, the runs performed during that shift were labeled in the database with both their type (e.g. production, polarimetry, reversed magnetic polarity) and with their data quality (good, not all good, junk). From this information, a list of good runs could be compiled. However, occasionally runs would slip through or be mismarked, leading to production runs being lost or bad/non-production data being averaged in to the final result.

Once the analysis phase of the experiment began, it was necessary to look through all of the data taken to ensure that the data being analyzed was of good quality. Since the replay portion of the analysis was divided among several collaborators, a data quality checklist was employed to allow a uniform standard to be applied across all run periods regardless of which collaborator was responsible for that run period. The checklist consisted of creating plots of asymmetries, yields and beam parameters, such as position and charge asymmetry, as a function of run number for each octant to verify that the values were consistent across the run period and octants. These plots were produced for both Pass 1 and Pass 3 to ensure that the corrections applied did not cause any problems to appear in the data. Select data from the replay were also compared with the summary

files from the online analysis. Additionally, the CED and FPD singles rates were plotted as a function of run number to check that all detectors were behaving properly.

Any runs that varied too far from the average were inspected in more detail, including referring to the online logbook to see if the shift team had noted any problems when the run was taken. If a problem with a given run was documented or if the average of the quantity was several sigma from all other runs in the run period, the run was removed from the average. The exclusion of runs was dependent on averages of beam parameters and rates. No runs were excluded based on the value of the detector asymmetries. Once data quality checks were performed for all the data, a final “good run” list was compiled for future analysis.

### **4.3.1 Bad PMTs**

While studying the implementation of the Pass 4 corrections for one run period, an anomaly in the linear regression slopes for one CED in one octant (CED5/OCT1) was discovered. Upon further study, it was determined that during a given run, the yield per MPS for this CED would begin at one value, stay consistent for a short period and then jump to a different value where it would then remain consistently for the rest of the run. This resulted in a two-peak distribution of the yield per MPS for the run and a run-averaged yield in CED5/OCT1 that was below that seen in the same CED in other octants during the same run. Through looking at singles rates, this low yield could be attributed to the signal coming from the right PMT on CED 5. Since this was only showing up in one PMT, it was determined that this was a defect in this PMT that lead to the yields not being recorded properly.

In order to determine the scope of this problem, a full survey of the data was done,

plotting the run-averaged right and left PMT single rates as a function of run number for all detectors (CED and FPD) in all octants. This survey showed that the right PMT for CED 5/OCT1 was misbehaving throughout the entire experimental run and also that a second PMT (CED8/OCT5) was exhibiting similar behavior. While the impact of these bad PMTs was minimal, the behavior pointed to physical issues with the PMTs themselves. Thus, the decision was made to remove the affected data, CED5/OCT1 and CED8/OCT5, from any averaging.

### **4.3.2 Bad Octants**

In some cases, problematic data were only present in some of the octants. To account for this, the software allowed for averaging to be done with specified octants left out. This was especially important in the low-energy deuterium run period, when the scaler counting problem was being diagnosed. Rather than lose beam time by devoting the entire apparatus to testing, a single octant was unplugged and its electronics tested while the remaining seven octants collected production data. In other instances, the bad octants were due to cabling or detector power supply issues. A list of bad octant runs was determined both by looking at the data quality and by checking the online log book for notes made by the collaborators on shift when the data were taken. These octants were then marked in the database so they could be left out of the averaging. For most of the run periods, the number of bad octant runs was negligible. However, for the low-energy deuterium run period, the number of runs containing at least one bad octant was significant enough that removing these runs in their entirety from the run list would have reduced the total amount of data collected by roughly 9%.

## 4.4 Beam Polarization Corrections

The final beam-related corrections applied involve the beam polarization. As discussed in Section 3.4,  $G^0$  required the use of a longitudinally polarized electron beam. The magnitude of the polarization is dependent on the polarized electron source used, while its direction depends on the Wein filter settings, which are chosen to offset the precession of the spin of the electrons as they move through the accelerator. Ideally, the beam would have 100% polarization entirely in the longitudinal direction, but, since no beam is perfect, the polarization magnitude will be reduced and there will be some component of the beam in the transverse direction. The magnitude of the polarization affects the asymmetry by shifting it to a lower value. In order to compare to theory, which assumes full polarization, it is necessary to shift the asymmetry back to the fully polarized value. The transverse component of the beam leads to a false asymmetry that, if large enough, can impact the measured asymmetry. To correct for this effect, the false asymmetry must be computed so it can be subtracted out. The two polarization corrections will be discussed individually in the sections that follow.

### 4.4.1 Longitudinal Beam Polarization Correction

The size of the longitudinal beam polarization correction was determined using the Hall C Møller polarimeter, as described in Section 3.4. The correction is applied to the asymmetry according to

$$A_{bpol} = \frac{P}{100}(A_{pass4} \pm \sigma_{pass4}), \quad (4.15)$$

where  $P$  is the measured polarization. The beam's polarization was found to be consistent throughout the  $G^0$  Backward Angle run. The correction applied for both the hydrogen

and the deuterium high-energy run periods was  $P = (85 \pm 0.07_{stat} \pm 1.38_{sys})\%$ .

#### 4.4.2 Transverse Beam Polarization Correction

The transverse asymmetry arises from an interference between reactions involving single photon and two photon exchanges and, unlike the longitudinal asymmetry of interest, is parity-conserving [64]. Since the incoming electron beam has components in the two polarization directions, the measured parity-violating asymmetry will be a linear combination of longitudinal and transverse asymmetry components. The measured transverse asymmetry,  $A_T$ , is given as [65]

$$A_T = B_n \vec{p}_e \cdot \hat{n}, \quad (4.16)$$

where  $\vec{p}_e$  is the beam polarization and  $\hat{n}$  is the vector normal to the scattering plane.  $B_n$ , the beam-normal single spin asymmetry, is the asymmetry that arises from interference between single and two photon exchanges and can be written

$$B_n = \frac{\sigma_{\uparrow} - \sigma_{\downarrow}}{\sigma_{\uparrow} + \sigma_{\downarrow}}, \quad (4.17)$$

where  $\sigma_{\uparrow}$  ( $\sigma_{\downarrow}$ ) represents the scattering cross section for beam polarization parallel (antiparallel) to  $\hat{n}$ .

The impact of the transverse polarization can be seen by studying the octant dependence of the asymmetry. For longitudinally polarized beam, the asymmetry will be constant across all octants, while for transversely polarized beam the shape of the asymmetry across the octants will be sinusoidal due to  $B_n$ . The sinusoidal shape is due to the orientation of the polarization vector relative to the scattering plane. The transverse polarization direction is determined relative to an axis where beam left, or detector octant 3, is

considered  $0^\circ$  in  $\phi$ . For transverse running,  $\phi$  is set to  $90^\circ$ . In a symmetrical detector system, such as the one used in  $G^0$ , the effect of the transverse polarization component on the asymmetry should cancel out when averaging over the octants. However, any misalignment within or between the octants can cause the individual octant acceptances to differ, leaving the cancellation incomplete. Thus, it is important to understand the transverse polarization and asymmetry to determine if a correction must be applied.

In order to subtract out the false asymmetry due to the transverse component from  $A_{meas}$ , both the degree of transverse polarization ( $\frac{P_T}{P}$ ) and the magnitude of the transverse asymmetry ( $A_T$ ) must be known. Additionally, an estimate for the detector misalignment,  $M_{det}$ , must be determined, as this is the factor that allows  $A_T$  to impact  $A_{meas}$ . The size of the correction is defined to be

$$A_T^{corr} = A_T M_{det} \frac{P_T}{P}. \quad (4.18)$$

The magnitude of the transverse polarization,  $A_T$ , was determined by taking data with the beam polarized in the transverse direction. This was done by adjusting the settings on the Wein filter in the injector region of the accelerator. Since the polarization is determined at the source with the Wein filter altering only its direction, and because measurements from the polarimeters showed consistent polarization throughout the  $G^0$  experimental run, the magnitude of the polarization is taken to be consistent between the two directions. The locus average asymmetry is fit as a function of octant to a sinusoidal function with the amplitude ( $A_T$ ), phase ( $\phi$ ) and offset ( $c$ ) all allowed to vary. Figure 4.4 shows the inelastic transverse asymmetry for the hydrogen and deuterium data at 687 MeV. A summary of the fit parameters is given in Table 4.4. Though the measured transverse asymmetry is only used here for the purpose of correcting the longitudinal data, the determination of  $B_n$  is of interest to aid in the understanding of the two-photon exchange.

$G^0$  transverse data has been used to measure  $B_n$  in the elastic locus using both the hydrogen and deuterium targets at backward angle [10] and the hydrogen target at forward angle [9].

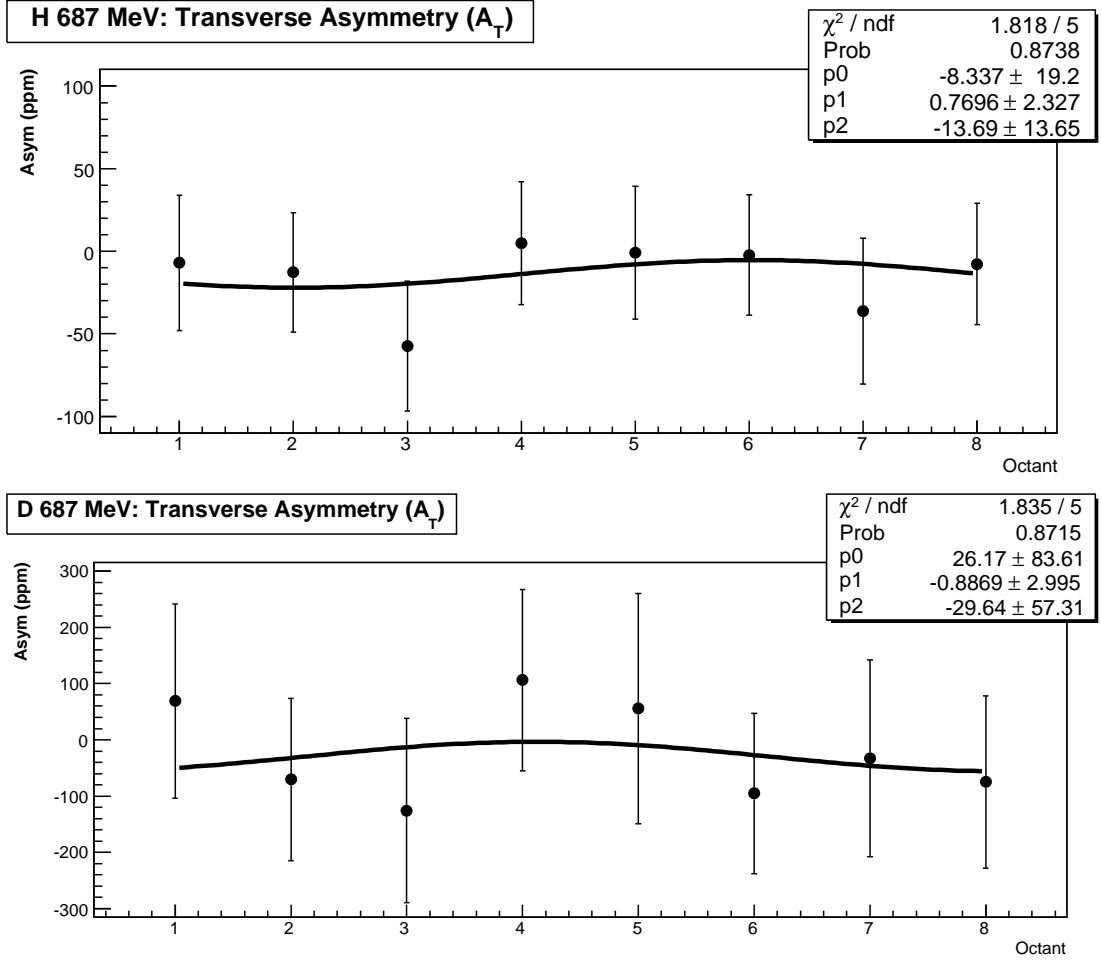


FIG. 4.4: Measured inelastic transverse asymmetry as a function of octant for hydrogen (top) and deuterium (bottom). Each plot has been fit to a sine curve with all parameters allowed to vary freely. The parameters p0, p1 and p2 represent the amplitude ( $A_T^{inel}$ ), phase ( $\phi_0$ ) and offset ( $c$ ), respectively.

The size of the transverse component during longitudinal running can be deduced from studying the data from the luminosity monitors (LUMIs). Since the LUMIs measure scattering at very forward angles, the measured rates are higher than those from

Data Set	$A_T^{inel}(ppm)$	$\phi_0(^{\circ})$	$c(ppm)$	$\chi^2/NDF$
H 687	$-8.3 \pm 19$	$0.770 \pm 2$	$-13.7 \pm 14$	0.36
D 687	$26.1 \pm 84$	$0.887 \pm 3$	$-29.6 \pm 57$	0.37

TABLE 4.4: Fit parameters for the measured inelastic transverse asymmetry as a function of octant.

the primary detectors, leading to high statistical precision. The added precision allows for octant-to-octant fluctuations in these data to be more easily seen than in the lower-rate backward-scattered data. While the value of the LUMI asymmetry differs from the backward-angle asymmetry, the ratio of longitudinal to transverse will be consistent with that of the primary detectors. The proportion of transverse polarization during longitudinal running can be estimated by taking the ratio of the longitudinal to transverse LUMI asymmetry, such that

$$\frac{P_T}{P} = \frac{A_L^{LUMI}}{A_T^{LUMI}}, \quad (4.19)$$

where  $A_{L/T}^{LUMI}$  represents the octant average LUMI asymmetries for the two polarization directions. Figure 4.5 shows the asymmetry measured by the LUMIs as a function of octant for both longitudinal and transverse beam. The curves represent sinusoidal fits to the data where the amplitude, phase and offset are all left as free parameters. Table 4.5 summarizes the LUMI asymmetries and polarization ratio for the two data sets of interest to the inelastic measurement.

Data Set	$A_L^{LUMI}(ppm)$	$A_T^{LUMI}(ppm)$	$P_T/P$
H 687	$0.71 \pm 0.04$	$19.0 \pm 0.3$	0.037
D 687	$0.37 \pm 0.02$	$18.3 \pm 0.4$	0.020

TABLE 4.5: Longitudinal and transverse LUMI asymmetries and their ratio for both data sets.

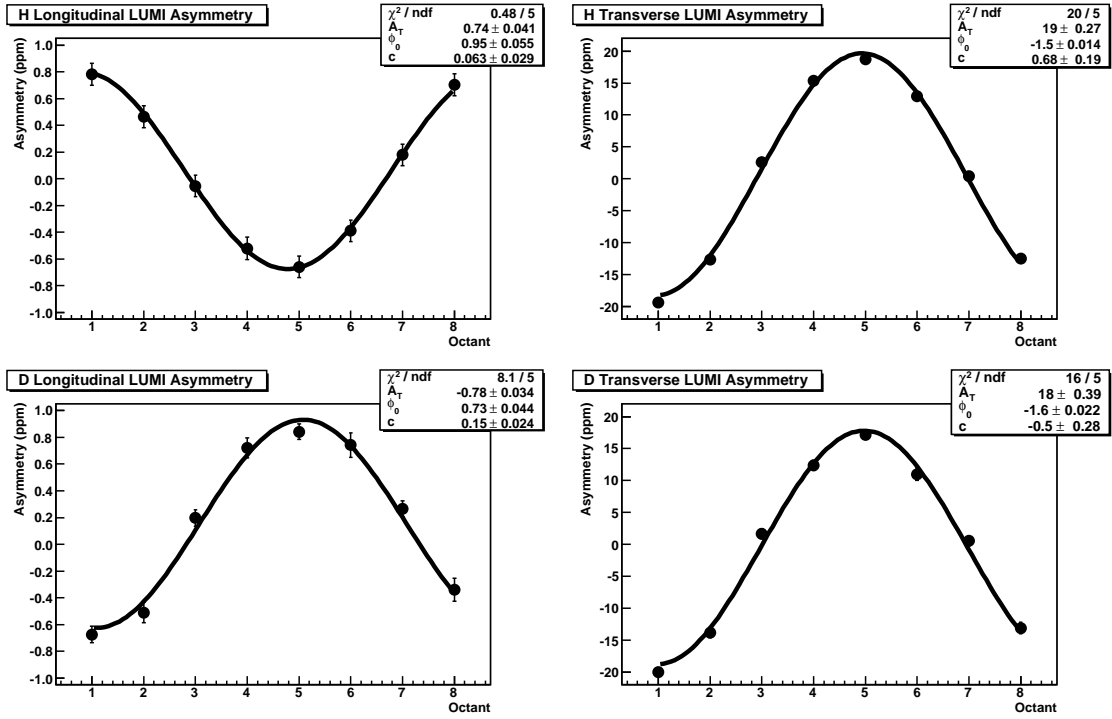


FIG. 4.5: Asymmetry measured by the luminosity monitors (LUMIs) as a function of octant for hydrogen (top) and deuterium (bottom). The plots on the left show the asymmetry for longitudinally polarized beam while those on the right show asymmetry for transversely polarized beam. Each plot has been fit to a sine curve, with all parameters allowed to vary freely. The fit parameters represent the amplitude ( $A_T^{inel}$ ), phase ( $\phi_0$ ) and offset ( $c$ ), respectively. Note that the scales on the asymmetry differ significantly between the plots on the left and those on the right.

The final piece that is needed to determine the size of the transverse correction is the detector misalignment,  $M_{det}$ . What  $M_{det}$  provides is a quantitative measure of the imperfections in the primary detector system. Because there are many factors that can contribute to this misalignment, this is a difficult quantity to determine. However, estimates can be made by considering the variations in the measured yield between the different octants. These yield differences can be due to several factors, including differing electronics and misalignment of collimators within the magnet. Additionally, if two opposing detector octants were not perfectly aligned it would lead to differing kinematics for electrons detected in these octants and, thus, different octant yields. By assuming the differences in yield across the octants are due entirely to imperfections in the octant alignment, an upper bound for  $M_{det}$  can be deduced.

One measure of detector yield is the statistical error on the asymmetry. When the octant average asymmetry is computed, the errors are used as weighting factors. If all octants have the same yield, the statistical error in each will be identical and the octant average will be consistent, whether or not weighting was used. Thus, the detector misalignment can be estimated to be the percent change between the weighted and unweighted octant averages, such that

$$M_{det} = \frac{A_{avg}^w - A_{avg}^u}{A_{avg}^w}, \quad (4.20)$$

where the superscripts  $w$  and  $u$  denote weighted and unweighted averages, respectively.

Using the results found in Tables 4.4 - 4.6 and Equation 4.18, the size of the transverse correction is computed to be

$$\begin{aligned} A_T^{corr,H} &\leq -0.03 \text{ ppm} , \\ A_T^{corr,D} &\leq 0.02 \text{ ppm} . \end{aligned}$$

Data set	$A_{avg}^w$ (ppm)	$A_{avg}^u$ (ppm)	$M_{det}$
H 687	-22.33	-21.64	0.0309
D 687	-26.41	-26.13	0.0106

TABLE 4.6: Estimate of the detector misalignment,  $M_{det}$ . The results shown here provide an upper bound on the physical asymmetry due to detector misalignment.

These results, when taken in context with the large statistical error present in the inelastic asymmetry, indicate that the transverse asymmetry does not have a significant enough impact on the inelastic asymmetry to require applying a correction. Instead, the bounds computed here will be treated as an uncertainty.

## 4.5 Summary of Beam and Instrumentation Corrections

Table 4.7 summarizes the corrections applied in this chapter. In the table, the error has been presented in three different ways. The first quantity,  $\sigma_{tot}$ , is the total uncertainty at a given stage in the analysis, including statistics and all systematic contributions. The uncertainty is then subdivided, with  $\sigma_{stat}$  and  $\sigma_{sys}$  being the total statistical and systematic errors after each correction was applied. Next,  $\sigma_{cor}$  gives the systematic uncertainty due to each correction. The final column, dA, is the change in the asymmetry as a result of applying a given correction. It should be noted that  $\sigma_{cor}$  is not an additional systematic error but rather is a subset of the quoted  $\sigma_{sys}$ . It has been presented separately to highlight the contribution of each correction to the total systematic error. The asymmetries and errors, given in parts-per-million (ppm), have been averaged across the inelastic locus cells, all octants and all runs in the indicated run period.

$A_{inel}$  for H 687MeV

	$A$	$\sigma_{tot}$	$\sigma_{stat}$	$\sigma_{sys}$	$\sigma_{cor}$	dA
Pass 1: Raw	-20.23	2.00	2.00	0.00	—	—
Pass 2: Scaler Correction	-20.00	1.99	1.99	0.00	0.00	+0.23
Pass 3: Rate Corrections	-22.17	2.26	2.25	0.16	0.16	-2.17
Pass 4: Linear Regression	-22.33	2.25	2.24	0.23	0.16	-0.16
Beam Polarization	-26.27	2.67	2.64	0.43	0.36	-3.91
Transverse Polarization	-26.27	2.67	2.64	0.43	0.03	—

 $A_{inel}$  for D 687MeV

	$A$	$\sigma_{tot}$	$\sigma_{stat}$	$\sigma_{sys}$	$\sigma_{cor}$	dA
Pass 1: Raw	-14.11	2.62	2.62	0.00	—	—
Pass 2: Scaler Correction	-14.06	2.62	2.62	0.00	0.00	+0.05
Pass 3: Rate Corrections	-26.66	5.99	5.87	1.20	1.20	-12.6
Pass 4: Linear Regression	-26.41	6.01	5.88	1.23	0.25	+0.25
Beam Polarization	-31.07	7.04	6.92	1.30	0.43	-4.66
Transverse Polarization	-31.07	7.04	6.92	1.30	0.02	—

*All values in ppm*

TABLE 4.7: Inelastic asymmetry following each stage of corrections applied.

## **CHAPTER 5**

# **Data Analysis: Corrections for Backgrounds and Radiative Effects**

After applying the corrections discussed in the previous chapter, further corrections to the inelastic asymmetry for backgrounds and radiative effects were applied. The background correction, applied first, is the largest of these corrections. Correcting for backgrounds required an understanding of the asymmetry of the various possible contributing processes along with their fractional contributions to the total yield. These yields and asymmetries were determined using both simulation and data collected during the experimental run. Once backgrounds were subtracted, electromagnetic (EM) radiative effects were taken into account. The final correction applied was to account for acceptance averaging. The background correction was applied to both the hydrogen and deuterium data while the radiative and acceptance averaging corrections were applied only to the hydrogen data. The analysis that follows is unique to the inelastic measurement.

## 5.1 The *G0GEANT* Simulation

Simulation is an important tool in the understanding of the measured yields and asymmetries. By recreating the experimental conditions in software, the different processes present in the data can be disentangled and their impacts studied individually. In order to perform these simulations, the  $G^0$  experiment used *GEANT3*, a Monte Carlo simulation package developed at CERN that simulates the passage of elementary particles through matter [66]. *GEANT* is useful in the design of high energy and nuclear physics experiments, in testing data analysis and in the interpretation of experimental results. This last use represents the primary role of simulation in this analysis, with *GEANT* being used in the determination of backgrounds, radiative corrections and theoretical asymmetry values. An overview of the  $G^0$  implementation of *GEANT*, *G0GEANT*, will be given in this section while the specific usage of the simulation will be discussed in the appropriate sections later in the chapter.

*G0GEANT* consists of the core package of *GEANT* subroutines that allow for the tracking of particles, along with geometry definitions and event generators specific to the  $G^0$  experiment. Information about the design and location in the hall of the target, magnet, collimators and detectors is contained in a geometry file that is used as input when running the simulation. Flags contained in a separate input file set experimental parameters such as beam energy, magnetic field strength and a window of allowed scattering angles. The input file also defines the target type (liquid or gas, hydrogen or deuterium), tracked particles and the point of interaction within the target. The interaction point is generally a randomly chosen location along the  $z$ -axis within the hydrogen target cell. However, the user can also choose a random position along the  $z$ -axis within the helium cell, a fixed position within the hydrogen cell or a fixed position at one of the aluminum

target windows. In addition to the experimentally defined input parameters, there is also a flag to select the scattering process. The processes implemented in G0GEANT are elastic and inelastic electron scattering from hydrogen, deuterium, aluminum and helium, pion photoproduction and  $\pi^0$  decay.

For a given scattering event, the simulation generates a scattered electron with kinematic properties randomly chosen to lie within the ranges defined by the user. The scattered particle is then tracked as it travels through the experimental apparatus. In addition to the primary reaction, the simulation can also track particle trajectories from secondary reactions, such as electromagnetic showers. For every event generated, output, including kinematic variables, particle type, cross section weighting factor and asymmetry, is written to an ntuple. The simulation treats the detectors independently, storing information on how many detectors were struck during a given event and how much energy was deposited in each detector by the event. After the simulation is completed, a separate script is run to create coincidences, plot the asymmetry, yield and kinematic variables as histograms, and write the information to a new output file. Coincidence events are defined as events in which 4 detectors (a CED, a Cherenkov and the two planes of FPDs) were struck, in the correct order, by the primary particle or any secondaries such that at least 0.5 MeV of energy was deposited on the detector.

### 5.1.1 Cross Section Models

The simulated yields are determined by counting the number of events in a given coincidence cell, multiplying each by a unique weighting factor. The weighting factor is computed in the simulation and consists of the scattering cross section weighted by the phase space volume and target luminosity. The weighting factor is defined such that

the simulated yields, like the data, are in units of Hz/ $\mu\text{A}$ . G0GEANT contains models for the computation of elastic and inelastic scattering cross sections from hydrogen and deuterium, along with  $\pi^0$  decay and pion photoproduction on both the proton and the deuteron. Additionally, cross sections from electron scattering from aluminum and helium, which are present in the target system, can also be determined.

For inelastic scattering from hydrogen, the cross section model used was a fit to data performed by Bosted and Christy in 2007 [67]. The model fit high-precision data taken at Jefferson Lab over a wide range of momentum transfer,  $Q^2$ , and invariant mass,  $W$ , along with some older data from other sources. Data taken with longitudinal and transverse virtual photon polarization were treated separately and then summed to compute a total cross section. A minimization procedure was then used to minimize the difference between the model prediction and existing cross section data. To simulate inelastic scattering from deuterium, a separate model from Bosted and Christy [68] based on a fit to deuterium data was used to compute the cross section for the proton, with a correction made to account for Fermi motion within the nucleus. No explicit calculation of the neutron cross section is included in the model, so an approximation based on the ratio of the magnetic moments of the proton and the neutron is used. This approximation assumes the neutron cross section is 25% smaller than that of the proton. Thus, the deuteron cross section is defined as  $1.75 \sigma_p^{fermi}$ , where  $\sigma_p^{fermi}$  is the proton cross section with Fermi motion included. The inelastic cross section for scattering from aluminum or helium is determined in the same manner as for deuterium, with the scaling factor altered to represent the appropriate number of protons and neutrons within the nucleus. Aluminum contains 13 protons and 14 neutrons, leading to a cross section scaling of  $23.5 \sigma_p^{fermi}$ , while helium contains 2 protons and 2 neutrons, resulting in a scaling of  $3.5 \sigma_p^{fermi}$ .

Before the addition of the Bosted/Christy model, a previous version of G0GEANT

used a fit to inelastic electron-proton data performed by Keppel in 1994 [69]. Since this model was fully implemented in the code, it was available to be used for comparison purposes in order to estimate uncertainty. Like the Bosted/Christy Model, the Keppel model is only available for scattering from the proton. As such, the same cross section weighting to approximate the neutron contribution was used in determining yields when scattering from heavier nuclei. However, unlike the Bosted/Christy model, the Fermi motion is not accounted for when using the Keppel model.

The cross section used for elastic scattering from the hydrogen target was based on a parameterization from Kelly [70], while quasi-elastic scattering from the deuteron was determined using a model by Schiavella *et al.* [71]. More detail on the simulations run for elastic scattering is available elsewhere [72] [73]. The  $\pi^0$  electroproduction cross section was determined using MAID 2000 [74], a software program that models pion photo- and electroproduction. Additionally, a model for  $\pi^-$  photoproduction from the proton and the neutron was developed using cross sections from MAID 2000 and then applying additional physics corrections. A detailed description of the implementation of this model is given in [43].

### 5.1.2 Inelastic Asymmetry Models

The primary model used for the inelastic asymmetry was developed by  $G^0$  collaborators based on the Musolf model described in Chapter 2. In this model, the asymmetry is written

$$\begin{aligned}
 A_{inel} &= A_1 + A_2 + A_3 \\
 &= \frac{-G_F Q^2}{4\pi\alpha\sqrt{(2)}} \left[ \Delta_{(1)}^\pi + \Delta_{(2)}^\pi + \Delta_{(3)}^\pi \right] , \tag{5.1}
 \end{aligned}$$

where  $\Delta_{(1)}^\pi$  is a structure-independent constant term representing the resonant vector hadron component of the asymmetry,  $\Delta_{(2)}^\pi$  represents non-resonant vector hadron processes and  $\Delta_{(3)}^\pi$  is the term containing the information about the axial transition. Each of these components is defined in detail in Section 2.3 and their implementation in the simulation will be briefly explained here. The implementation of  $\Delta_{(1)}^\pi$  was simple as this quantity is a constant dependent only on Standard Model couplings, while the other two terms in the asymmetry required the use of input from data and theoretical models.

As shown in Section 2.3.3, Equation 2.57, the computation of  $\Delta_{(2)}^\pi$  requires the sum over angular momentum of electric and magnetic multipoles which can be computed using MAID 2007 [74] for each simulated event. However, since this process is time and CPU intensive, the multipoles were instead computed independently and the results used as lookup tables within the simulation. Since the values of the multipoles changed more rapidly with  $W$  than with  $Q^2$ , the decision was made to simplify the code by performing a 1-dimensional interpolation in  $W$  for fixed  $Q^2$  rather than interpolating over both  $W$  and  $Q^2$ . Three sets of lookup tables were created with multipoles computed over a range of  $W$  for three fixed  $Q^2$  values. The values of  $Q^2$  (0.3, 0.34 and 0.38 (GeV/c)<sup>2</sup>) and range of  $W$  (1.075 to 1.250 GeV) that were used in determining the multipoles were chosen based on the distributions of these quantities in the inelastic locus seen in the simulation. The validity of this approach was tested by eliminating two of the  $Q^2$  ranges and using the multipoles computed for the central  $Q^2$  for all events. The resulting change in the asymmetry was  $< 0.05$  ppm. Since computing all multipoles from the average  $Q^2$  resulted in such a small change, the inclusion of further  $Q^2$  values would not improve precision.

Because the computation of  $\Delta_{(2)}^\pi$  relies on an infinite sum over angular momentum,  $l$ , a second approximation was needed wherein the sum was terminated after the  $l = 2$  term. The choice of where to end the series was made by studying the individual values

for a given multipole at a given  $Q^2$  and  $W$ . In each case, the value of the multipoles decreased with increasing  $l$ . As such, it was assumed that leaving off higher order terms in  $l$  would not impact the computed asymmetry. A test was performed in which the sum was terminated first after the  $l = 1$  term, then after the  $l = 0$  term and the resulting asymmetries were compared to the asymmetry computed using the first three terms. The tests showed that the change in the asymmetry was  $< 0.1$  ppm when the  $l = 1$  and  $l = 0$  terms were used and  $< 0.5$  ppm when using only a single term in the sum ( $l = 0$ ). Since the multipoles used to compute higher-order terms in the sum are smaller than those used in the first three terms, including more terms in the sum would have a negligible impact on the theoretical asymmetry.

A third consideration in the computation of  $\Delta_{(2)}^\pi$  was the version of MAID used to compute the multipoles. As new data become available, the fits performed within MAID to model the data are updated to include the latest information. In order to test the dependence of  $\Delta_{(2)}^\pi$  on the fit used, all the needed multipoles were computed for the three  $Q^2$  values given above using both the 2003 and 2007 versions of MAID. The simulation was then run for each set of multipoles with all other parameters in the simulation fixed. The resulting values for  $A_2$  differed by  $\sim 0.1$  ppm, indicating that the impact of the multipole fit was minimal. Since they were the newest available at the time at the time the  $\Delta_{(2)}^\pi$  code was implemented in G0GEANT, the MAID2007 multipoles were used as the nominal values.

The definition of  $\Delta_{(3)}^\pi$ , given in Section 2.3.4 in Chapter 2, consists of the product of two functions:  $H_{EM}$ , which contains the electromagnetic form factors,  $C_i^\gamma$ , and  $G_{N\Delta}^A$  which contains the axial form factors,  $C_i^A$ . Both  $H_{EM}$  and  $G_{N\Delta}^A$  rely on a dipole parameterization of the form factors along with  $Q^2 = 0$  coefficients that are dependent on models of hadronic structure. Several values of these coefficients based on different fits to form

factor data are available. The coefficients used nominally in G0GEANT are those from Adler [8] [27] but other coefficients were also tested within the code to approximate the uncertainty due to the fit chosen and will be discussed in Chapter 6. The impact on the asymmetry of changing the coefficients was found to be  $< 1$  ppm. Additionally, the dipole parameterization introduces a new parameter, the dipole mass, into the computation of the form factors. The vector dipole mass,  $M_V$ , present in the electromagnetic form factors, is used in the elastic form factors and, as such, has been well determined from data. More uncertainty is associated with the axial mass,  $M_A$ , which appears in the parameterization of the axial form factors. In each case, the current world value for the dipole mass, given in Section 2.3.4, was used in the simulation.

A separate model based on the formalism used by Matsui *et al.* [39] was also implemented in the simulation. In this model, the basic form of the inelastic asymmetry, with the separation into three components, is the same as that given in Equation 5.1, while the parameterizations used to determine the vector and axial contributions,  $\Delta_{(2)}^\pi$  and  $\Delta_{(3)}^\pi$ , differ. Unlike the nominal model, for which the calculation of  $A_{inel}$  has been implemented explicitly in the code, these asymmetries were determined event-by-event within the simulation by performing a two dimensional interpolation in  $Q^2$  and  $W$  using a set of lookup tables computed by Matsui *et al.* for the  $G^0$  kinematics [75]. More detail on the determination of the theoretical asymmetry from simulation and its uncertainty will be given in Chapter 6.

## 5.2 Background Correction

The background correction was the most significant correction applied to the inelastic asymmetry. Since the experiment was designed to measure elastic events, the appara-

tus used was not optimized for inelastic scattering. As a result, the yield in the inelastic region of the matrix contained a high percentage of backgrounds. Since the quantity of interest in this measurement is the asymmetry, the impact of these backgrounds on the result depends on the asymmetry of the various backgrounds present. If the background asymmetries were very close in value to each other and to the true inelastic asymmetry, their impact would be negligible. Unfortunately, for this measurement, the processes that contribute to the total asymmetry in a given cell generally have individual asymmetries that vary significantly from each other and from the cell average. These background asymmetries act as a dilution on the average, resulting in a potentially significant difference between the measured and true inelastic asymmetry values.

In order to properly remove the backgrounds from the average, the size of each contribution must be determined individually and must be well understood. A procedure was developed for the determination of the background contributions that was unique to the inelastic measurement and made use of both background measurements and simulated yields. The contribution of a given background was treated as a percentage of the total yield, referred to as the dilution factor ( $f_i^{bg}$ ), and used to subtract the background asymmetry ( $A_{bg}$ ) from the cell average asymmetry ( $A_{meas}$ ) according to

$$A_{inel} = \frac{A_{meas} - \sum f_i^{bg} A_i^{bg}}{1 - \sum f_i^{bg}} . \quad (5.2)$$

For each contributing process, dilution factors were determined on a cell by cell basis for the entire coincidence matrix, allowing for the computation of the total background yield and a background corrected asymmetry for any region of the matrix. In addition to the results presented for the inelastic asymmetry, dilution factors were computed for the elastic locus and the correction was applied to the elastic asymmetry. Since the procedure used differs from the method used in the elastic analysis, the results presented here can

be used as an independent verification of the published results.

### 5.2.1 Contributing Processes

In any given CED·FPD cell, there may be up to five major processes contributing to the total yield and average asymmetry: electrons scattered elastically from the target liquid, electrons scattered inelastically from the target liquid, electrons scattered elastically or inelastically from the aluminum target windows,  $\pi^0$  decay and misidentified  $\pi^-$ . These can be grouped as electron scattering processes and pion-related processes. The yield from the three electron scattering processes comes from scattered electrons that either enter the detector system directly or interact with material in their path to produce electrons from secondary reactions that then enter the detector system. The methods through which the pion sources lead to electron events differ from the electron sources and from each other. While the  $\pi^-$  contamination is mostly the result of the pions themselves being counted as electrons, the  $\pi^0$  contribution to the background is due to electrons that are emitted through secondary processes as the pion decays. In most cases, the  $\pi^0$  decays into two photons, which can then interact with material in their path, such as shielding, leading to the emission of electron-positron pairs. In some instances, the  $\pi^0$  instead decays directly into a photon and an electron-positron pair. Because of the polarity of the magnet, the positrons will be steered into the collimators, but the electrons can enter the detector system and trigger an event. Since the electrons that result from  $\pi^0$  decay do not have the same asymmetry as those scattered from the target liquid, they must be accounted for as a background.

To determine the yield due to scattering from the target windows and from pion contamination, special measurements made during the experimental run could be used.

For the remaining processes, a fitting procedure that made use of simulated yields was used instead. Details on the methods used to determine the cell-by-cell yield contribution from each process will be presented in this section.

### **Empty Target Data**

The scattering rates from the aluminum target windows were determined using data taken with the  $G^0$  target filled with gaseous hydrogen ( $GH_2$ ). Note that these data also contain some rate from electrons that scattered from the helium in the cell located just upstream of the target cell. Because of the location of the helium cell, these events are not likely to make it past the collimators and into the detectors. As a result, the empty target yield is dominated by scattering from the aluminum windows.

Before the information obtained from the gaseous target could be applied to the nominal liquid hydrogen ( $LH_2$ ) or deuterium ( $LD_2$ ) scattering data, a series of steps had to be taken to account for the presence of the gas and any differences in the running conditions between the different data sets. The first of these steps was to isolate the aluminum yield by subtracting the gas contribution from the total yield. Next, a scaling was done to account for the difference in beam current during the  $GH_2$  runs as compared to the nominal current. The final step was to apply a correction to account for small differences in the energy lost by the incident electron in the target due to the difference in density between  $GH_2$ ,  $LH_2$  and  $LD_2$ .

For the gas subtraction, two methods were available. The first involves determining the density of the gas from the available target monitoring data and subtracting off the proper proportion of the yield. During the gas target running, the temperature of the gas was 19 K and the pressure was 2.29 atm. Using van der Waal's equation, the density was

determined to be  $1.82 \times 10^{-3} \text{ g/cm}^3$  while the density of the liquid hydrogen target was  $0.0723 \text{ g/cm}^3$  under nominal running conditions ( $P = 1.7 \text{ atm}$ ,  $T = 19 \text{ K}$ ). Based on these densities, the scaling factor  $\alpha_{ET}$  was determined to be 0.025 with a 50% uncertainty assigned. The scaling was applied to remove the gas using the following equation:

$$\begin{aligned} R_{empty} &= R_{LH_2} - \frac{R_{LH_2} - R_{GH_2}}{1 - \alpha_{ET}} \\ &= R_{LH_2} - 1.026(R_{LH_2} - R_{GH_2}), \end{aligned} \quad (5.3)$$

where  $R_{empty}$  is the total empty target yield for a given cell,  $R_{LH_2(GH_2)}$  is the cell yield for the liquid (gaseous) target and  $\alpha_{ET}$  is defined as above. Since this method is based entirely on measured quantities, the empty target yield determined using this method was used to compute the final dilutions. The second method for subtracting the gas was used as a consistency check. In this method, the simulation was run with the  $GH_2$  target for both elastic and inelastic scattering and the simulated yields were subtracted from the measured gas target yields. Comparing the resulting yields cell-by-cell to the yields from the first method, it was found that the two methods differed by less than 10% across the inelastic locus. The differences computed were added to the uncertainty on the empty target cell yields.

To account for the difference in beam current, the gas-subtracted data was scaled by a percentage determined from previous analysis of residual dead time [61]. Even though both the full and empty target yields have been corrected for dead time, the effect may not have been removed completely and some yield may still be missing. Since these effects are rate dependent, they will affect the full and empty target data sets differently. Thus, in order to truly compare the Al rates from the  $GH_2$  runs to the Al rates during a nominal  $LH_2$  run, this residual effect must be taken into account. This is done by assuming that the current used to determine the empty target yields is so low that the residual is negligible,

making this the true yield due to the target windows. In a nominal run at full current, a percentage of this true empty target yield will be lost. The correction is applied as a percentage reduction of the empty target yield according to the previously determined residuals found to be 4% for both targets [61].

Finally, in order to determine the size of the energy loss correction, scattering from the three target windows was simulated assuming  $LH_2$ ,  $LD_2$  and  $GH_2$  targets and the results compared to see the impact of target density on the empty target yield. Since most of the empty target yield comes from the entrance window, before the electrons have passed through the target gas/liquid, this effect was small ( $< 7\%$  in the loci). The correction was computed as

$$s_{CEloss} = \frac{Y_{liq}^{Al} - Y_{gas}^{Al}}{Y_{liq}^{Al}}, \quad (5.4)$$

where  $Y_{liq(gas)}^{Al}$  represents the total simulated yield from all three target windows for the liquid (gas) target. The scale factor,  $s_{CEloss}$ , was computed separately for hydrogen and deuterium and applied cell-by-cell as a percentage of the empty target yield. The cell values for  $s_{CEloss}$  within the inelastic locus ranged from about  $\pm(0.5 - 7)\%$  in the elastic and inelastic loci. Once this final scaling was complete, the  $GH_2$  yields could be treated as empty target yields and subtracted from the full target data.

### **Pion ( $\pi^-$ ) Contamination**

The presence of  $\pi^-$  events in the electron matrix is due to several factors, including electronics and detector effects that cause pions to be misidentified and physical effects that allow pions events to legitimately trigger the detectors. The effects related to electronics and instrumentation can be further separated into rate-dependent and rate-independent effects. The events due to rate-dependent effects were accounted for in the application

of the contamination correction discussed in Section 4.2.3, while those related to rate-independent instrumentation effects and to physics effects need to be subtracted out separately. Since the main source of  $\pi^-$  in the data is photoproduction from the neutron, the pion contamination was significant only in the deuterium run periods.

The primary physical effect is the creation of delta rays, secondary electrons resulting from a pion interacting with the CEDs, the Cherenkov shielding or the aerogel contained within the Cherenkov detector. If these electrons have enough energy, they can fire the Cherenkov detector, leading the electronics to record the event as an electron. Since these scattered electrons originated from a secondary reaction, they will carry the asymmetry of the primary particle (the  $\pi^-$ ), diluting the measured asymmetry. The contribution of the delta rays to the total yield was determined through simulation [43].

The remaining contribution is from those events triggered by rate-independent effects in the detectors and electronics, such as spontaneous emission of electrons in the Cherenkov PMTs or electronic noise. This portion of the  $\pi^-$  contamination was determined through analysis of data from the Analog Ring Sampler (ARS), a component of the electronics that measured the detector pulse height and converted the analog detector readout to a digital signal [76]. The ARS was associated with the FASTBUS electronics, which triggered periodically to record a sample of events digitally for monitoring purposes. When a FASTBUS event was triggered, the ARS began sampling the signals from the Cherenkov PMTs at a rate of 1/ns during a 128 ns time window. The 128 readings create a spectrum of pulse heights across the time window that can be used to determine the response of the Cherenkov. The ARS output essentially provides a digital oscilloscope image of the PMT signals in the time window. Using the ARS signal integrated across the time window to represent the ADC readout and the ARS arrival time to represent the trigger, the electron and pion spectra across all four Cherenkov PMTs for a particular

octant could be recreated in software.

The contamination was determined by fitting the integrated ARS signal using information on delta rays and photon energies determined through simulation. A detailed description of the fitting algorithm and determination of the elastic locus pion contamination is available elsewhere [43]. Although the analysis for the inelastic locus was performed separately from the elastic locus, the fitting routines and methodology were identical. Fits were performed on an octant-by-octant basis with the contamination determined as an average across all inelastic cells. The contamination determined for the inelastic locus is 11.07% while the elastic locus contamination is 4.66 %. The error on these contaminations is taken to be 30% of the contamination value and represents a conservative estimate of the reliability of the methodology used.

The fitting procedure was used to determine octant and locus average pion contaminations for the elastic and inelastic loci only. Since the background correction is applied on a cell-by-cell basis, it is necessary to know the contamination for every cell in the matrix. By using approximations, the elastic and inelastic contaminations were used to extrapolate the ARS results to the entire matrix. For the background and superelastic regions, the pion contamination was assumed to be negligible, but this assumption could not be made for the cells on either side of the elastic locus that are not contained in any locus. Generally, these cells exhibit behavior consistent with the elastic locus but were not included in the locus because they had higher background rates than the locus cells. For these non-locus cells, an average of the contamination in the cells on either side was used. These assumptions are based, in part, on the pion yield distribution which shows that most of the events in the pion matrix appear in the inelastic locus cells. The values used for the pion contamination along with their errors can be seen in Figure 5.1.

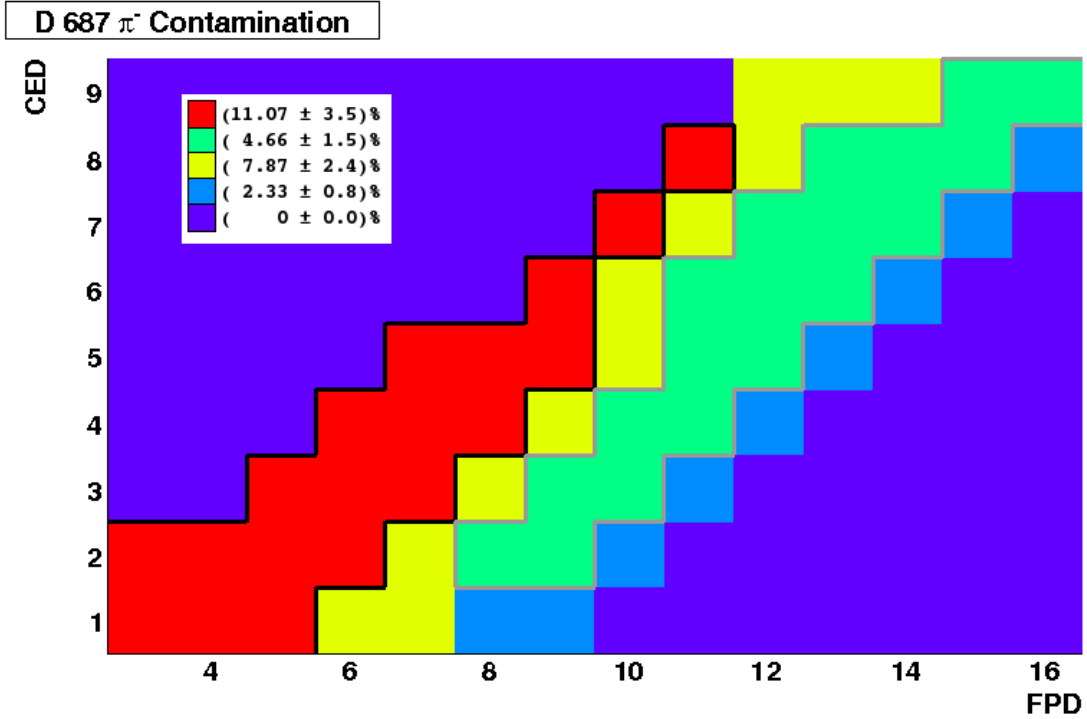


FIG. 5.1: Pion contamination values for each cell in the matrix. Each color represents a value as indicated in the legend. Cells in the inelastic (elastic) locus have been outlined in black (gray). The contaminations for cells outside the elastic and inelastic loci are estimated. The contamination is given in percent of total cell yield.

### Simulated Yields

The yield in a given cell due to elastic or inelastic scattering from the target liquid or from  $\pi^0$  decay was approximated using the G0GEANT simulation. Simulations were run separately for hydrogen and deuterium using the elastic and inelastic generators described in Section 5.1. For  $\pi^0$  decay, the simulation was run only for hydrogen and this output was scaled to give the deuterium yields. The scale factor used,  $Y_D = 1.85Y_H$ , was determined from data taken with the polarity of the magnet reversed. When the magnetic field is reversed, it causes the electrons scattered from hydrogen to be steered into the collimators present in the magnet while any positrons present make it to the detectors. Since  $\pi^0$  decay

is the dominant source of positrons in the system, these data contain information about  $\pi^0$  decay yields. Because of the possible contribution from  $\pi^+$  contamination in this data set, the reverse polarity data cannot be used directly to determine  $\pi^0$  decay yields in the elastic and inelastic loci. However, the region of high CED and low FPD, referred to as the *background* locus, is dominated by electrons from  $\pi^0$  decay and outside the area where  $\pi^\pm$  contamination is significant. The deuterium scale factor was determined by summing the yield across the background locus separately for the hydrogen and deuterium reversed polarity data and then taking the ratio.

Once the simulated yields were known, the efficiency of the Cherenkov detectors had to be taken into account. Since the Cherenkov detectors were used for particle identification, events were not counted toward the electron yield if the Cherenkov failed to fire. The Cherenkov efficiency corresponds to the percentage of the true electron yield that was recorded in the data. Several studies were done of the Cherenkov efficiencies using data obtained during the experimental run. In most of those cases, the efficiencies were determined as a locus average for the elastic and inelastic loci rather than on a cell-by-cell basis. In order to compute the efficiencies for each cell, simulation was used to model the behavior of the Cherenkov detectors using the length of the electron's path and its distance from the PMTs as it traveled through the aerogel. This information, which was available from G0GEANT, was used in conjunction with data, where possible, to compute efficiencies for every cell within the matrix. The results from the fit were compared to results obtained from data and were found to be consistent [65]. This detector efficiency is not taken into account within G0GEANT, so all simulated yields must be scaled accordingly before they can be compared to data. In the inelastic locus, the average Cherenkov efficiency was found to be roughly 75%. The efficiency was higher in the elastic locus,  $\sim$  85%, as the design was optimized for this region.

While the simulation was trusted to reproduce the shapes of the various distributions, model dependence in the cross sections and Cherenkov efficiencies led to uncertainty in the normalization. As such, a fit to the data that allowed the individual simulated yields to vary by an overall scale factor was applied. The scaled simulated yields were then used to determine the dilution rather than using values directly from the simulation. The fitting procedure is described in the next section.

## 5.2.2 Determining the Dilution Factors

Before dilution factors could be computed, a fit was needed to determine the proper normalizations for the simulated processes. Since the empty target and  $\pi^-$  contributions were determined from data, it was assumed that these yields did not require any scaling. Consequently, the  $\pi^-$  and empty target yields were subtracted, in that order, from the measured yield prior to performing the fit. The remaining reduced yields were then plotted as a function of FPD for each CED, with all octants included sequentially. The fit consisted of a point by point scaling of the simulated yields rather than a fit to a function. In the fit, the yields from each of the three simulated processes (elastics, inelastics and  $\pi^0$  decay) were allowed to vary independently and could be scaled up or down as needed. The fit function is defined as

$$Y_{fit}(c, f) = \begin{cases} P_{el}(c)Y_{el}^{sim}(c, f) + P_{inel}(c)Y_{inel}^{sim}(c, f) + P_{\pi^0}(c)Y_{\pi^0}^{sim}(c, f) & \text{CED 1 - 6} \\ P_{el}(c)Y_{el}^{sim}(c, f) + P_{\pi^0}(c)Y_{\pi^0}^{sim}(c, f) & \text{CED 7 - 9} \end{cases}, \quad (5.5)$$

where  $Y_i^{sim}(c, f)$  is the unscaled simulated yield as a function of CED and FPD and  $P_i(c)$  is the scale factor as a function of CED for the three simulated processes (elastic (el), inelastic (inel), and  $\pi^0$ ). Since the inelastic simulation shows very little yield ( $< 0.1$

Hz/ $\mu$ A) for any FPD in the higher numbered CEDs, the inelastic contribution is removed from the fit for CEDs 7-9. The scale factors are constant across all FPDs and all octants for a given CED. The only additional constraint placed on the fit was that the scale factors remain positive.

The full fit for two typical CEDs for each target can be seen in Figures 5.2 through 5.5. Also included are close up views of selected individual octants for the same CEDs. The results highlighted here are typical of the results for all CEDs and all octants. In all figures the green points are the total data yields and the black curve is the total fit,  $Y_{fit}(c, f)$ , with the contributions from the empty target and the pion contamination added in. The individual contributions from the scaled simulations, empty target data and pion contamination are also shown. The total fitted yield and individual contributions are drawn as curves rather than individual points to make the picture clearer. The shape of the lines comes only from connecting the individual points together and has no other significance.

The scale factors determined for each process are shown as a function of CED in Figures 5.6 (hydrogen) and 5.7 (deuterium). Generally, the scale factors varied smoothly across the CEDs but in some cases, especially for the  $\pi^0$  decay, the behavior was not as consistent. To account for this behavior, a fit of scale factor as a function of CED was performed. Each scale factor plot was fit independently to a polynomial consistent with the general shape of the observed dependence on CED number. For both targets, the elastic scale factors were fit to a quadratic function and the  $\pi^0$  decay to a cubic. The inelastic scale factors were fit to a linear function for the hydrogen and a quadratic for the deuterium. The value computed from these fit functions for a given CED was used as the scale factor when determining the dilution factors rather than using the results of the individual fits to Equation 5.5 directly.

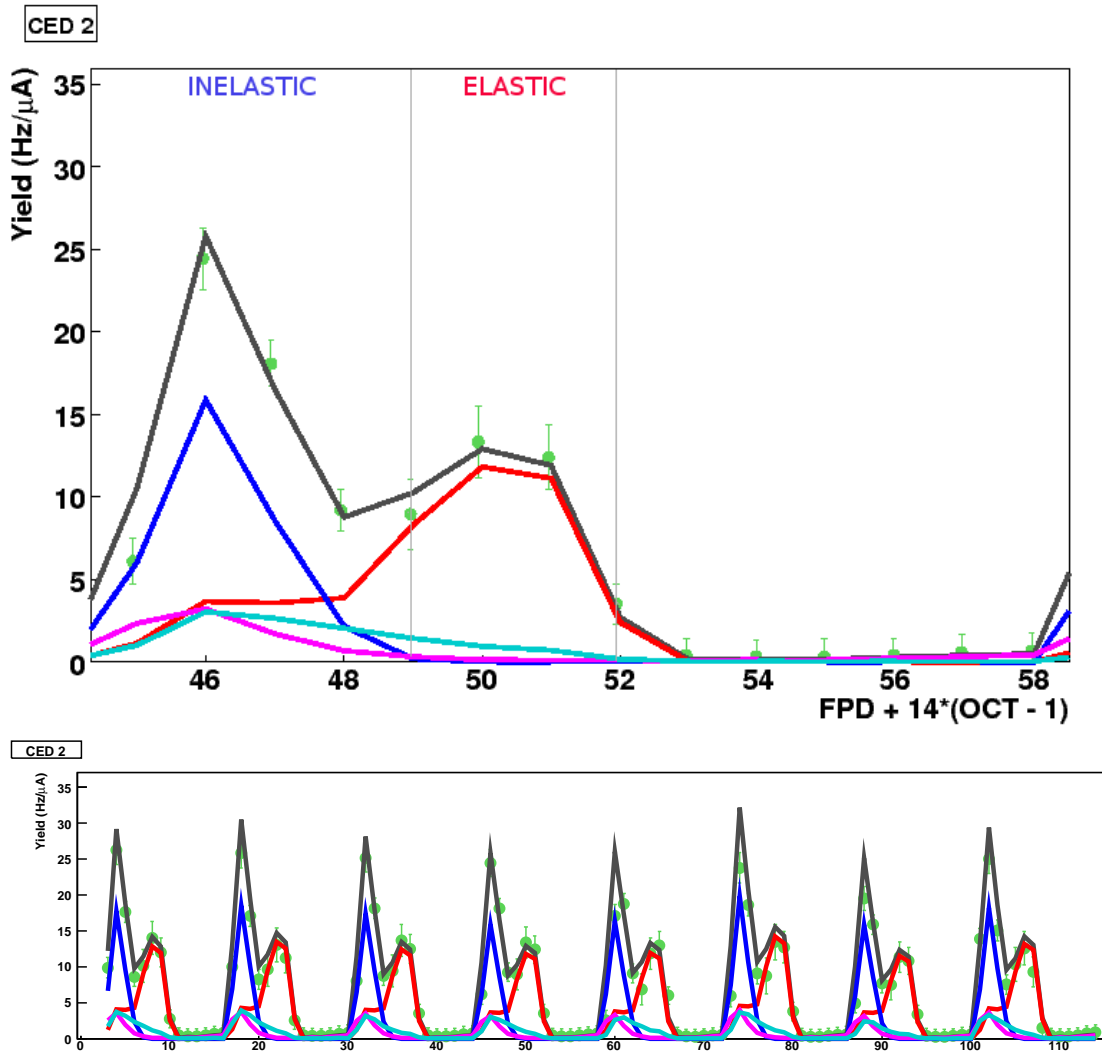


FIG. 5.2: Fit result for the hydrogen CED 2 yields as a function of FPD. The top plot shows the result for a typical octant (octant 4), while the bottom plot shows the full fit for all octants. The green points represent the data and the black curve represents the sum of all the processes, including both the fit yields and those from data. The scaled inelastic simulation is in blue, elastic in red and  $\pi^0$  decay in pink. The empty target data is shown in light blue. The curves here do not represent a fit but are just lines connecting the individual FPD points. The vertical lines are included to denote cells in the inelastic or elastic locus as indicated by the labels. The points that intersect the vertical lines are non-locus cells.

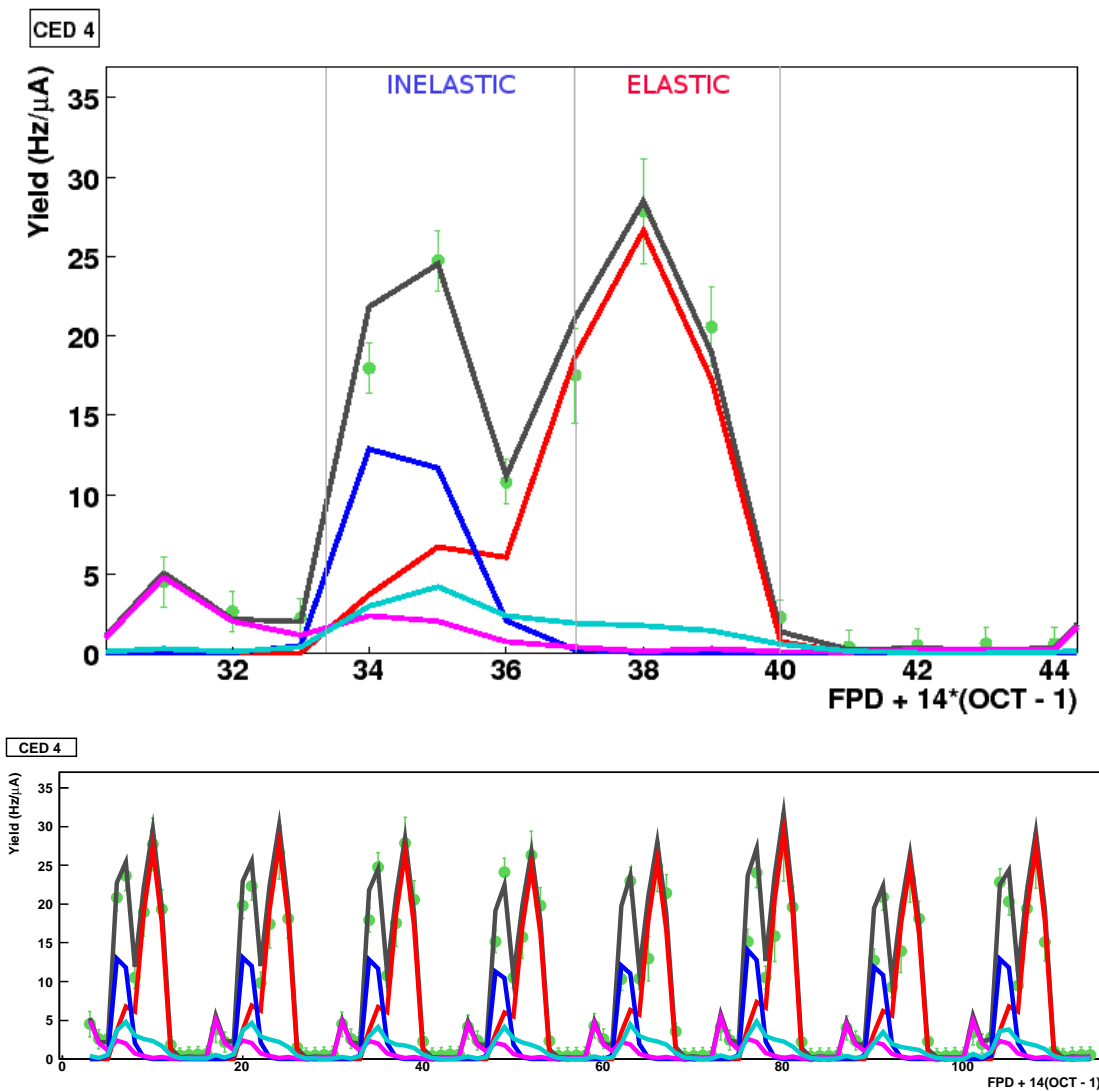


FIG. 5.3: Fit result for the hydrogen CED 4 yields as a function of FPD. The top plot shows the result for a typical octant (octant 3), while the bottom plot shows the full fit for all octants. The green points represent the data and the black curve represents the sum of all the processes, including both the fit yields and those from data. The scaled inelastic simulation is in blue, elastic in red and  $\pi^0$  decay in pink. The empty target data is shown in light blue. The curves here do not represent a fit but are just lines connecting the individual FPD points. The vertical lines are included to denote cells in the inelastic or elastic locus as indicated by the labels. The points that intersect the vertical lines are non-locus cells.

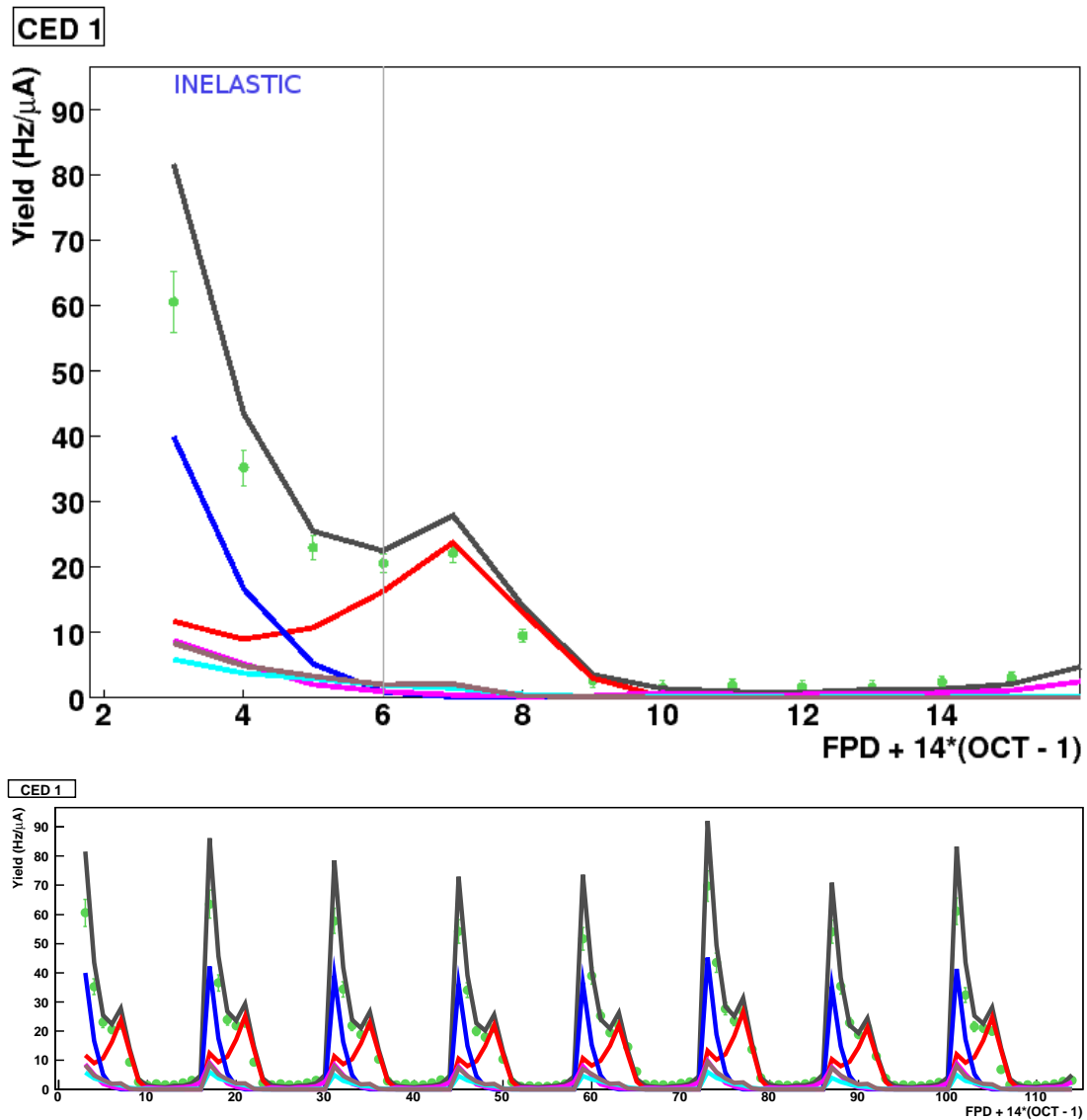


FIG. 5.4: Fit result for the deuterium CED 1 yields as a function of FPD. The top plot shows the result for a typical octant (octant 1), while the bottom plot shows the full fit for all octants. The green points represent the data and the black curve represents the sum of all the processes, including both the fit yields and those from data. The scaled inelastic simulation is in blue, elastic in red and  $\pi^0$  decay in pink. The empty target data is shown in light blue and the  $\pi^-$  contribution is in brown. The curves here do not represent a fit but are just lines connecting the individual FPD points. The vertical line is included to denote cells in the inelastic locus as indicated by the label. The point that intersects the vertical line is a non-locus cell.

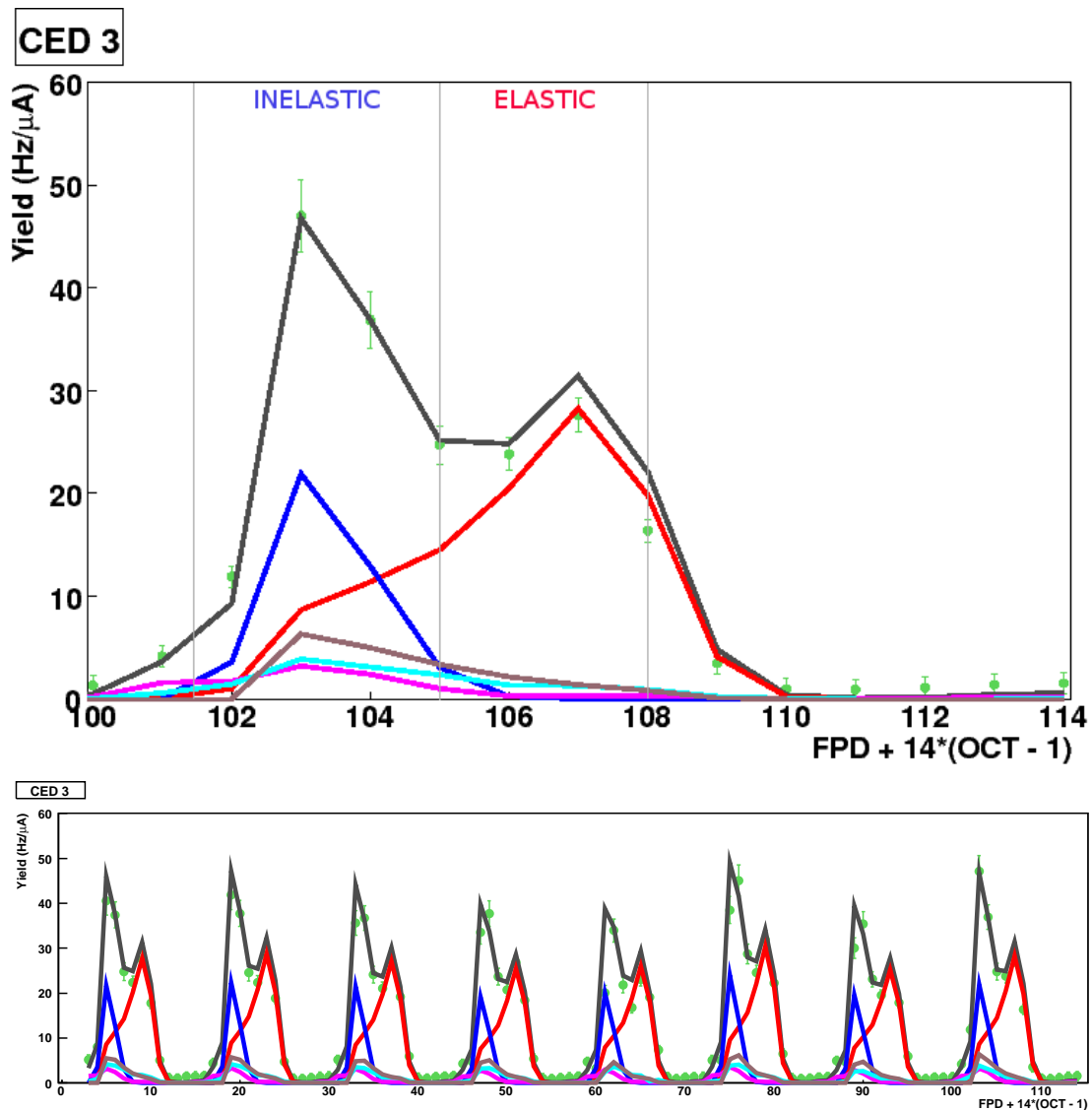


FIG. 5.5: Fit result for the deuterium CED 4 yields as a function of FPD. The top plot shows the result for a typical octant (octant 8), while the bottom plot shows the full fit for all octants. The green points represent the data and the black curve represents the sum of all the processes, including both the fit yields and those from data. The scaled inelastic simulation is in blue, elastic in red and  $\pi^0$  decay in pink. The empty target data is shown in light blue and the  $\pi^-$  contribution is in brown. The curves here do not represent a fit but are just lines connecting the individual FPD points. The vertical lines are included to denote cells in the inelastic or elastic locus as indicated by the labels. The points that intersect the vertical lines are non-locus cells.

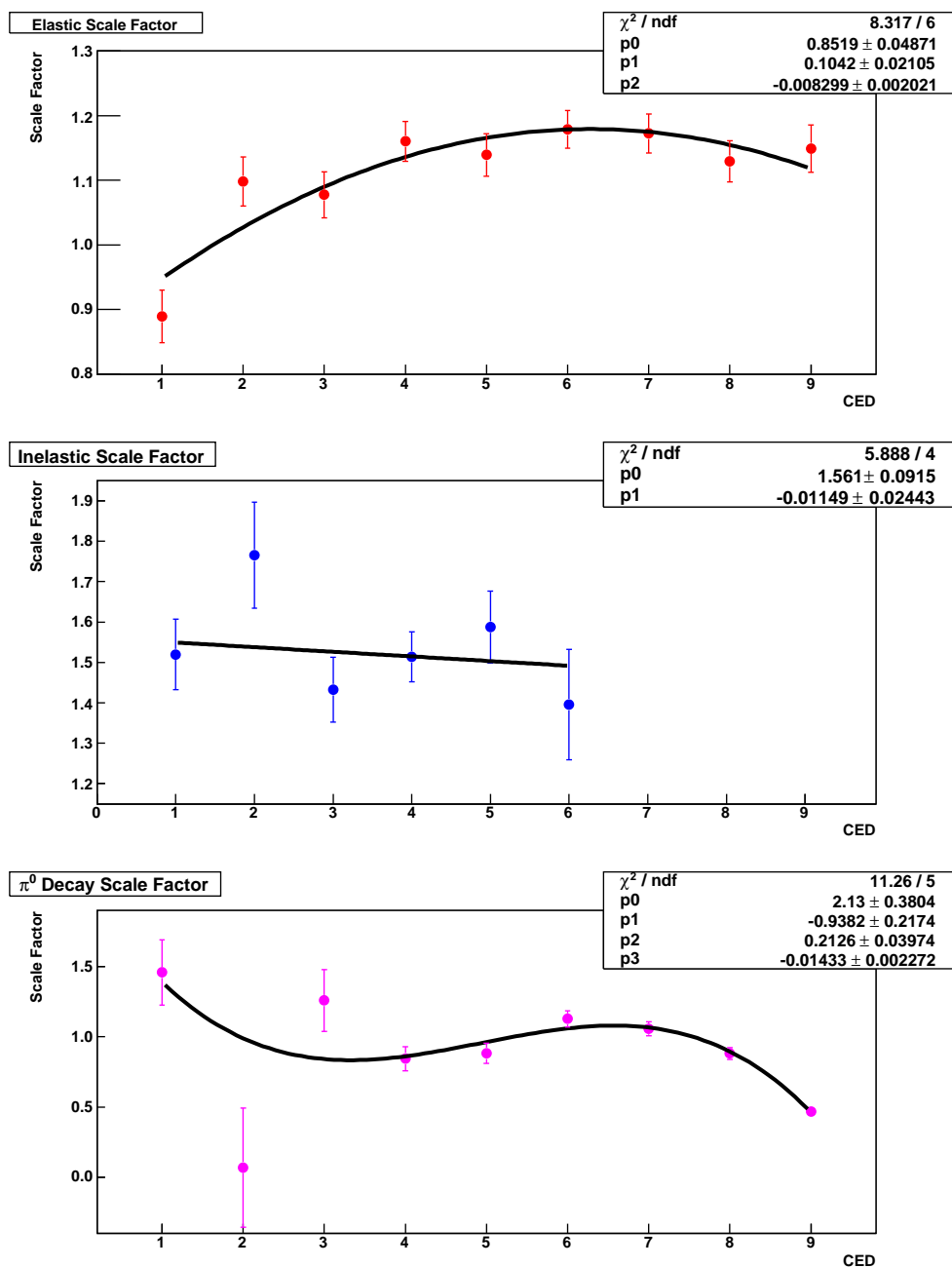


FIG. 5.6: Scale factor as a function of CED for the hydrogen elastic (top), inelastic (middle) and  $\pi^0$  decay (bottom) simulations. In each case, a polynomial fit appropriate to the shape of the distribution has been applied. Note that the inelastic plot only includes CEDs 1-6 since the inelastic simulation is not included in the fit for the remaining three CEDs.

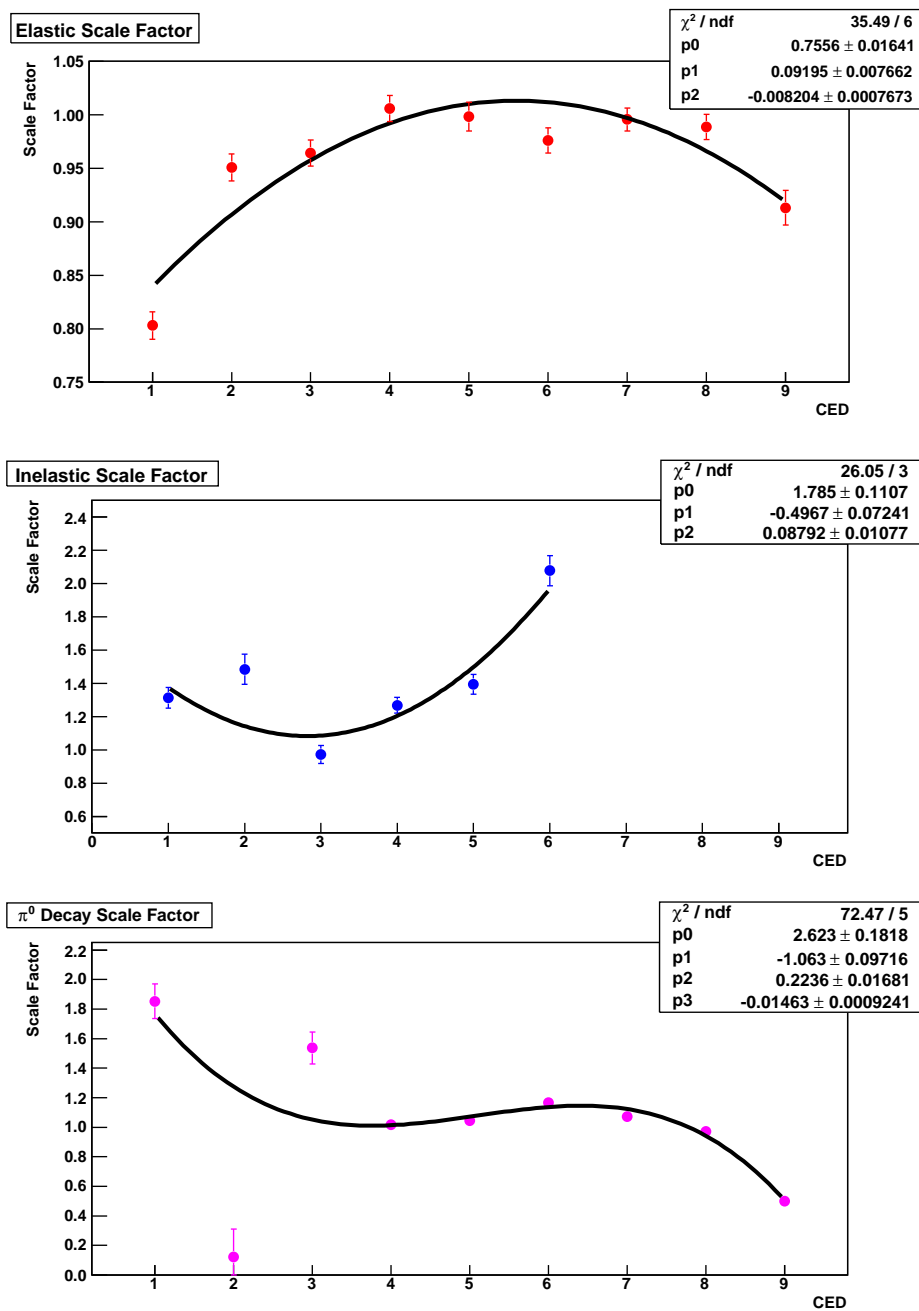


FIG. 5.7: Scale factor as a function of CED for the deuterium elastic (top), inelastic (middle) and  $\pi^0$  decay (bottom) simulations. In each case, a polynomial fit appropriate to the shape of the distribution has been applied. Note that the inelastic plot only includes CEDs 1-6 since the inelastic simulation is not included in the fit for the remaining three CEDs.

Once both the reduced data and scale factor fits were performed, the dilution factors could be computed. For the measured processes (empty target and  $\pi^-$ ), the dilution factor is simply the ratio of measured yield for the process to total yield for a given coincidence cell,

$$f_i^{meas} = \frac{Y_i^{meas}(c, f)}{Y_{tot}^{dat}(c, f)}. \quad (5.6)$$

The dilution factors for the simulated processes were computed by scaling the simulated yield by the fitted scale factor and dividing by the total fit yield. The ratio of reduced yield to total yield,  $R_{red}$ , is then needed to properly normalize the fitted yield to the total yield,

$$f_i^{sim} = R_{red} \frac{P_i(c)Y_i^{sim}(c, f)}{Y_{tot}^{fit}(c, f)}. \quad (5.7)$$

Dilution factors were computed on a cell-by-cell, octant-by-octant basis for all processes.

### 5.2.3 Determining the Dilution Factor Uncertainty

The uncertainty associated with the dilution factors was computed individually for each process using a variety of methods. For the simulated yields, the sources of error include the cross section models and fitting routines used. The sources of error for the measured yields include statistical precision and the methods used to determine the yields.

The simulation model uncertainties were determined using different methods for each of the simulated processes. For the elastic electrons, the model error is defined as 5% of the dilution. This error was chosen to approximate the uncertainty due to the behavior of the radiative tail. For the inelastic simulation, dilution factors were computed using the different cross section models described in Section 5.1.1 to determine the simulated yields and the model error was defined as the difference in the resulting dilution factors. For the hydrogen data, the comparison was made between the nominal dilution factors

computed using the Bosted/Christy model and those computed using Keppel model. In the case of the deuterium, two models were available for comparison. Since the deuterium cross section is determined by scaling the proton cross section, both the Keppel and Bosted/Christy proton models could be compared to the nominal values computed using the Bosted/Christy proton model that includes a correction for Fermi motion. The error was then defined as the maximum separation between the three sets of dilutions.

The  $\pi^0$  decay simulation model error was determined by comparison of the simulated yields to the reversed polarity data. Although, as explained in Section 5.2.1, these data cannot be used directly to obtain information about electron yields, they can be used to determine uncertainty by looking at the  $\pi^0$  decay-dominated background locus. The total yield in this locus was summed in both the reverse polarity data and the  $\pi^0$  decay simulation and compared. Since the data had a 25% higher yield across the background locus, this was set as the simulation error. Another possible source of model error was the use of scaled hydrogen as the deuterium yield rather than a direct deuterium model. To test how important this scaling was to the final dilution factors, the deuterium fit was performed using the unscaled hydrogen target yields. Although the  $\pi^0$  scale factors themselves were significantly higher, the resulting dilution factors were nearly identical. This indicated that the fit was blind to the scale factor used on the deuterium  $\pi^0$  decay yields. As such, no additional uncertainty was needed to account for this scaling.

The elastic, inelastic and  $\pi^0$  decay dilution factors also have errors associated with both the primary fit and the scale factor fit. The error due to the main fit is determined during the fitting routine by MINUIT [77]. The error on these scale factors gives an indication of the uncertainty of the fit which is in part dependent on the error associated with the data. The error on the data was computed as the sum of the statistical error from the data and the simulations, the Cherenkov efficiency error and a 5% error to account

for observed run-to-run variations in the yield during a given run period. To determine the error due to the scale factor fit, dilutions were computed using both the fitted and unfitted scale factors. The error was then defined as the difference in these dilutions. For the elastic scale factor error, dilutions were also computed using a constant scale factor fit and compared to the dilutions computed with the unfit and quadratic fit dilutions. This additional comparison for the elastics was made because the elastic scale factors were nearly constant for higher-numbered CEDs.

The error on the  $\pi^-$  contribution to the deuterium yield is defined as 30% of the contamination value. This value is based on the accuracy of the fitting and signal reconstruction methods in the ARS analysis described in Section 5.2.1 and is used for both the computed and interpolated contamination values. For the empty target data, several factors were taken into account. The most significant error is the 5% run-to-run yield variation. The statistical error from the measurement is also included but is negligible. The remaining errors are associated with the gas subtraction and scalings. There is an error of 1% of the yield to account for the difference in beam current between the empty and full target data and the dead time scaling, an error of 1.3% on the density calculation and a cell-by-cell error ( $< 10\%$ ) on the gas subtraction method as described in Section 5.2.1.

Many of the errors described in this section are correlated either across the locus or across the CEDs, and most of the correlated errors are also correlated across the octants. When considering results on a cell-by-cell basis this is not an issue, but any correlated errors must be separated out when computing locus and octant averages to avoid double-counting. Table 5.1 contains a summary of the dilution factor errors on each process and specifies any correlations.

Summary of Dilution Factor Errors			
	Value	Correlated?	Correlation
Inelastic			
Model Dependence	Varies	N	
Scale Factor Fit	Varies	N	
Fit Error	Varies	Y	CED, Octant
Elastic			
Model Dependence	5.0%	N	
Scale Factor Fit	Varies	N	
Fit Error	Varies	Y	CED, Octant
Pion			
Model Dependence	25%	Y	Locus, Octant
Scale Factor Fit	Varies	N	
Fit Error	Varies	Y	CED, Octant
Pion Contamination	30%	Y	Locus, Octant
Empty Target (Al)			
Run Variation	5.0%	Y	Locus, Octant
Current Difference	1.0%	Y	Locus, Octant
Density Calculation	1.3%	Y	Locus, Octant
Gas Subtraction	Varies	N	
Statistics	Varies	N	

TABLE 5.1: Summary of errors on the dilution factors for each process.

### 5.2.4 Summary of Dilution Factors

When applying the background correction, the dilution factors for each process are treated individually for each cell. However, for the purposes of studying the total background, it is useful to sum over the backgrounds and locus cells. The total background in the inelastic and elastic loci for each octant is listed for both targets in Table 5.2. The locus dilution is computed by summing the total yield from all background processes across the locus and dividing by the total locus yield. The errors quoted include all sources of error, with the correlated and uncorrelated errors added at the appropriate times. For both loci, the backgrounds include the target windows and  $\pi^0$  decay and, in the case of deuterium,  $\pi^-$  contamination. Additionally, the inelastic locus background contains the elastic contribution within the locus while the elastic locus contains the inelastic contribution.

The total background in each cell within the inelastic locus is presented as a percentage of total cell yield in Figures 5.8 (hydrogen) and 5.9 (deuterium). This background dilution has been computed and plotted separately for each octant to show that the octant variation is minimal. For the purposes of plotting, the cells have been grouped by CED and ordered such that the lowest CED and FPD are listed first. It is important to note this ordering scheme when studying the cell-to-cell variations. Locus average dilutions for each individual process are shown as a function of octant in Figure 5.10 for hydrogen and Figure 5.11 for deuterium. Note that while the values on the vertical axis differ in each case, the range is always 10%. This allows for a comparison of the sizes of the relative errors of the different pieces of the total background, showing that for both targets the  $\pi^0$  decay dilution has significantly higher errors than the other processes shown. For deuterium, the  $\pi^-$  contribution is a consistent  $0.110 \pm 0.035$  across the locus for all octants, so it was not included in the figure. More detail about the dilution factors for individual

processes and cells is given in Appendix C.

In the case of hydrogen, the single biggest contribution to the background for the inelastic locus comes from the elastic electrons, which contribute an average 25% across the locus. The target windows also contribute significantly, at about 16%, with inelastic scattering from aluminum the dominant effect. Finally, electrons from  $\pi^0$  decay contribute about 11%, leading to a total background of just over 50%. For the deuterium target, the total background is much higher, in part due to the pion contamination, with a total background of roughly 65%. Here, as with the hydrogen, it is the elastic electrons that contribute the most, at just over 30%. The  $\pi^0$  decay dilution factor is about 14% and  $\pi^-$  contribution is set to the constant 11% that was determined through the ARS analysis. The aluminum here contributes the least, at less than 10%.

The ratio of elastic to inelastic contributions within the inelastic locus differs between the two targets, with the elastics contributing in a larger proportion in deuterium than in hydrogen. This is due to the Fermi motion within the deuterium nucleus which results in a broadening of the elastic peak. This widening of the elastic distribution leads to more elastic events making their way into inelastic cells. Meanwhile, the aluminum contribution is reduced going from hydrogen to deuterium. As was noted previously in Section 5.2.1, the majority of the yield from the aluminum windows comes from the entrance window (i.e. electrons that have not passed through the target liquid). As such, when going from the hydrogen to the deuterium target, the absolute aluminum rate remains nearly constant. The total yield, however, is about twice as high for the deuterium as it is for the hydrogen. This doubling of the total yield while the aluminum yield remains constant leads to a reduction by half of the dilution factor.

Dilution factors were also computed for the elastic locus, where the backgrounds are much smaller and fewer processes contribute in a significant manner. For the hydrogen

data, the total background in the elastic locus is just over 10% with the aluminum contributing about 8% and  $\pi^0$  decay around 2%. In deuterium, the background is slightly higher at 14% due, as with the inelastics, to the presence of the  $\pi^-$ . Aluminum again is the largest contribution, at about 6%, while the  $\pi^0$  decay contributes just over 3% and the  $\pi^-$  contributes about 5%. The inelastic contribution in the elastic locus for both targets is negligible.

Summary of Total Dilutions (%)				
	H 687MeV		D 687MeV	
Octant	$f_{bg}^{inel}$	$f_{bg}^{el}$	$f_{bg}^{inel}$	$f_{bg}^{el}$
1	$51.2 \pm 4.5$	$11.1 \pm 1.4$	$64.1 \pm 5.6$	$14.8 \pm 1.8$
2	$52.9 \pm 4.2$	$11.0 \pm 1.3$	$64.5 \pm 5.3$	$14.3 \pm 1.8$
3	$51.8 \pm 4.2$	$9.1 \pm 1.4$	$64.5 \pm 5.3$	$13.2 \pm 1.7$
4	$52.2 \pm 4.2$	$9.8 \pm 1.3$	$64.9 \pm 5.3$	$13.6 \pm 1.7$
5	$54.8 \pm 4.0$	$11.5 \pm 1.4$	$66.4 \pm 5.3$	$14.6 \pm 1.8$
6	$53.6 \pm 4.1$	$10.8 \pm 1.3$	$64.9 \pm 5.3$	$13.5 \pm 1.7$
7	$52.2 \pm 4.2$	$8.8 \pm 1.4$	$64.4 \pm 5.4$	$12.5 \pm 1.7$
8	$51.6 \pm 4.3$	$10.0 \pm 1.4$	$63.3 \pm 5.5$	$13.6 \pm 1.8$
Avg	$52.5 \pm 3.9$	$10.2 \pm 1.3$	$64.9 \pm 5.0$	$13.7 \pm 1.7$

TABLE 5.2: Per octant total background dilutions for the elastic and inelastic loci. For the elastic locus, the total background includes the inelastic, pion and aluminum contributions. For the inelastic locus, the total background includes the elastic, pion and aluminum contributions.

### Comparison to Other Methods

In addition to the method described here (the inelastic method), dilutions were computed independently using two alternate methods. The first, the “field scan method” [72], involves applying a cell-by-cell fit to yield as a function of SMS current using data that

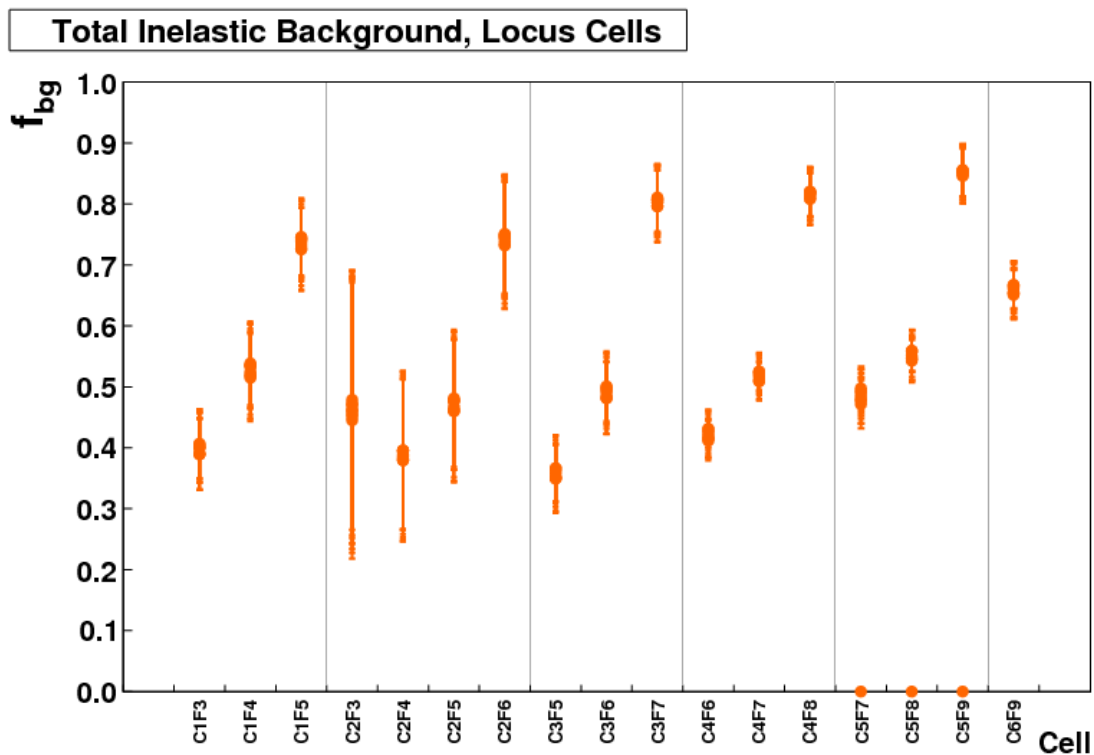


FIG. 5.8: Cell dilutions for the total inelastic background (elastic + pion + empty target) for all octants for hydrogen. The labels on the  $x$ -axis refer to the CED(C) and FPD(F) number that defines each cell and the vertical lines separate the cells by CED. The error bars shown include all correlated and uncorrelated errors. Note that the three points at 0 in CED 5 are due to the bad PMTs in octant 1. These have not been included in any averaging.

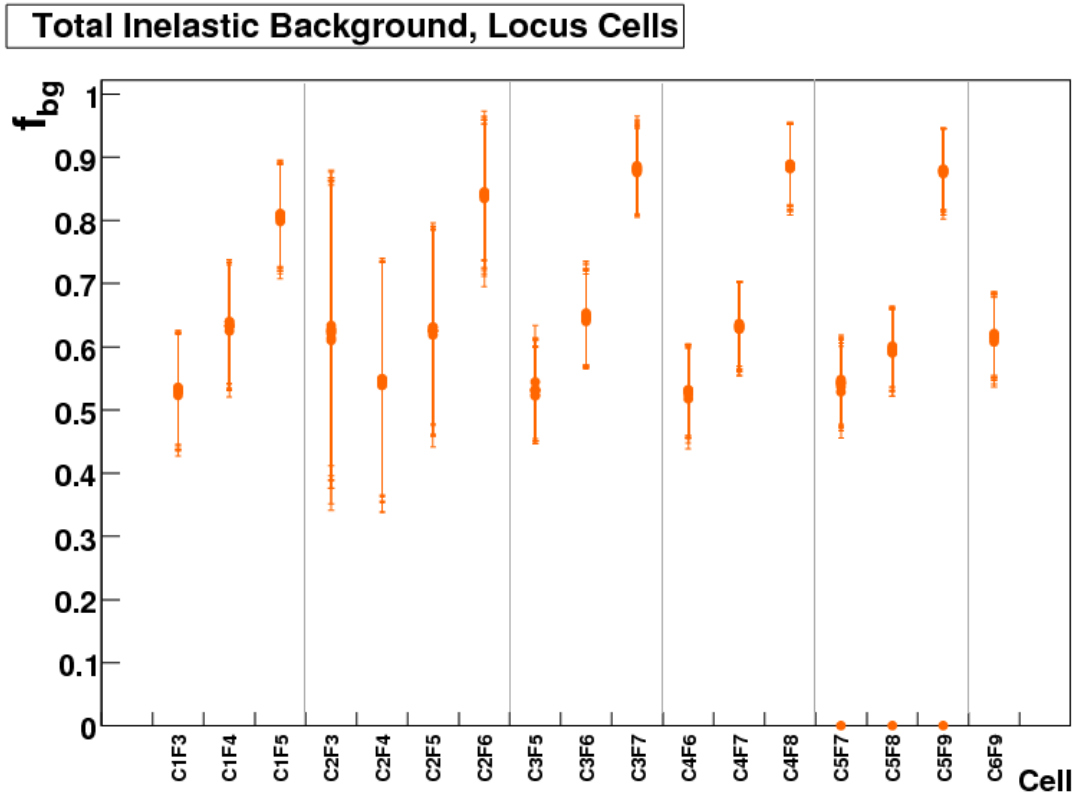


FIG. 5.9: Cell dilutions for the total inelastic background (elastic + pion + empty target) for all octants for deuterium. The labels on the  $x$ -axis refer to the CED(C) and FPD(F) number that defines each cell and the vertical lines separate the cells by CED. The error bars shown include all correlated and uncorrelated errors. Note that the three points at 0 in CED 5 are due to the bad PMTs in octant 1. These have not been included in any averaging.

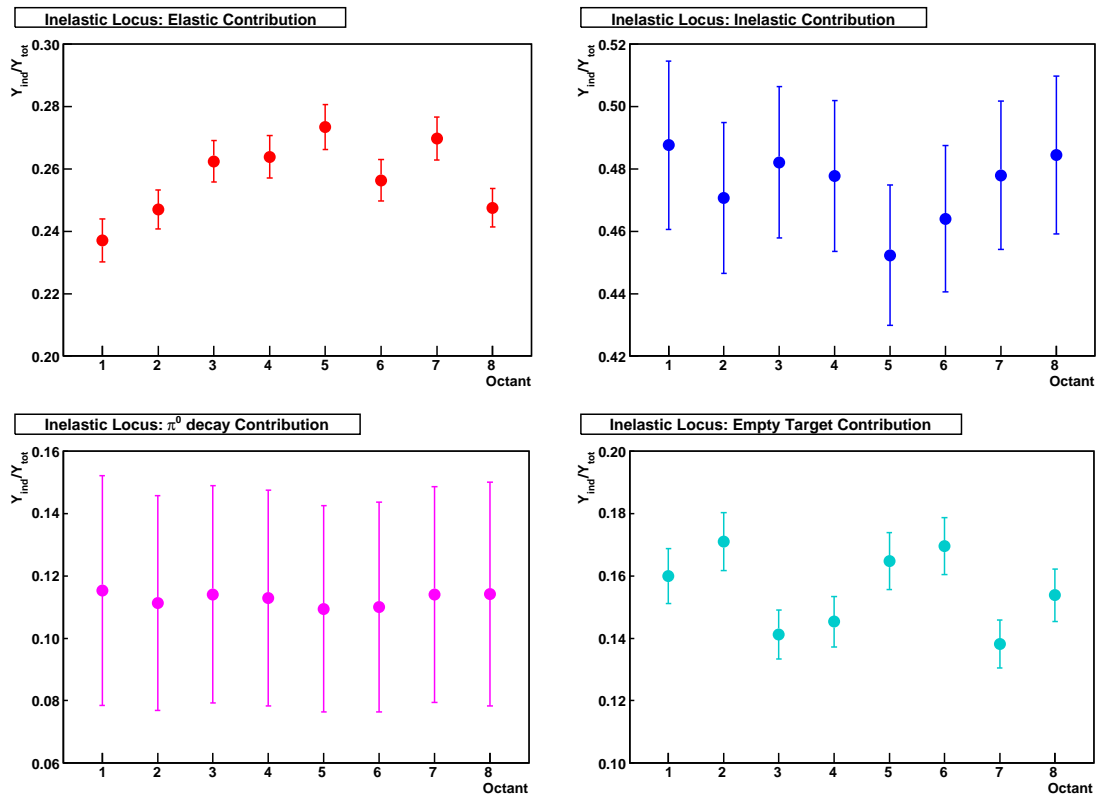


FIG. 5.10: Inelastic locus sum dilutions for each individual process as a function of octant for the hydrogen target.

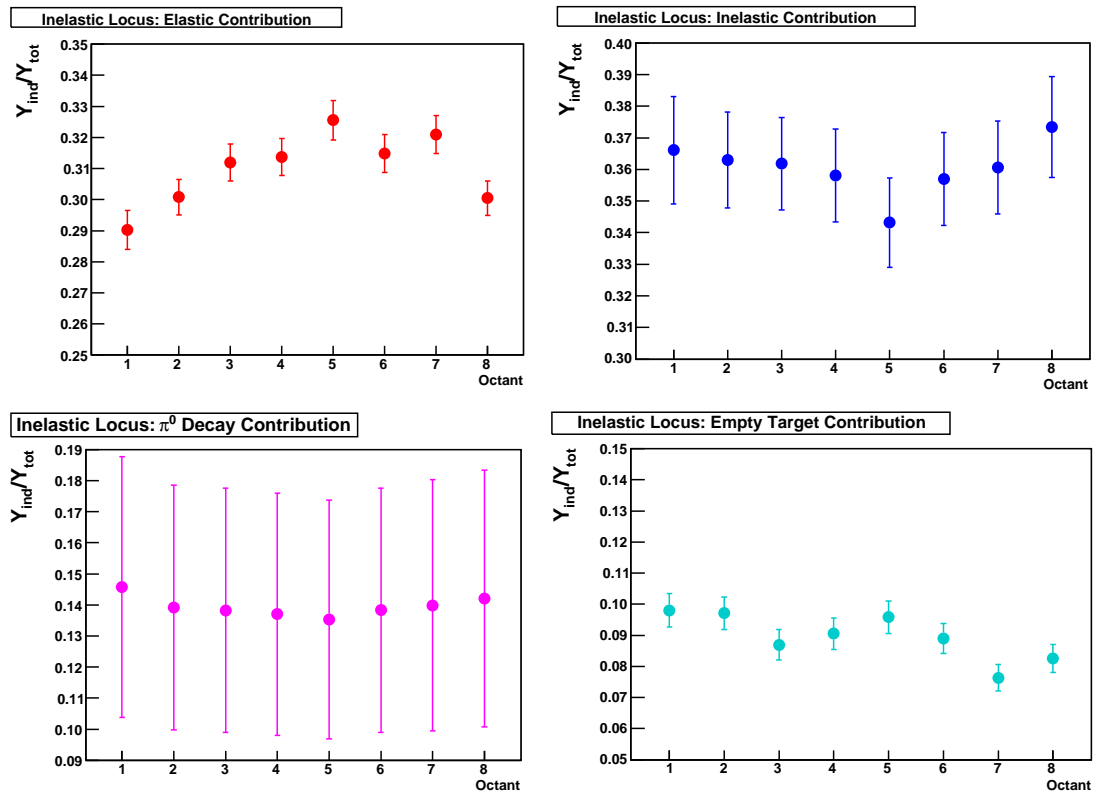


FIG. 5.11: Inelastic locus sum dilutions for each individual process as a function of octant for the deuterium target.

was obtained at several magnet currents during the experimental run. This is the method that was used to perform the correction applied to yield the published elastic asymmetry [20]. The second method, the “matrix fit method” [65], is similar to the fit performed here in that the yields were fit as a function of FPD across the matrix but the functional forms and fitting routine used were different. Dilutions for both hydrogen and deuterium were determined using the field scan and inelastic methods, while the matrix fit method was only performed for the hydrogen data.

The hydrogen elastic locus dilutions for all three methods are shown in Figure 5.12. The matrix fit and inelastic method dilutions are plotted for each octant while only the octant average is shown for the field scan method. The solid line represents the average field scan method dilution while the dashed lines represent its error. The total background results from the inelastic and matrix fit methods each agree within errors with the field scan method, but do not agree with each other in all octants. A comparison of deuterium dilutions is shown in Figure 5.13, with the inelastic method again shown for each octant and the field scan method octant average shown as a single line. Cell-by-cell comparisons of the different methods for the elastic locus, along with comparisons between the methods for the inelastic locus are discussed in Appendix C.

### 5.2.5 Applying the Correction to the Asymmetry

The background correction is defined as

$$A_{inel} = \frac{A_{meas} - \sum f_i^{bg} A_i^{bg}}{1 - \sum f_i^{bg}}, \quad (5.8)$$

where  $A_{meas}$  is the beam and instrumentation corrected asymmetry determined in Chapter 4 and  $f_i^{bg}$  is the dilution factor for the  $i^{th}$  background process. For hydrogen, the backgrounds are elastic,  $\pi^0$ , and aluminum. For deuterium, the backgrounds are elastic,

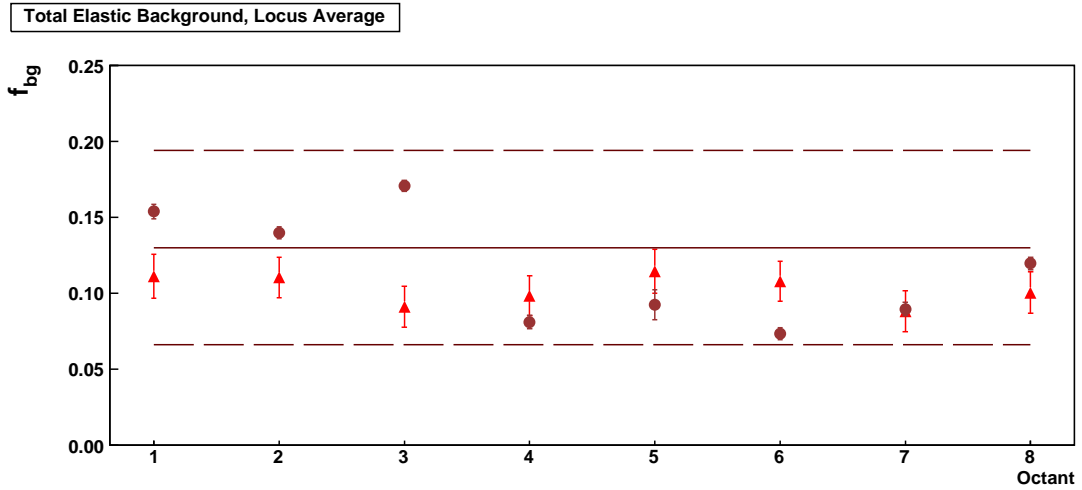


FIG. 5.12: Comparison of inelastic method, field scan method and matrix fit method elastic locus dilutions for hydrogen. The octant average dilution from the field scan method is shown as a solid line, while the error range is shown as dashed lines. The inelastic method (triangles) and matrix fit method (circles) are shown as points. The dilution here is the total background (inelastic, Al and  $\pi^0$  decay) in the locus.

$\pi^0$ , and  $\pi^-$ . In the case of deuterium the aluminum contribution is not subtracted out because it is taken to have the same asymmetry as the inelastics. More will be said about this asymmetry below. The correction is applied cell by cell according to Equation 5.8 within each octant and then the locus average for the octant is determined by taking the weighted average of the cell asymmetries. The final corrected asymmetry,  $A_{inel}$ , is the weighted average of the octant asymmetries.

### Background Asymmetries

When applying the correction, asymmetries measured by  $G^0$  were used for the backgrounds. While the elastic and pion asymmetries were measured directly, the aluminum asymmetry was not. In the inelastic locus, the aluminum contribution is dominated by inelastic ( $\pi$  production) scattering, the asymmetry of which has never been measured. This asymmetry can be approximated, however, using the measured deuterium asymme-

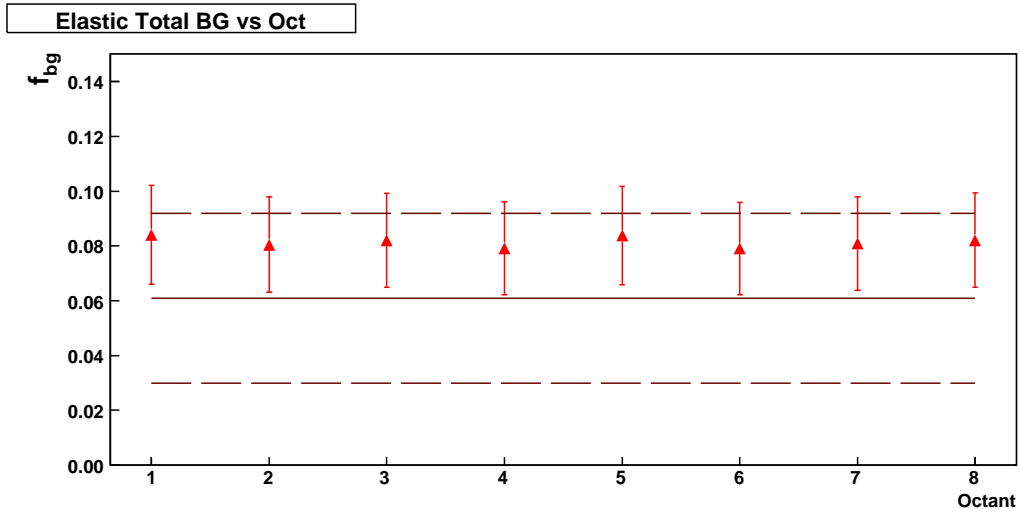


FIG. 5.13: Comparison of inelastic method and field scan method elastic locus dilutions for deuterium. The octant average dilution from the field scan method is shown as a solid line, while the error range is shown as dashed lines. The dilution here is the total background (inelastic, Al,  $\pi^0$  decay, and  $\pi^-$ ) in the locus.

try. This asymmetry is expected to differ slightly from the true aluminum asymmetry due to the difference in proton to neutron ratio between the two nuclei (D is 1:1 while Al is 13:14 or 1:1.08) but this difference is small compared to the error in the measurement.

The pion asymmetry at  $Q^2 \sim 0$  was measured alongside the electron asymmetries during the low-energy deuterium run period. Since simulation indicated that the majority of the pions present in the data were photoproduced rather than electroproduced [43], the resulting asymmetry could be applied to the high energy data. This finding was consistent with the data and inelastic simulation which showed that electron matrix yield from inelastic scattering at the  $\Delta$  resonance was negligible at these kinematics. The photoproduction analysis found the asymmetry to be consistent with zero [43]. Thus, when applying the correction, the asymmetry associated with both  $\pi^0$  decay and  $\pi^-$  contamination is given the value  $0 \pm 3$  ppm.

For the elastic asymmetry, the  $G^0$  Backward-angle results [20] can be used, but a

scaling must be applied to account for electromagnetic radiative effects. The scaling is necessary because the average values published represent the peak value for the elastic asymmetry but the background under the inelastic locus comes from events in the elastic radiative tail. To determine the proper scaling, elastic simulations were run with radiative effects included for both hydrogen and deuterium. The resulting cell asymmetries can be seen in Figure 5.14. The elastic locus average was computed and each cell in the inelastic locus divided by this value to get the cell by cell scaling. The locus average elastic asymmetry,  $A_{el}$ , for both the elastic and inelastic loci is shown in Table 5.3.

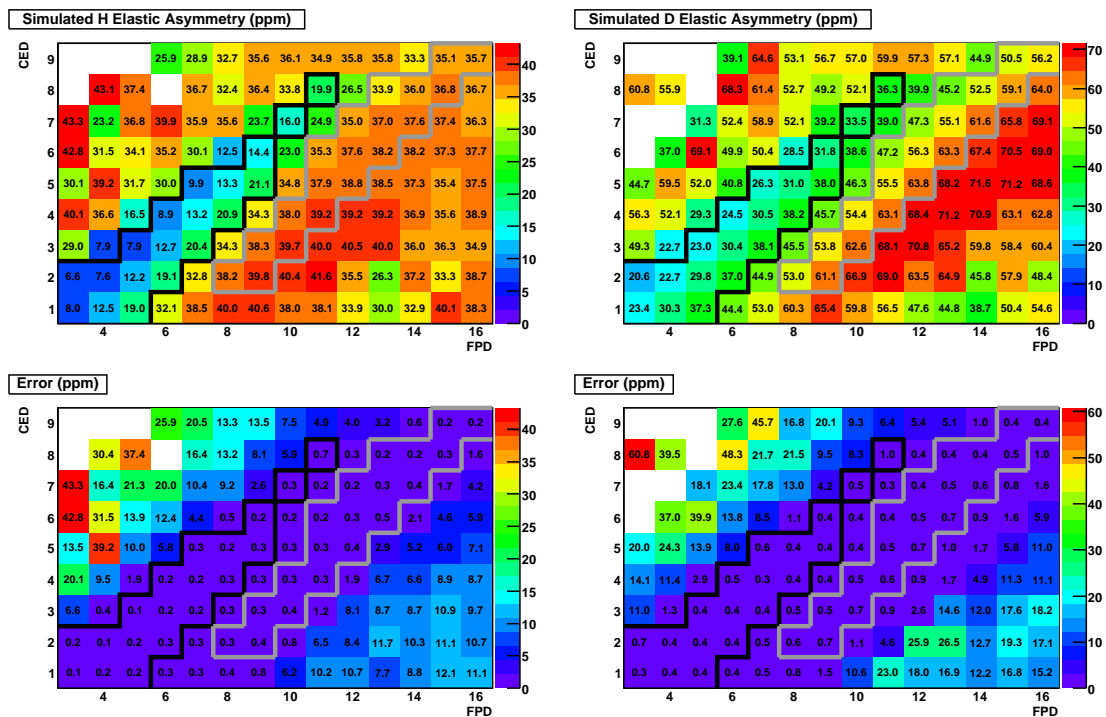


FIG. 5.14: Cell-by-cell simulated elastic asymmetry (in ppm) for both the hydrogen and deuterium targets. The cells outlined in black represent the inelastic locus while those outlined in gray are the elastic locus. Note that the magnitude of the asymmetry,  $|A_{el}|$ , has been plotted here to simplify the figure. The true simulated asymmetries are negative in every cell.

Simulated $A_{el}$ (ppm)		
	H 687MeV	D 687MeV
Elastic Locus	$-36.77 \pm 0.06$	$-54.22 \pm 0.12$
Inelastic Locus	$-11.65 \pm 0.04$	$-30.66 \pm 0.10$

TABLE 5.3: Summary of simulated elastic asymmetry, averaged across the elastic and inelastic loci.

### Error on the Corrected Asymmetry

The error on the corrected asymmetry is determined by differentiating Equation 5.8 with respect to  $A_{meas}$ ,  $A_i^{bg}$ , and  $f_i^{bg}$  and combining the terms in quadrature according to

$$(\delta A_{inel})^2 = \left( \frac{\partial A_{inel}}{\partial A_{meas}} \delta A_{meas} \right)^2 + \sum \left( \frac{\partial A_{inel}}{\partial A_i} \delta A_i \right)^2 + \sum \left( \frac{\partial A_{inel}}{\partial f_i} \delta f_i \right)^2. \quad (5.9)$$

After evaluating the derivatives and simplifying, the error can be written as

$$(\delta A_{inel})^2 = \left( \frac{\delta A_{meas}}{1 - \sum f_i} \right)^2 + \sum \left( \frac{f_i \delta A_i}{1 - \sum f_i} \right)^2 + \sum \left[ \left( \frac{A_{meas} - \sum f_i A_i}{(1 - \sum f_i)^2} - \frac{A_i}{1 - \sum f_i} \right) \delta f_i \right]^2, \quad (5.10)$$

where all sums are over  $i$ , which represents the individual background processes.

When the individual dilutions are computed, each process has an associated error, including the inelastics. In Equation 5.8, the inelastic dilution factor is not explicitly present and, as such, the inelastic dilution factor error is not present in Equation 5.10. This poses a problem since this error should not be ignored when computing the total. In order to understand the importance of this missing error, it must be noted that, although each individual process has its own independent rate, the dilution factors are constrained to sum to 1. As an example, assuming the simplest case where there is a single background,  $f_{inel} + f_{bg} = 1$ . An increase of 5% in  $f_{inel}$  would require a corresponding decrease of 5%

in  $f_{bg}$  for the equation to hold. Since any uncertainty in the inelastic fraction will impact the background fraction, it must be taken into account when computing the corrected asymmetry.

The contribution of the inelastic uncertainty as it relates to each process can be approximated by distributing it proportionally among the backgrounds according to

$$\delta f_i = \sqrt{(\delta f_i^0)^2 + \left(\frac{f_i}{f_{bg}} \delta f_{inel}\right)^2}, \quad (5.11)$$

where  $\delta f_i^0$  is the dilution factor error for the  $i^{th}$  process,  $f_i$  is its dilution factor and  $f_{bg}$  is the total background dilution. If the individual background errors are defined in this way, Equation 5.10 will give an adequate approximation of the total error. In the case of deuterium,  $\delta f_{inel}$  can be replaced with  $\delta f_{tot}$ , where this total is the inelastic and aluminum dilution factor errors summed in quadrature.

## 5.2.6 Background Correction Summary

The asymmetries for both targets before and after the correction is applied are given in Table 5.4. The error is separated into statistical (stat) and systematic (sys) components, with the systematic error being further separated into uncorrelated (uc) and correlated (c) errors. The correlations are in reference to correlations across octants and detectors. The systematic errors include both the dilution factor errors summarized in Table 5.1 and the errors associated with the background asymmetries. The statistical errors on both targets increase because of the reduction in rate as the backgrounds are subtracted, with the hydrogen statistical error increasing from 10% to 15% and the deuterium statistical error from 22% to 33%.

The systematic error for the hydrogen target is nearly equal to the statistical error, with  $\sigma_{sys}^{tot} = 5.10$  ppm, or 15%. For the deuterium, the total systematic error of  $\sigma_{sys}^{tot} = 6.22$

ppm, or 14%, is much smaller than the statistical error. The deuterium error is the largest contribution to the systematic error of the hydrogen asymmetry, meaning the precision of the hydrogen result is directly affected by the imprecision of the deuterium. The total error on the asymmetry (the sum of statistical and systematic) is 7.35 ppm, or 22%, for hydrogen and 15.9 ppm, or 37%, for deuterium.

$A \pm \sigma_{stat} \pm \sigma_{sys}^{uc} \pm \sigma_{sys}^c$ (ppm)		
	H 687	D 687
$A_{bpol}$	$-26.27 \pm 2.64 \pm 0.00 \pm 0.43$	$-31.07 \pm 6.92 \pm 0.00 \pm 1.30$
$A_{inel}$	$-33.60 \pm 5.30 \pm 3.88 \pm 3.31$	$-43.57 \pm 14.64 \pm 0.25 \pm 6.22$

TABLE 5.4: Inelastic asymmetry with error before and after applying the background correction. The “before” asymmetry,  $A_{bpol}$ , is the inelastic asymmetry after applying the corrections in Chapter 4.

### Studying the Error

Ideally, the background corrections should be applied in such a way as to maintain the highest precision possible in the final result. Although the primary source of error on the asymmetries given in Table 5.4 is statistics, which cannot be improved at this stage, it is useful to study the sources of the systematic error to see if improvements could be made. In order to determine how to reduce the error it is necessary to know which processes contribute most to the error. A study was done by computing the total asymmetry error with certain individual contributions “switched off” to isolate the causes of error. It is unrealistic to assume sources of error can completely eliminated, but using the extreme case can help identify the areas that might be of the most benefit to improve. Table 5.5 shows the resulting systematic error for the cases tested. The first row of the table contains the total errors while each subsequent row shows the remaining error when

the indicated source is removed.

The results shown in Table 5.4 indicate that the main source of systematic error for the deuterium comes from the correlated errors while for hydrogen the uncorrelated errors are larger. The large uncorrelated errors for hydrogen are due to the use of the background-corrected deuterium asymmetry when subtracting the aluminum background. As was discussed previously, when the correction is applied, the statistical error on the deuterium becomes an uncorrelated systematic error on the hydrogen. Because of this relationship, the effect of the precision of the deuterium asymmetry on the hydrogen result was studied first. The primary source of error here is the error on the asymmetry rather than the dilution factor error. The second and third rows of the table show the impact of first removing the correlated systematic error on the deuterium asymmetry (the uncorrelated error is negligible) and then the impact of removing its statistical error. The remaining systematic error on the hydrogen asymmetry after removing the deuterium statistical error from the correction is equal to the correlated error shown in Table 5.4. These results confirm that the deuterium statistics dominate the uncorrelated hydrogen statistical errors while the systematic deuterium error contributes less than 1 ppm to the hydrogen correlated systematic error.

The source of the systematic errors for both hydrogen and deuterium was studied next. If the statistical error on the deuterium is excluded, the dominant source of systematic error for both targets comes from the correlated errors. The suspicion was that the primary source of correlated error was from the pion related dilutions, so these were eliminated first. The fifth row of Table 5.5 shows the remaining systematic error, consisting of only the errors associated with the elastic and aluminum backgrounds and the pion asymmetry. Note that here the statistical error from the deuterium asymmetry has also been removed to make the impact of the correlated errors more visible for the hydrogen.

The error in both cases is nearly reduced in half, confirming that the  $\pi^0$  decay and  $\pi^-$  dilution factor errors contribute significantly to this error. The next three rows of the table show the effect of removing the individual components of the pion errors: the scale factor fit error on the  $\pi^0$  decay, the 25% model error on the  $\pi^0$  decay and the 30% model/fit error on the  $\pi^-$ . From these results, it can be seen that the model errors have a larger impact than the error associated with the fit.

However, this impact is still small in comparison to the size of the statistical error on both data sets and the increased systematic error on hydrogen due to the statistical error on the deuterium. Because of this, any improvements that could be made to models and fits would not have a significant impact on the final uncertainty.

Error Study: Isolate Errors				
	$\sigma_{sys}^H$	$\sigma_{sys}/A_{inel}^H$	$\sigma_{sys}^D$	$\sigma_{sys}/A_{inel}^D$
Original Total Systematic Error	5.10	0.152	6.22	0.143
Set $\delta A_{Al} = 0$	4.68	0.139	—	—
Set $\delta A_D^{stat} = 0$	3.31	0.099	—	—
Set $\delta A_D^{stat} = 0, \delta f_{cor} = 0$	0.22	0.007	0.24	0.005
Set $\delta A_D^{stat} = 0, \delta f_{\pi} = 0$	1.79	0.053	3.64	0.084
Set $\delta A_D^{stat} = 0, \delta f_{scfac}^{\pi^0} = 0$	3.13	0.093	6.16	0.141
Set $\delta A_D^{stat} = 0, \delta f_{model}^{\pi^0} = 0$	2.39	0.071	5.12	0.118
Set $\delta A_D^{stat} = 0, \delta f_{model}^{\pi^-} = 0$	3.12	0.093	5.18	0.119

TABLE 5.5: Summary of the asymmetry error study. Only systematic errors are shown.

A second error study involving the definition of the inelastic locus was also performed. The locus definition that was used to determine the average asymmetries and total dilution factors originated from estimates of where inelastic events would dominate the yield. Cells were chosen for the locus based on data taken over a range of magnetic

field settings and on simulation. As was shown in Table 5.2, this locus definition results in a total background fraction greater than 50% for hydrogen and 60% for deuterium. Further, as can be seen in Figures 5.8 and 5.9, for some cells within the locus the background was an even larger fraction. While the subtraction of backgrounds leads to an increase in the size of the statistical error, which impacts the hydrogen systematic error, optimization of the locus definition could lead to a reduction in the correlated systematic error studied previously.

To test the impact of the locus definition on the resulting asymmetry, the background corrected asymmetry was averaged across three different reduced loci. The results of this test are shown in Table 5.6. In each case, cells were chosen for removal based on the hydrogen dilution factors. If the total background dilution,  $f_{bg}$ , was greater than a specified maximum in any octant, the cell was removed from the locus. The first two loci tested, removing cells with 70% and 60% backgrounds, respectively, resulted in little change to the central value of the asymmetry. Although there was some reduction in the systematic error, the change was only a fraction of a ppm. When cells with backgrounds greater than 50% were removed, the impact on the central value was larger as was the impact on the statistics. The systematic error for the hydrogen was unchanged for this locus while that of the deuterium increased slightly. Based on this study, reducing the locus results in a loss of statistical precision for the deuterium that yields hardly any benefit in the hydrogen. Thus, there is nothing to be gained from removing high-background cells from the locus.

Error Study: Refine Locus			
	H 687MeV		
	$A_{inel} \pm \sigma_{stat} \pm \sigma_{sys}$	$\sigma_{tot}$	$\sigma_{tot}/A_{inel}$
$A_{inel}^{orig}$	$-33.60 \pm 5.3 \pm 5.1$	7.4	0.22
$f_{bg}^H < 0.7$	$-34.34 \pm 5.4 \pm 4.9$	7.3	0.21
$f_{bg}^H < 0.6$	$-34.55 \pm 5.5 \pm 4.9$	7.3	0.21
$f_{bg}^H < 0.5$	$-27.13 \pm 6.6 \pm 5.1$	8.4	0.31
	D 687MeV		
	$A_{inel} \pm \sigma_{stat} \pm \sigma_{sys}$	$\sigma_{tot}$	$\sigma_{tot}/A_{inel}$
$A_{inel}^{orig}$	$-43.57 \pm 14.6 \pm 6.2$	15.9	0.37
$f_{bg}^H < 0.7$	$-42.72 \pm 15.1 \pm 5.2$	16.0	0.37
$f_{bg}^H < 0.6$	$-41.03 \pm 15.8 \pm 5.1$	16.6	0.40
$f_{bg}^H < 0.5$	$-54.93 \pm 20.1 \pm 6.4$	21.0	0.38

*A and  $\sigma$  given in ppm*

TABLE 5.6: Background corrected inelastic locus asymmetry for various locus definitions. The percentage of background is based on the hydrogen dilutions and includes cells where at least one octant has a total background fraction greater than the indicated maximum. The same locus definition is used for both targets.

### Corrected Elastic Asymmetry

Background-corrected elastic asymmetries were also computed using dilutions from the method described in this thesis. A comparison of the corrected elastic asymmetry,  $A_{el}$ , to the published asymmetry values, with backgrounds determined using the field scan method, is shown in Table 5.7. Note that the deuterium data set used here is different than that which was used to determine the published  $A_{el}$ , so the errors will be different. For the published value, the full high-energy deuterium data set, including data taken November '06, December '06 and March '07, was used, while, for this analysis, only the data from the March '07 run period was included (roughly 35% of the total). Since the deuterium asymmetry is used as the aluminum background, this results in the error increasing for the hydrogen as well. Corrections for radiative effects and errors due to corrections other than the background correction were included based on the values presented in Table II of the published Letter [20]. Thus, the only differences between the two sets of data in the table are the manner in which the backgrounds were subtracted and the deuterium statistics. These results show that the corrected asymmetries from the method presented here match those obtained using the field scan method within errors and act as an independent verification of the elastic background analysis.

## 5.3 Radiative Corrections

Once the background correction was completed, the next step taken to determine the physics asymmetry was to correct for radiative effects. Radiative corrections account for higher order processes that contribute to the scattering cross section. The principal effect of this radiation is to alter the effective momentum transfer,  $Q^2$ , of the scattered

Background Corrected Elastic Asymmetry, $A_{el}$						
	Inelastic Method			Field Scan Method		
	$A$	$\sigma_{stat}$	$\sigma_{sys}$	$A$	$\sigma_{stat}$	$\sigma_{sys}$
H 687MeV	-44.16	2.28	2.48	-45.90	2.40	1.28
D 687MeV	-53.85	5.08	2.37	-55.50	3.30	2.12

*All values in ppm*

TABLE 5.7: Comparison of the resultant elastic asymmetry using two different methods to determine the backgrounds. The values in column two were determined using the field scan method to subtract the backgrounds [20].

electrons. This is an important consideration for the  $G^0$  experiment as the acceptance cut on the detectors is determined by the  $Q^2$  of the scattered electron. Since the asymmetry is determined at the interaction point, emission of a photon before the electron scatters will lead to a lower incident electron  $Q^2$  and, therefore, a different asymmetry. Emission after the interaction point will not impact the asymmetry but, due to acceptance, may lead to the scattered electron ending up in a different CED-FPD coincidence cell than it otherwise would have.

Up to this point, all corrections discussed have been applied in a similar manner to both the hydrogen and deuterium inelastic asymmetries. Because there is no currently available theoretical model for the deuterium asymmetry, radiative corrections cannot be computed. As such, the corrections in this section are only applicable to the hydrogen data. Had a model been available for the deuterium case, corrections would have been applied to the data using the same procedure.

### 5.3.1 Electromagnetic Radiative Corrections

Electromagnetic (EM) radiative corrections were computed in simulation according to the procedure outlined by Mo and Tsai [78] [79]. Corrections are made to the first-order, or tree-level, asymmetry to account for changes to the kinematics due to both the virtual photons present in loop processes and the real photons emitted through bremsstrahlung. Figure 5.15 shows the different effects that are taken into account. The first four diagrams represent the one-loop corrections at the electron vertex. Similar corrections could be made at the hadron vertex but are negligible due to the proton being significantly more massive than the electron. The final two diagrams in the figure show initial and final state photon emission through bremsstrahlung.

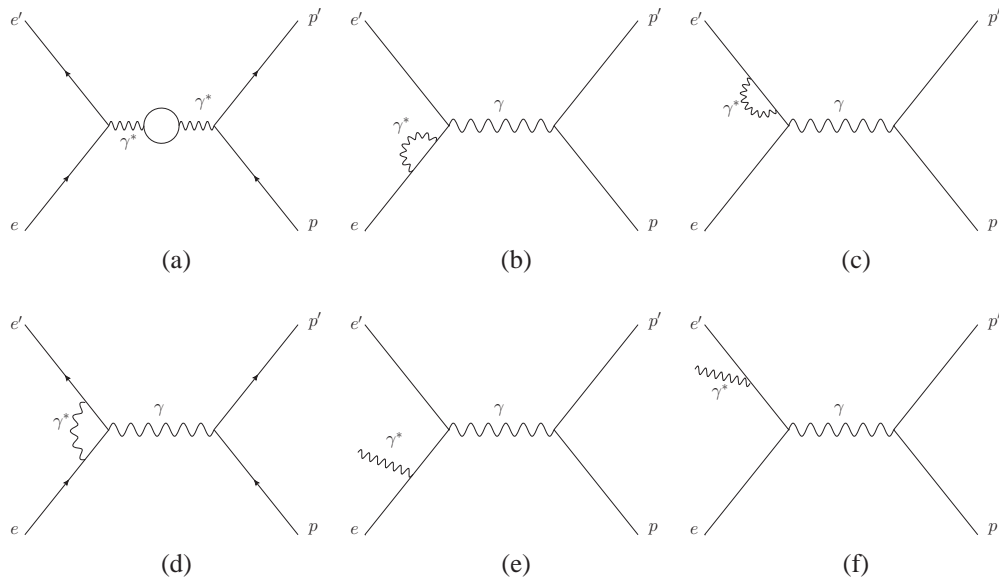


FIG. 5.15: Lowest order EM radiative corrections. Diagram (a) represents the vacuum polarization correction, Diagrams (b) and (c) show the two types of external leg corrections and Diagram (d) represents the vertex correction. The final two diagrams represent (e) initial and (f) final state bremsstrahlung.

Though radiative effects are present in all events, some events are impacted more

strongly by the radiation than others. This difference is dependent on the energy of the emitted photon, as this translates to energy lost by the electron. This energy loss, in turn, lowers the electron's  $Q^2$ . Ideally, the distribution of  $Q^2$  would be Gaussian in shape, but radiative effects shift the value of  $Q^2$  for a given event away from the mean, leading to a tail on low  $Q^2$  side of the peak. Because of this behavior, events in which the change in energy due to radiation is small ( $\sim 1$  MeV) are referred to as peak events, while those with larger changes in energy are referred to as tail events. To model this behavior in simulation, it is necessary to generate events that have both large and small shifts in energy due to radiation. In order to achieve this, each event in G0GEANT is designated as either peak or tail before any calculations are performed. The designation is made using a random number generator to define the probability that the event is in the peak. This probability is then compared to a previously defined minimum peak probability such that those with greater than the minimum value will be considered peak events while all others will be treated as tail events. Once the designation is made, the appropriate calculations are made and the corrections are applied. For peak events, the cross section is corrected for external and internal loop diagrams and ionization while the  $Q^2$  and asymmetry remain unchanged. Corrections for internal and external bremsstrahlung, virtual photons and ionization are applied to the cross section,  $Q^2$  and asymmetry for tail events. Details of the implementation of the radiative corrections in the simulation are given elsewhere [73].

The final correction is applied to the asymmetry through the use of a scale factor,  $R_c$ , determined from the G0GEANT simulation. Simulations were run with and without radiative effects included and the average asymmetry across the inelastic locus was computed in each case.  $R_c$  is then defined as the ratio of the two conditions according to

$$R_c = \frac{A_{inel}^{tree}}{A_{inel}^{radcor}}, \quad (5.12)$$

where  $A_{inel}^{tree}$  is the inelastic locus average asymmetry without EM radiative effects and  $A_{inel}^{radcor}$  is the asymmetry with the effects included.  $R_c$  represents the fractional shift in the asymmetry due to the presence of radiative effects and their impact on the  $Q^2$  distribution. The correction is applied in such a way as to shift the asymmetry to the value expected at the unradiated  $Q^2$  using

$$A_{rc} = A_{meas}(1 + R_c). \quad (5.13)$$

The primary source of uncertainty in this calculation is the model used for the inelastic cross section. To quantify this uncertainty, simulations were run for each of the two hydrogen cross section models described in Section 5.1.1 and the resulting values for  $A$  and  $Q^2$  from each model were compared. Based on this comparison, an uncertainty of 50% of the correction was used and the correction for EM radiation was computed to be  $(1.17 \pm 0.6)\%$  or  $(0.39 \pm 0.2)$  ppm.

### 5.3.2 Electroweak Radiative Corrections

The electroweak (EW) radiative corrections stem from interactions involving the nucleon's constituent quarks. The reactions included are classified as one-quark or multi-quark interactions. The one-quark interactions are those in which the incident electron interacts with a single quark in the nucleon. One-quark corrections include effects such as vertex corrections similar to those shown in Figure 5.15 but involving the  $Z$  boson rather than the photon. Multi-quark interactions are weak interactions that occur between the quarks within the nucleon itself and contribute at parity-violating vertices.

The EW radiative corrections impact the asymmetry differently for the vector and axial pieces. The vector contribution, which in the notation of the inelastic asymmetry involves corrections to  $\Delta_1^\pi$  and  $\Delta_2^\pi$ , is both small and well understood. Given the uncer-

tainty on the  $G^0$  measurement, these corrections, which amount to a  $< 2\%$  effect on the asymmetry, are negligible. Conversely, studies of elastic  $ep$  scattering in the SAMPLE experiment revealed that radiative corrections related to the axial vector coupling, unlike their vector counterparts, can be significant and are not well-understood theoretically [18] [80]. The axial form factor measurements from the  $G^0$  elastic asymmetry, which were taken at higher  $Q^2$  than the SAMPLE measurements, lend further experimental evidence of the theoretical predictions made by Zhu *et al.* [18]. Applying these findings to inelastic scattering, one can infer that these corrections have the potential to significantly alter the axial component of the inelastic asymmetry,  $\Delta_3^\pi$ , in a similar manner. As such, the axial EW radiative corrections cannot be neglected.

The one-quark axial corrections, denoted  $R_A^{ewk}$ , are well known and can be calculated from Standard Model couplings. The uncertainty on these corrections comes only from the understanding of the Standard Model quantities, such as  $\sin^2 \theta_W$  and the  $V(e) \times A(q)$  couplings,  $C_{2q}$ . The dominant uncertainty, instead, lies in the understanding of the multi-quark contributions. These include, to first order in  $\alpha$ , the transition anapole, Siegert, and  $d$ -wave contributions. The transition anapole and Siegert contributions both originate at the parity-violating  $\gamma N \Delta$  vertex, while the  $d$ -wave contribution stems from the parity-violating  $\pi N \Delta$  vertex. While the anapole contribution has an analogue in the axial elastic channel, describing the  $\gamma NN$  vertex, the Siegert and  $d$ -wave corrections are unique to  $\Delta$  production.

For the EM radiation discussed in the previous section, corrections were applied to offset the impact of radiative effects and shift the measured asymmetry to the unradiated kinematics. This allowed for a comparison between the data and the tree-level results from theory. The EW radiative corrections will be treated in the opposite manner. Instead of applying a correction to the measured asymmetry to offset the radiative effects, the

theoretical asymmetry calculation will be altered to include the effects of EW radiation that are present in the data. This different approach is, in part, due to the theoretical uncertainty involving the axial EW radiative corrections. Because the determination of EW radiative corrections is more closely related to the theoretical interpretation of the asymmetry than to the determination of the measured asymmetry, a complete discussion of these corrections will be postponed until Chapter 6.

## 5.4 Acceptance Averaging

In order to compare the measured asymmetry to theory, it is necessary to know the kinematics of the measurement. For  $A_{inel}$ , the relevant variables are beam energy,  $E$ , momentum transfer,  $Q^2$ , and invariant mass,  $W$ . These variables can be altered though both physics effects like radiation and design effects like detector acceptance. The previous section dealt with the shift in  $Q^2$  due to EM radiative effects, with a correction applied to shift the locus average asymmetry to the non-radiated  $Q^2$ . Once the EM radiative corrections are applied, the final step needed to determine  $A_{inel}$  is to apply a correction to account for detector acceptance.

The measured asymmetry quoted in previous sections is an average over the entire inelastic region. The kinematic variables on which the asymmetry is dependent, such as  $Q^2$  and  $W$ , vary across this region. Though the average kinematics in the locus can be determined through simulation, depending on the distributions of the kinematic variables and the asymmetry across the region, the average asymmetry,  $\langle A(Q^2, W) \rangle$  may not be equal to the asymmetry at the average kinematics,  $A(\langle Q^2 \rangle, \langle W \rangle)$ . If the distributions of the individual asymmetry components across the  $Q^2$  acceptance were each Gaussian, then  $\langle A(Q^2, W) \rangle$  and  $A(\langle Q^2 \rangle, \langle W \rangle)$  would be identical. If not, any variation from a

Gaussian would need to be taken into account in order to provide an accurate result for the asymmetry at a quoted  $Q^2$  and  $W$ .

To determine the size of the shift,  $\epsilon_{acc}$ , the average values of the kinematic variables required for the asymmetry model were taken from histograms produced by the simulation without EM radiative effects. These averages were then used as inputs to determine a single theoretical asymmetry at the average kinematics and  $\epsilon_{acc}$  was computed according to

$$\epsilon_{acc} = \frac{A(\langle P_i \rangle) - \langle A(P_i) \rangle}{A(\langle P_i \rangle)}, \quad (5.14)$$

where  $P_i$  denotes the set of variables necessary for the asymmetry model. A result for  $\epsilon_{acc}$  was determined for each of the two asymmetry models available in the simulation. The averages of the kinematic variables used to compute the asymmetry are given in Table 5.8. The distributions across the  $G^0$  acceptance of the relevant kinematic variables, including  $Q^2$ ,  $W$  and  $\theta$ , are given in Appendix A. The difference in the size of the shift between the two models was used as the uncertainty on the correction. Table 5.9 summarizes the average asymmetry and the asymmetry computed at the average kinematics for each model. Based on these values,  $\epsilon_{acc}$  was computed to be  $(-1.6 \pm 0.6)\%$ , or  $(-0.55 \pm 0.2)$  ppm.

Simulation Averages	
$Q^2$	0.338 GeV/c <sup>2</sup>
$W$	1.178 GeV
$E$	0.680 GeV
$E'$	0.229 GeV
$\theta$	94.81°

TABLE 5.8: Summary of the average kinematics in the inelastic locus as determined through simulation.

	Musolf		Matsui	
	$\langle A(P_i) \rangle$	$A(\langle P_i \rangle)$	$\langle A(P_i) \rangle$	$A(\langle P_i \rangle)$
$A_{tot}$	-38.72	-38.11	-36.34	-36.71
$A_1$	-32.69	-32.68	-32.62	-32.68
$A_2$	-1.13	-0.56	0.22	0.11
$A_3$	-4.84	-4.86	-3.95	-4.14

*All values in ppm*

TABLE 5.9: Summary of  $\langle A(P_i) \rangle$  and  $A(\langle P_i \rangle)$  for each component of the asymmetry for each model.

## 5.5 Final Corrected Asymmetry

The corrections applied in this chapter are summarized in Table 5.10, with the starting point being the final asymmetry given in Table 4.7 at the end of Chapter 4. The uncertainty is shown both as a whole ( $\sigma_{tot}$ ) and divided into statistical ( $\sigma_{stat}$ ) and systematic ( $\sigma_{sys}$ ) components. Also included in the table are  $\sigma_{cor}$ , the systematic error associated with a given correction and  $dA$ , the correction's impact on the asymmetry. The quantity  $\sigma_{cor}$  is a subset of the systematic uncertainty and has been included in  $\sigma_{sys}$ . It is given separately here to show how much each individual correction contributes to the total systematic uncertainty. All asymmetries and errors represent locus and octant averages, and are given in ppm. Note that, due to the absence of an asymmetry model, the acceptance averaging and radiative corrections have not been applied to the deuterium data.

$A_{inel}$  for H 687 MeV

	$A$	$\sigma_{tot}$	$\sigma_{stat}$	$\sigma_{sys}$	$\sigma_{cor}$	dA
Raw (“Pass 1”)	2 -20.23	2.00	2.00	0.00	—	—
Beam & Instrumentation	-26.27	2.67	2.64	0.43	—	—
Backgrounds	-33.60	7.36	5.30	5.10	4.93	-7.33
EM Radiative Effects	-33.99	7.36	5.30	5.10	0.20	-0.39
Acceptance Averaging	-33.44	7.36	5.30	5.11	0.20	-0.55

 $A_{inel}$  for D 687 MeV

	$A$	$\sigma_{tot}$	$\sigma_{stat}$	$\sigma_{sys}$	$\sigma_{cor}$	dA
Raw (“Pass 1”)	-14.11	2.62	2.62	0.00	—	—
Beam & Instrumentation	-31.07	7.04	6.92	1.30	—	—
Backgrounds	-43.57	15.91	14.64	6.23	5.52	-12.5

*All values in ppm*

TABLE 5.10: Inelastic asymmetry following each stage of corrections applied. The total error,  $\sigma_{tot}$ , is the sum in quadrature of  $\sigma_{stat}$  and  $\sigma_{sys}$ . Note that the correction uncertainty,  $\sigma_{cor}$  is included in  $\sigma_{sys}$  and is only shown individually to highlight the error due to each correction. The details of the individual beam and instrumentation corrections are given in Table 4.7 at the end of Chapter 4.

## CHAPTER 6

# Theoretical Asymmetry and Interpretation of Results

In the previous two chapters, corrections have been applied to the raw asymmetry to determine a final measured asymmetry,  $A_{inel}$ , for each of the two experimental targets. It is now possible to interpret these results for the purposes of extracting information about the axial response of the proton during the transition to the  $\Delta$ . Before this can be done, however, the theoretical asymmetry and its uncertainty must be computed. Additionally, the electroweak radiative corrections discussed briefly in the previous chapter must be taken into account. Once these two tasks have been completed, an estimate for the axial contribution,  $A_3$ , can be extracted from the measured hydrogen asymmetry. From  $A_3$ , a value for the axial transition form factor,  $G_{N\Delta}^A$ , can be determined. Due to the absence of a theoretical representation of the neutron asymmetry, it is not possible at present to extract further information from the deuterium asymmetry. Therefore, the discussion in this chapter will involve only the hydrogen measurement.

## 6.1 Theoretical Asymmetry

The asymmetry was first computed by using G0GEANT to simulate inelastic events over the entire  $G^0$  acceptance. Through this simulation, the distribution of the asymmetry across the inelastic locus was able to be studied. However, the final value of  $A_{inel}^{th}$  that will be compared to the measured asymmetry,  $A_{inel}$ , is a singular value computed using the central values of the kinematic variables needed for the calculation. Before the final comparison can be made, one last effect present in the data that has not previously been included, electroweak radiative effects, needs to be taken into account. Unlike their electromagnetic counterpart, the electroweak radiative corrections will not be computed using the simulation. Instead, theoretical input will be used to estimate the size of the effects and the theoretical, rather than the measured, asymmetry will be adjusted to take them into account. This is in contrast to the acceptance averaging and electromagnetic radiative corrections discussed in the previous chapter which each used simulated asymmetry values to remove their effects from the measured asymmetry.

The models used to compute the three components of the theoretical asymmetry have already been presented in detail in Chapter 2 and their implementation in the G0GEANT simulation was discussed in Chapter 5. In this section, an overview of the theoretical asymmetry results will be given along with a discussion of the corrections needed to account for electroweak radiative effects.

### 6.1.1 Computing $A_{theory}$

For the theoretical asymmetry, two perspectives are available for study, each offering its own benefits. First, the asymmetry can be looked at in the framework of the  $G^0$  detector system, allowing for an understanding of how it behaves across the experimental

acceptance. By studying the output from the G0GEANT simulation, one can gain insight into what the measured asymmetry looks like both averaged across the locus and in the individual CED·FPD cells. Since the  $G^0$  spectrometer bins events by  $Q^2$ , the evolution of the asymmetry across the inelastic locus could potentially be used to study its  $Q^2$  dependence. Unfortunately, the present statistical uncertainty is such that no precise statements can be made about the asymmetry on a cell by cell basis or for a sub-set of cells with similar  $Q^2$  within the locus. Further, the absence of additional data points from the low-energy run period makes a study of the  $Q^2$  evolution of the asymmetry from the present data impossible. The primary use of the simulated asymmetry was in confirming that the distribution of  $A_{inel}$  was essentially uniform across the acceptance and in computing the acceptance averaging and electromagnetic radiative corrections.

Figure 6.1 shows the distribution of the simulated asymmetry summed across the entire locus while Figure 6.2 shows the cell-by-cell average values. Note that for the cell asymmetries the total asymmetry,  $A_{tot}$ , has been plotted without the minus sign for the purposes of simplifying the figure and, in reality, all asymmetries shown are negative. Also note that the asymmetries in these figures have been computed using the primary model of this thesis, the Musolf model. The Matsui model will be presented separately below. In Figure 6.1, the total asymmetry is presented along with the three individual sub-terms. These histograms represent the sum of the events in all inelastic locus cells and have been weighted by the cross-section-dependent weighting factor discussed in Section 5.1. The distributions of  $A_1$  and  $A_3$  are both approximately Gaussian while  $A_2$  has a significantly different shape. This non-Gaussian shape is due to the behavior of the model as the kinematics approach the pion threshold. Although the model begins to become unreliable as this limit is reached, this unreliability is offset by the fact that the inelastic cross section shrinks in the same region. The locus-average asymmetry is based

on the central values of these distributions, although note that acceptance averaging has not been taken into account here. Based on the distributions in the figure, the average total asymmetry across the locus is roughly -38 ppm.  $A_1$ , which represents the resonant vector hadron portion of the asymmetry, is the dominant term with an average of about -32 ppm. The axial portion,  $A_3$  contributes between -4 and -5 ppm to the total, while the non-resonant vector term,  $A_2$ , contributes only about -1 ppm to the total.

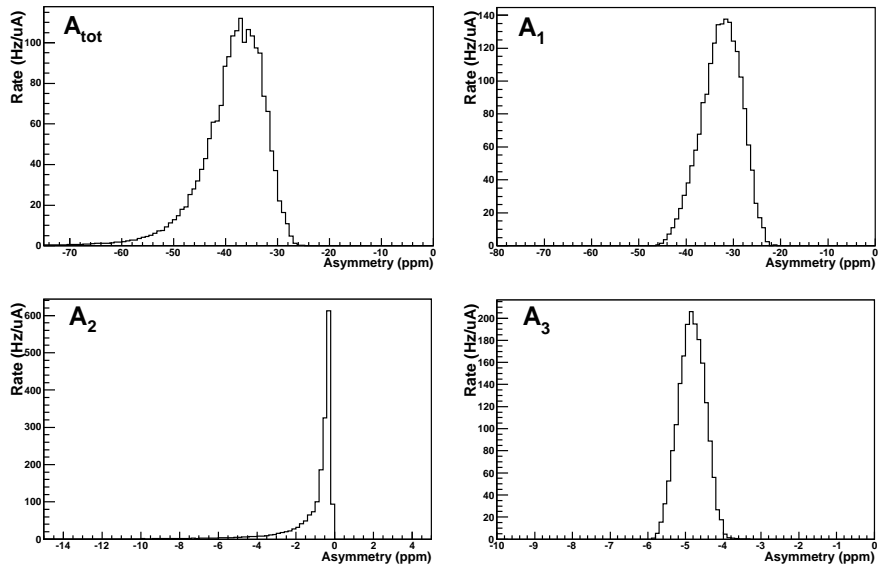


FIG. 6.1: Simulated inelastic asymmetry distributions for events in all inelastic locus cells. The top left plot shows the total asymmetry while the other three show the individual components. In each case,  $A_i$  is proportional to  $\Delta_{(i)}^\pi$ .

Looking at the cell asymmetries, the variation seen in Figure 6.2 is indicative of the  $Q^2$  variation across the locus. The large cell values present at the edge of the locus are those in the tail of the  $A_2$  distribution shown in Figure 6.1. Referring again to that figure, the weighting for events where the magnitude of  $A_{tot}$  is greater than 60 ppm is very low. As such, these high asymmetries do not contribute significantly enough to skew the locus average. The asymmetries in the highest-yield cells are generally more consistent,

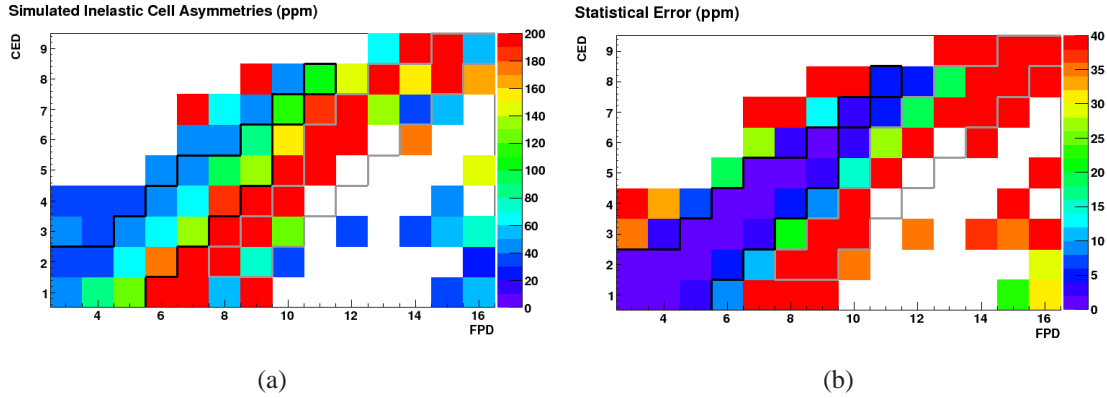


FIG. 6.2: Simulated inelastic asymmetry (left) and statistical error (right) shown for each cell in the coincidence matrix. The inelastic locus has been outlined in black, while the elastic locus is outlined in grey. Note that the asymmetry is shown for all cells, even those with very low statistics.

although they still show about a 30 ppm spread, ranging from about 35 ppm to 65 ppm. For cells outside the inelastic locus, note that while the asymmetry is large, in many cases so is the statistical uncertainty from the simulation, as very few inelastic events are present in these cells.

While the two figures previously discussed are useful in making qualitative observations about the asymmetry, for more rigorous study and comparison to data, a second perspective that is independent of the  $G^0$  acceptance is more appropriate. Here, the ability to recreate the experimental apparatus in simulation is not necessary. Rather, all that is needed is the ability to compute the asymmetry at a single kinematic point consistent with the average kinematics of the locus. Figure 6.3 shows the total asymmetry and each of the three components as functions of  $Q^2$  for the experimental kinematics ( $E = 0.680$  GeV and  $\theta = 95^\circ$ ). The average  $Q^2$  in the inelastic locus, determined through simulation, is indicated by the dashed line. Since the asymmetry here is not cross section weighted like in Figure 6.1, the behavior of  $A_2$  at  $Q^2$  higher than the experimental value is more pronounced. As was discussed previously, this is due to the limitations of the model used

to calculate  $A_2$ . The dominant term for much of the range shown here is  $A_1$ , which is linear in  $Q^2$ . Prior to the point where the model begins to break down,  $A_2$  is consistently small ( $< 1$  ppm). The axial term,  $A_3$ , is smaller than  $A_1$  by roughly a factor of 10 but larger than  $A_2$  by nearly the same order of magnitude.

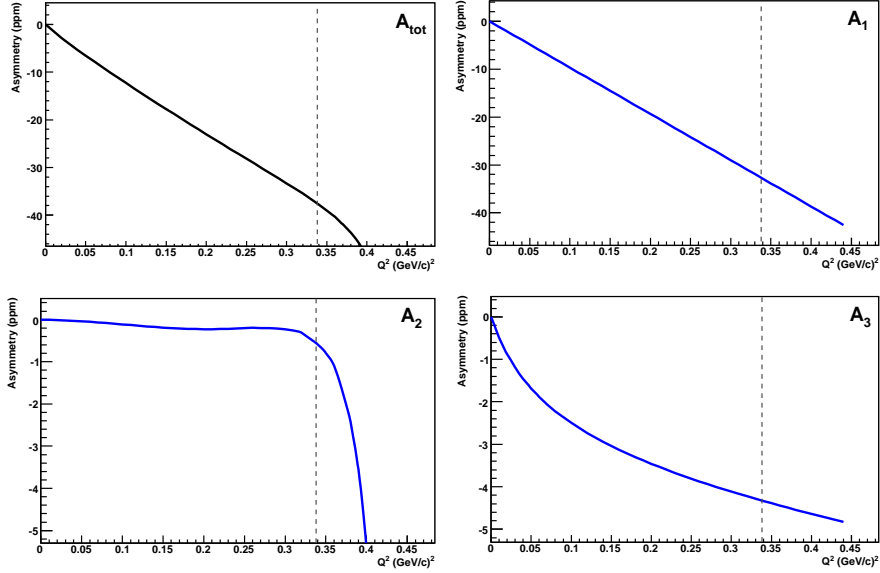


FIG. 6.3: Theoretical asymmetry as a function of  $Q^2$  for the total asymmetry and each individual component. The asymmetry is plotted over a range of  $Q^2$  that is consistent with the full experimental acceptance and has been extended to include the  $Q^2 = 0$  point.

The figures in this section represent the tree-level asymmetry and do not include any higher-order effects. In the next section, calculations for electroweak radiative effects will be used to adjust each of the theoretical asymmetry terms. Electromagnetic radiative effects, however, will not be included in the theoretical asymmetry as these effects have been removed from the measured value.

### Theoretical Asymmetry from the Matsui Model

A secondary model for the asymmetry, developed by Matsui, Sato and Lee [39], was presented in Section 2.3.5. In this model,  $\Delta_{(1)}^\pi$  is the same as the Musolf model, but  $\Delta_{(2)}^\pi$  and  $\Delta_{(3)}^\pi$  terms are calculated differently. Instead of using a multipole expansion,  $\Delta_{(2)}^\pi$  is defined using structure functions in an analogous manner to  $\Delta_{(3)}^\pi$ . This enables them to use a dynamical model they have developed to compute the non-resonant vector asymmetry. For  $\Delta_{(3)}^\pi$ , they use the same basic structure for the form factors as the Musolf model, with the axial form factor consisting of a coefficient representing the value at  $Q^2 = 0$ , a dipole and an additional  $Q^2$  parameterization function  $\xi^A(Q^2)$ . Where the two models differ primarily is in the definition of  $\xi^A(Q^2)$ , where the Matsui model uses an exponential rather than a  $\frac{Q^2}{1+Q^2}$  form.

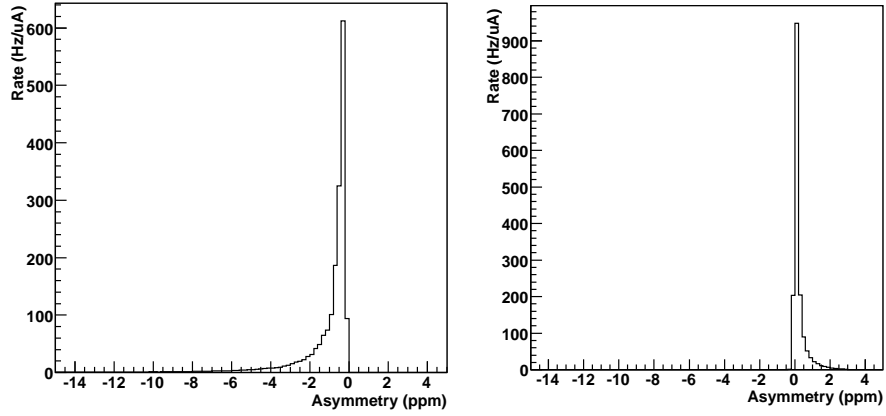


FIG. 6.4: Simulated  $A_2$  distribution for the Musolf model (left) and the Matsui model (right).

The Matsui model was implemented in the simulation so that a comparison between the two models in the context of the  $G^0$  measurement could be made. Figures 6.4 and 6.5 show the simulated asymmetry distributions for  $A_2$  and  $A_3$ , respectively. In each figure, the plot on the left was created using the Musolf model and the one on the right using the Matsui model. For  $A_2$ , the two distributions are quite different. Most noticeably is the

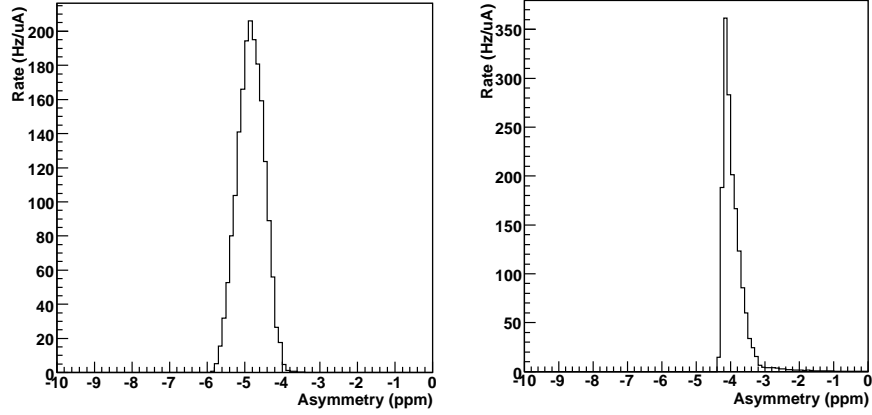


FIG. 6.5: Simulated  $A_3$  distribution for the Musolf model (left) and the Matsui model (right).

fact that the Musolf  $A_2$  is never positive while the Matsui model shows mostly positive events. The Matsui model also lacks the tail arising from kinematics approaching the pion threshold that is present in the Musolf asymmetry. The distributions of  $A_3$  are more similar, with the Matsui model having a narrower width and a slightly shifted central value. The behavior of the two models can also be compared as a function of  $Q^2$  at the experimental kinematics. Figure 6.6 shows  $A_2$  and  $A_3$  plotted as functions of  $Q^2$ . The value of  $A_2$  at the experimental  $Q^2$  is 0.11 ppm for the Matsui model and -0.56 ppm for the Musolf model. While these two asymmetries differ in sign and differ significantly in magnitude, both are close to zero, indicating that the non-resonant contribution to the overall asymmetry is small. For the axial term, the two models are in closer agreement.  $A_3$  is -4.14 ppm for the Matsui model compared to -4.33 ppm for the Musolf model, a difference of  $\sim 4\%$ . As with the previous section, none of the asymmetries discussed here include electroweak radiative effects.

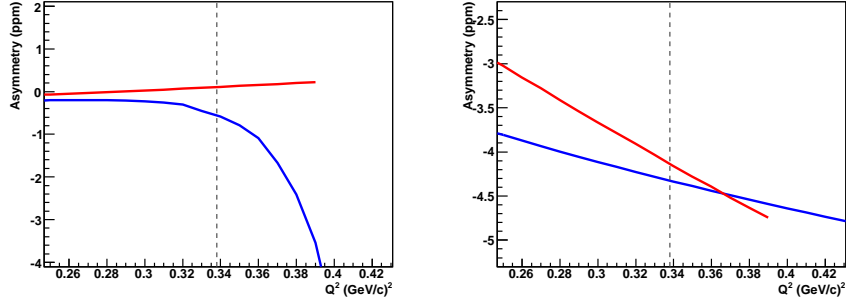


FIG. 6.6: Theoretical asymmetry as a function of  $Q^2$  for  $A_2$  (left) and  $A_3$  (right). The blue curve represents the Musolf model, while the red curve is the Matsui model.

## 6.1.2 Electroweak Radiative Corrections

Corrections for electroweak (EW) radiative effects, which were introduced briefly in Section 5.3.2 in the previous chapter, will be applied to the theoretical asymmetry. The corrections are computed for and applied to each of the  $\Delta_{(i)}^\pi$  terms individually and include both well-understood corrections to Standard Model parameters and less-understood behaviors related to the axial coupling.

Before going further, an important aspect of the EW radiative corrections that should be noted is the dependence on the renormalization scheme used. The corrections applied will be carried out to a particular order in  $\alpha$  and then the sum will be truncated. Although, when taken in full, all renormalization schemes are equal, differences in notation lead to differences in the ordering and grouping of contributing diagrams. Thus, ending the series at a certain order could lead to different diagrams included, leading to different results. The corrections discussed in this section will use couplings and corrections determined using the modified minimal subtraction, or  $\overline{MS}$ , renormalization scheme [81].

As discussed in the previous chapter, the EW radiative corrections can be classified as those involving the photon or  $Z^0$  boson interacting with a single quark (“one-quark corrections”), and those involving electroweak interactions among the quarks in the nucleon

(“multi-quark corrections”). The one-quark corrections involve the Standard Model couplings contained in the three asymmetry terms, namely  $g_A^e$ ,  $g_V^e$  and  $\xi_V^n$ . For the two vector hadron pieces of the asymmetry,  $\Delta_{(1)}^\pi$  and  $\Delta_{(2)}^\pi$ , vector current conservation and other considerations not applicable to the axial couplings limit the impact of possible multi-quark corrections [25]. As such, only the one-quark contributions need to be considered for these two terms.

One-quark corrections can be easily computed by rewriting the couplings in terms of quark couplings  $C_{iq}$ , where the value of  $i$  indicates whether the axial vector is at the electron vertex ( $i = 1$ ) or the hadron vertex ( $i = 2$ ) and the subscript  $q$  represents the quark flavor. When applying the corrections, only the valence quarks are considered. Therefore, in the case of the proton and  $\Delta$ ,  $q$  will be either the up quark or the down quark. The Standard Model expressions for these couplings are [2]

$$\begin{aligned}
C_{1u} &= \rho_e' \left( -\frac{1}{2} + \frac{4}{3} \hat{\kappa}' \sin^2 \theta_W \right) + \lambda' , \\
C_{1d} &= \rho_e' \left( \frac{1}{2} - \frac{2}{3} \hat{\kappa}' \sin^2 \theta_W \right) - 2\lambda' , \\
C_{2u} &= \rho_e \left( -\frac{1}{2} + 2\hat{\kappa} \sin^2 \theta_W \right) + \lambda_u , \\
C_{2d} &= \rho_e \left( \frac{1}{2} - 2\hat{\kappa} \sin^2 \theta_W \right) + \lambda_d ,
\end{aligned} \tag{6.1}$$

where the  $\rho_e$ ,  $\hat{\kappa}$  and  $\lambda$  terms contain the radiative corrections. At tree level,  $\rho_e = \hat{\kappa} = 1$ , while  $\lambda = 0$ . As higher order effects are added in, these quantities begin to diverge from their tree level values. Table 6.1 contains the current values of these terms with radiative effects included as reported by the Particle Data Group [2].

The one-quark EW radiative corrections are computed as the ratio of the corrected asymmetry to its tree-level value,

$$R_i^{ewk} = \frac{(\Delta_{(i)}^\pi)^{EWRC}}{(\Delta_{(i)}^\pi)^{tree}} - 1 . \tag{6.2}$$

Since the radiative effects describe the interaction between electrons and quarks, they only impact the couplings used in the determination of the asymmetry and not the structure of the asymmetry itself. Thus, the form factors contained within the  $\Delta_{(i)}^\pi$  terms cancel out and Equation 6.2 becomes a ratio of couplings.

Parameter	Tree Level	EWRC
$\rho'_e$	1	0.9877
$\rho_e$	1	1.0006
$\hat{\kappa}'_e$	1	1.0026
$\hat{\kappa}_e$	1	1.0299
$\lambda'$	0	$-1.8 \times 10^{-5}$
$\lambda_u$	0	-0.0118
$\lambda_d$	0	-0.0029

TABLE 6.1: Current world values for the quantities associated with the Standard Model couplings at tree level and with electroweak radiative effects (EWRC) included.

The two vector hadron pieces of the asymmetry are written in terms of the quark couplings as

$$\Delta_1^\pi = g_A^e \xi_V^{T=1} = 2(1 - 2 \sin^2 \theta_W) = -2(C_{1u} - C_{1d}), \quad (6.3)$$

$$\Delta_2^\pi \sim -2g_A^e \xi_V^n = -1 = -2(C_{1u} + 2C_{1d}). \quad (6.4)$$

Because the axial term involves both one-quark and multi-quark corrections, it will be treated separately. The forms given in the above equation are determined from the definitions of  $C_{iq}$  given in Equation 6.1 and of the asymmetry terms given in Chapter 2. Note that the details of  $\Delta_{(2)}^\pi$ , which was defined in Equation 2.57, have been neglected and “ $\sim$ ” is used to simplify the notation, as only the couplings that multiply the sum over multipoles need to be considered.

Using  $\rho_e = \hat{\kappa} = 1$  and  $\lambda' = 0$ , the tree-level values for the asymmetry can be computed as

$$\Delta_{(1)}^\pi = 2(C_{1u} - C_{1d}) = 2(1 - 2\sin^2\theta_W) = 1.075, \quad (6.5)$$

$$\Delta_{(2)}^\pi \sim -2(C_{1u} + 2C_{1d}) = -1. \quad (6.6)$$

To include the radiative effects, the full definitions of the  $C_{1q}$  from Equation 6.1 can be substituted into Equations 6.3 and 6.4. Then, using the values for  $\rho'$  and  $\hat{\kappa}'$  presented in Table 6.1, the corrected values are,

$$\Delta_{(1)}^\pi = 2(C_{1u} - C_{1d}) = 2 \left[ \rho' \left( 1 - 2\hat{\kappa}' \sin^2\theta_W \right) - 3\lambda \right] = 1.060, \quad (6.7)$$

$$\Delta_{(2)}^\pi \sim -2(C_{1u} + 2C_{1d}) = -\rho' + 8\lambda' = -0.988. \quad (6.8)$$

The results from Equations 6.5 through 6.8 lead to a -1.44% correction for  $\Delta_{(1)}^\pi$  and a -1.24% correction for  $\Delta_{(2)}^\pi$ .

For the axial term,  $\Delta_{(3)}^\pi$ , the one-quark and multi-quark corrections are summed together and included as part of a multiplicative term to rewrite the asymmetry [25]

$$\Delta_{(3)}^\pi = 2(1 - 4\sin^2\theta_W^0)(1 - R_A^\Delta)F(Q^2, s), \quad (6.9)$$

where  $F(Q^2, s)$  is the function containing the electromagnetic and axial form factors described in Chapter 2 and  $\sin^2\theta_W^0$  is the tree level value of the mixing angle defined as

$$\sin^2\theta_W^0(1 - \sin^2\theta_W^0) = \frac{\pi\alpha}{\sqrt{2}G_F M_Z^2}. \quad (6.10)$$

From this equation,  $\sin^2\theta_W^0$  is calculated to be 0.2122, whereas the world value of  $\sin^2\theta_W$  in the  $\overline{MS}$  renormalization scheme is 0.2312. The term  $R_A^\Delta$  is the sum of all electroweak radiative corrections and can be defined as

$$\begin{aligned} R_A^\Delta &= R_A^{ewk} + R_A^{multi} \\ &= R_A^{ewk} + R_A^{Siegert} + R_A^{anapole} + R_A^{d-wave} + \dots \end{aligned} \quad (6.11)$$

The first term,  $R_A^{ewk}$ , is the one-quark correction and can be directly computed using Equation 6.2. The remaining terms are multi-quark corrections, with three that have garnered theoretical interest listed explicitly. The ellipsis represents all other possible multi-quark corrections. Note that at tree level  $R_A^\Delta = 0$ , and the equation for  $\Delta_{(3)}^\pi$  is as it was originally defined in Chapter 2.

Rewriting in terms of the axial quark couplings,  $R_A^{ewk}$  can be expressed

$$R_A^{ewk} = \frac{-2(C_{2u} - C_{2d})}{-2(C_{2u}^{tree} - C_{2d}^{tree})} - 1, \quad (6.12)$$

where  $C_{2q}$  are given in Equation 6.1. Using the tree level and radiated values of the coefficients given in Table 6.1,  $R_A^{ewk}$  is computed to be -58.8%. This is a significantly larger contribution from one-quark radiative effects for the axial term than for the vector terms. Since the total correction is the sum of the one-quark and multi-quark corrections, the true impact of this result depends on the magnitude and sign of the other contributions. For this thesis, however, the multi-quark corrections will not be computed, as there is not sufficient precision to determine their value in light of theoretical uncertainties. As a result, the only axial correction that will be applied to the theoretical asymmetry is the one-quark correction computed here.

Although they will not be calculated or included in the final result, some information on the three multi-quark corrections highlighted in Equation 6.11 can be gleaned from the calculations performed by Zhu *et al.* [25]. Because the renormalization scheme and kinematics considered by Zhu *et al.* differ from those of the present measurement, direct application of their results is not possible. However, their plot of the ratio of the asymmetry contribution of the three corrections to the total asymmetry as a function of  $Q^2$  can be used to estimate the relative sizes of these contributions at the experimental  $Q^2$ . The plot has been reproduced in Figure 6.7 with the blue vertical line indicating the

$Q^2$  of the present measurement.

At this  $Q^2$ , Zhu *et al.* find the contribution of  $A_3$  to  $A_{tot}$ , shown as a solid line, to be about 12%, which is consistent with  $A_{theory}$  as shown in Figure 6.3. The dotted line is the Siegert term plotted assuming  $d_\Delta$  equal to the  $25g_\pi$  upper bound determined from the  $G^0$  pion photoproduction data [43]. According to their calculation, this results in a  $\sim 1\%$  effect. For the anapole term, lower and upper bounds representing a “reasonable range” are shown as dashed lines, leading to a range of about 1-5% at the experimental  $Q^2$ . The  $d$ -wave term, shown as a long-dashed line, does not contribute at all at these kinematics. These results indicate that the largest multi-quark electroweak radiative correction at the present kinematics may be the anapole contribution. However, without more theoretical input, including a calculation at the  $G^0$  kinematics, and precise data, no conclusions can be drawn about these corrections.

### 6.1.3 Corrected Theoretical Asymmetry

The electroweak radiative corrections computed above are given in terms of percentage shifts of the tree values of each  $\Delta_{(i)}^\pi$  term. The corrections can be applied to the theoretical asymmetry in the same manner as the electromagnetic radiative corrections such that the corrected value is given by

$$A_i^{ewrc} = A_i^{tree}(1 + R_i^{ewk}), \quad (6.13)$$

where the subscript  $i = 1,2,3$  denotes the  $i$ th term in the asymmetry. Table 6.2 provides a summary of the electroweak radiative corrections applied. After applying the corrections to each component individually, the three terms can be added to give a total corrected theoretical asymmetry of  $A_{theory} = -34.6$  ppm. The net effect of the electroweak radiative corrections is an 8% reduction in the total theoretical asymmetry.

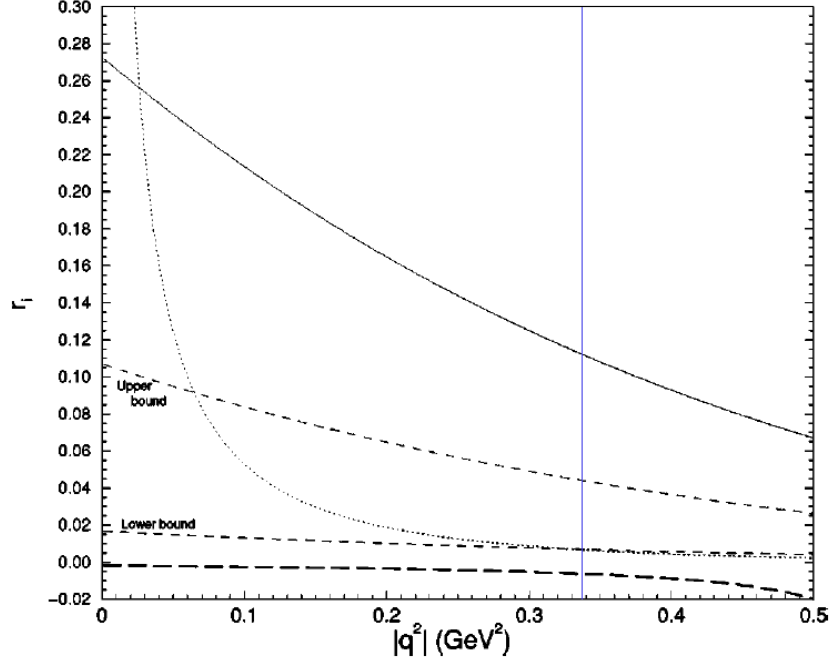


FIG. 6.7: Ratio of the contribution of  $A_3$  and three multi-quark electroweak radiative corrections to the total asymmetry ( $r_i$ ) as a function of  $Q^2$ . The solid, dotted and long-dashed line are  $A_3$ ,  $A_{Siegert}$  and  $A_{d-wave}$ , respectively. The Siegert term has been calculated assuming  $d_\Delta = 25g_\pi$ . The two dashed lines marked “Upper bound” and “Lower bound” give a possible range of the anapole contribution. The vertical line denotes the  $Q^2$  of the present measurement. This plot has been reproduced from [25] with the only change being the addition of the vertical line. Note that the theoretical calculations presented in this plot were performed at different kinematics than those of the present measurement.

	$A^{tree}$ (ppm)	$A^{ewrc}$ (ppm)	$R_i^{ewk}$
$A_1$	-32.7	-32.2	-1.4%
$A_2$	-0.56	-0.55	-1.2%
$A_3$	-4.3	-1.8	-58.8%
$A_{tot}$	-37.6	-34.6	-8.0%

TABLE 6.2: Summary of theoretical asymmetry terms with and without electroweak radiative corrections applied. The total asymmetry is given by summing the three components.

## 6.2 Theoretical Uncertainty

Before extracting information from the measured asymmetry, the uncertainty must be finalized. In the previous two chapters, the experimental systematic uncertainty was determined for each correction applied. Additionally, the statistical uncertainty, which is a function of the amount of data collected, was altered as corrections for effects such as dead time and backgrounds added and subtracted events. The final source of uncertainty that must be considered is the theoretical uncertainty. Though it will be a small contribution to the total uncertainty, knowledge of the theoretical uncertainty will provide insight into where improvements can be made to aid in interpreting future experimental results.

To extract information about the axial response from the measured asymmetry, it is first necessary to isolate the axial term,  $\Delta_{(3)}^\pi$ , from the vector terms,  $\Delta_{(1)}^\pi$  and  $\Delta_{(2)}^\pi$ . How well  $\Delta_{(3)}^\pi$  can be determined will depend on how well the vector contributions are known. Since  $\Delta_{(1)}^\pi$  depends only on Standard Model couplings, which are well known, it can be treated as exact. The same cannot be done with  $\Delta_{(2)}^\pi$ , the uncertainty of which will depend on the model used and approximations needed to implement the primary model in simulation. Once  $\Delta_{(3)}^\pi$  is determined, the axial transition form factor,  $G_{N\Delta}^A$ , can be extracted. The uncertainty will then need to be expanded to include factors related to the parameterizations used to compute  $\Delta_{(3)}^\pi$  and to account for the neglected non-resonant axial contribution. In this section, the sources of theoretical uncertainty will be presented and the total theoretical uncertainty computed.

### 6.2.1 Uncertainty on $\Delta_{(2)}^\pi$

For the non-resonant vector term in the asymmetry,  $\Delta_{(2)}^\pi$ , the sources of uncertainty were first introduced in Section 5.1.2. These sources include approximations required to

implement the model in simulation and the fit used to compute the transverse magnetic, transverse electric and longitudinal multipoles. A series of studies was performed to test the impact of the approximations and fits used on the asymmetry. The results of these tests will be used to estimate an uncertainty on the  $\Delta_{(2)}^\pi$  calculation.

As explained previously,  $\Delta_{(2)}^\pi$  is expressed as a sum over multipoles that can be computed using MAID [74]. While MAID can be interfaced with G0GEANT to compute the multipoles on an event-by-event basis, the processing power and time required to do this made it impractical. Instead, MAID was run independently and the multipoles were computed over a range of  $W$  for each of three different  $Q^2$  values that spanned the acceptance. These values were chosen based on the distribution of  $W$  and  $Q^2$  across the inelastic locus as determined by G0GEANT. The MAID output was grouped into lookup tables and the multipoles for a given event were calculated by first choosing the lookup table for the  $Q^2$  that most closely matched the event  $Q^2$  and then using a 1-dimensional interpolation in  $W$ . In the process of implementing the code, a test was performed to determine if this approach was sufficient or if more precision in  $Q^2$  was needed. Rather than further subdividing the  $Q^2$  range to check for increased precision, the code was altered to use multipoles for a single constant  $Q^2$ , the locus average, regardless of the event  $Q^2$ . The resulting asymmetry difference of 0.04 ppm will be used as a conservative estimate of the uncertainty due to the  $Q^2$  binning approximation.

The second approximation involved the truncation of the series after the first three terms. Again, this was tested in the context of implementing the model to ensure that accuracy of the simulated asymmetry was not affected. The assumption that ending the series after the  $l = 2$  term was based on the observation that the individual multipoles for a given kinematic point decreased with increasing  $l$ . As was discussed in the previous chapter, the assumption was tested by ending the series sooner and seeing how this im-

pacted the results. The results of the test performed were that ending the series at  $l = 1$  increased  $A_2$  by 0.08 ppm, while including only the  $l = 0$  term decreased the asymmetry in magnitude by 0.4 ppm. Based on these results, an uncertainty of 0.5 ppm will be included in the total.

The last implementation related consideration is the version of the MAID fit used to compute the multipoles. The MAID collaborators regularly update their fits to include the most recent world data, resulting in slight changes to the computed multipoles. In the simulation, the MAID2003 and MAID2007 versions of the multipoles were available. To determine the uncertainty,  $A_2$  was computed using the two versions and the uncertainty was defined as the difference between the two, resulting in an uncertainty of 0.1 ppm. As an aside, there was additional information available to confirm this finding. The test to determine when to end the series was performed originally using the 2003 multipoles, then re-performed when the newer version was implemented. Comparing the two sets of results from that test, the change between the fits was consistently 0.1 ppm.

Adding this uncertainty in quadrature to the 0.5 ppm uncertainty arising from truncating the series and 0.04 ppm from the  $Q^2$  binning leads to a total simulation uncertainty of 0.5 ppm. In terms of the theoretical  $A_2$  quoted in the previous section, this amounts to an uncertainty of nearly 100%. This represents a fairly conservative estimate of the limitations of the implementation of the model in simulation.

One final consideration for the  $\Delta_{(2)}^\pi$  uncertainty is the model itself. As was discussed in Section 6.1.1, a second model for the asymmetry was implemented in the simulation. Computing the asymmetry at the average experimental kinematics leads to an  $A_2$  value of 0.11 ppm in the Matsui model compared to  $-0.55 \pm 0.5$  ppm using the Musolf model as implemented in GOGENT. In order to accommodate this difference, the uncertainty on  $A_2$  will be expanded to 0.7 ppm. This is equivalent to adding a 0.5 ppm uncertainty for

the model. This leads to a final theoretical value of  $A_2 = -0.55 \pm 0.7$  ppm.

### 6.2.2 Uncertainty in the Axial Term

The uncertainty in the axial component of the asymmetry,  $\Delta_{(3)}^\pi$ , stems from the parameterization of the form factors and from the decision to neglect the non-resonant contribution. Expanding on previously provided definitions,  $\Delta_{(3)}^\pi$  can be written

$$\Delta_{(3)}^\pi = \frac{2(E + E')}{M} (1 - 4 \sin^2 \theta_W^0) (1 - R_A^{ewk}) H^{EM}(Q^2, \theta) G_{N\Delta}^A(Q^2) + (\Delta_{(3)}^\pi)_{nonres}, \quad (6.14)$$

where  $\sin^2 \theta_W^0$  is the tree level value defined in Equation 6.10,  $(\Delta_{(3)}^\pi)_{nonres}$  contains any non-resonant axial contributions to the asymmetry,  $R_A^{ewk}$  represents the one-quark electroweak radiative correction and the multi-quark electroweak radiative corrections have been neglected. Since the physics of interest is contained in the form factor  $G_{N\Delta}^A(Q^2)$ , it is necessary to determine the uncertainty on the remaining terms. Any uncertainty on  $\sin^2 \theta_W^0$  and  $R_A^{ewk}$  stems from the knowledge of Standard Model parameters and one-quark electroweak radiative corrections. Since these have been well determined, the associated uncertainties can be neglected.

The non-resonant axial contribution,  $(\Delta_{(3)}^\pi)_{nonres}$ , was studied by both Hammer and Dreschel [26], and Mukhopadhyay *et al.* [24] and found to be small. As discussed in Section 2.3.4, Hammer and Dreschel found that their complete model differed from the resonant models by  $< 10\%$ . Based on these findings, a conservative uncertainty of 10%, or 0.18 ppm, will be applied to account for the presence of non-resonant processes. This leaves  $H^{EM}(Q^2, \theta)$  as the final piece that must be taken into account.

The function  $H^{EM}(Q^2, \theta)$  depends on the electromagnetic form factors  $C_i^\gamma(Q^2)$  which are computed using a dipole form for the  $Q^2$  parameterization. The full defini-

tion of  $H^{EM}(Q^2, \theta)$  was given in Chapter 2 in Equation 2.70. The  $C^\gamma$  are defined

$$C_i^\gamma(Q^2) = C_i^\gamma(0)G_D^V(Q^2), \quad i = 3, 4, \quad (6.15)$$

where  $G_D^V(Q^2)$  is given by

$$G_D^V(Q^2) = \left[1 + \frac{Q^2}{M_V^2}\right]^{-2}. \quad (6.16)$$

Since the world value of the vector dipole mass,  $M_V$ , used to compute  $C_i^\gamma(Q^2)$  is well-determined, its uncertainty can be neglected. The two  $C_i^\gamma(0)$  values used in this thesis are those determined by Adler as quoted by Nath [12]. Since these coefficients depend on model input and data, the uncertainty due to the choice of model can be estimated by computing the asymmetry using  $C_i^\gamma(0)$  computed using different models.

Mukhopahdyay *et al.* [24] summarized the value of the form factors at  $Q^2 = 0$  for several different calculations in their Table 1. The asymmetry at the  $G^0$  kinematics was computed using the values from a selection of the sources they presented and the resulting  $A_3$  for each is given in Table 6.3. The deviations from the nominal  $A_3$ , given in the table as the percent change, range from about 10% to 35%, which translates to a range of 0.18 to 0.62 ppm. From these findings, an uncertainty of 0.62 ppm can be assigned to  $H^{EM}$ . Adding this to the uncertainty due to the non-resonant contribution leads to a total uncertainty on the axial term of 0.65 ppm.

### 6.2.3 Summary of Theoretical Uncertainty

The total theoretical uncertainty,  $\sigma_{th}$ , can now be computed by summing the various sources presented above. Table 6.4 summarizes the different contributions, denoted  $\sigma_i$ , to the uncertainty along with the sum for each  $\Delta_{(i)}^\pi$  term summed individually. The only source of uncertainty in  $\Delta_{(1)}^\pi$  is the electroweak radiative corrections, which have a

Ref	$C_3^\gamma(0)$	$C_4^\gamma(0)$	$A_3^{tree}$ (ppm)	% change
Nath [12]	1.85	-0.89	-4.33	—
Ravndal [82]	1.70	-1.30	-4.77	10.2%
Orsay [83]	1.54	-1.17	-5.27	21.7%
Jones & Petcov [31]	2.05	-1.56	-3.96	-8.5%
Hemmert <i>et al.</i> [40]	1.39	-1.06	-5.83	34.6%

TABLE 6.3: Theoretical  $A_3$  computed using values for the Adler form factors at  $Q^2 = 0$  computed using several different approaches. The nominal value used in this thesis is given in the first row and the percent change is computed by dividing the difference between each alternate  $A_3$  and the nominal  $A_3$  by the nominal value.

negligible uncertainty. The two remaining terms in the asymmetry,  $\Delta_{(2)}^\pi$  and  $\Delta_{(3)}^\pi$ , each contribute between 0.6-0.8 ppm. Summing these contributions in quadrature leads to a total theoretical uncertainty of 0.96 ppm. In terms of the total theoretical asymmetry,  $A_{theory} = -34.6$  ppm, this is a small ( $< 3\%$ ) error, but relative to the axial term,  $A_3 = -1.8$  ppm, the effect is larger, at 54%. These findings suggest that even without the large experimental error found in the present measurement, a precise determination of  $A_3$  and, in turn,  $G_{N\Delta}^A$ , would not be possible. Note that the multi-quark electroweak radiative corrections, and their uncertainty, have been completely neglected here.

### 6.3 Extracting the Axial Contribution from $A_{inel}$

Now that the corrections to the asymmetry have been applied and the total uncertainty is determined, the axial contribution to the asymmetry can be extracted from the measured asymmetry,  $A_{inel}$ . Recall that the asymmetry is the sum of three terms, as

Source	$\sigma_{th}^i$ (ppm)	Source	$\sigma_{th}^i$ (ppm)
$R_1^{ewk}$	0.00	$R_2^{ewk}$	0.00
Total $d\Delta_{(1)}^\pi$	0.00	$Q^2$ binning	0.04
$R_A^{ewk}$	0.00	Series Truncation	0.50
$(\Delta_{(3)}^\pi)_{nonres}$	0.18	MAID version	0.10
$H^{EM}(Q^2, \theta)$	0.62	Model	0.50
Total $d\Delta_{(3)}^\pi$	0.65	Total $d\Delta_{(2)}^\pi$	0.72
Total $dA_{theory} = 0.96$ ppm			

TABLE 6.4: Summary of theoretical uncertainties.

defined in Chapter 2,

$$\begin{aligned}
 A_{inel} &= A_1 + A_2 + A_3 \\
 &= \frac{1}{2}A^0 [\Delta_{(1)}^\pi + \Delta_{(2)}^\pi + \Delta_{(3)}^\pi] , \tag{6.17}
 \end{aligned}$$

where  $A^0$  is a  $Q^2$  dependent term that is defined in Equation 2.43. The axial term,  $\Delta_{(3)}^\pi$ , is then defined as in Equation 6.14 in the previous section. The final goal is to determine the value of the axial transition form factor,  $G_{N\Delta}^A$ . This will be done through a two step process that involves first determining  $A_3$  from  $A_{inel}$  and then extracting  $G_{N\Delta}^A$  from  $A_3$ .

The inelastic asymmetry from the high-energy hydrogen run period, originally given in Table 5.10, is

$$A_{inel} = -33.44 \pm (5.3)_{stat} \pm (5.1)_{sys} \text{ ppm} . \tag{6.18}$$

Figure 6.8 shows this asymmetry and the Musolf model predictions plotted as a function of  $Q^2$ . Given the size of the experimental error in comparison with the model prediction for  $A_3$ , it will not be possible to make any conclusive statements about the axial contribution. However,  $A_3$  can still be computed. In order to determine the contribution from  $A_3$

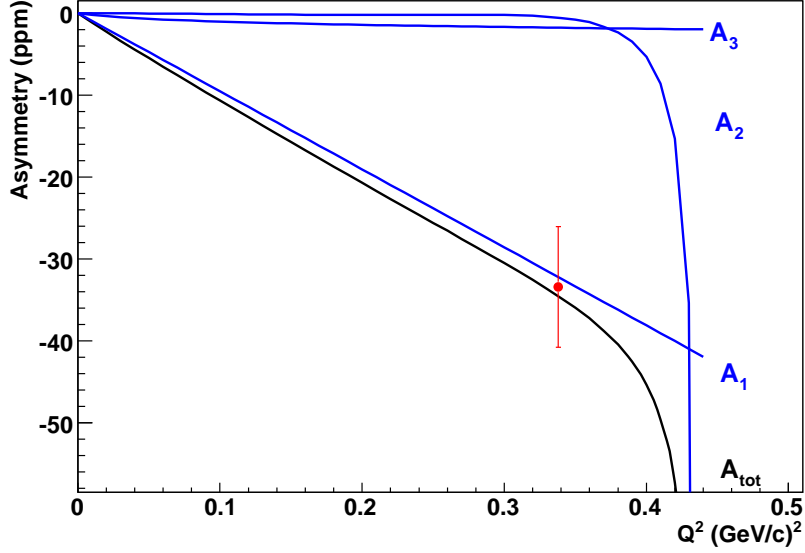
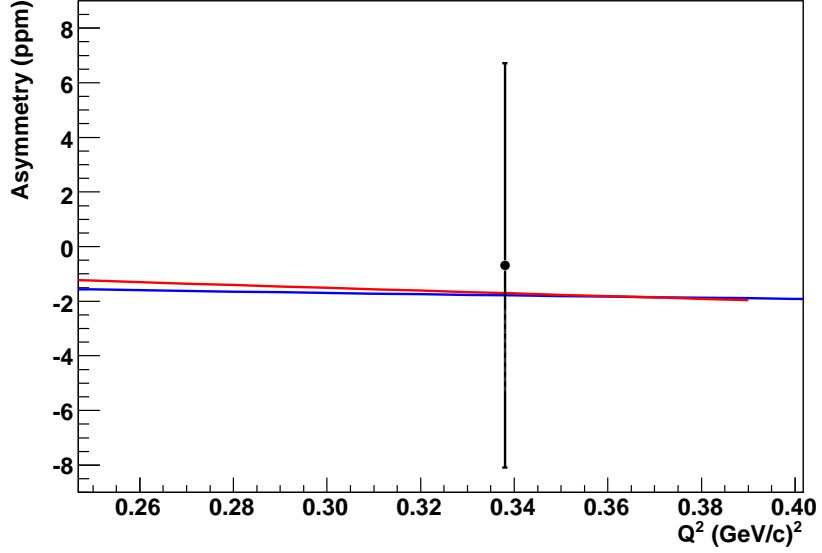


FIG. 6.8: Measured asymmetry,  $A_{inel}$ , plotted with the theoretical value from the Musolf model. The blue curves represent the individual components of the asymmetry and the black curve is the total asymmetry.

to the measured asymmetry, the theoretical values of  $A_1$  and  $A_2$  will be used to subtract the vector contributions, leaving only the axial piece of the asymmetry. As shown in Table 6.2, the theoretical  $A_1^{th} = -32.2$  ppm and  $A_2^{th} = -0.55$  ppm. Subtracting these from the measured asymmetry of 33.44 ppm and propagating the errors leads to

$$A_3 = -0.69 \pm (5.3)_{stat} \pm (5.1)_{sys} \pm (0.7)_{th} \text{ ppm} . \quad (6.19)$$

These findings indicate that, within the present errors, the axial term of the asymmetry is consistent with zero. This is not a surprising result when one considers that the theoretical value of  $A_3^{th} = -1.8$  ppm is significantly lower than the experimental uncertainty of  $\sim 7$  ppm. The large errors also prohibit this result from being used to distinguish between the model used in this thesis and the Matsui model, which leads to an  $A_3^{th}$  of -1.7 ppm. Since these two model asymmetries only differ by  $\sim 0.1$  ppm, a significant improvement in the precision would be needed to determine if the experimental results favor one



ht

FIG. 6.9: Theoretical  $A_3$  as a function of  $Q^2$  with the extracted value and error shown as a point. The primary model of this thesis, the Musolf model, is shown in blue, while the Matsui model prediction is in red.

or the other. The extracted value for  $A_3$  is plotted as a function of  $Q^2$  along with both models in Figure 6.9.

The extracted  $A_3$  can be used to determine  $G_{N\Delta}^A$  by dividing out the contribution of  $H^{EM}$ , such that

$$G_{N\Delta}^A = -\frac{M}{E + E'} \frac{2\pi\alpha\sqrt{2}}{G_F Q^2} \frac{A_3}{2H^{EM}(Q^2, \theta)[1 - 4\sin^2\theta_W^0]}. \quad (6.20)$$

World values for  $\alpha$ ,  $M$  and  $G_F$  are well determined and have been compiled by the Particle Data Group [2], while the electromagnetic contribution  $H^{EM}$ , scattered electron energy  $E'$  and  $Q^2$  have been determined from simulation. The value used for the incident electron energy,  $E$ , is the beam energy of 0.685 MeV measured during the high-energy hydrogen run period with a reduction included to account for energy loss in the target. This energy loss, determined through simulation, leads to an effective incident electron energy of 0.680 GeV. Table 6.5 summarizes the values of all quantities used to compute

Quantities Used to Determine $A_3$				
$A_{inel}$	-33.4	ppm	$\alpha$ [2]	$7.3 \times 10^{-3}$
$A_1^{th}$	-32.2	ppm	$G_F$ [2]	$1.17 \times 10^{-5} \text{ GeV}^{-2}$
$A_2^{th}$	-0.55	ppm	$M$ [2]	0.938 $\text{GeV}/c^2$
$E$	0.680	GeV	$E'$	0.229 GeV
$Q^2$	0.338	$(\text{GeV}/c)^2$	$\sin^2 \theta_W^0$ [25]	0.21
$H_{EM}$	-0.84			

TABLE 6.5: Summary of quantities needed to extract  $A_3$  and  $G_{N\Delta}^A$  from  $A_{inel}$ . Only the central values are given here. Uncertainties on physical constants are neglected.

$A_3$  and  $G_{N\Delta}^A$ . Using the values in this table leads to a  $G_{N\Delta}^A$  of

$$G_{N\Delta}^A = -0.046 \pm (0.35)_{stat} \pm (0.34)_{sys} \pm (0.06)_{th} . \quad (6.21)$$

The theoretical prediction of  $G_{N\Delta}^A$  calculated in simulation for the experimental kinematics is -0.196. In the present case, the uncertainty is so large that any difference between these two values is insignificant in comparison. If a precise measurement were available, agreement or disagreement with the theoretical calculation could be used to verify the parameterization used when defining the form factor.

$G_{N\Delta}^A$  depends on the axial form factors,  $C_i^A$ . The form factors themselves are parameterized using a dipole form, such that

$$C_i^A(Q^2) = C_i^A(0)G_D^A(Q^2)\xi^A(Q^2) , \quad (6.22)$$

where  $G_D^A(Q^2)$  is given by,

$$G_D^A(Q^2) = \left[ 1 + \frac{Q^2}{M_A^2} \right]^{-2} . \quad (6.23)$$

The dipole form is used here not only because it is a convenient parameterization, but also because it works reasonably well for the nucleon form factors. To account for the

differences that occur in the transition to the  $\Delta$ , an additional function,  $\xi^A$  is used to give more complexity to the  $Q^2$  dependence. The definition of  $\xi^A$  used in this thesis was given by Schreiner and von Hippel [30],

$$\xi^A(Q^2) = 1 + \left( \frac{a'Q^2}{b' + Q^2} \right), \quad (6.24)$$

where  $a'$  and  $b'$  were determined from fits to the Adler form factors. The Matsui model instead uses an exponential dependence, defining  $\xi^A$  as

$$\xi^A(Q^2) = (1 + aQ^2)e^{bQ^2}, \quad (6.25)$$

where  $a$  and  $b$  were determined by Matsui *et al.* through fits to data. A precise measurement of  $G_{N\Delta}^A$  could help distinguish between these two parameterizations of  $Q^2$ , giving insight into the true  $Q^2$  dependence of the form factor.

Additional possible causes for differences between the measured and theoretical values of  $G_{N\Delta}^A$  include the axial mass  $M_A$ , which has been determined through experiment, and the values of the form factors at  $Q^2 = 0$ , which depend on modeling and fits to data. The computation of the theoretical asymmetry in this thesis made use of the current world value for  $M_A$ . Since there is some recent controversy over this value, which was discussed in Section 2.3.4, a discussion of the limitations on the determination of the axial mass from this measurement will be postponed until Section 6.4.1. The coefficients  $C_i^A(0)$  used to compute the theoretical  $G_{N\Delta}^A$  are the Adler values, but there are other values available from different sources that have been computed using different methods. A similar study to that performed in Section 6.2.1 to find the uncertainty on  $H^{EM}$  could be used to compute  $G_{N\Delta}^A$  for different values for  $C_i^A(0)$ . By comparing the values of the form factor computed using different coefficients to the measured value, one could potentially make a statement about the different methods used. Once again, however, the limited precision

of this measurement precludes drawing any conclusions about these coefficients or the methods used to determine them. Therefore, such a study would not be practical at this time.

## 6.4 Additional Extracted Quantities

The  $A_3$  and  $G_{N\Delta}^A$  found in the previous section represent the primary focus of this thesis. In addition to these quantities, the asymmetry resulting from this type of measurement can be used to compute other quantities that are of experimental and theoretical interest. In this section, three possible applications of the inelastic asymmetry will be presented. As with  $A_3$ , the large uncertainty on the measured asymmetry makes any precise determination of these quantities impossible. However, computing them can give an idea of how precise a measurement would need to be in order for such findings to be useful.

### 6.4.1 Axial Mass

As was discussed in Section 2.3.4, the axial mass,  $M_A$ , has been a topic of theoretical and experimental interest, with recent experimental results indicating a possible value that differs significantly from the world average.  $M_A$  is a quantity that arises from the dipole parameterization used to define the  $Q^2$  dependence of the axial form factors,  $C_i^A$ . A precise measurement of the inelastic asymmetry could lead to an extraction of  $M_A$  at a given  $Q^2$  point, while multiple measurements could lead to a functional form for the axial mass as a function of  $Q^2$ .

In Section 2.3.4, a plot of  $A_3$  as a function of  $M_A$  over a range that covers all of the different proposed values was presented. From this plot it could be seen that in order to

distinguish between the world value and the newly determined higher values, one would need a  $\sim 1$  ppm precision determination of  $A_3$ . The figure has been reproduced here in Figure 6.10 with the extracted  $A_3$  included on the plot to illustrate the limitations of the present measurement. Note that the theoretical uncertainty on  $A_3$  as determined in Section 6.2 is about 50%. Therefore, even if reductions were made in the experimental uncertainty, improvements would need to be made on the theoretical calculation of the asymmetry in order to gain precise information from this measurement of  $A_3$ .

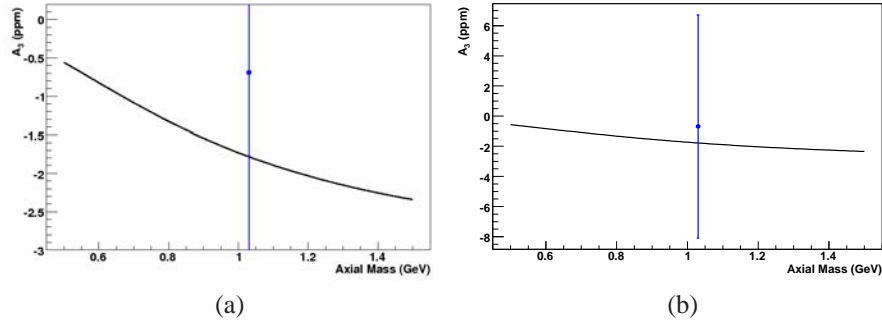


FIG. 6.10: Axial component of the asymmetry,  $A_3$ , plotted as a function of axial mass,  $M_A$ . The extracted value of  $A_3$  is shown as a single point. The two plots are the same except for the  $y$ -axis range.

### 6.4.2 Standard Model Test

Originally, a measurement of the inelastic asymmetry, specifically  $\Delta_{(1)}^{\pi}$ , was proposed as a possible Standard Model test because of its direct relationship to the weak mixing angle,  $\theta_W$ . Though there is current experimental and theoretical interest in the behavior of  $\sin^2 \theta_W$  at very low  $Q^2$ , its value is well understood for the  $Q^2$  region studied in this thesis. As such, given the lack of precision, there is no new information that can be obtained by extracting the weak mixing angle from this measurement. Additionally, the

theoretically uncertain, and potentially large, electroweak radiative corrections studied by Zhu *et al.* [25] indicate that the use of this type of measurement to precisely determine  $\sin^2 \theta_W$  would not be practical.

However, since the information is available, an estimate of  $\sin^2 \theta_W$  from  $A_{inel}$  can still be made. The asymmetry can be written in terms of the weak mixing angle as

$$A_{inel} = \frac{1}{2} A^0 [2(1 - 2 \sin^2 \theta_W) + \Delta_{(2)}^\pi + 2(1 - 4 \sin^2 \theta_W F(Q^2, s))] , \quad (6.26)$$

where both  $\Delta_{(1)}^\pi$  and  $\Delta_{(3)}^\pi$  are dependent on  $\sin^2 \theta_W$  and  $\Delta_{(2)}^\pi$  is not. Solving for  $\sin^2 \theta_W$  leads to

$$\sin^2 \theta_W = \frac{1}{2(1 + 2F(Q^2, s))} \left( 1 + F(Q^2, s) - \frac{A_{inel} - A_2}{A^0} \right) , \quad (6.27)$$

where  $A_{inel}$  is the measured asymmetry of -33.4 ppm,  $A^0$  is computed from values given in Table 6.5 and is found to be -61 ppm, and  $A_2$ , computed using the Musolf model, is -0.55 ppm.  $F(Q^2, s)$  is computed using  $H^{EM}$  and the theoretical  $G_{N\Delta}^A$ , along with the initial and final electron energies and proton mass and found to be 0.16. The full uncertainty in the measurement, along with all theoretical uncertainty, will be assigned to the computed  $\sin^2 \theta_W$ .

Substituting these values into Equation 6.27 leads to

$$\sin^2 \theta_W = 0.2353 \pm (0.033)_{stat} \pm (0.032)_{sys} \pm (0.006)_{th} . \quad (6.28)$$

Summing the different contributions to the uncertainty in quadrature leads to a total uncertainty of 0.05. The current world value of  $\sin^2 \theta_W$  is  $0.23116 \pm 0.00013$  [2]. The result here is consistent with the world value within errors, but the uncertainty is too large to give meaningful results. Even without the experimental errors, the theoretical uncertainty alone is an order of magnitude larger than the uncertainty on the world value.

### 6.4.3 Electroweak Radiative Effects: Anapole and Siegert terms

In the discussion of electroweak radiative corrections in Section 6.1.2, it was noted that multi-quark electroweak radiative effects may be present in the data. Two such radiative corrections that potentially contribute in a non-trivial way at the present kinematics are the anapole and Siegert terms. Because of the uncertainty involved in the theoretical interpretation of these effects, they have been neglected in the results discussed thus far. As a result, these effects could account for any difference between the measured and theoretical  $A_3$ . Unfortunately, the large uncertainty on  $A_3$  makes any precise statements about these effects impossible. In order to determine what precision would be necessary, a rough calculation can be done to estimate the contributions of each of these terms to the asymmetry.

The anapole and Siegert asymmetry contributions are written in terms of coupling constants  $a_\Delta$  and  $d_\Delta$  such that

$$A_{anapole} = 0.006 \left( \frac{a_\Delta}{g_\pi} \right), \quad (6.29)$$

$$A_{Siegert} = -0.006 \left( \frac{d_\Delta}{g_\pi} \right), \quad (6.30)$$

where these equations have been adapted from Zhu *et al.* [25] to compute the asymmetry at the present kinematics. The  $G^0$  measurement of pion asymmetry at low  $Q^2$  placed a  $\pm 25g_\pi$  bound on  $d_\Delta$  [43]. Substituting this value into the equation above leads to  $A_{Siegert} \leq \mp 0.15$  ppm. For the anapole contribution, no measurements have been performed to bound  $a_\Delta$ , but Zhu *et al.* assert that a reasonable guess would be that the  $a_\Delta$  and  $d_\Delta$  are roughly equal in magnitude, though they may differ in sign. Assuming  $a_\Delta \sim 25g_\pi$  leads to  $|A_{anapole}| = 0.14$  ppm.

To take these effects into account, the total asymmetry can be written

$$A_{inel} = A_1 + A_2 + A_3 + A_{anapole} + A_{Siegert} . \quad (6.31)$$

Assuming the  $25g_\pi$  bound for  $a_\Delta$  is reasonable, the quantity  $A_{anapole} + A_{Siegert}$  is in the range  $\pm 0.31$  ppm, with the exact value depending on the relative signs of the two terms. Therefore, in order for the measurement to be sensitive to these electroweak radiative effects, the uncertainty would likely have to be  $< 0.3$  ppm.

# CHAPTER 7

## Conclusion

The parity-violating asymmetry from inelastic electron scattering at backward angle near the  $\Delta$  resonance has been measured for both hydrogen and deuterium targets as part of the  $G^0$  experiment. This measurement represents the first measurement of the inelastic parity-violating asymmetry in the neutral weak sector. The possibility of such a measurement was first proposed by Cahn and Gilman in 1978 for use as a Standard Model test [11]. For the present measurement, the asymmetry was used to access the axial response of the proton as it transitions to the  $\Delta$ . This response is characterized by the axial transition form factor,  $G_{N\Delta}^A$ . Unfortunately, the uncertainty of this measurement is too large to make any conclusive statements about  $G_{N\Delta}^A$ . The large uncertainty stemmed from several sources. The parasitic nature of this measurement, which used background data collected while measuring elastic scattering, placed a constraint on the statistical precision. The  $G^0$  spectrometer settings were optimized to focus the elastic peak on the detectors, meaning the inelastic peak was only partially covered by the detector acceptance. The lack of optimization also led to high systematic errors from backgrounds.

In spite of the large uncertainty, the findings indicate that the theoretical expressions for the total asymmetry first presented by Cahn and Gilman, and later expanded upon by Musolf *et al.* [22], accurately predict the asymmetry within the 22% uncertainty of the hydrogen measurement. As was expected, the structure-independent resonant vector term in the asymmetry dominated the results and the impact of the non-resonant vector and axial responses was small in comparison. Due to the lack of experimental precision, conclusive statements about the axial response and  $G_{N\Delta}^A$  cannot be made.

## 7.1 Potential Improvements

In order to make a more precise measurement, steps would first need to be taken to achieve higher statistical precision. This could be accomplished using the  $G^0$  experimental apparatus by collecting data over a longer period of time, increasing the beam current or target length to collect more data, or changing the spectrometer settings to focus the inelastic peak onto the detectors. However, these improvements still may not be enough to gather the precision necessary to extract  $G_{N\Delta}^A$  from  $A_{inel}$ .

Optimizing the detectors for the inelastic measurement would also potentially reduce the systematic error by reducing backgrounds. A further reduction could be made by having a better understanding of the backgrounds. One source of systematic uncertainty in the hydrogen measurement was the high statistical uncertainty in the deuterium asymmetry which was used to approximate the false asymmetry due to the aluminum target windows. A more precise measurement of the deuterium asymmetry or a measurement of the aluminum asymmetry itself could reduce this error. The largest background in the inelastic locus was the radiative tail of the elastics. Simulation of the inelastic asymmetry at 360 MeV, the beam energy for the other two  $G^0$  backward angle measurements, indicated

that the separation between the peaks increased as the beam energy decreased. Therefore, running at a lower beam energy could lead to more separation between the elastic and inelastic peaks, reducing the rates from the elastic tail in the inelastic locus. However, the simulation also showed that this would lead to lower rates, meaning that a longer run period would likely be needed to offset the loss in statistical precision.

As an example, one can consider the Qweak experiment discussed in Chapter 2 which plans to make a precise measurement of  $A_{inel}$  at very low  $Q^2$ . To achieve higher statistics, they will perform dedicated “inelastic” runs where the inelastic events will be focused onto the detectors. In addition to these dedicated runs, the Qweak experiment features a longer target than was used by  $G^0$ , measures forward angle scattering and will run at higher beam current. These factors will all combine to increase the measured rates and, therefore, decrease the statistical error. If one were to repeat the  $G^0$  hydrogen measurement using the Qweak target, which is roughly twice as long, and run at the Qweak beam current, which is roughly three times higher, it would result in an increase in the amount of data collected by about a factor of six. The statistical uncertainty is related to the square root of this count, so this would improve the precision by a factor of  $\sqrt{6}$ , or  $\sim 2.5$ . Thus, the statistical uncertainty of 5.3 ppm would be reduced to 2.1 ppm, still greater than 100% of the theoretical  $A_3$  of 1.8 ppm.

To make a 25% measurement of  $A_3$ , the uncertainty on  $A_{inel}$  would need to be 0.45 ppm or further reduced by a factor of 5. To reduce the statistical uncertainty by a factor of 5, one would need to collect 25 times more data. This could be done by further increasing the target length and beam current or by running longer. The hydrogen run period collected  $\sim 550$  hours of data. Multiplying this by 25 would lead to over 13,000 hours, or more than 18 months, of continuous data taking. Assuming this could all be done, and  $A_3$  was determined to within 0.5 ppm, the uncertainty on the extracted  $G_{N\Delta}^A$  would be

0.03, which is about 15% of the theoretical  $G_{N\Delta}^A$ . This, of course, completely neglects any systematic uncertainty. This exercise indicates that the level of precision needed to determine  $G_{N\Delta}^A$  cannot be practically attained using a measurement like  $G^0$ .

With a more precise measurement, the theoretical uncertainty involving the electroweak radiative corrections discussed in Section 6.1.2 could complicate the interpretation of results. As was shown in Section 6.4.3, a measurement at the 0.3 ppm level of precision would begin to be sensitive to these effects. In addition to further theoretical input, measurements taken at different  $Q^2$  could lead to a better understanding of the anapole and Siegert responses, thereby lowering the theoretical uncertainty.

## 7.2 Final Summary

Measurements of the parity-violating asymmetry at  $Q^2 = 0.34 \text{ (GeV/c)}^2$  were performed on both hydrogen and deuterium targets using a longitudinally polarized 0.680 MeV electron beam. The experimental apparatus consisted of a 20 cm liquid target, a toroidal magnet and a symmetrical detector system containing two sets of scintillators, labeled CEDs and FPDs, to provide kinematic resolution and Cherenkov (CER) detectors for particle identification. Scattered electron rates were measured by counting coincidences of one of each scintillator with the Cherenkov, or CED·FPD·CER. The helicity of the beam was flipped at regular intervals, allowing for a calculation of the asymmetry from the measured rates at the two helicities. The measured asymmetry was corrected for beam polarization, detector and electronics dead time, random coincidences, helicity correlated beam properties and backgrounds. Additional corrections for acceptance averaging and electromagnetic radiative effects were also applied to the hydrogen asymmetry that could not be applied to the deuterium asymmetry because they require theoretical

input not available for the neutron.

The corrected asymmetries are

$$A_{inel} = -33.4 \pm (5.3)_{stat} \pm (5.1)_{sys} \text{ ppm} , \quad (7.1)$$

$$A_{inel}^D = -43.6 \pm (14.6)_{stat} \pm (6.2)_{sys} \text{ ppm} . \quad (7.2)$$

The total uncertainty on the hydrogen measurement is 7.4 ppm, or 22%, while that of the deuterium is much higher, at 16 ppm or 37%. The biggest correction for both measurements was the background correction, which also contributed most significantly to the systematic uncertainty. For the deuterium data, the rate corrections were large due to the high rates from the deuterium target, contributing nearly as much to the uncertainty as the background correction.

The hydrogen asymmetry is modeled as the sum of resonant and non-resonant vector hadron terms and a resonant axial hadron term. The non-resonant axial effects are treated as a 10% theoretical uncertainty. The axial response can be isolated by subtracting off the two vector terms, leading to

$$A_3 = -0.69 \pm (5.3)_{stat} \pm (5.1)_{sys} \pm (0.7)_{th} \text{ ppm} . \quad (7.3)$$

From this asymmetry, the axial transition form factor,  $G_{N,\Delta}^A$ , can be extracted.  $G_{N,\Delta}^A$  describes the re-arrangement of spin that occurs as the proton transitions to the  $\Delta$ . From the measured asymmetry, the form factor is found to be

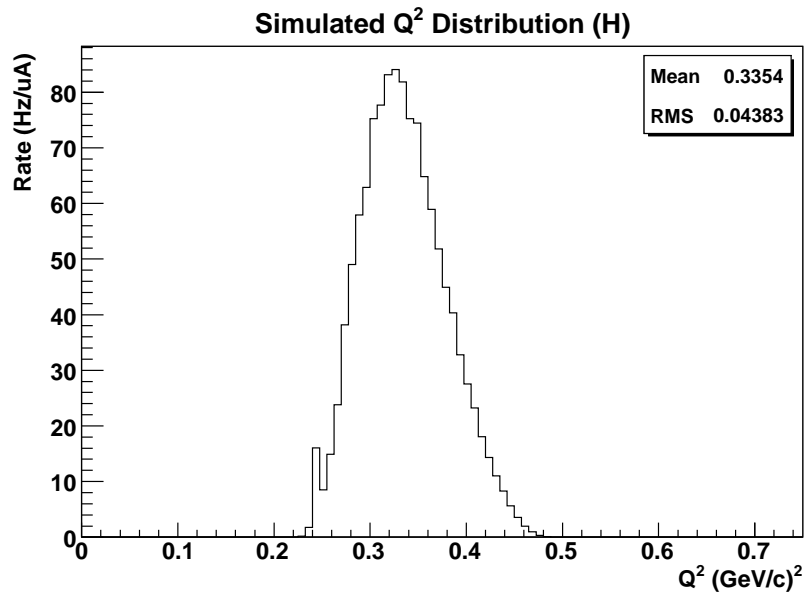
$$G_{N\Delta}^A = -0.046 \pm (0.35)_{stat} \pm (0.34)_{sys} \pm (0.06)_{th} . \quad (7.4)$$

The uncertainty in this measurement is so large that no conclusive statements can be made about either  $A_3$  or  $G_{N\Delta}^A$ . However, these results are still significant in that they represent the first measurement of  $A_{inel}$  and the first experimental study of the axial response using a neutral current reaction.

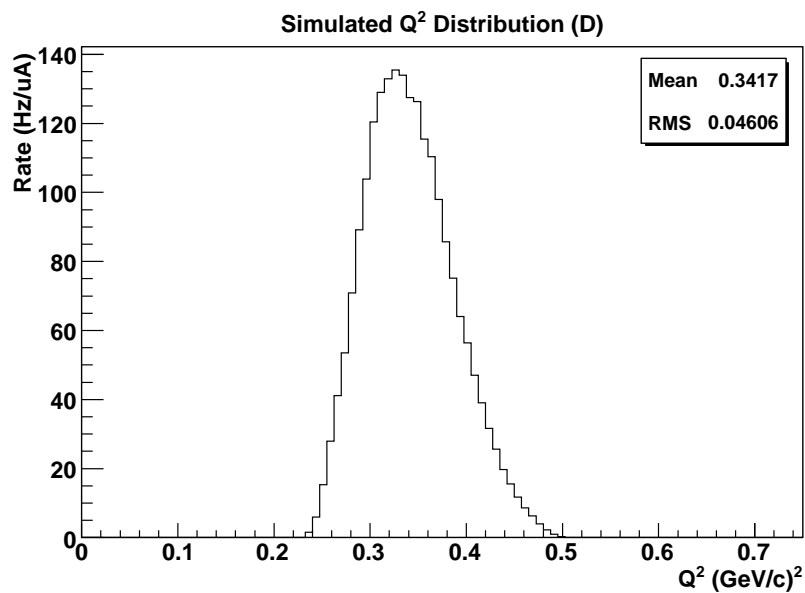
# APPENDIX A

## Experimental Kinematics

This appendix contains figures representing the distributions of assorted kinematic variables across the experimental acceptance for inelastic events as determined from the G0GEANT simulation. The figures include only inelastically scattered events. In Figures A.1 through A.5, distributions for both the hydrogen and deuterium kinematics are presented as one-dimensional histograms with the kinematic variable on the horizontal axis and cross-section weighted yield on the vertical axis. These figures represent locus average kinematics and include only events in inelastic locus cells. In Figures A.6 and A.7, distributions for both hydrogen and deuterium  $Q^2$  and  $W$  are given for each cell in the CED·FPD coincidence matrix. The average cell kinematics are indicated both numerically and using a color scale. In a given cell, the average is based on the cross-section weighted distribution of events in that cell. In all figures, the cross sections have been corrected for the electromagnetic radiative effects discussed in Section 5.3.



(a)



(b)

FIG. A.1: Simulated  $Q^2$  distributions for the (a) hydrogen and (b) deuterium targets. The mean and RMS of the distribution are given on the plot in units of (GeV/c)<sup>2</sup>.

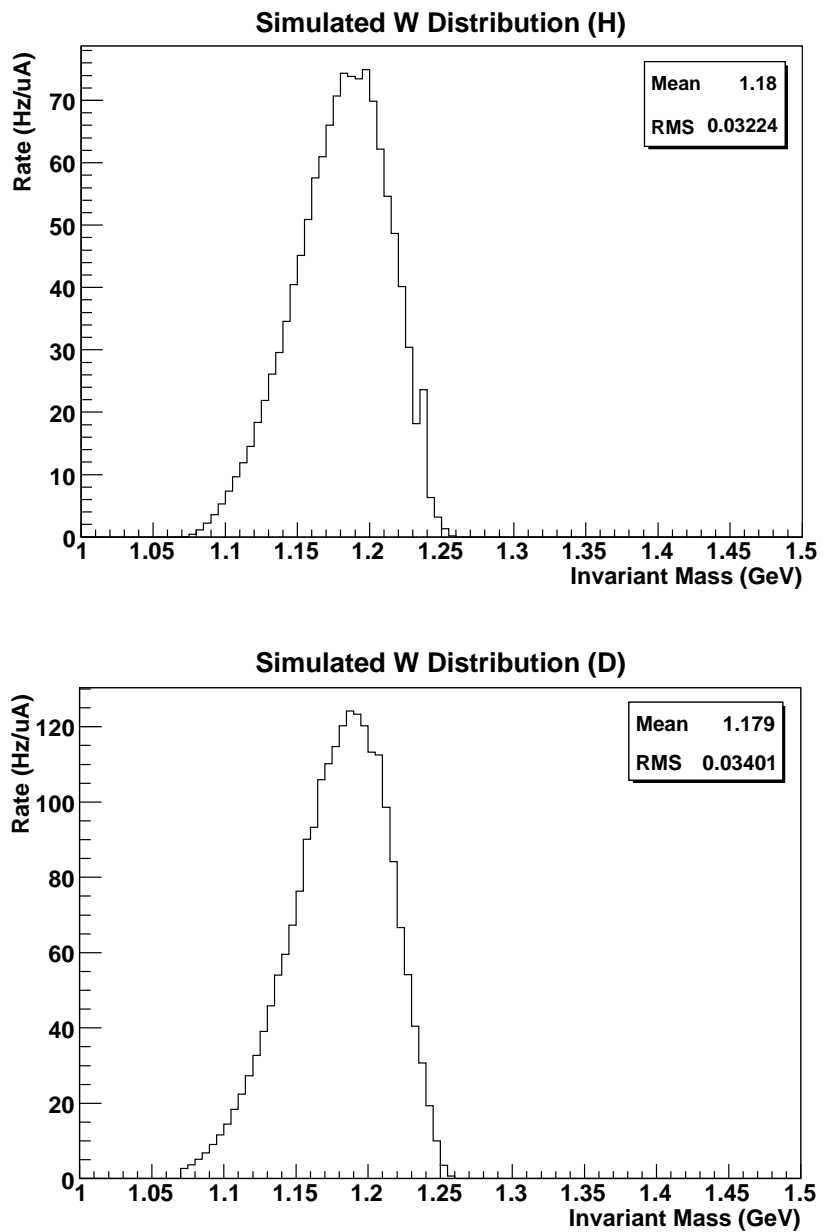
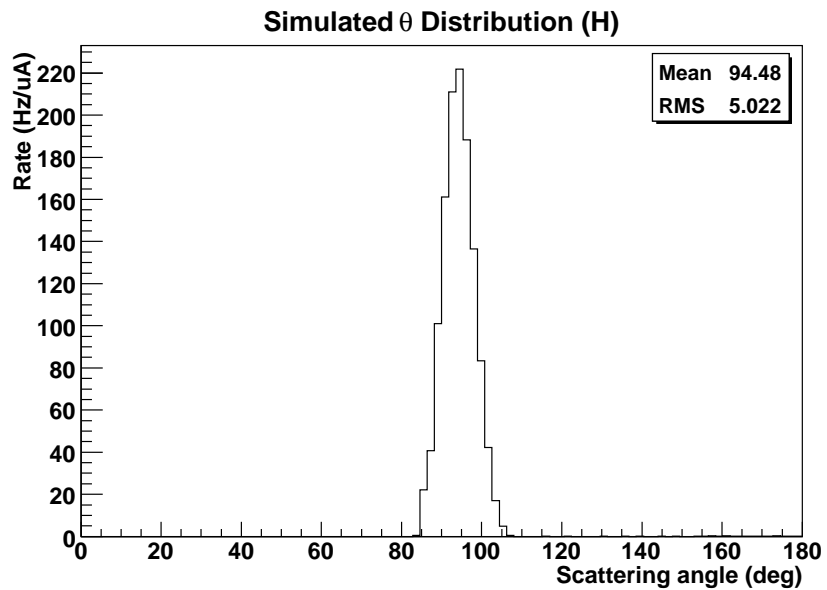
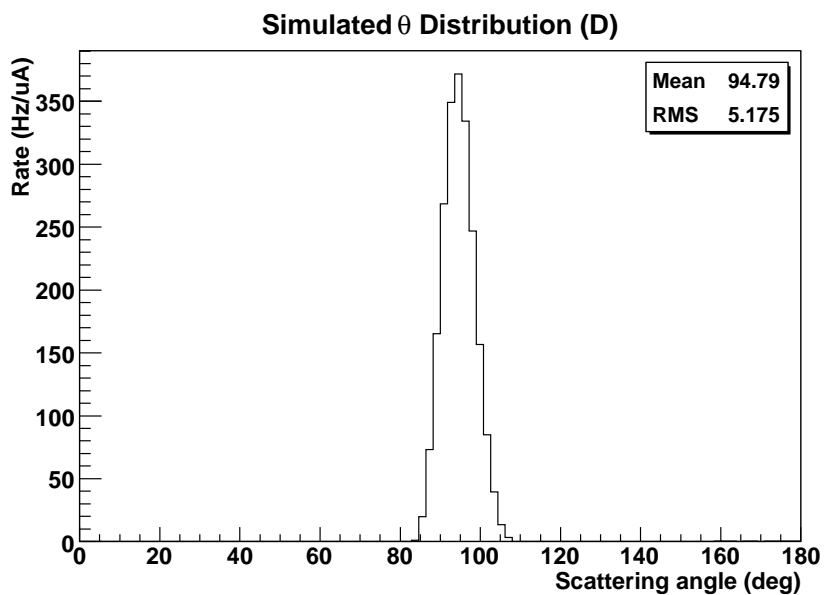


FIG. A.2: Simulated  $W$  distributions for the (a) hydrogen and (b) deuterium targets. The mean and RMS of the distribution are given on the plot in units of GeV.

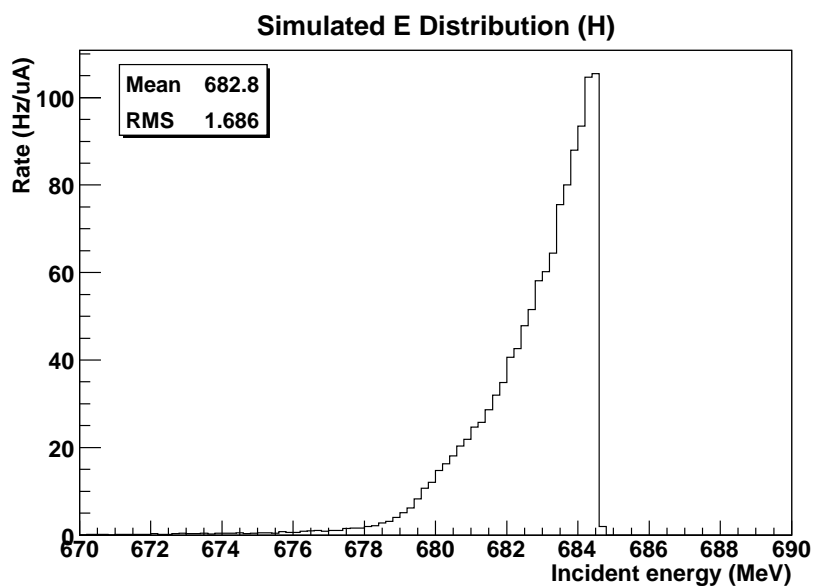


(a)

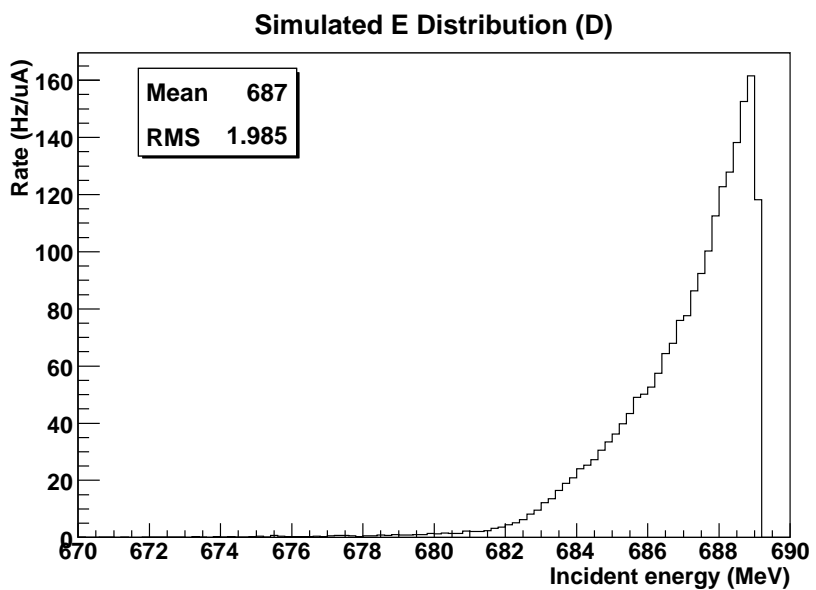


(b)

FIG. A.3: Simulated  $\theta$  distributions for the (a) hydrogen and (b) deuterium targets. The mean and RMS of the distribution are given on the plot in units of degrees.

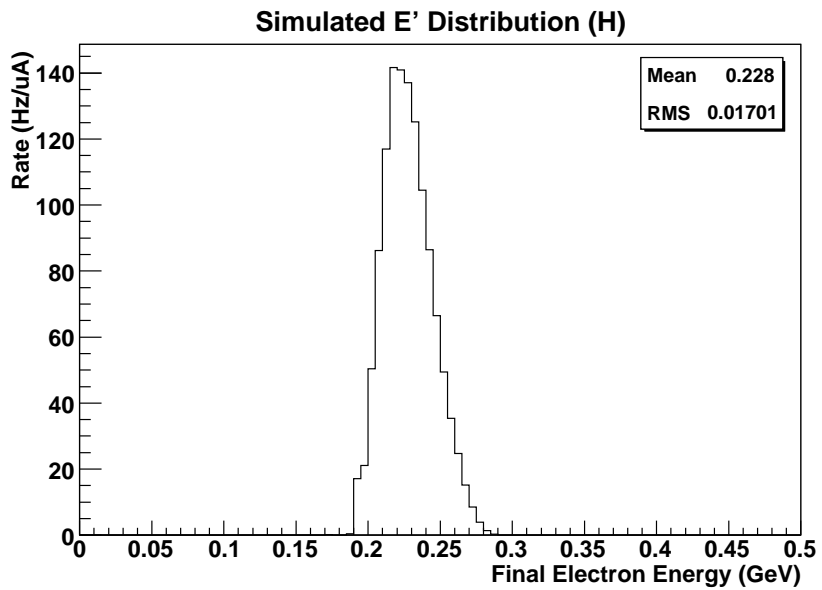


(a)

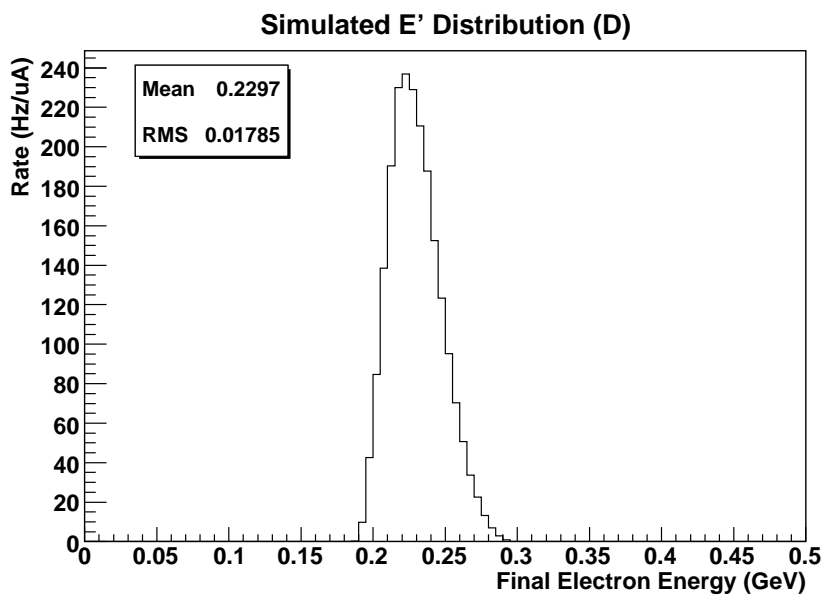


(b)

FIG. A.4: Simulated  $E$  distributions for the (a) hydrogen and (b) deuterium targets. The mean and RMS of the distribution are given on the plot in units of MeV. Note that while the measured experimental beam energy is used as an input to the simulation, the simulation accounts for energy loss in the target and electromagnetic radiation occurring before the interaction point, leading to the non-constant incident electron energy seen in the figure.

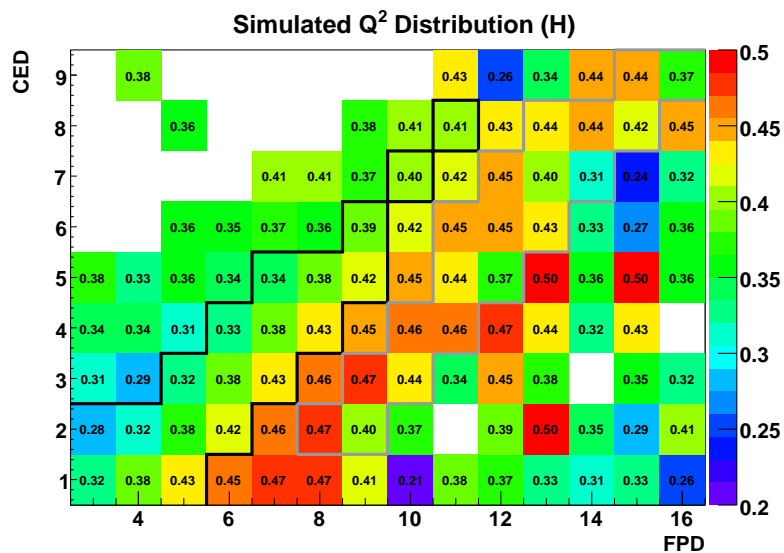


(a)

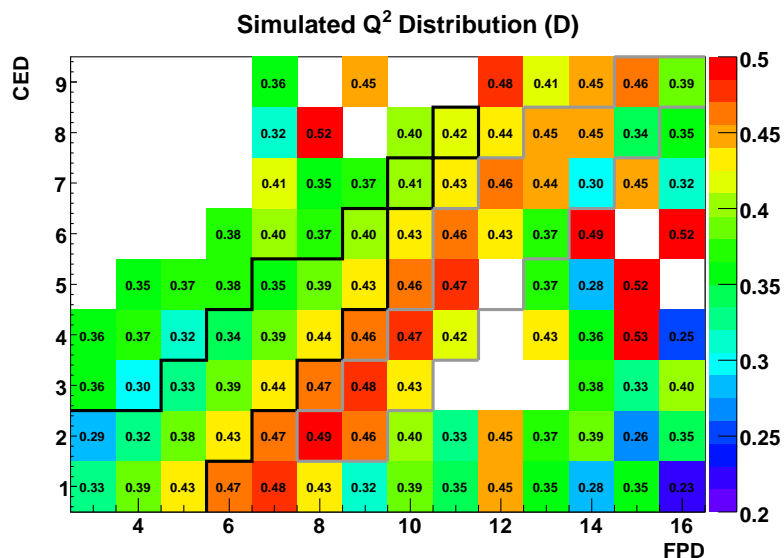


(b)

FIG. A.5: Simulated  $E'$  distributions for the (a) hydrogen and (b) deuterium targets. The mean and RMS of the distribution are given on the plot in units of GeV.

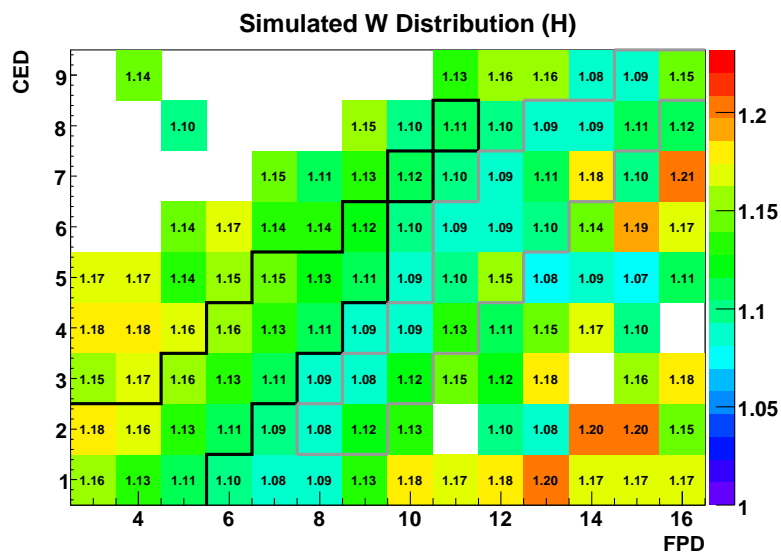


(a)

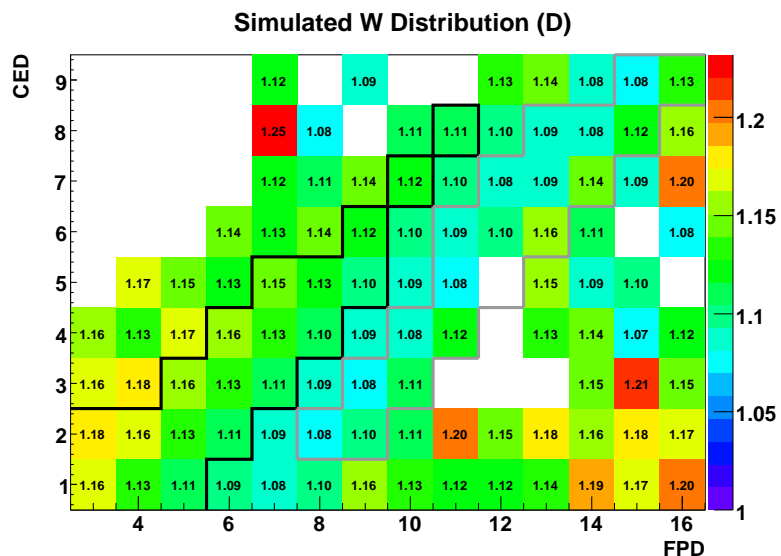


(b)

FIG. A.6: Simulated cell-by-cell  $Q^2$  distribution for the (a) hydrogen and (b) deuterium targets. Each block on the figure represents a CED·FPD coincidence cell. The average  $Q^2$  is indicated both by the color scale given on the right and the label on each cell, and is given in units of  $(\text{GeV}/c)^2$ . Inelastic (elastic) locus cells are outlined in black (gray). Note that all events are inelastic, even those that are present in elastic locus cells.



(a)



(b)

FIG. A.7: Simulated cell-by-cell  $W$  distribution for the (a) hydrogen and (b) deuterium targets. Each block on the figure represents a CED- $FPD$  coincidence cell. The average  $W$  is indicated both by the color scale given on the right and the label on each cell, and is given in GeV. Inelastic (elastic) locus cells are outlined in black (gray). Note that all events are inelastic, even those that are present in elastic locus cells.

## **APPENDIX B**

# **Details of the Scaler Counting Problem and the Correction Applied**

A combination of the choice of logic used in the coincidence electronics for the North American (NA) octants and timing delays present in the scaler boards that recorded electron and pion events led to bits being dropped by the scalers. This resulted in improper yields being recorded for a small percentage of MPSs within a given run, which, in turn, lead to a tail on one side of the yield distribution that affected its mean. Since the problem was not intrinsically helicity dependent, the impact on the mean of the asymmetry distribution was smaller, with problematic events appearing on both sides of the central value rather than as a tail on one side.

Although the electronics problem was present from the beginning of the backward-angle phase of the experiment, the effect of this problem was only significant in the low-energy deuterium data. Thus, although the problem was present in all hydrogen data and two-thirds of the high-energy deuterium data, it did not greatly impact these data.

Once the source of the problem was discovered, the NA electronics were reprogrammed to avoid the output that led to the bits being dropped. This fix occurred roughly halfway through the low-energy deuterium run period, allowing the second half of the low-energy deuterium and final third of the high-energy deuterium run periods to be performed without the problem present. Additionally, since the electronics differed between the NA and French (FR) octants, all FR octant data were unaffected.

In the sections that follow, details of the cause of the problem and its solution will be presented, along with a description of the correction applied to remove the affected events. Although the effect was small and the correction had a negligible effect on the physics asymmetry, it was important to understand the source of the problem and to be sure the correction applied did not bias the results. This appendix presents aspects of the testing and correction for the scaler counting problem that have not been documented elsewhere.

## B.1 Discovery and Diagnosis of the Problem

The scaler counting problem was first diagnosed through the routine checks performed during each data-taking shift. One of the plots that were regularly checked showed the ratio-to-counting statistics (RCS) as a function of run number for each octant. The RCS is defined as the standard deviation of the asymmetry,  $\sigma_A$ , divided by the standard deviation expected from counting statistics,  $\sigma_{cnt}$ ,

$$RCS = \frac{\sigma_A}{\sigma_{cnt}} = \frac{\sigma_A}{\sqrt{N}}, \quad (\text{B.1})$$

where  $N$  is the number of events. Figure B.1 shows the RCS in each octant for all runs performed in the low-energy deuterium run period before the problem was solved. The

limits on the axes in each plot are the same, with the  $y$ -axis centered at 1.0 and a range of  $\pm 30\%$ . The average RCS during this period for each octant was determined by fitting to a constant. If the data were obeying counting statistics, the RCS should have been equal to 1. This was the case for the FR octants, where the RCS was within 1% of 1 in each octant. For the NA octants, however, the average RCS in every octant was 20% too high, indicating that there was some significant systematic difference between the two sets of octants.

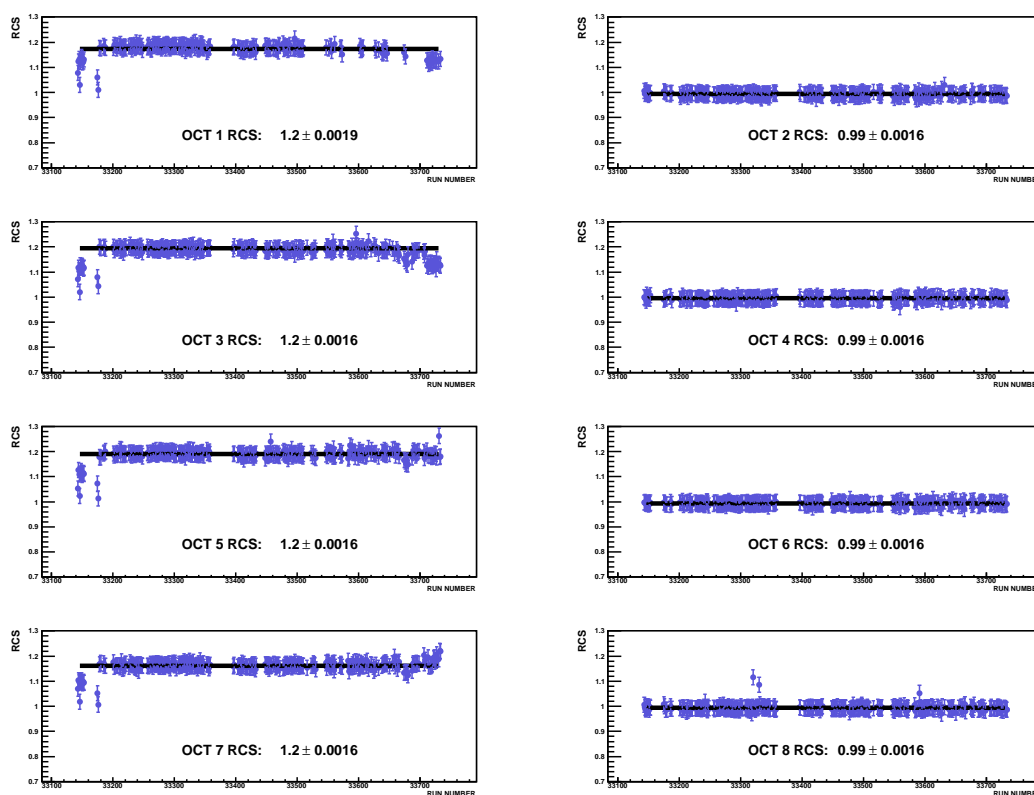


FIG. B.1: Octant-by-octant ratio to counting statistics (RCS) as a function of run number for each run from the low-energy deuterium run period performed before the scaler counting problem was fixed. NA octants are shown on the left and FR octants on the right. In each plot, the RCS has been fit to a constant and the average is presented. Note that the first several  $\mu\text{A}$  runs taken during the run period were performed at currents lower than the nominal value of  $35 \mu\text{A}$ . The rate-dependent nature of the problem meant that the effect was smaller for these runs.

### B.1.1 Impact on the Data

The problem manifested itself in the data primarily as a tail on one side of the main yield distribution, although some cells had tails on both sides, and was most noticeable in high yield cells. The MPS yield distributions of some high yield cells in the elastic locus are given in Figure B.2. The yields shown are from a single run from the low-energy deuterium run period. Because the number of events in the tail is significantly lower than the number in the main peak, a logarithmic scale has been used on the  $y$ -axis to enable the tails to be more easily seen.

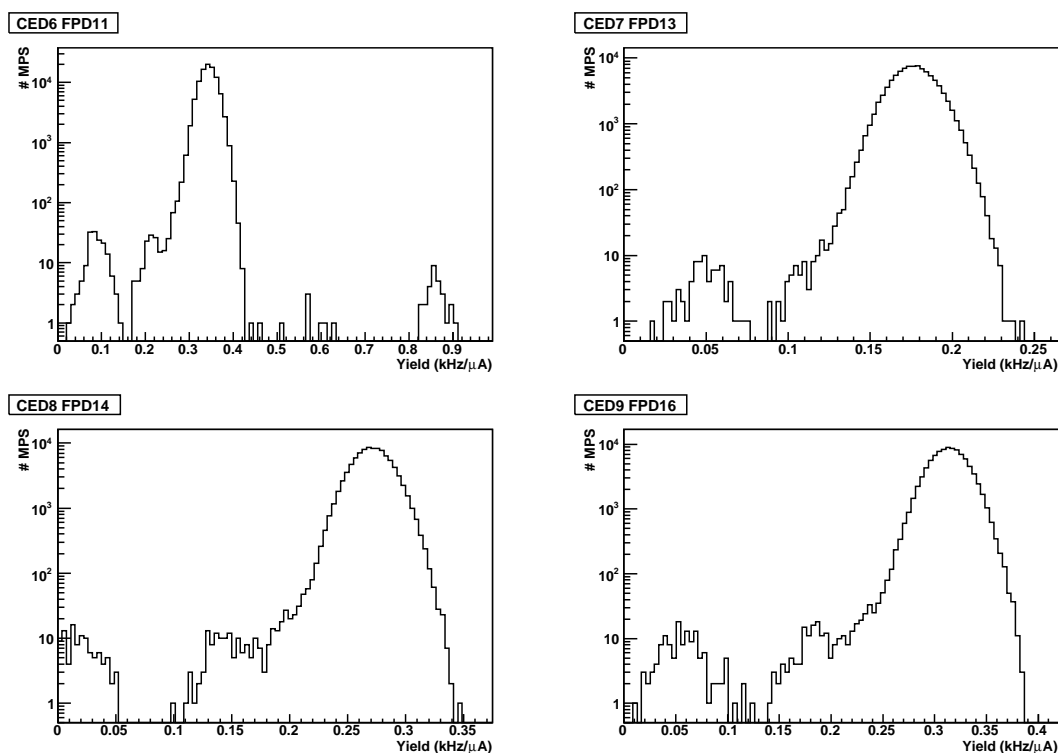


FIG. B.2: MPS yields for 4 cells within the elastic locus shown for a single run affected by the scaler counting problem. The data shown are all from a single NA octant, Octant 3. Note that a logarithmic scale has been used on the  $y$ -axis to highlight the tail events.

The asymmetry, which is computed from the MPS yields for each quartet (See Equ-

tion 3.1), was also affected by this problem. Unlike the yields, in which the affected events generally created a tail on one side of the peak, the problem manifested itself in every cell as wings on either side of the main peak of the distribution. Figure B.3 shows the quartet asymmetry for the cells shown in Figure B.2.

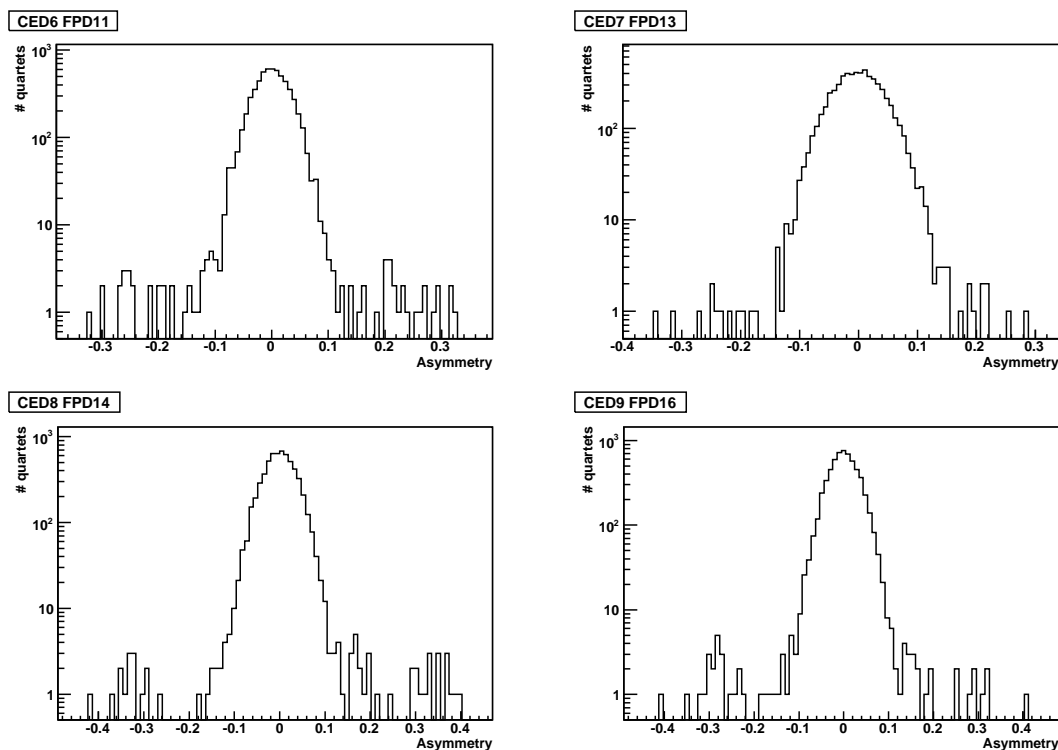


FIG. B.3: Quartet asymmetry for 4 cells within the elastic locus shown for a single run affected by the scaler counting problem. The data shown are all from a single NA octant, Octant 3. Note that a logarithmic scale has been used on the  $y$ -axis to highlight the tail events.

While these irregularities were visible in the yield and asymmetry distributions in all NA octants, the FR octant data was unaffected (See Figure 4.2 in Chapter 4). This indicated that the source of the problem involved the coincidence electronics, as the design used differed between the NA and FR octants.

### **B.1.2 Testing the Electronics**

In order to understand the source of the bad events, tests were performed on the NA electronics in an effort to duplicate the problem. Most of the tests performed involved studying the individual components of the electronics rather than making use of the full experimental apparatus and beam. One simple test, however, that could be performed using the beam was to check the rate dependence of the runs by taking data at several beam currents. Figure B.4 shows the MPS yield of a given cell for runs taken at several different beam currents. These plots indicate that the amount of events in the tail increased with the beam current, confirming that the problem was rate dependent. For the remaining tests, a single octant was used so that the testing did not completely disrupt the experiment. Instead of the signal from the detectors, signals such as random noise or pulsed signals of different widths were sent to the electronics to test their response. When these tests indicated that the problem involved input signals with narrow widths, tests were performed using a series of narrow pulsed signals with both fixed and random timing.

Although these tests were not able to exactly reproduce the behavior seen in the data, they allowed for a diagnosis of the problem to be determined during the experimental run. The tests indicated that the problematic events arose when two narrow signals arrived at a given scaler channel within a small time window. The problem did not arise for pulses wider than 7 ns nor did it arise when two sufficiently narrow pulses arrived more than 10 ns apart. Another facet of the problem was that the electronics' response was not uniform across all channels in a given scaler. If the same signal was fed in to two channels, problematic output would occur in both channels, but not always from the same event. This indicated that there was little to no correlation between bad events across the scaler.

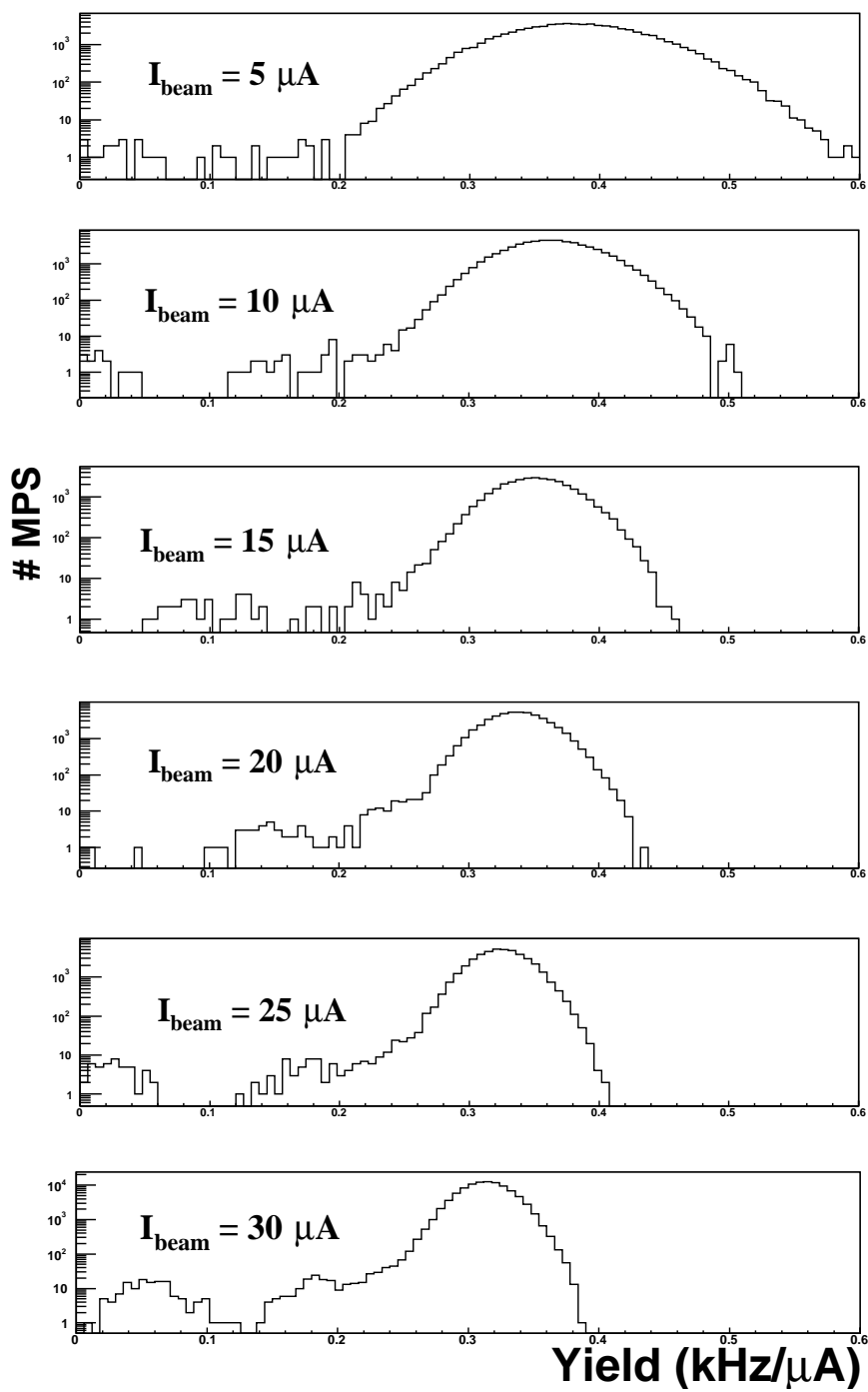


FIG. B.4: MPS yield in a single cell for runs taken at different beam currents. Note that a logarithmic scale has been used on the  $y$ -axis to highlight the tail events.

In addition to the bench tests that were performed to diagnose the problem, a simulation was developed to model the scaler electronics. Although it was not possible to reproduce the problem quantitatively, the simulation provided a qualitative tool with which to study the scaler response to the problematic signals. The simulation, along with offline studies of the behavior of the scaler electronics, aided in developing a further understanding of the problem after the solution was implemented.

### **B.1.3 Description of the Problem**

The signals from the individual CED, FPD and Cherenkov detectors were all read into coincidence electronics that combined the signals to determine if a coincidence had occurred. When a coincidence occurred, a signal was output from the coincidence board to a scaler board that incremented the event count in the appropriate coincidence cell. The count was reset at the start of each MPS, incremented during the MPS and recorded when the MPS terminated. The MPS yield was then defined as the number of events in a given cell weighted by the beam current during the run. The design of the coincidence electronics differed between NA and FR octants, but the scaler modules used in all octants were identical.

The scaler boards consisted of 32 channels that each represented a single CED-FPD coincidence cell. Each scaler channel stored up to 32 bits of data distributed across four 8-bit chips. When a signal entered a block, it was duplicated and sent to the input of each bit simultaneously. However, the design of the circuit was such that the processing time for all bits was not equal. For the first bit in the first block, the input was fed directly into an XOR logic gate where it was combined with the bit's existing value. The output of this gate was then the updated value of the bit. For all other bits, the input was first

ANDed with the non-updated values of all lower order bits. The outcome of that AND was then XORed with the existing value of the bit to give the updated value of the bit. Additionally, the output of each full block was used as the input to the next 8-bit block. Because of this design, the amount of time to process an event differed from bit to bit, with the higher order bits taking longer to process. If a new signal were received before the previous signal had been fully processed, it was possible that the inputs to the AND gates of higher order bits could have changed before the AND was performed. This change could potentially alter the output of the AND gate and, consequently, result in errant outputs from the affected bits. A survey was performed to measure the rise- and fall-times of each bit in the scaler. Through these measurements, it was determined that the minimum time needed for each bit in the chain to fully process an event was about 7.1 ns. This led to a maximum operational frequency for the scalers of 140 MHz.

As was discussed previously, the scalers receive their input from the outputs of the coincidence boards. The coincidence electronics used in the FR octants were programmed with a minimum output width of 10 ns in place, effectively limiting the input to the scalers in the FR octants to <100 MHz. The NA octants, however, were given no minimum output width. Instead, the width of the output from the NA coincidence electronics was simply the overlap of the CED, FPD and trigger signals, whatever that width might be. The CED and FPD mean-timers output signals with a width of 20 ns. If the output of any CED and FPD pair overlapped, a 15 ns trigger signal was initiated after a short delay. In the NA electronics, the coincidence was then defined as the logical AND of the FPD, CED and trigger signals. If a second signal was received from the CED or FPD in question while the trigger window was still open, two narrow signals could be output to the scalers. An example of problematic timing is given in Figure B.5. In this instance, an FPD has fired, followed by a CED, initiating a trigger signal. The timing of the FPD and CED

outputs, combined with the width and delay of the trigger, leads to the output of a 3 ns signal. This narrow signal alone would not cause any problem with the scaler. However, when the FPD triggers a second time 5 ns later, a second narrow signal is created. If the leading edge of the second signal arrives at the scaler within 7.1 ns of the first signal, the count may not be incremented properly in the scaler. In retrospect, a minimum output width should have been in place in these electronics. The failure to include one was due to miscommunication on the part of the coincidence and scaler board designers.

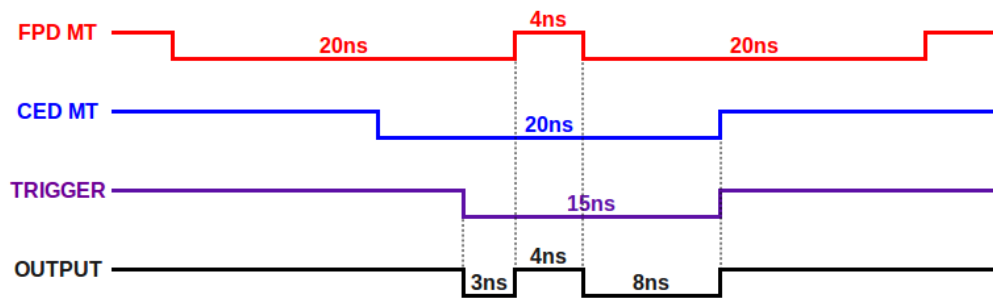


FIG. B.5: Example of the timing of signals in the NA coincidence boards that could have led to the dropped bits in the scaler. The output signal is the logical AND of the FPD, CED and trigger signals. In this example, the second FPD signal overlaps with the CED and trigger from the initial coincidence, leading to a second output signal being sent to the scaler 7 ns after the first.

The logic used within the scaler contributed to the rate-dependence of the problem. Since the time required to process a signal increased with each bit, the probability that the first event would not be processed before the second arrived also increased with bit number. The lower the yield in the cell, the fewer bits required to store the count and, thus, the less likely it was that the problem would occur. Higher rates also increased the likelihood of problematic narrow pulses occurring in the coincidence boards, which will be discussed in the next section.

### **B.1.4 Possible Causes of the Narrow Signals**

Once it is understood which types of signals cause the problem and how the problem occurs in the scaler, the causes of the problematic signals can be determined. In some cases, the narrow signals were due to two real events firing a given CED or FPD in close proximity. In a situation like the one shown in Figure B.5, the second FPD signal could be due to a particle firing the FPD in coincidence with another CED while the trigger window of the first coincidence was still active. In this instance, the event would be double-counted, appearing in two CED-FPD cells. Other possible causes of two signals do not involve real events but, rather, are a result of noise in the detectors. Examples of two such types of noise are given below.

A single, very large pulse could lead to a second triggering of a CED or FPD as the detectors require more time to recover from large pulses and may exhibit low-voltage oscillations before returning to their base level. If one of these secondary peaks was large enough to overcome the threshold set on the detector, the electronics would treat the peak as though a new signal had occurred. In general, the thresholds were set high enough to avoid triggers from noise but there was still some small probability that a large enough secondary pulse could occur.

Additionally, the second output signal could be caused by noise in one of the PMTs connected to either end of each FPD pair and each CED. Outputs from the two PMTs were sent to a mean-timer (MT) that averaged the signals together to yield a single output value. The MT computed the average by taking the signals from the two PMTs and passing them through a series of 2 ns delays. The delayed outputs for each PMT were then ANDed to determine the MT output. The total delay time in the MT was 22 ns. If one of the PMTs were to fire twice during this time window, the MT would yield two

outputs. As an example, consider a situation in which the right and left PMTs in a given detector fired 10 ns apart and then, 2 ns later, the right PMT fired again. In this instance, the MT would output the average of the left PMT signal with each of the two right PMT signals.

### **B.1.5 Solution**

The diagnosis of the problem was complicated by the fact that the dropped bits were caused by a combination of effects in two separate components of the electronics. The lack of a minimum output signal width in the NA boards coupled with the inappropriate handling by the scaler of events arriving too closely together worked together to create the tails on the measured yields. This aided the solution, however, in that correcting only one of these issues was sufficient to eliminate the problem. Since the NA coincidence boards made use of FPGA chips, the electronics could be re-programmed to include a minimum output signal width of 10 ns with minimal disruption. This re-programming was performed soon after the problem was diagnosed and the effects were seen immediately in the data. With the minimum output width of 10 ns on signals from the coincidence boards in place, the tails on the yields disappeared and the RCS of the NA octants matched that of the FR octants.

## **B.2 Applying a Correction**

Since the electronics problem had a noticeable impact on the low-energy deuterium yield data, a correction was needed to remove the affected events. The correction was applied by placing a cut on the measured yields such that MPSs with yield outside a spec-

ified window were removed from averaging, as was the quartet containing the MPS. The asymmetry was then computed on a quartet-by-quartet basis for the remaining quartets. The width of the window of acceptable yield was defined as an integer multiple of the standard deviation,  $\sigma$ , of the run-averaged yield distribution determined from a previous analysis pass and was centered around the mean yield. The width of the window was chosen through testing of several widths to determine the optimum cut value. For the sake of consistency, the correction was then applied uniformly to the yields in all octants for all run periods.

### **B.2.1 Determining the Size of the Cut**

When the correction was first being developed, testing was performed in a limited basis to test the principle behind the cut and its initial implementation. Typical results from the first level of testing performed are given in Figure B.6, which shows the impact of the correction on both the asymmetry and the yield for several cut values. Each plot shows the quartet yield and asymmetry for a high-yield cell within the elastic locus summed across several runs. Since the cut is placed on the yield before the asymmetry is computed, the bottom plots do not show the cut directly but rather show the impact of the yield cut on the asymmetry. These initial tests, which were only performed for the low-energy deuterium, involved analyzing one NA and one FR octant for a small number of runs, creating ntuple output files and studying the impact of the yield cut through histograms.

Once the implementation of the correction in `g0analysis` was finalized, run-averaged values stored in the database were used to study the correction on a larger scale. For each run period, a “mini-replay” applying the Pass 1 and Pass 2 corrections was performed on subset of runs using different values for the width of the yield cut. Since the low-energy

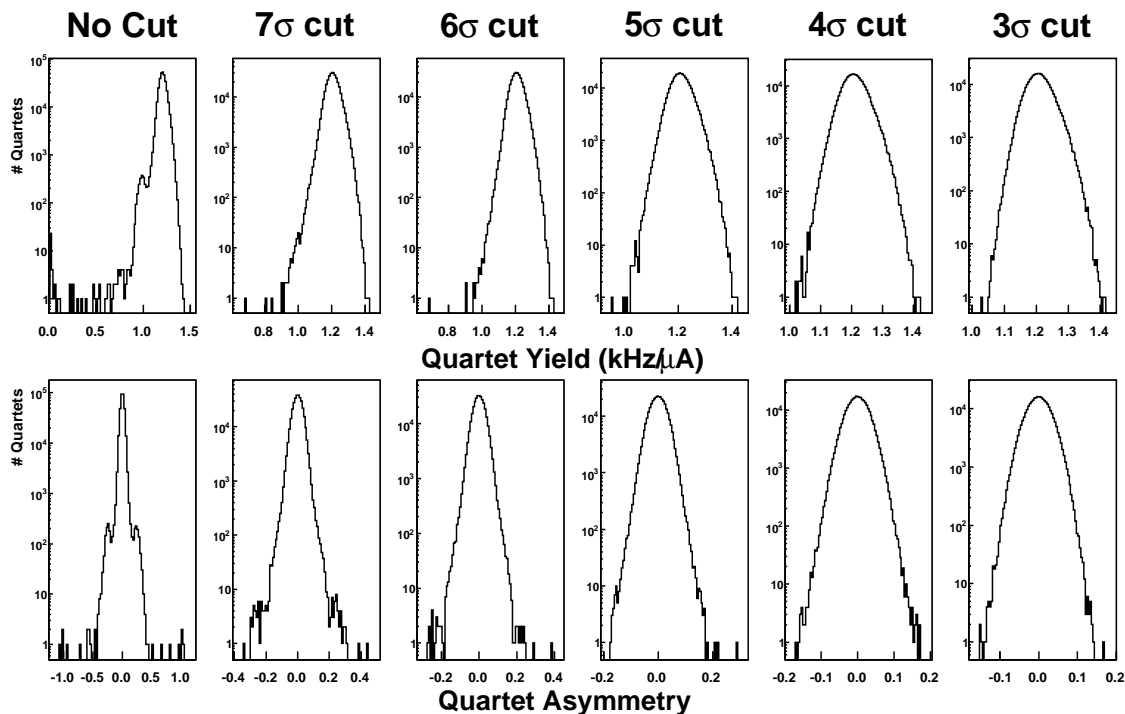


FIG. B.6: Quartet yield (top) and asymmetry (bottom) in a single high-yield cell for a small group of runs from the low-energy deuterium run period. Each plot represents a different size window for the scaler counting correction, with window width decreasing from left to right. A logarithmic scale is used on the  $y$ -axis to allow the problem to be more easily seen.

deuterium run period was the one most affected by the problem, the tests performed on those data were the most in-depth and were used to determine the optimum width of the cut. Tests were then performed on other data sets to confirm that the width chosen did not negatively impact the other run periods.

For the low-energy deuterium run period, the data were treated both as a whole and in subsets to determine the impact of the correction on the affected and unaffected data. Since the correction applied within `g0analysis` was applied to all octants, comparisons could be made between the NA and FR octants. In addition, since the problem was fixed midway through the run period, the data from the NA octants with and without the problem present were available. Having these different sets of data to compare allowed

for studies to be done to be sure the correction applied did not bias the results.

Cuts based on a 3, 4, 5, 6 and 7  $\sigma$  window were performed for the low energy deuterium data set while only those for 4-6  $\sigma$  were tested for the other run periods. For each cut value, the total number of quartets, average asymmetry and RCS for the elastic locus were used to study the impact of the cut. These quantities each gave a unique indication of the impact and the effectiveness of applying the correction.

Since the RCS was the quantity that gave the first indication that there was a problem, the RCS of the NA octants after applying the cut was used as a measure of the effectiveness of the correction. Additionally, the impact of the correction on the RCS in the FR octants helped to show that the yield cut did not introduce bias into the results. If a particular cut had resulted in an RCS in the FR octants that was far from 1, it would indicate a new systematic effect had been introduced. Table B.1 gives the elastic locus RCS values for each octant for the different cuts applied. Each cut applied reduces the RCS of the NA octants before the fit, with the  $3\sigma$  set having the RCS closest to 1. This same cut leads to only a small ( $\sim 1\%$ ) reduction in the RCS for the FR octants. These results show that, even for a narrow window width, applying the cut lowers the RCS for the affected NA octants without having a significant negative impact on the value for the FR octants or the NA octants after the problem was fixed.

The number of quartets cut was computed as an indicator of how much of the data was affected by the cut. The optimal cut value was one that resulted in the least number of quartets being lost while keeping the RCS in the NA octants close to 1. The octant-by-octant percentage of quartets removed for each cut value is given in Table B.2. These values indicate that even for the narrowest window,  $3\sigma$ , the amount of data cut is less than 3% in all octants for all run sets. Although this value is small, a potential problem was seen upon closer inspection of the data unaffected by the scaler counting problem (all FR

Elastic Locus RCS for Runs Before Fix (D 362)								
	NA OCTANTS				FR OCTANTS			
	1	3	5	7	2	4	6	8
Uncut	1.14	1.14	1.17	1.13	1.00	1.00	1.00	1.00
$7\sigma$	1.08	1.07	1.09	1.07	1.00	1.00	1.00	1.00
$6\sigma$	1.07	1.06	1.08	1.06	1.00	1.00	1.00	1.00
$5\sigma$	1.06	1.05	1.06	1.05	1.00	1.00	1.00	1.00
$4\sigma$	1.04	1.04	1.05	1.04	1.00	1.00	1.00	1.00
$3\sigma$	1.02	1.02	1.02	1.02	0.99	0.99	0.99	0.99

Elastic Locus RCS for Runs After Fix (D 362)								
	NA OCTANTS				FR OCTANTS			
	1	3	5	7	2	4	6	8
Uncut	1.00	1.00	1.00	1.00	1.00	1.00	1.00	1.00
$7\sigma$	1.00	1.00	1.00	1.00	1.00	1.00	1.00	1.00
$6\sigma$	1.00	1.00	1.00	1.00	1.00	1.00	1.00	1.00
$5\sigma$	1.00	1.00	1.00	1.00	1.00	1.00	1.00	1.00
$4\sigma$	1.00	1.00	1.00	1.00	1.00	1.00	1.00	1.00
$3\sigma$	0.99	0.99	0.99	0.98	0.99	0.99	0.99	0.99

Elastic Locus RCS for All Runs (D 362)								
	NA OCTANTS				FR OCTANTS			
	1	3	5	7	2	4	6	8
Uncut	1.06	1.06	1.07	1.06	1.00	1.00	1.00	1.00
$7\sigma$	1.04	1.03	1.04	1.03	1.00	1.00	1.00	1.00
$6\sigma$	1.03	1.03	1.03	1.03	1.00	1.00	1.00	1.00
$5\sigma$	1.03	1.02	1.03	1.02	1.00	1.00	1.00	1.00
$4\sigma$	1.02	1.02	1.02	1.01	1.00	1.00	1.00	1.00
$3\sigma$	1.00	1.00	1.00	1.00	0.99	0.99	0.99	0.99

TABLE B.1: Octant by octant elastic locus average RCS for several values of the cut applied by the scaler counting correction. All data are from the low-energy deuterium run period and have been presented both averaged across the entire period and split between run taken before and after the scaler counting problem was corrected. Note that the octants have been grouped by make (NA or FR) rather than being listed numerically.

octant data and the NA octant data after the fix). For these octants, the amount of data cut was consistent for widths from  $7\sigma$  to  $4\sigma$ . However, when the window was narrowed from  $4\sigma$  to  $3\sigma$ , the percentage of quartets cut from the data unaffected by the problem increased by an order of magnitude, going from just over 0.1% in each octant to over 1%. This increase indicated that the cut was beginning to impact the main peak of the data rather than just removing the tail. As such, the  $3\sigma$  cut was deemed too narrow to be used for the final correction. Using this information along with information from all of the tests performed, the decision was made to apply a  $5\sigma$  cut for all run periods.

The impact of the correction on the asymmetry was noted for each cut as a measure of the impact of the cut on the final values. Since this was the quantity of interest in the experiment, decisions on the correction were not made based directly on these results. Instead, they were computed to verify that the correction did not have any obviously biasing effect on the averages (e.g. altering the asymmetry by several orders of magnitude). Table B.3 shows the octant average elastic asymmetry for each of the cut values. As with the other tables, the run period has been separated into before and after the electronics fix to show the impact of the cut on the unaffected data. In addition to the full octant average, the average asymmetry was computed separately for the NA and FR octants and is shown in Table B.4.

## **B.2.2 Applying the Correction: Locus vs. Cell-by-cell**

The final consideration that was made involved how the cut should be applied. The correction is implemented in such a way as to allow it to be applied both cell-by-cell and to the locus as a whole. In the initial studies of the analysis pass corrections, statistical considerations related to the linear regression slopes needed for Pass 4 dictated that these

% Quartets Cut from Elastic Locus - Before Fix (D 362)								
	NA OCTANTS				FR OCTANTS			
	1	3	5	7	2	4	6	8
$7\sigma$	0.40	0.38	0.46	0.39	0.10	0.10	0.10	0.10
$6\sigma$	0.51	0.46	0.62	0.49	0.10	0.10	0.10	0.10
$5\sigma$	0.70	0.62	0.85	0.65	0.10	0.10	0.10	0.10
$4\sigma$	1.10	0.98	1.26	1.00	0.14	0.14	0.14	0.14
$3\sigma$	2.32	2.19	2.42	2.16	1.23	1.24	1.23	1.24

% Quartets Cut from Elastic Locus - After Fix (D 362)								
	NA OCTANTS				FR OCTANTS			
	1	3	5	7	2	4	6	8
$7\sigma$	0.11	0.11	0.11	0.11	0.11	0.11	0.11	0.11
$6\sigma$	0.11	0.11	0.11	0.11	0.11	0.11	0.11	0.11
$5\sigma$	0.11	0.11	0.11	0.11	0.11	0.11	0.11	0.11
$4\sigma$	0.14	0.14	0.14	0.14	0.15	0.14	0.14	0.14
$3\sigma$	1.21	1.21	1.18	1.21	1.21	1.21	1.21	1.21

% Quartets Cut from Elastic Locus - All Runs (D 362)								
	NA OCTANTS				FR OCTANTS			
	1	3	5	7	2	4	6	8
$7\sigma$	0.25	0.24	0.27	0.24	0.10	0.10	0.10	0.10
$6\sigma$	0.30	0.27	0.35	0.29	0.10	0.10	0.10	0.10
$5\sigma$	0.39	0.35	0.46	0.36	0.11	0.11	0.11	0.11
$4\sigma$	0.59	0.53	0.66	0.54	0.14	0.14	0.14	0.14
$3\sigma$	1.73	1.67	1.76	1.65	1.22	1.22	1.22	1.22

*All values given in %*

TABLE B.2: Percentage of quartets cut from the elastic locus in each octant by the scaler counting correction for several cut values. All data are from the low-energy deuterium run period and have been presented both averaged across the entire period and split between run taken before and after the scaler counting problem was corrected. Note that the octants have been grouped by make (NA or FR) rather than being listed numerically. All values in the table are given in % of total quartets.

Octant Average Elastic Locus Asymmetry (D 362)			
	Before Fix	After Fix	All Runs
Uncut	$-13.33 \pm 1.0$	$-14.09 \pm 0.8$	$-13.77 \pm 0.6$
$7\sigma$	$-12.99 \pm 0.9$	$-14.03 \pm 0.8$	$-13.57 \pm 0.6$
$6\sigma$	$-13.14 \pm 0.9$	$-14.03 \pm 0.8$	$-13.63 \pm 0.6$
$5\sigma$	$-13.11 \pm 0.9$	$-14.07 \pm 0.8$	$-13.64 \pm 0.6$
$4\sigma$	$-13.03 \pm 0.9$	$-14.03 \pm 0.8$	$-13.58 \pm 0.6$
$3\sigma$	$-12.37 \pm 0.9$	$-13.53 \pm 0.8$	$-13.01 \pm 0.6$

*All values given in ppm*

TABLE B.3: Elastic locus asymmetry averaged across all octants for the low-energy deuterium run period. The run period has been separated into runs performed before (Before Fix) and after (After Fix) the problem was solved. The final column shows the average elastic asymmetry across the entire run period.

corrections be applied to the locus average rather than to each cell individually. As a result, all locus-averaged asymmetries reported were those that resulted from corrections applied to the locus as computed within g0analysis. However, because of the uncorrelated nature of the bad events, this approach was problematic for the scaler counting correction. In this instance, for reasons that will be stated below, it was preferable for the cut to be applied on a cell-by-cell basis with the locus average being computed after all corrections were applied.

When the cut was applied to the locus, a bad event in a single cell within the locus resulted in the quartet being removed from all locus cells, not just the one affected. This resulted in a significantly higher number of quartets being cut across the locus than was cut when the correction was applied cell-by-cell. Table B.5 shows an octant by octant comparison of the two methods of applying the correction to the low-energy deuterium data.

NA Octant Average Elastic Locus Asymmetry (D 362)			
	Before Fix	After Fix	All Runs
Uncut	$-12.23 \pm 1.6$	$-13.56 \pm 1.2$	$-13.08 \pm 1.0$
$7\sigma$	$-11.68 \pm 1.4$	$-13.57 \pm 1.2$	$-12.79 \pm 0.9$
$6\sigma$	$-11.94 \pm 1.4$	$-13.56 \pm 1.2$	$-13.41 \pm 0.9$
$5\sigma$	$-12.01 \pm 1.4$	$-13.57 \pm 1.2$	$-12.90 \pm 0.9$
$4\sigma$	$-11.89 \pm 1.4$	$-13.51 \pm 1.2$	$-12.81 \pm 0.9$
$3\sigma$	$-11.13 \pm 1.4$	$-12.95 \pm 1.2$	$-12.17 \pm 0.9$

NA Octant Average Elastic Locus Asymmetry (D 362)			
	Before Fix	After Fix	All Runs
Uncut	$-14.02 \pm 1.3$	$-14.59 \pm 1.2$	$-14.33 \pm 0.9$
$7\sigma$	$-14.02 \pm 1.3$	$-14.46 \pm 1.2$	$-14.25 \pm 0.9$
$6\sigma$	$-14.10 \pm 1.3$	$-14.48 \pm 1.2$	$-14.31 \pm 0.9$
$5\sigma$	$-14.01 \pm 1.3$	$-14.55 \pm 1.2$	$-14.30 \pm 0.9$
$4\sigma$	$-13.99 \pm 1.3$	$-14.52 \pm 1.2$	$-14.27 \pm 0.9$
$3\sigma$	$-13.41 \pm 1.2$	$-14.08 \pm 1.2$	$-13.77 \pm 0.8$

*All values given in ppm*

TABLE B.4: Elastic locus asymmetry averaged across the NA (1,3,5,7) and FR (2,4,6,8) octants separately for the low-energy deuterium run period. The run period has been separated into runs performed before (Before Fix) and after (After Fix) the problem was solved. The final column shows the average across the entire run period. The full octant average is given in Table B.3.

Percentage of Quartets Removed by the Scaler Counting Correction (D 362)						
	Before Fix		After Fix		Total	
OCT	Cut on Locus	Cut on Cells	Cut on Locus	Cut on Cells	Cut on Locus	Cut on Cells
1	23.43	1.08	0.12	0.22	11.55	0.64
3	21.19	0.98	0.12	0.22	10.45	0.59
5	25.19	1.17	0.12	0.22	12.41	0.68
7	21.59	0.99	0.12	0.22	10.64	0.60
Total NA	22.85	1.05	0.12	0.22	11.26	0.63
2	0.11	0.10	0.12	0.22	0.12	0.16
4	0.11	0.10	0.12	0.22	0.12	0.16
6	0.11	0.10	0.12	0.22	0.12	0.16
8	0.11	0.10	0.12	0.22	0.12	0.16
Total FR	0.11	0.10	0.12	0.22	0.12	0.16
Total ALL	11.48	0.58	0.12	0.22	5.69	0.40

TABLE B.5: Comparison of the percentage of quartets removed by the scaler counting correction for the low-energy deuterium run period. Percentages are presented for the runs before and after the problem was fixed along with the total for the run period. The cut was applied using the nominal  $5\sigma$  width.

For runs performed before the electronics were fixed, the percentage of quartets removed by the cut from each cell in the elastic locus was roughly 1%. Since there was little overlap between bad events from one cell to another, the events removed differed from cell to cell. This meant that the 1% of quartets that had to be removed from a given cell were not necessarily the same quartets that were removed from another cell. By the time this behavior was extended across the 27-cell elastic locus, nearly 25% of the quartets in the NA octants were removed by the  $5\sigma$  cut on the locus. When the cut was applied cell-by-cell and the locus computed from the corrected values, the same data set saw a loss of only 1% of the data. Although, once summed over all octants and the entire run period, the total number of quartets cut by the locus cut was less than 6%, the loss represented an unnecessary removal of good data. In order to avoid this loss of data, the implementation of the linear regression correction applied in Pass 4 was altered so as to allow for all corrections to be applied cell-by-cell and locus averages computed within `g0analysis` were no longer used.

### **B.2.3 Residual False Asymmetry**

The scaler counting correction is designed to remove events that are far from the main peak of the yield distribution, but it ignores any bad events that may be under the peak or within the designated cut window. In order to be certain that these remaining events are not impacting the corrected asymmetry, one would need to know the false asymmetry due to the bad events. Because it was caused by a problem in the electronics, which treat all events the same regardless of helicity, the problem itself was not helicity-correlated. However, the rate-dependent nature of the problem meant that it could impact the two helicity states differently if a charge or physics asymmetry large enough to create

a non-negligible rate difference between the states was present. Although there is not enough information about the residual events to compute the false asymmetry directly, an upper bound can be determined.

The measured asymmetry can be written

$$A_{meas} = (1 - p_+ - p_-)A_{phys} + p_+(A_{phys} + A_{false}) + p_-(A_{phys} - A_{false}) , \quad (\text{B.2})$$

where  $p_{\pm}$  is the helicity dependent probability that a bad MPS is present,  $A_{phys}$  is the physics asymmetry, and  $A_{false}$  is the false asymmetry due to the presence of the bad events.  $A_{false}$  is dependent on the distance of the bad event from the mean of the asymmetry distribution. Since the bad events can only have a false asymmetry if the yields are helicity-dependent, the false asymmetry due to the events is bounded by the physics asymmetry. Thus, the probability of a bad MPS can be written

$$p_{\pm} = \frac{\alpha}{2}(1 \pm A_{phys}) , \quad (\text{B.3})$$

where  $\alpha$  represents the percentage of bad MPSs in the peak. An estimate of  $\alpha$  can be made by extrapolating the distribution of tail events in a typical cell (See Figure B.2) to the center of the peak.

An upper bound can be estimated by assuming that the bad MPSs under the peak have been shifted the maximum amount, that the shift has an asymmetry equal to the physics asymmetry and that the number of bad MPSs is large. The maximum amount an event can be shifted and remain after the cut is  $\frac{n\sigma}{2}$ , where  $n\sigma$  is the width of the cut window. Assuming this maximum shift,  $A_{false}$  can then be bounded by  $A_{phys}$  such that

$$A_{false} \leq \alpha \frac{n\sigma_{stat}}{2} A_{phys} . \quad (\text{B.4})$$

To make a conservative estimate of this bound, assume that the percentage of bad MPSs within the cut window is twice that of the MPSs that are cut. Depending on the

width of the cut window, the results in Table B.2 indicate that up to 2.5% of the data is outside the cut window. Thus, a very safe estimate for  $\alpha$  would be 5%. If the width of the cut is then taken to be  $5\sigma$  and the statistical error to be 5%, Equation B.4 leads to  $A_{false} \leq 1\% A_{phys}$ . Since even a conservative bound represents a small fraction of the physics asymmetry, no additional corrections were applied to account for the residual events.

### B.3 Conclusion

The scaler counting problem, an electronics issue first noticed in the low-energy deuterium run period, was diagnosed during the run period and corrected by reprogramming the NA coincidence boards to alter the widths of the signals that were sent to the scalers. During the analysis phase of the experiment, a correction was applied to the yields to remove quartets that were affected by this problem. The asymmetries presented in this thesis and in other backward-angle  $G^0$  theses [72] [65] [61] [73] [63] [43] and publications [20] [10] have been corrected for the scaler counting problem using a  $5\sigma$  cut on the yield. Table B.6 summarizes the elastic asymmetry before and after the cut for all run periods. The inelastic asymmetry is also given in the table for the run periods where it is available. The rate-dependent nature of the problem meant that its impact in the inelastic locus, where the rates were generally low, was even smaller than in the elastic locus.

Figure B.7 shows the corrected RCS values for all octants for the entire low-energy deuterium run period. The vertical line in each octant indicates the point at which the electronics were fixed. All runs to the right of the line were performed after the electronics were reprogrammed and, as such, were unaffected by the problem. For these runs, the RCS in each octant is consistent with 1 with and without a correction applied. The corrected RCS in the NA octants for runs performed before the fix is higher than the FR

octants. However, averaging less than 1.1 in each octant, these RCS values are still significantly lower than the uncorrected values, presented in Figure B.1, where the RCS is consistently 1.2.

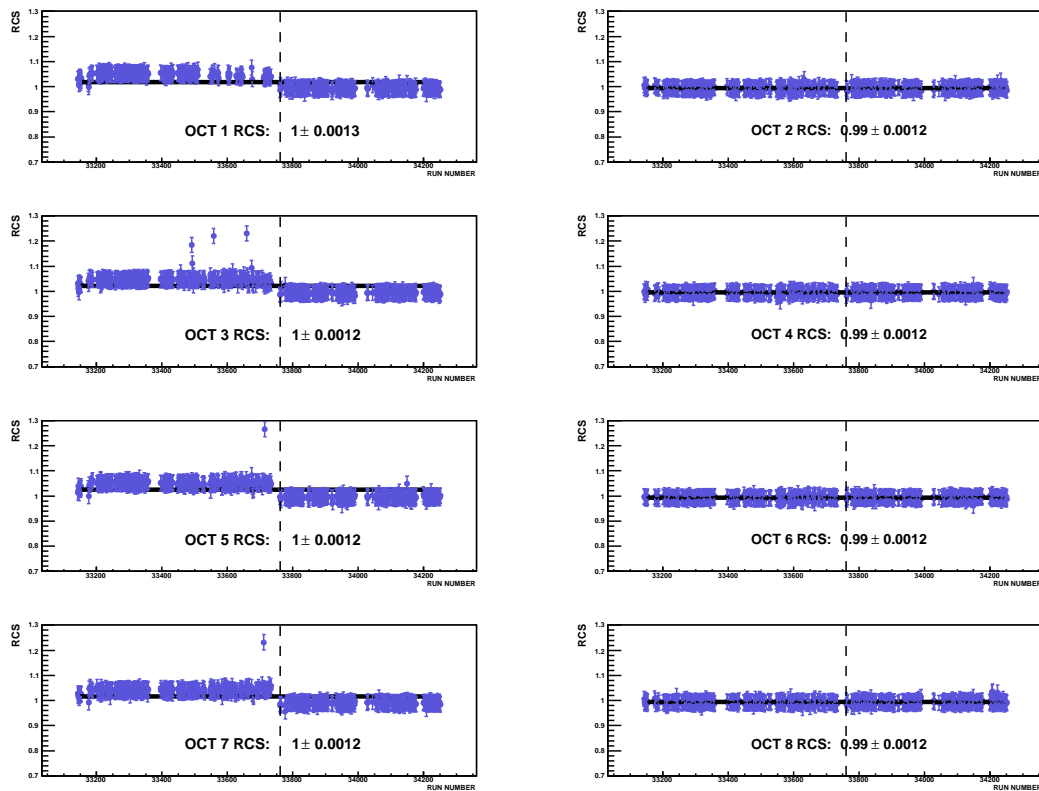


FIG. B.7: Corrected octant-by-octant RCS as a function of run number for all runs performed during the low-energy deuterium run period. NA octants are shown on the left and FR octants on the right. The vertical line indicates when the electronics were reprogrammed. All runs to the left of the line were performed with the problem present and all runs to the right were performed without. In each plot, the RCS has been fit to a constant and the average is presented.

Comparison of Pass 1 and Pass 2 Asymmetries			
		$A_{elastic}$	$A_{inelastic}$
H 362	Pass 1	$-9.78 \pm 0.63$	—
	Pass 2	$-9.74 \pm 0.60$	—
D 362	Pass 1	$-13.56 \pm 0.61$	—
	Pass 2	$-13.49 \pm 0.59$	—
H 687a	Pass 1	$-33.46 \pm 4.1$	$-19.16 \pm 4.9$
	Pass 2	$-33.37 \pm 4.1$	$-18.85 \pm 4.8$
H 687b	Pass 1	$-36.51 \pm 1.7$	$-20.23 \pm 2.0$
	Pass 2	$-36.83 \pm 1.7$	$-20.00 \pm 2.0$
D 687a	Pass 1	$-39.26 \pm 2.9$	$-15.74 \pm 2.7$
	Pass 2	$-38.98 \pm 2.8$	$-15.48 \pm 2.7$
D 687b	Pass 1	$-35.79 \pm 3.0$	$-14.11 \pm 2.6$
	Pass 2	$-35.76 \pm 3.0$	$-14.06 \pm 2.6$

*All values given in ppm*

TABLE B.6: Elastic and inelastic locus average asymmetries from all run periods with and without the scaler counting correction applied.

# APPENDIX C

## Background Correction

The background correction was the largest correction applied to the inelastic asymmetry and had the largest systematic effect on the error. Detailed analysis using a combination of data and simulation was performed to determine the proportion in which the major background processes contributed to the measured yield in each cell. While a summary of the correction to the asymmetry is given in Chapter 5, details of the individual contributions to the yield will be presented here. Additionally, detailed comparisons among the background correction method used in this analysis and two methods used for the elastic analysis will be presented.

### C.1 Contributions to the Yield

The yield in the inelastic locus contains significant contributions from as many as four additional processes: elastic scattering, scattering from the target windows,  $\pi^0$  decay and  $\pi^-$  contamination. A summary of the percent contributions, or dilution factors  $f_{bg}$ ,

found for each process for both the hydrogen and deuterium targets can be found in Tables C.1 - C.4. Each table contains the dilution factor in each octant for the indicated process averaged across both the inelastic and the elastic loci. Individual cell results for cells in the inelastic locus are presented in Figures C.1 and C.2 for each process with all octants plotted separately. The ordering of the cells on the  $x$ -axis was chosen such that the cell with the lowest numbered CED and FPD is first and cells are grouped by CED. The contribution from the  $\pi^-$  contamination present in the deuterium data is not included in the tables or figures as this value is taken to be constant across all cells and octants.

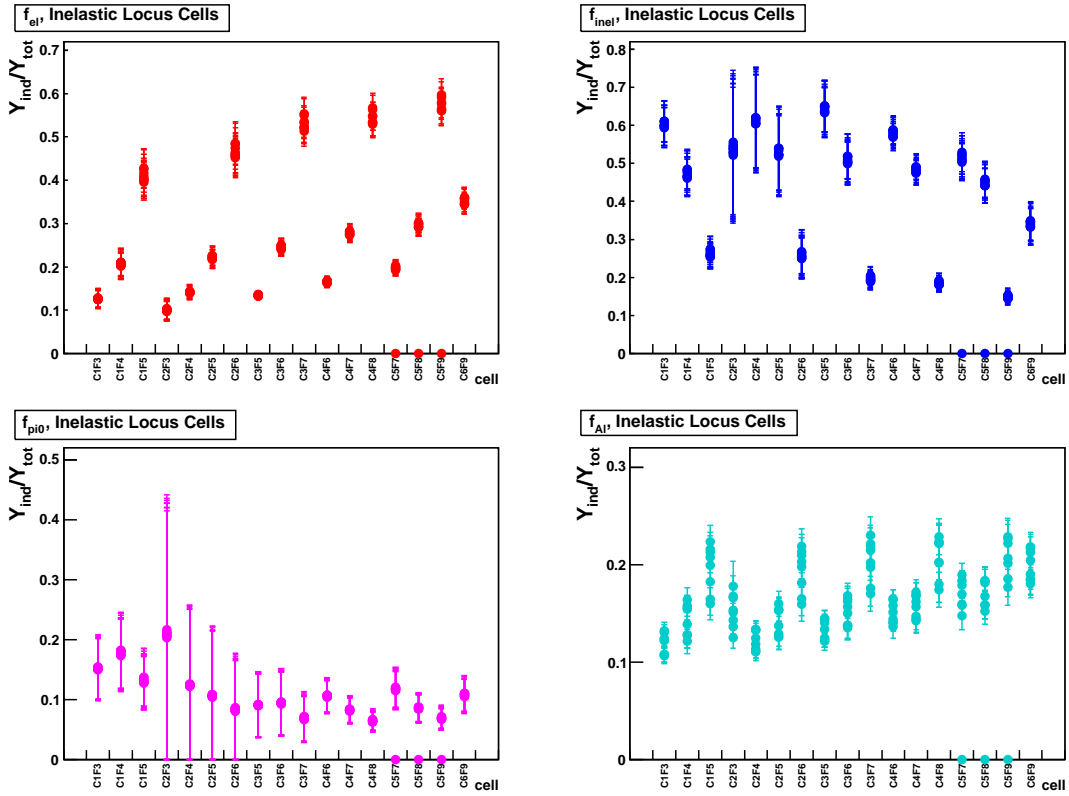


FIG. C.1: Cell dilution factors for each process for all octants for hydrogen. The errorbars shown include all correlated and uncorrelated errors. Note that the three points at 0 in CED 5 are due to the bad PMTs in octant 1. These have not been included in any averaging.

Summary of Inelastic Dilution Factors				
	H 687MeV		D 687MeV	
Octant	$f_i^{inel}$	$f_i^{el}$	$f_i^{inel}$	$f_i^{el}$
1	$48.77 \pm 2.7$	$0.02 \pm 0.01$	$36.96 \pm 2.2$	$0.06 \pm 0.02$
2	$47.07 \pm 2.4$	$0.02 \pm 0.01$	$36.63 \pm 2.0$	$0.05 \pm 0.02$
3	$48.21 \pm 2.4$	$0.02 \pm 0.01$	$36.51 \pm 1.9$	$0.05 \pm 0.02$
4	$47.78 \pm 2.4$	$0.02 \pm 0.01$	$36.14 \pm 1.9$	$0.05 \pm 0.02$
5	$45.23 \pm 2.3$	$0.02 \pm 0.01$	$34.68 \pm 1.9$	$0.06 \pm 0.02$
6	$46.40 \pm 2.4$	$0.02 \pm 0.01$	$36.05 \pm 2.0$	$0.05 \pm 0.02$
7	$47.80 \pm 2.4$	$0.02 \pm 0.01$	$36.42 \pm 1.9$	$0.05 \pm 0.02$
8	$48.44 \pm 2.5$	$0.02 \pm 0.01$	$37.65 \pm 2.1$	$0.06 \pm 0.02$
Avg	$47.48 \pm 2.1$	$0.02 \pm 0.00$	$36.41 \pm 1.2$	$0.06 \pm 0.01$

TABLE C.1: Per octant inelastic dilution factors for the elastic and inelastic loci.

Summary of Elastic Dilution Factors				
	H 687MeV		D 687MeV	
Octant	$f_i^{inel}$	$f_i^{el}$	$f_i^{inel}$	$f_i^{el}$
1	$23.70 \pm 0.69$	$88.84 \pm 1.7$	$29.04 \pm 0.60$	$85.52 \pm 1.2$
2	$24.70 \pm 0.63$	$88.93 \pm 1.6$	$30.08 \pm 0.55$	$86.04 \pm 1.2$
3	$26.25 \pm 0.67$	$90.85 \pm 1.6$	$31.19 \pm 0.57$	$87.08 \pm 1.2$
4	$26.39 \pm 0.68$	$90.14 \pm 1.6$	$31.36 \pm 0.58$	$86.65 \pm 1.2$
5	$27.35 \pm 0.72$	$88.53 \pm 1.7$	$32.53 \pm 0.62$	$85.71 \pm 1.3$
6	$25.63 \pm 0.66$	$89.17 \pm 1.6$	$31.47 \pm 0.59$	$86.72 \pm 1.2$
7	$26.98 \pm 0.69$	$91.14 \pm 1.6$	$32.08 \pm 0.60$	$87.69 \pm 1.2$
8	$24.75 \pm 0.62$	$89.92 \pm 1.6$	$30.05 \pm 0.55$	$86.64 \pm 1.2$
Avg	$25.68 \pm 0.43$	$89.72 \pm 1.2$	$30.95 \pm 0.26$	$86.53 \pm 0.59$

TABLE C.2: Per octant elastic dilution factors for the elastic and inelastic loci.

Summary of $\pi^0$ Decay Dilution Factors				
	H 687MeV		D 687MeV	
Octant	$f_i^{inel}$	$f_i^{el}$	$f_i^{inel}$	$f_i^{el}$
1	$11.54 \pm 3.7$	$2.60 \pm 0.66$	$14.21 \pm 4.2$	$3.70 \pm 1.04$
2	$11.13 \pm 3.6$	$2.36 \pm 0.59$	$13.59 \pm 4.0$	$3.33 \pm 0.94$
3	$11.41 \pm 3.5$	$2.43 \pm 0.61$	$13.49 \pm 4.0$	$3.49 \pm 0.89$
4	$11.30 \pm 3.5$	$2.27 \pm 0.57$	$13.37 \pm 3.9$	$3.20 \pm 0.86$
5	$10.95 \pm 3.3$	$2.56 \pm 0.65$	$13.19 \pm 3.9$	$3.66 \pm 1.03$
6	$11.01 \pm 3.4$	$2.26 \pm 0.57$	$13.49 \pm 4.0$	$3.19 \pm 0.85$
7	$11.41 \pm 3.5$	$2.40 \pm 0.60$	$13.64 \pm 4.1$	$3.38 \pm 0.86$
8	$11.42 \pm 3.6$	$2.46 \pm 0.62$	$13.89 \pm 4.2$	$3.50 \pm 0.91$
Avg	$11.27 \pm 3.2$	$2.41 \pm 0.61$	$13.61 \pm 3.6$	$3.43 \pm 0.87$

TABLE C.3: Per octant  $\pi^0$  decay dilution factors for the elastic and inelastic loci.

Summary of Empty Target (Al) Dilution Factors				
	H 687MeV		D 687MeV	
Octant	$f_i^{inel}$	$f_i^{el}$	$f_i^{inel}$	$f_i^{el}$
1	$15.99 \pm 0.88$	$8.50 \pm 0.45$	$9.80 \pm 0.54$	$6.36 \pm 0.34$
2	$17.10 \pm 0.93$	$8.65 \pm 0.47$	$9.71 \pm 0.53$	$6.20 \pm 0.33$
3	$14.13 \pm 0.79$	$6.66 \pm 0.35$	$8.70 \pm 0.48$	$4.95 \pm 0.26$
4	$14.54 \pm 0.81$	$7.53 \pm 0.40$	$9.05 \pm 0.51$	$5.70 \pm 0.30$
5	$16.47 \pm 0.91$	$8.87 \pm 0.48$	$9.58 \pm 0.53$	$6.20 \pm 0.34$
6	$16.96 \pm 0.92$	$8.50 \pm 0.46$	$8.90 \pm 0.48$	$5.64 \pm 0.31$
7	$13.82 \pm 0.76$	$6.41 \pm 0.34$	$7.63 \pm 0.42$	$4.43 \pm 0.24$
8	$15.38 \pm 0.84$	$7.55 \pm 0.42$	$8.25 \pm 0.45$	$5.39 \pm 0.30$
Avg	$15.57 \pm 0.82$	$7.80 \pm 0.41$	$8.95 \pm 0.47$	$5.59 \pm 0.29$

TABLE C.4: Per octant aluminum/empty target dilution factors for the elastic and inelastic loci.

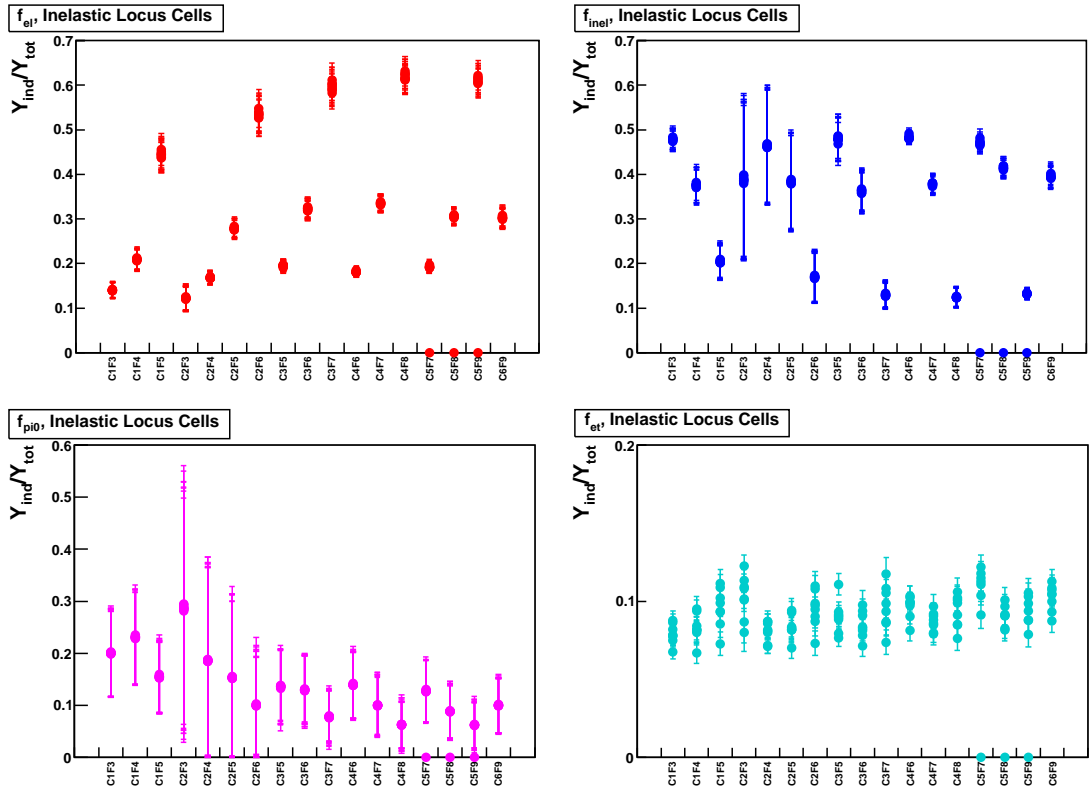


FIG. C.2: Cell dilution factors for each process for all octants for deuterium. The errorbars shown include all correlated and uncorrelated errors. Note that the three points at 0 in CED 5 are due to the bad PMTs in octant 1. These have not been included in any averaging.

## C.2 Comparisons to Other Methods

In addition to the method used to correct the inelastic asymmetry, which was unique to the inelastic analysis, two other methods were used to determine backgrounds: the field scan method and the matrix fit method. The field scan method was used to apply the correction for the published elastic asymmetry, while the matrix fit method was used as a confirmation of the elastic results for hydrogen. Each of these methods provided cell-by-cell information for each contributing process, allowing for comparisons to be made among the results anywhere in the matrix. A comparison of all three methods within the inelastic locus will be presented here along with cell-by-cell results in the elastic locus. Locus average results for the elastic locus were given in Section 5.2.4.

Figures C.3 and C.4 show a comparison of the hydrogen results from the different methods for the inelastic locus. In each plot, results from a typical octant are shown for the inelastic and field scan methods, while the octant average is shown for the matrix fit method. For the field scan method, the errors shown represent an estimate of the minimum error in each cell and are set to 10% of the dilution. The actual error is likely higher, so the value used here should be thought of as a lower bound. In Figure C.3, total inelastic dilutions for the field scan, matrix fit and inelastic methods are shown cell-by-cell. All three methods agree within errors in every cell, although, in general, the central values of the matrix fit and field scan methods are slightly higher than those of the inelastic method. The individual contributions are shown in Figure C.4. Although the total background generally agrees, the individual contributions differ for the empty target and  $\pi^0$  decay dilution factors. The inelastic method found the aluminum to contribute at least as much, if not more, than  $\pi^0$  decay. While the field scan method finds the same general trend, the matrix fit results show  $\pi^0$  decay contributing significantly more. It is

not clear why these results differ. All three methods used the same implementation of  $\pi^0$  decay in the simulation, and both the matrix fit and field scan methods used simulation for the yield from the target windows.

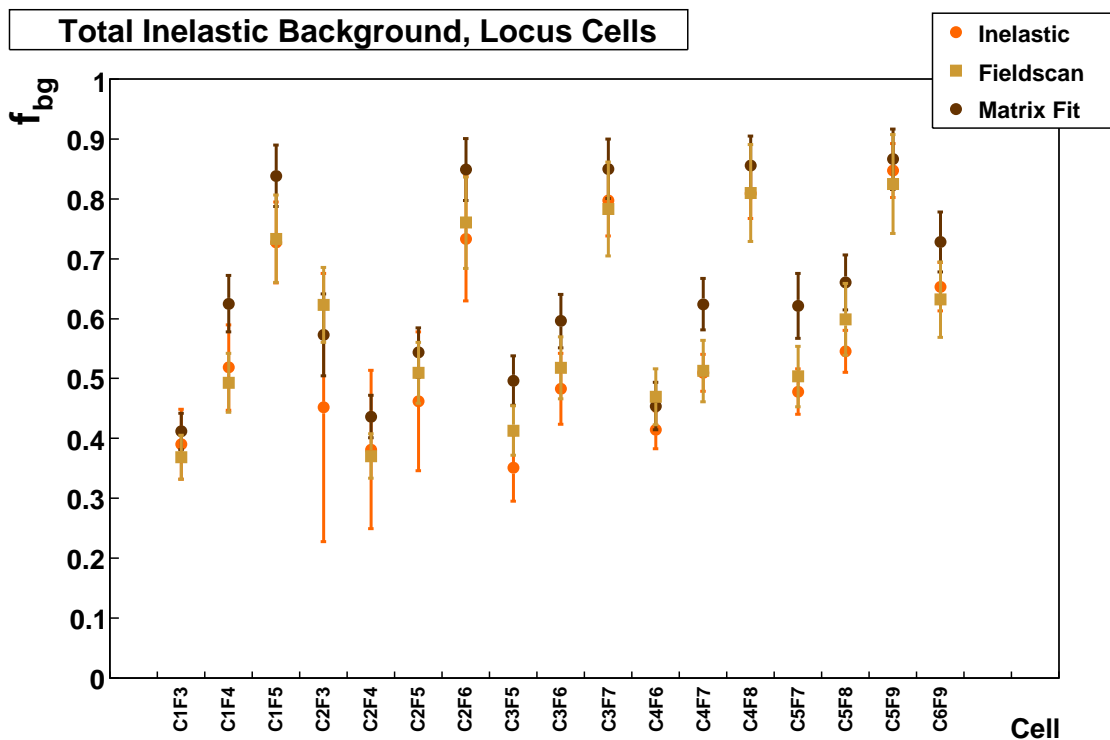


FIG. C.3: Comparison of inelastic, field scan and matrix fit method hydrogen total inelastic dilution factors cell-by-cell.

Figure C.5 shows the total background in the elastic locus cell-by-cell for the hydrogen data. The inelastic and field scan method dilution factors are given for all octants while the matrix fit result shown is the octant average. The three methods generally agree within errors, although in some cells bordering the superelastic region the matrix fit result is significantly higher than the other two. A comparison of the total cell background determined by the inelastic and field scan methods for the deuterium data is shown in Figure C.6. The matrix fit was not performed for the deuterium data. As with the hydrogen

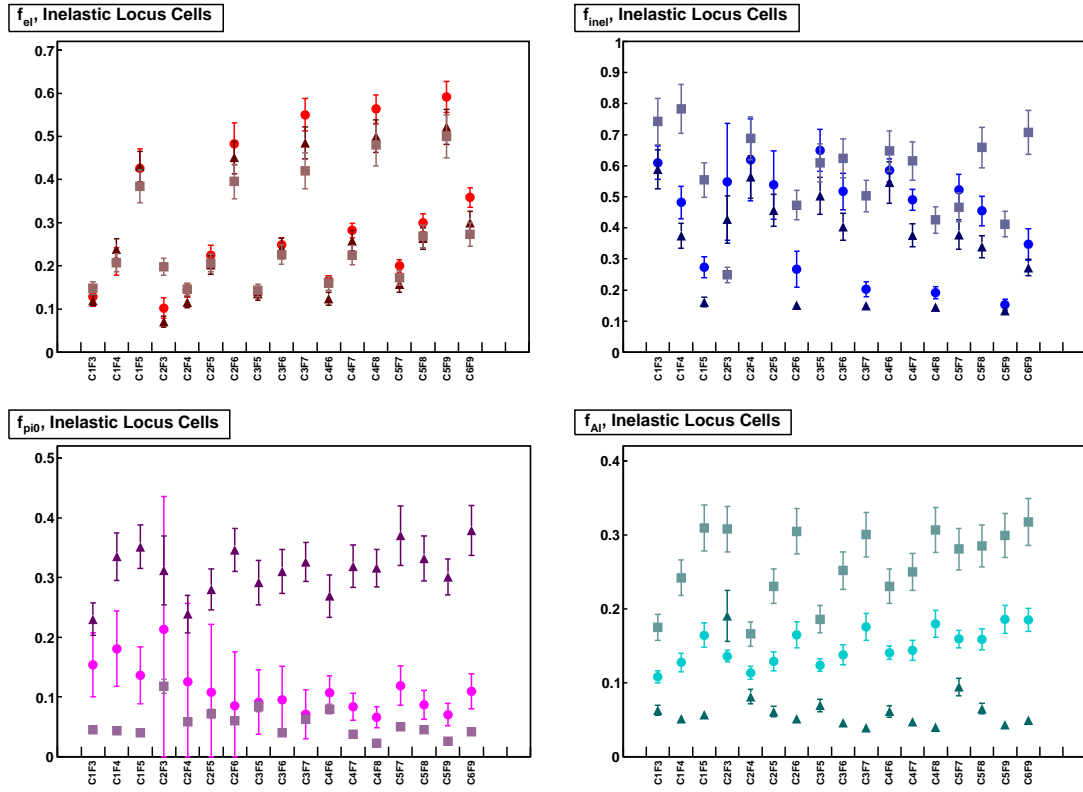


FIG. C.4: Comparison of inelastic (circle), field scan (square) and matrix fit (triangle) method dilution factors cell-by-cell in the inelastic locus for each process. Note that in one cell, CED2/FPD5, the field scan value for the inelastic contribution was greater than 1, so it does not appear in the plot.

comparison, the total background contribution is given for every octant in all cells within the elastic locus. Again the inelastic and field scan methods agree within errors in every cell. The five points that show zero are the cells affected by the bad PMTs and have not been included in any fits or averaging.

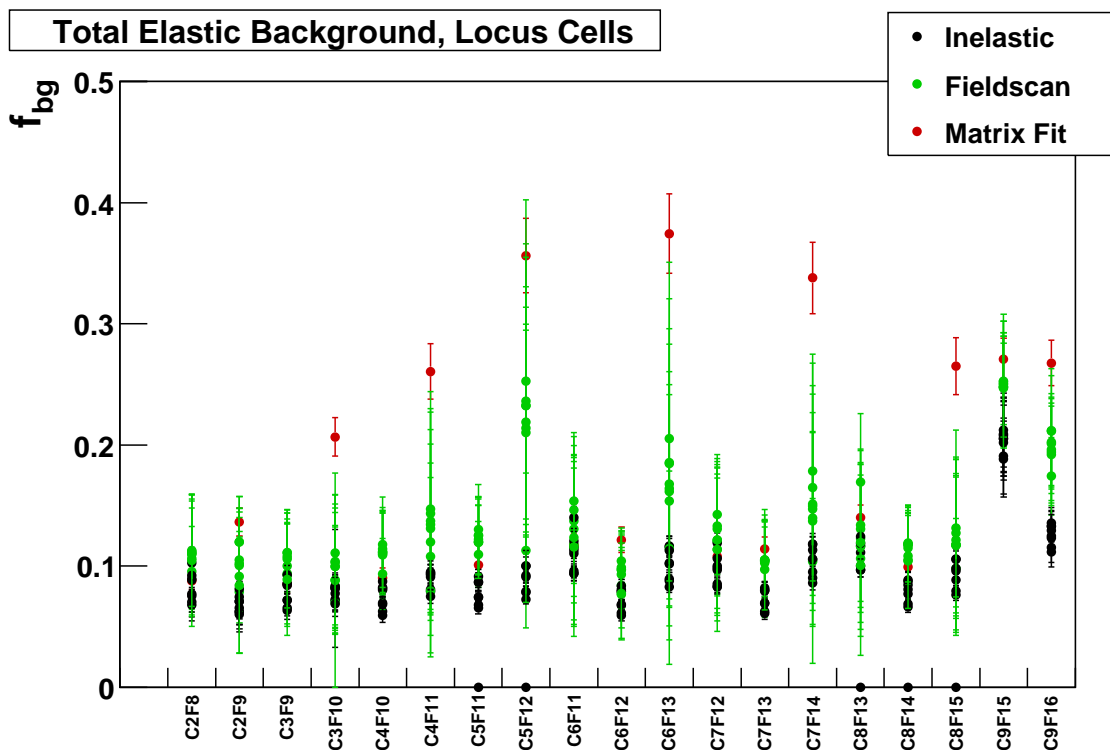


FIG. C.5: Comparison of inelastic method, field scan method and matrix fit method elastic locus dilution factors cell-by-cell for hydrogen. The dilution here is the total background (inelastic, Al and  $\pi^0$  decay) in the locus.

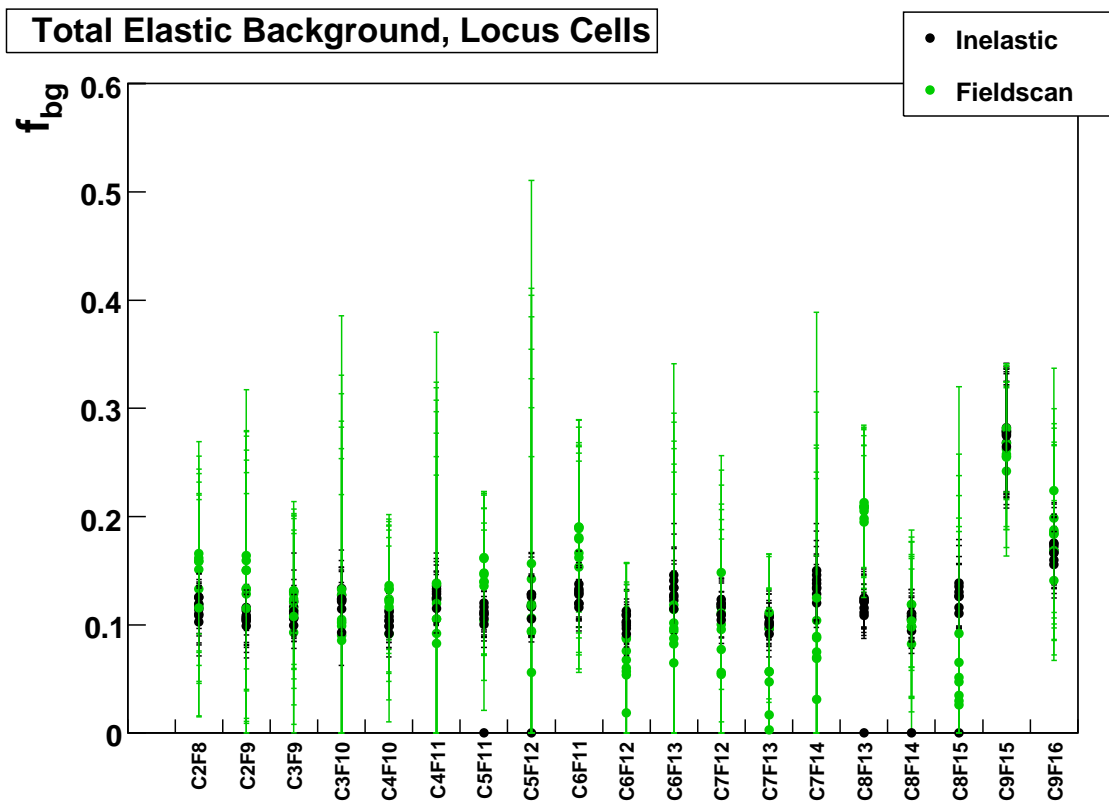


FIG. C.6: Comparison of inelastic method and field scan method elastic dilution factors cell-by-cell for deuterium. The dilution here is the total background relative to the elastics (inelastic, A1 and  $\pi^0$  decay).

## Bibliography

- [1] E. M. Lyman, A. O. Hanson and M. B. Scott, Phys. Rev. **84**, 626 (1951).
- [2] K. Nakamura *et al.* (Particle Data Group), J. Phys. G **37**, 075021 (2010).
- [3] T. D. Lee and C. N. Yang, Phys. Rev. **104**, 254 (1956), and references therein.
- [4] C. S. Wu, E. Ambler, R. W. Hayward, D. D. Hoppes and R. P. Hudson, Phys. Rev. **105**, 1413 (1957).
- [5] J. I. Friedman and V. L. Telegdi, Phys. Rev. **105**, 1681 (1957).
- [6] S. S. M. Wong, *Introductory Nuclear Physics* (Prentice Hall, 1990).
- [7] I. Niculescu, Ph.D. thesis, Hampton University, 1999, unpublished.
- [8] S. L. Adler, Ann. Phys. **50**, 189 (1968).
- [9] D. S. Armstrong *et al.* (G0 Collaboration), Phys. Rev. Lett. **99**, 092301 (2007).
- [10] The  $G^0$  Collaboration, B. Pasquini, M. Vanderhaeghen, Phys. Rev. Lett. **107**, 022501 (2011).
- [11] R. N. Cahn and F. J. Gilman, Phys. Rev. D **17**, 1313 (1978).
- [12] L. M. Nath, K. Schilcher and M. Kretzschmar, Phys. Rev. D **25**, 2300 (1982).
- [13] D. H. Beck and R. D. McKeown, Ann. Rev. Nucl. Part. Sci. **51**, 189 (2001).

- [14] C. H. Llewellyn Smith, Phys. Rept. **3**, 261 (1972).
- [15] W. Rarita and J. Schwinger, Phys. Rev. **60**, 61 (1941).
- [16] F. Halzen and A. D. Martin, *Quarks & Leptons: An Introductory Course in Modern Particle Physics* (John Wiley & Sons, 1984).
- [17] K. Kumar and P. Souder, Prog. Part. Nucl. Phys. **45**, S333 (2000).
- [18] S.-L. Zhu, S. J. Puglia, B. R. Holstein and M. J. Ramsey-Musolf, Phys. Rev. D **62**, 033008 (2000).
- [19] D. S. Armstrong *et al.* ( $G^0$  Collaboration), Phys. Rev. Lett. **95**, 092001 (2005).
- [20] D. Androić *et al.* ( $G^0$  Collaboration), Phys. Rev. Lett. **104**, 012001 (2010).
- [21] K. Paschke, A. Thomas, R. Michaels and D. Armstrong, J. Phys. : Conf. Ser. **299**, 012003 (2011).
- [22] M. J. Musolf *et al.*, Phys. Rept. **239** (1994).
- [23] P. Q. Hung and J. J. Sakurai, Ann. Rev. Nucl. Part. Sci. **31**, 375 (1981).
- [24] N. C. Mukhopadhyay *et al.*, Nucl. Phys. A **633**, 481 (1998).
- [25] S.-L. Zhu, C. M. Maekawa, G. Sacco, B. R. Holstein and M. J. Ramsey-Musolf, Phys. Rev. D **65**, 033001 (2001).
- [26] H. W. Hammer and D. Dreschel, Z. Phys A. **353**, 321 (1995).
- [27] S. L. Adler, Phys. Rev. D **12**, 2644 (1975).

- [28] J. Arrington, K. de Jager and C. F. Perdrisat, J. Phys. : Conf. Ser. **299**, 012002 (2011).
- [29] V. Bernard, L. Elouadrhiri and U.-G. Meissner, J. Phys. G **28**, R1 (2002).
- [30] P. A. Schreiner and F. von Hippel, Nucl. Phys. B **58**, 333 (1973).
- [31] D. Jones and S. Petcov, Phys. Lett. B **91**, 137 (1980).
- [32] C. Juszczak, J. T. Sobczyk and J. Żmuda, Phys. Rev. C **82**, 045502 (2010).
- [33] R. Gran, E. J. Jeon *et al.* (K2K Collaboration), Phys. Rev. D **74**, 052002 (2006).
- [34] X. Espinal and F. Sánchez, AIP Conf. Proc. **967**, 117 (2007).
- [35] M. Dorman (MINOS Collaboration), AIP Conf. Proc. **1189**, 133 (2009).
- [36] V. Lyubushkin *et al.*, Eur. Phys J. C **63**, 355 (2009).
- [37] B. Bhattacharya, R. J. Hill and G. Paz, Phys. Rev. D **84**, 073006 (2011).
- [38] J. Nieves, I. Ruiz-Simo and M. Vicente-Vacas (2011), arXiv:1110.1200v1 [hep-ph].
- [39] K. Matsui, T. Sato and T. S. H. Lee, Phys. Rev. C **72**, 025204 (2005).
- [40] T. R. Hemmert, B. R. Holstein and N. C. Mukhopadhyay, Phys. Rev. D **51**, 158 (1995).
- [41] A. J. F. Siegert, Phys. Rev. **52**, 787 (1937).
- [42] J. L. Friar and S. Fallieros, Phys. Rev. C **29**, 1645 (1984).
- [43] A. F. C. Coppens, Ph.D. thesis, University of Manitoba, 2010, unpublished.

- [44] S. P. Wells, T. A. Forest and K. E. Myers, Qweak Document: Qweak-doc-1093-v2 (2009), unpublished.
- [45] S. P. Wells, private communication.
- [46] J.-F. Rajotte (The Qweak Collaboration) (2011), arXiv:1110.2218v1 [hep-ex].
- [47] D. Androić *et al.*, Nucl. Instrum. Meth. **A646**, 59 (2011).
- [48] C. W. Leemann *et al.*, Annu. Rev. Nucl. Part. Sci. **51**, 413 (2001).
- [49] R. D. McKeown, J. Phys. : Conf. Ser. **312**, 032014 (2011).
- [50] C. K. Sinclair *et al.*, Phys. Rev. ST Accel. Beams **10**, 023501 (2007).
- [51] M. Hauger *et al.*, Nucl. Instrum. Meth. **A462**, 382 (2001).
- [52] J. M. Grames *et al.*, Phys. Rev. ST Accel. Beams **7**, 042802 (2004).
- [53] D. Gaskell and T. Horn (2008),  $G^0$  Document 804-v1, unpublished.
- [54] J. M. Grames, Ph.D. thesis, University of Illinois at Urbana-Champaign, 2000.
- [55] N. Sherman, Physical Review **103**, 1601 (1956).
- [56] S. D. Covrig *et al.*, Nucl. Instrum. Meth. **A551**, 218 (2005).
- [57] L. Lee (2006),  $G^0$  Document 633-v1, unpublished.
- [58] H. Breuer *et al.* (2006),  $G^0$  Document 677-v1, unpublished.
- [59] Jefferson Lab Data Acquisition Group, coda.jlab.org.
- [60] ROOT Development Team, root.cern.ch.

- [61] M. Versteegen, Ph.D. thesis, Université Joseph Fourier Grenoble 1, 2010, unpublished.
- [62] P. Pillot and C. Furget, Deadtime Correction Report and Addendum (Internal Report)  $G^0$  Document 679-v1, unpublished.
- [63] J. Schaub, Ph.D. thesis, New Mexico State University, 2010, unpublished.
- [64] C. E. Carlson and M. Vanderhaeghen, *Ann. Rev. Nucl. Part. Sci.* **57**, 171 (2007).
- [65] J. M. Mammei, Ph.D. thesis, Virginia Polytechnic Institute and State University, 2010, unpublished.
- [66] CERN Applications Software Group, CERN Program Library Long Writeup W5013, unpublished.
- [67] M.E. Christy, P.B. Bosted (2007), arXiv:0712.3731v3 [hep-ph].
- [68] M.E. Christy, P.B. Bosted (2008), arXiv:0711.0159v4 [hep-ph].
- [69] C. Keppel, Ph.D. thesis, American University, 1994.
- [70] J. J. Kelly, *Phys. Rev. C* **70**, 068202 (2004).
- [71] R. Schiavilla, J. Carlson and M. Paris, *Phys. Rev. C* **70**, 044007 (2004).
- [72] M. Muether, Ph.D. thesis, University of Illinois at Urbana-Champaign, 2010, unpublished.
- [73] C. Ellis, Ph.D. thesis, University of Maryland, College Park, 2010, unpublished.
- [74] D. Drechsel, S.S. Kamalov, L. Tiator, *Nucl. Phys.* **A645**, 145 (1999).

- [75] T. S. H. Lee, private communication.
- [76] F. Feinstein, Nucl. Instrum. Meth. **A504**, 258 (2003).
- [77] F. James, CERN Program Library Long Writeup D506, unpublished.
- [78] L. Mo and Y. Tsai, Rev. Mod. Phys **41**, 205 (1969).
- [79] Y. Tsai (1971), SLAC-PUB-848.
- [80] E. Beise, M. Pitt and D. Spayde, Prog. Part. Nucl. Phys. **54**, 289 (2005).
- [81] S. Fanchiotti, B. Kniehl and A. Sirlin, Phys. Rev. D **48**, 307 (1993).
- [82] F. Ravndal, Nuovo Cim. A **18**, 385 (1973).
- [83] A. Le Yaouanc, L. Oliver, O. Pène, J. C. Raynal and C. Longuemare, Phys. Rev. D **15**, 2447 (1977).